Dissertation

submitted to the
Combined Faculties of the Natural Sciences and Mathematics
of the Ruperto-Carola-University of Heidelberg, Germany
for the degree of
Doctor of Natural Sciences

Put forward by
Yifan Liu
born in JiangXi, China

Oral examination: June 26th, 2019

Two-Color Pump-Probe Experiments on O_2 and N_2 at the Free-Electron Laser in Hamburg

Referees: Priv.-Doz. Dr. Robert Moshammer
Prof. Dr. Andreas Wolf

Abstract

Within this thesis, the photoionization, fragmentation and autoionization of highly excited states of diatomic molecules (O_2 and N_2) induced by intense extreme-ultraviolet (XUV) radiation delivered by the Free-Electron-Laser in Hamburg (FLASH), is studied employing coincident three-dimensional recoil-ion momentum spectroscopy.

First, with an XUV-pump/THz-probe scheme, the relaxation dynamics of highly excited states of O_2 created by absorption of a single 60 eV XUV photon is investigated. The relative time shift between the first emitted photoelectron and a second low-energetic photoelectron carries information about the time difference between both photoemission steps or the autoionization lifetime. We have measured that the lifetime of the autoionizing excited cation state $^4\Sigma_g^-$ with a kinetic energy release (KER) of 4 eV is 102 ± 30 fs.

Second, the IR-assisted XUV multiphoton experiments of N_2 were performed in combination with a synchronized femtosecond optical laser. Aligned N_2^{n+} ions are created by sequential absorption of XUV photons and further excited or ionized by a delayed NIR laser pulse. By tracing the time-dependent KERs of double ionization products $N_2^{2+} \rightarrow N^+ + N^+$ (N(1,1)) and triple ionization products $N_2^{3+} \rightarrow N^{2+} + N^+$ (N(2,1)), we find an enhancement factor for N(1,1) of 2.2 and for N(2,1) of 5.7 compared to without NIR. The detailed dissociative pathways are traced by KERs and angular distribution of ionic fragments.

Zusammenfassung

In dieser Arbeit wird mittels dreidimensionaler Rückstoss-Ionen-Impuls-Spektroskopie die Photoionisation, Fragmentierung und Autoionisation hochangereger Zustände von zweiatomigen Molekülen (O_2 und N_2) untersucht, die durch intensive, extrem ultraviolette (XUV) Strahlung des Freie-Elektronen-Lasers (FLASH) in Hamburg induziert wird.

Das erste Experiment bestand darin, innerhalb eines XUV-Pump/THz-Probe-Schema, die Relaxationsdynamik hochangeregter Molekülzustände von O_2 zu untersuchen, die durch Absorption eines einzelnen 60 eV XUV-Photons angeregt wurden. Die zeitliche Verzögerung zwischen dem zuerst emittierten Photoelektron und einem zweiten niederenergetischen Photoelektron beinhaltet Information über die Zeitdifferenz zwischen den beiden Photoemissions-Schritten oder der Autoionisations Lebenszeit. Für das niederenergetische Autoionisierungselektron aus dem hochangeregten Molekülzustand $^4\Sigma_g^-$ mit einer KER von 4 eV haben wir eine Lebenszeit von 102 ± 30 fs gemessen.

Im zweiten Experiment wurde IR-gestützte XUV-Multiphotoionisation von N_2 in Kombination mit einem synchronisierten optischen Femtosekundenlaser durchgeführt. Sequentielle Absorption von XUV Photonen erzeugte räumliche ausgerichtete N_2^{n+} Photonen, die durch NIR Laser Pulse weiter angeregt oder ionisiert wurden. Durch Verfolgen der zeitabhängigen kinetischen Energiefreisetzung (KER) der Doppelionisations-Produkte $N_2^{2+} \rightarrow N^+ + N^+$ (N(1,1)) und Dreifachionisations-Produkte $N_2^{3+} \rightarrow N^{2+} + N^+$ (N(2,1)), finden wir einen Verstärkungsfaktor in der Ionisationsrate für N(1,1) von 2.2 und für N(2,1) von 5.7 verglichen zum Fall ohne NIR. Die detaillierten Dissoziations-Pfade konnten durch KERs und die Winkelverteilung von ionischen Fragmenten zurückverfolgt werden.

Contents

Chapter 1

Introduction

The investigation of the interaction between matter and intense laser fields is one of the most flourishing areas of current research in atomic, molecular and optical (AMO) physics. The research on photoionization and ultrafast fragmentation reactions of few-body quantum systems allows a deeper insight into the atomic and molecular dynamics and the intermediate processes involved in various physical, chemical and biological reactions [1].

Photoionization is an important aspect of this thesis. In 1905, Albert Einstein explained the photoelectric effect by assuming that electromagnetic radiation of frequency ω can be treated in a particle-like manner [2, 3]. Matter can be ionized by absorbing a single photon and a photoelectron emitted. Therefore, the photon energy requires to be larger than the ionization potential. Due to the limited light intensity accessible in those days, the photoionization processes investigated can be well-described as a single photon ionization. The working principle of a laser (Light Amplification by Stimulated Emission of Radiation) was proposed by Einstein in 1916 [4], but only until 1960, the laser was invented [5]. Because of the high intensity of the laser pulse, the strength of the electromagnetic field is of the order of the atomic Coulomb field, the theoretical description of photoionization by an optical laser is complicated [3]. In 1965, L.V. Keldysh introduced the Keldysh parameter ($\gamma = \sqrt{\frac{I_p}{2U_p}}$, I_p being the ionization potential and U_p the ponderomotive energy) to distinguish different ionization mechanisms in a strong electromagnetic field [6]: the multiphoton ionization and tunneling ionization. If the binding energy of an electron is larger than its ponderomotive energy, several photons are needed to ionize the target which is described by a multiphoton ionization picture. However, if the ponderomotive energy is far larger than the binding energy, tunneling ionization picture is used to describe the ionization process. By increasing the strength and wavelength of the electromagnetic field, the tunneling ionization becomes a dominant process for the photoionization of atoms and molecules [7, 8]. Although the two ionization mechanisms can be well understood, many questions remain. For instance, with the Keldysh parameter around 1, both ionization mechanisms have a contribution to the ionization yield.

Atoms and molecules exposed to an intense laser field, thus lose one or more-electrons. Now, let us take a look at photoionization and the relaxation processes induced by XUV radiation. An XUV laser pulse with (sub-) femtoseconds pulses length triggers the elec-

tronic motion by inducing valence or core photoelectron emission. The electrons are either excited to an unoccupied orbital ("shake-up") or excited into the continuum ("shake-off") [9, 10]. An inner-valence electron of an atomic and molecular system is ionized and results in a vacancy. Subsequently, the vacancy can be filled by an outer-valence electron. Once the target is ionized, a series of fragmentation and relaxation processes are triggered. The fragmentation ions will dissociate or Coulomb explode into different stable states. Some of the highly excited states will decay by transferring the excess energy to other electrons or by ejecting an electron carrying away the released energy. The fundamental processes such as Auger Decay and Autoionization will also take place if it is energetically allowed. Autoionization is a basic process that takes place in atoms, molecules and biological systems, which is essential to reveal the electronic many-body problems play in the highly excited energy regime [11–13]. In the fragmentation process of the molecular systems, the molecular environment plays a vital role [12, 14]. The reason is that the final states changed in a molecular ion during the electronic and nuclear motion, and thus the ionization threshold is lowered. For instance, the interatomic or intermolecular Coulombic decay (ICD) process takes place in weakly bound van-der-Waals and hydrogen bound clusters [15–17].

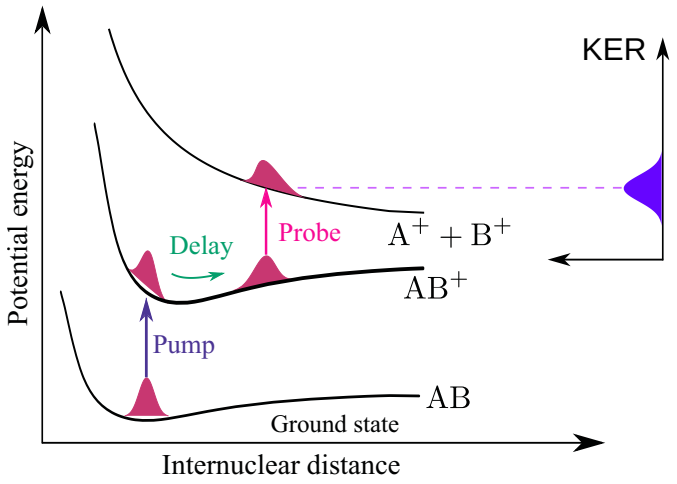

Figure 1.1: Illustration of the pump-probe technique in the molecular system *AB*. The internuclear distance dependent KER spectrum is plotted. The time delay indicates the detailed fragmentation information. Figure adapted from [16].

The invention of the pump-probe technique has become one of the fundamental tools for probing the dynamics of inter- and intra-molecular chemical reactions on femtosecond time scales. In Fig. 1.1, the principle of the pump-probe technique is shown, firstly, a pump-pulse is used to ionize and simultaneously populate the molecule *AB* to an excited state, thereby triggering the nuclear motion. After a time delay, the second probe pulse further ionizes the molecular ion to a highly lying dissociative state, leading to its fragmentation by Coulomb explosion [16, 18]. The physical description of photo-excitation and subsequent ionization of the molecular system are based on the Born-Oppenheimer approximation [19] and Franck-Condon principle [20]. The underlying assumption of the Born-Oppenheimer approximation is that the nuclear coordinate is frozen during an

electronic transition from the initial state to another [21]. The reaction pathways can be inferred from the kinetic energy release (KER, the total kinetic energy of fragments) distribution of the fragments. The KER distributions depend on the final dissociative states and are determined by the internuclear distance at the moment of dissociation. It is the basis for us to identify the different dissociative states after the target is ionized.

In order to probe and resolve the ultrafast dynamics that take place during a photon-matter interaction, an ultrashort laser pulse is required. The typical scales of length are smaller than a nanometer (1 nm = 10^{-9} m) for small molecules, and the scales of time vary from attoseconds (1 as = 10^{-18} s) for the electronic dynamics, to femtoseconds (1 fs = 10^{-15} s) for molecular vibration, to picoseconds (1 ps = 10^{-12} s) for molecular rotation [21]. With the advent of ultrashort laser pulses and the development of the pump-probe technique, it has become feasible to resolve the ultrafast dynamics of molecules on their natural timescale [22–30]. Intense femtosecond pulses from Free-Electron-Lasers (FELs) allow combining pump-probe techniques developed in modern femtochemistry, with the distinct imaging capabilities of X-rays, nurturing the dream of producing a "movie" of molecular reactions on their natural length and time scales [21, 22, 31, 32].

Recently, the development of FELs has enabled us to study and image complex systems with atomic resolution on ultrafast time scales [22, 33, 34]. FEL Imaging of complex systems relies on the "diffract-before-destroy" concept, where an ultrashort X-ray pulse yields a diffraction pattern before Coulomb explosion and reconstruction of many such patterns will render a three-dimensional model of the system [21, 35]. Generally, using the accelerator-based X-ray light sources one can probe ultrafast structural and electronic dynamics [30, 36], perform multidimensional non-linear X-ray spectroscopy of molecules [37], study non-linear process and coherent control of few-body quantum systems [38], investigate multiphoton processes and polarization control at short-wavelength FELs [39, 40], carry out single particle imaging and scattering in AMO physics [41], and explore electronic structure at high X-ray intensity [32]. All these femtosecond time scale dynamics can be probed by an ultrashort laser pulse and have been intensively investigated in the last decades [1, 42].

Improving the temporal and spatial resolution of pump-probe experiments is another essential technical in AMO physics. One of the crucial limitations for imaging the ultrafast dynamics is the pulse length of the probing laser pulse. It is possible to resolve the ultrafast dynamics only if the pulse length is shorter than the time scale of the molecular dynamics. The Nobel Prize in Physics 2018 was awarded one half to Gérard Mourou and Donna Strickland for the invention of high-intensity, ultra-short optical pulses which have significantly applied in basic research and practical applications [43]. In principle, attosecond laser pulse from high harmonic generation (HHG) is an ideal tool to resolve ultrafast electronic dynamics. However, the photon flux produced by HHG is many orders of magnitude lower than the XUV radiation delivered by FEL facilities [44]. Therefore, nowadays, the XUV laser pulses with sub-100 fs duration still play a dominant role in carrying out the pump-probe experiments. Apart from the duration of the pump pulse, another factor related to the experimental results of pump-probe experiments is the jitter and the long-term drift of pump and probe laser pulses during the measurement, especially in two-color pump-probe experiments. In order to improve the time resolution of this experiment, one possibility is to monitor the jitter of the pump- and probe-pulse. An

improvement in the timing precision of synchronization of the two laser pulses is essential to the shot-to-shot imaging experiments. The other factor involves achieving better spatial resolution and that depends on detection systems and imaging methods [23, 41].

In order to study and resolve the response of molecules to intense XUV radiation, two-color pump-probe experiments on O_2 and N_2 were performed at FLASH. Both experiments on small molecular systems presented in this thesis are performed employing recoil-ion momentum spectroscopy with a Reaction Microscope (REMI). It enables the determination of the ion and electron momentum vectors. The kinematically complete measurements ensure a solid angle acceptance of 4π for ions and electrons [23]. Utilizing the REMI and a split-and-delay (SD) unit [23, 45], we obtained the spatial and temporal information of the fragmentation and relaxation after XUV radiation.

In the THz streaking experiment on the autoionizing molecular cation state, the detailed autoionization process will be presented. When the molecule is ionized by XUV radiation, a highly excited state can be created which then subsequently ejects another electron through autoionization [12]. A so-called atomic-like autoionization process was observed after the inner-valence electron of molecular Oxygen was ionized by XUV radiation [11–13, 46–48]. With a high-resolution coincident ion-electron study, the detailed atomic-like character of the autoionization spectrum indicates that the autoionization takes place at large internuclear distances [12, 48]. In previous works [12, 49], the autoionization processes have been studied via ions and electrons coincidence measurements. From their time-dependent ions and electrons spectroscopy, the lifetimes of the autoionization processes are obtained. However, in our experiment, we adopted the THz streaking technique to track and separate the first emitted photoelectron and secondary autoionization electron directly. Using THz streaking technique, we can identify the photoelectrons from a direct ionization process or autoionization process as the autoionization electrons having time delays of tens to hundreds of femtoseconds. The details are discussed in Chapter 5.

In the second experiment, the IR-assisted XUV multiphoton ionization of N_2 is investigated. Few-photon multiple ionization pictures of molecules are essential to explore the photoionization steps. Within the regime of multiphoton ionization, one distinguishes between sequential and non-sequential photoionization. Sequential ionization is understood as a step-wise absorption via stationary intermediate real molecular states. In contrast, the non-sequential ionization is treated as a direct ionization via virtual intermediate states [50]. In order to understand the ionization mechanisms in N_2, the light-intensity dependence of the yields of charged particles will be shown. For the photoionization in the intense near-infrared laser (NIR) laser field (Keldysh parameter ~ 0.7), both multiphoton ionization and tunneling ionization can be used to interpret the experimental results [51, 52]. Once we know the photon absorption steps and KER distributions for various dissociation channels, then the detailed transition pathways can be identified. In the end, in order to find the relationship between the ionization gains and the polarization of the NIR field, the fragment ions angular distributions will be presented. Then, we will answer the question of whether the ionization rate depends on the relative alignment of the laser field and molecule orientation.

This thesis is organized as follows: Chapter 2 gives the theoretical background on the

photon-interaction and relaxation process and provides the basis for the explanation of the experimental results. Two basic ionization mechanisms, multiphoton ionization and tunneling ionization, will be introduced. Then, sequential ionization and non-sequential ionization will be discussed to characterize the photon absorption steps. In addition, the decay and relaxation processes of atomic and molecular systems are introduced. Furthermore, fragment ion angular distribution is presented to explain the formation of aligned molecular ions and enhanced ionization in the two color laser fields. In Chapter 3, the light sources provided by the FLASH facility, the detailed description of experimental set-ups and operation principles will be discussed. By utilizing the light sources delivered at FLASH, O_2 and N_2 molecules were ionized and a series of fragmentation and relaxation processes can be triggered. By means of REMI and SD optics, we can perform time and position resolved momentum spectroscopy on the produced ions and electrons. In Chapter 4, a brief introduction of THz streaking and THz-field-induced time shifts in molecular photoemission is given. In Chapter 5, the single- and double-photoionization of O_2, and the autoionization process streaked by a synchronized THz pulse will be discussed. In Chapter 6, the experimental results of the XUV-pump/IR-probe experiments on N_2 will be shown. The photoionization, fragmentation, and angular distribution of ionic fragments induced by the XUV and NIR radiation will be analyzed. In the final Chapter 7, two experimental results are summarized and an outlook is given.

Chapter 2

Background and Basic Principles

In this thesis, we will focus on the interaction of extreme ultraviolet radiation (XUV) and near-infrared radiation (NIR) with small molecules, which usually leads to photoionization and dissociation. The understanding of matter's response to the radiation requires different theoretical models and descriptions.

Photoionization is a fundamental process when the matter exposed to electromagnetic radiation. By absorbing one or multiple photons, the target is ionized and a series of subsequent relaxation processes can be triggered, such as dissociation, the re-distribution of energy and charge, and decay which take place within a few femtoseconds to tens of picoseconds [36, 53, 54]. The analysis of the response of atomic and molecular systems to electromagnetic radiation, especially radiation in the X-ray regime, is of vital importance for the understanding of the photon-matter interactions. This response depends on the wavelength and the field strength of the radiation. With the development of Free-Electron-Lasers (FELs) and pump-probe technique in recent decades, we have the opportunity to explore ultrafast molecular dynamics in a photoionization regime [1, 22, 42]. An X-ray is an excellent tool for direct imaging of matter on the length scales of atomic structure, which is on the order of Ångström [21]. Depending on which physical process to investigate, different wavelengths and strength of electromagnetic radiation are selected.

In this chapter, a detailed physical picture of atomic and molecular systems in intense laser fields will be introduced and discussed. The main topic of this thesis is the dynamics of small molecular systems (O_2 and N_2). The fundamental theories and mechanisms used in the following chapters are outlined in order to make it easier to understand the following experimental results. First, the different ionization pictures, multiphoton ionization and tunneling ionization, are discussed on a step-by-step basis in Sec. 2.1. The process of sequential and non-sequential ionization are presented in Sec. 2.2. In the following Sec. 2.3, Sec. 2.4 and Sec. 2.5, the theoretical description of the photoionization of atomic and molecular systems is presented. After the atomic and molecular systems are ionized by intense radiation, a series of relaxation processes can be followed, the relaxation and decay processes, especially after inner-shell ionization and autoionization process, which is commonly observed in molecular systems, are presented in Sec. 2.6. In the end, the fragment ion angular distribution is discussed in Sec. 2.7, which can be used to track the photoionization steps.

2.1 Single Ionization in Strong Fields

Single ionization is a fundamental subject which has been extensively studied by employing tabletop VUV (Vacuum ultraviolet) and HHG light sources and tunable synchrotron radiation. In this section, a brief overview is given for the ionization pictures of atoms in intense laser fields.

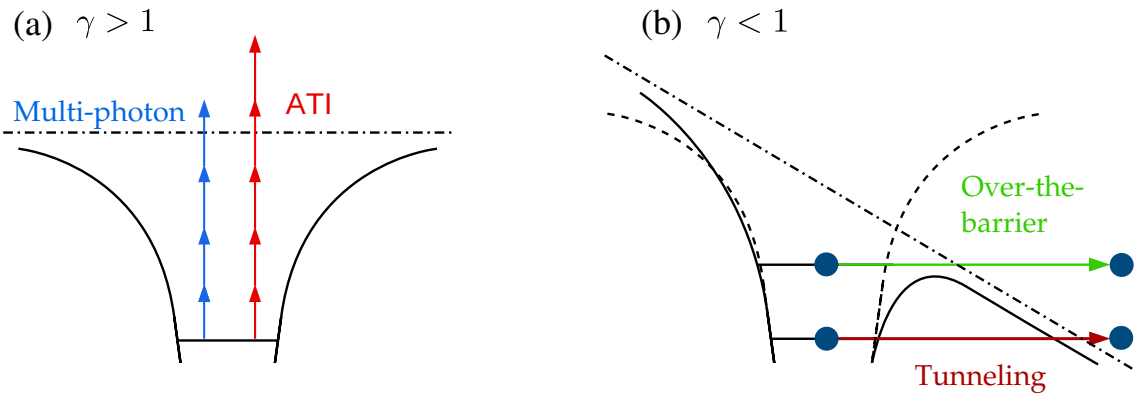

Figure 2.1: Photoionization processes in the atomic system. (a) Multi-photon ionization and Above Threshold ionization (ATI) regime ($\gamma \gg 1$). (b) Schematic diagram of strong-field photoionization for $\gamma \ll 1$ demonstrating tunnel ionization and over the barrier ionization. Figure adapted from [55].

In Fig. 2.1, the two different ionization pictures: multiphoton ionization and tunnel ionization are shown. Multiphoton ionization (MPI) and tunneling ionization (TI) are two significant pictures used to describe the ionization mechanism when an atom or a molecule is ionized in an intense laser field. The mechanisms depend on the ionization threshold and light intensity. In most experiments performed by synchrotron radiation sources, single-photon absorption is the dominant process due to the light intensities being low [7, 21]. However, with the advent of FELs with unprecedented intensities, multiphoton ionization has been one of the critical themes of photoionization physics in recent years [1]. In an intense FEL pulse, the number of photons per pulse is high enough that high-order processes involving multiple photons come into play.

Commonly, the Keldysh parameter used to specify the regime of the two ionization mechanisms is defined as [6]:

$$\gamma = \sqrt{\frac{\mathrm{I_p}}{2\,\mathrm{U_p}}}, \tag{2.1}$$

where $\mathrm{I_p}$ is the field-free ionization potential and $\mathrm{U_p}$ is the ponderomotive energy of an electron in the laser field. The Keldysh parameter equals the ratio between the tunneling time of an electron through a potential well and the period of the laser field. The ponderomotive energy $\mathrm{U_p}$ is the mean kinetic energy of a free electron gained in the laser field and is defined by

$$U_\mathrm{p} = \frac{e^2 E_0^2}{4 m_e \omega_\mathrm{laser}^2} = 9.338 \times 10^{-14}\,\mathrm{I\,[W/cm^2]}\,\lambda^2\,[\mu\mathrm{m}], \tag{2.2}$$

where E_0 is the maximum electric field strength of the oscillating field with frequency ω_{laser}, e denotes the absolute value of its charge and m_e is the mass of the electron. The Keldysh parameter γ indicates how strongly the field modifies the atomic Coulomb potential. For $\gamma \ll 1$, the Coulomb barrier is modified in such a way that the electron can tunnel out (tunneling picture), while for $\gamma \gg 1$ the electron is freed by a net absorption of many photons (multiphoton picture). In the X-ray regime, the ponderomotive energy ($U_p \sim 0.1$ eV) of an electron is far smaller than the ionization potential, so multiphoton is the dominant process. However, for $\gamma \sim 1$, there is no clear boundary between multiphoton ionization and tunneling ionization. In the following, we will discuss the two pictures in atomic systems.

Multiphoton Ionization

Here, let us discuss the multiphoton ionization reaction:

$$A^q + n\hbar\omega \longrightarrow A^{q+1} + e^-, \tag{2.3}$$

where q is the charge of the atomic system A, $\hbar\omega$ is the photon energy, and n is the number of photons. This process is a single electron process. A single photon cannot ionize an atom or molecule when the photon energy is less than the ionization potential I_p. Several photons have to be absorbed simultaneously to fulfill the condition: $n \cdot \hbar\omega \geq I_p$. Since the direct multiphoton ionization has a small cross-section, it requires high intensity for photoionization. By measuring the kinetic energy of the photoelectrons, the number of absorbing photons can be calculated. According to the perturbation theory, the absorption of n photons is thereby described by the n-th order of perturbation theory [56]. It states that the ionization rate is proportional to the n-th power of the light intensity:

$$\Gamma_n = \sigma_n \cdot I^n, \tag{2.4}$$

where σ_n is the n-photon ionization cross section and I is the laser intensity [57].

With the increase of the light intensity, the atomic system could absorb excess-photons which are larger than the minimum number required for ionization. The phenomena are known as above-threshold ionization (ATI). ATI is an extension of MPI where even more photons are absorbed than actually would be necessary to ionize the atom [58]. Similar to Eq. 2.4, the ATI rate after the absorption of n + s photons can be described as

$$\Gamma_{n+s} = \sigma_{n+s} \cdot I^{n+s}, \tag{2.5}$$

where s is the number of excess photons. The excess energy is expressed by a higher electron kinetic energy than that which would result from multiphoton ionization with a minimum number of photons so that the sum of their photon energies is just above the ionization potential I_p. More precisely, multiple peaks can be observed in the photoelectron spectrum which is separated by the photon energy [7]. This ionization only exists under specified experimental conditions and is not valid at high light intensity for the initial state is depleted, and therefore the yield saturates [59]. The physics of multiphoton ionization is different from the X-ray regime when compared to an intense NIR laser. In the X-ray regime, a single photon is sufficient to ionize the target, whereas in the NIR regime multiple photons are needed even for single ionization.

Tunneling Ionization

As shown in Fig. 2.1 (b), tunnel ionization is a process in which the electron in an atom (or a molecule) passes through its potential barrier and gets liberated from the system [60]. If the laser field is strong enough to distort the atomic potential, the electron can tunnel through, or even overcome the low and narrow barrier between a bound state and the continuum state [8]. These phenomena are called tunnel ionization and over-the-barrier ionization, respectively. These processes take place when the oscillation period of the external laser field is quite longer than the time needed for the wavepacket to tunnel through the barrier. In this circumstance, the Keldysh parameter is far less than 1. As a non-zero probability event which is used to describe a particle escaping from the deformed Coulomb potential barrier by the intense laser field, this is forbidden in the classical picture, since in the classical physics an electron does not have sufficient energy to escape the barrier [60]. Tunneling ionization can be well-described by ADK theory. According to the ADK theory proposed by Ammosov, Delone, and Krainov [61, 62], the tunneling ionization rate Γ_{TI} is given by

$$\Gamma_{\mathrm{TI}} = N \cdot exp(-\frac{4\sqrt{2m_e}I_p^{2/3}}{3\hbar e E_0}), \tag{2.6}$$

where N is a slowly varying function that depends on the cycle-averaged field intensity. The equation can properly describe the ionization rate in a direct current electric field [63].

For the ionization of N_2, an infrared laser field with a central wavelength of 800 nm is used, with typical experimental intensities ranging from 10^{13} W/cm^2 to 10^{15} W/cm^2, the corresponding Keldysh parameter γ goes from 3.6 to 0.36. In this case, both MPI and Tunneling ionization mechanisms are involved. For an NIR laser intensity near 2.56×10^{14} W/cm^2 in the N_2 experiments, the Keldysh parameter is 0.7, thereby both MPI and Tunneling ionization have the same contribution to the double ionization of N_2 in the NIR laser field [51, 52].

2.2 Multiple Ionization and Double Ionization

In the previous section, we have already discussed the multiphoton single ionization process, in the following section, the multiple ionization will be discussed. The multiply charged ions that are created after the atom was absorbed a large number of photons. As the absorption ways, sequential ionization and non-sequential ionization are discussed. Moreover, the commonly observed phenomena in double ionization are introduced in the following discussion.

Multiple Ionization

In an intense laser field with pulses of 50 ps at 0.53 μm [64], the atomic system like the rare gas Xenon can be ionized to multiply charged states by absorption of multiple photons. In Fig. 2.2 (a), the number of multiple charged Xe ions as a function of light intensity is shown. By increasing the light intensity, the yield of Xe^+ ions reaches the saturation regime. The vertical dashed line indicates the saturation light intensity I_S. In this double-logarithmic plot, A. l'Huillier *et al.* estimated the slope of the fitting line to be

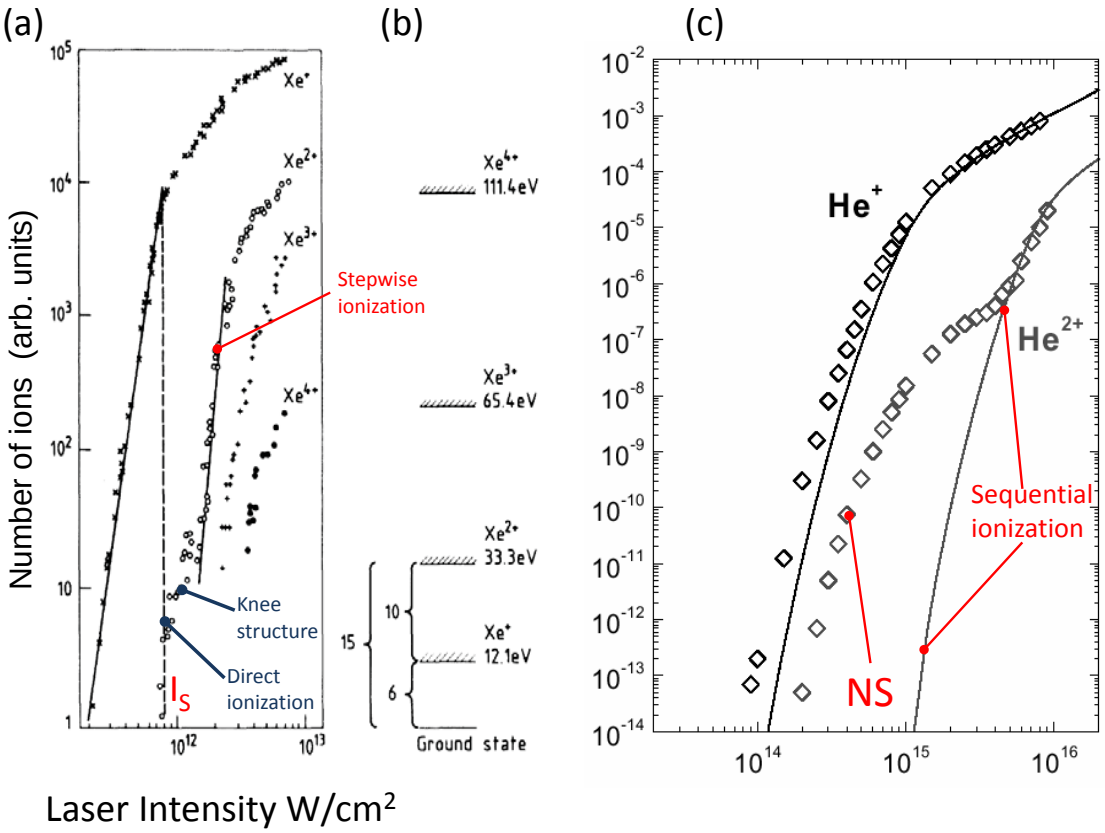

Figure 2.2: (a) The number of Xe^+, Xe^{2+}, Xe^{3+}, and Xe^{4+} ions as a function of the laser intensity with pulses of 50 ps at 0.53 μm [64]. The vertical line in the plot denotes the saturation light intensity I_S. We can observe a "knee structure" from the light intensity dependent Xe^{2+} ions. It comes from both contribution of the direction 15-photons ionization and stepwise ((b) 6 + 10 photons) ionization. (c) The similar "knee structure" can also be observed from the ion yield for ionization of Helium with 160 fs pulses at 780 nm [65]. The sequential ionization and non-sequential ionization can be identified from the precision-measurement of strong field double ionization of Helium.

6 ± 0.5. This means that the creation of singly charged Xe^+ atom has to absorb at least 6 photons. Near the light intensity I_S, we start to see the formation of doubly charged Xe^{2+} ions, they mainly come from the direct double ionization process by absorption of 15 photons from the ground state (see Fig. 2.2 (b)). With the increase of the light intensity, the stepwise or sequential ionization becomes the dominant process for the creation of Xe^{2+} ions, the reaction path is described by $Xe \longrightarrow Xe^+ \longrightarrow Xe^{2+}$. In Fig. 2.2 (c), as reported by B. Walker [65], the sequential ionization and non-sequential (NS) ionization can be properly distinguished from the ion yields of singly charged He^+ ions and doubly charged He^{2+} ions. The similar "knee structure" can be observed as well, indicating a non-sequential ionization process involved. Sequential ionization is understood as stepwise absorption via stationary intermediate real molecular states. In contrast, the non-sequential ionization is described as a direct ionization via virtual intermediate states [50].

Double Ionization

As discussed above, the created doubly charged Xe^{2+} ions have two ways to react: one is through sequential ionization process and the other is non-sequential ionization process. Whether sequential ionization or non-sequential, it depends on the wavelength and light intensity [64, 66]. For the sequential ionization, the doubly charged ions are produced through the ground state to singly charged state, then further ionized to the final doubly charged state. However, for the non-sequential ionization, the formation of the doubly charged ions are obtained from the detachment of two-electron from the atom at the same time [63, 64].

According to the perturbation theory, we start to discuss the evolution of the population of singly charged ions and doubly charged ions[1]. For a two-photon sequential double ionization process, the population of doubly charged ions per time is given by

$$\begin{aligned} \frac{dN_2^{\mathrm{SI}}}{dt} &= N_1(t)\sigma_{12}^{(1)}\left(\frac{I}{\hbar\omega}\right) \\ \text{with} \quad N_1(t) &= \int_{-\infty}^{t} N_0(t)\sigma_{01}^{(1)}\left(\frac{I}{\hbar\omega}\right)dt. \end{aligned} \tag{2.7}$$

Moreover, the number of doubly charged ions generated for the non-sequential channel N_2^{NSI} is given by

$$\frac{dN_2^{\mathrm{NSI}}}{dt} = N_0(t)\sigma_{02}^{(2)}\left(\frac{I}{\hbar\omega}\right)^2. \tag{2.8}$$

The lower index of the cross sections represents the steps of ionization in the initial and the final state of the respective process. The integers 1 and 2 in the upper index of the cross sections present the number of photons. The yields of singly and doubly charged ions then result from the coupled rate equations:

$$\begin{aligned} \frac{dN_0}{dt} &= -N_0(t)\sigma_{01}^{(1)}\left(\frac{I}{\hbar\omega}\right) - N_0(t)\sigma_{02}^{(2)}\left(\frac{I}{\hbar\omega}\right)^2 \\ \frac{dN_1}{dt} &= N_0(t)\sigma_{01}^{(1)}\left(\frac{I}{\hbar\omega}\right) - N_1(t)\sigma_{12}^{(1)}\left(\frac{I}{\hbar\omega}\right) \\ \frac{dN_2}{dt} &= N_0(t)\sigma_{02}^{(2)}\left(\frac{I}{\hbar\omega}\right)^2 + N_1(t)\sigma_{12}^{(1)}\left(\frac{I}{\hbar\omega}\right). \end{aligned} \tag{2.9}$$

The N_0, N_1 and N_2 are the relative populations of neutral, singly, and doubly ionized atoms at time t. From the above equations, we obtain the time-dependent population of the two ionization pathways which is essential for the analysis of the ionization yield in experiments. The different reaction channels have a different time dependence. While single ionization already starts at low intensities in the rising edge of the pulse, the occurrence of double ionization is limited to a narrow range around the maximum intensity [45]. The probability of the occurrence of sequential double ionization depends not only on the instantaneous light intensity but also on the population of neutral and singly

[1] Most of the content is complied from Ref. [45].

charged ions. In general, in the double ionization process with an increasing pulse duration the relative probability of the sequential process increases [67]. Also, the yield of the sequential process is higher than the yield of the non-sequential process by several orders of magnitude [45].

As an NSI process, taking the double ionization for example, the two emitted photoelectrons correlate with each other. The following phenomena can be well-described as non-sequential ionization processes[2].

Shake-off Mechanism

According to "sudden approximation", an electron in the atom or molecule can be quickly ionized by a strong laser field. The wavefunction of the remaining electrons will relax to a new eigenstate of the modified potential. Some of these new states are located in the continuum ("shake-off") or are still bound but excited ("shake-up"), which means that a second electron can be ionized or excited in the course of the following relaxation process [9]. The shake-up electron could be further tunnel-ionized in the next half-cycle of the laser field. This becomes one dominating mechanism of double ionization at very high photon energy typically in the keV range [9, 63].

Rescattering Mechanism

In an intense laser field, an electron is ionized at the maximum of the laser electric field and is driven by the electric field, away and back to the parent ion [63]. It is the basis of the production of High harmonic generation (HHG) [68]. Beside emitting HHG radiation, it could be elastically scattered and further excited or ionized the parent ion. If the recollision energy is larger than the ionization potential of the singly charged ion, then the parent ion can be further ionized by ejecting the second electron. This is known as the recollision induced direct ionization process [69]. However, if the recollision energy is less than the ionization potential, the bound electron of the singly charged ion can be excited to an another excited state [65]. Both the first emitted electron and the second ejected electron due to rescattering are correlated with each other.

In the experiments of N_2, the sequential ionization process is taking place in the photoionization of the molecular systems in the X-ray regime. For the molecule N_2 in the NIR laser field with a light intensity of 2.56×10^{14} W/cm^2, the non-sequential ionization process may adequately explain the ionization steps. The rescattering mechanism can be taken to explain the non-sequential double ionization of the molecule [52]. The details will be discussed in Chapter 6.

2.3 Photoionization of Atomic Systems

From the previous section, we get a rough idea of how to treat and identify the different ionization mechanisms in a strong laser field. In this section, the theoretical methods to describe the photoionization of atomic systems are presented[3]. We will first discuss the single-electron atomic systems and then extend to the multi-electron systems. We use the

[2]The following discussion is based on Ref. [63].

[3]The basic theory is compiled from Refs. [16, 21, 55, 70, 71].

time-dependent perturbation theory to describe the single- and two-photon absorption of an atom. After this, we will proceed to discuss multiphoton processes.

When an atom is placed in an external electromagnetic field with a vector potential[4]

$$\mathbf{A}(\mathbf{r},t) = A_0\varepsilon\left(e^{\mathrm{i}(\mathbf{kr}-\omega t)} + e^{-\mathrm{i}(\mathbf{kr}-\omega t)}\right), \tag{2.10}$$

where A_0 is the field strength, $\mathbf{k}$ is the wave vector, ω is the frequency and ε is the polarization vector, we obtain the external time-dependent perturbation Hamiltonian

$$\hat{H}_{\mathrm{int}}(t) = \mathbf{p}\cdot\mathbf{A}(\mathbf{r},t), \tag{2.11}$$

where $\mathbf{p}$ is the momentum operator of the atomic system. Correspondingly, the time-dependent Schrödinger equation is expressed as

$$\mathrm{i}\frac{\partial}{\partial t}\Psi(\mathbf{r},t) = \left(\hat{H}_0 + \lambda\hat{H}_{\mathrm{int}}(t)\right)\Psi(\mathbf{r},t), \tag{2.12}$$

where $\hat{H}_0 = -\frac{1}{2}\nabla^2 - \frac{Z}{\mathbf{r}}$ is the field-free (or unperturbed) Hamiltonian, $-\frac{Z}{\mathbf{r}}$ is the Coulomb potential, and $\hat{\lambda}$ is the perturbation parameter. The eigenstates $\psi_k(\mathbf{r})$ of the unperturbed Hamiltonian $\hat{H}_0$ is given by

$$\hat{H}_0\psi_k(\mathbf{r}) = E_k\psi_k(\mathbf{r}). \tag{2.13}$$

The following Schrödinger equation can describe the temporal evolution of the system:

$$\Psi(\mathbf{r},t) = \sum_k c_k(t)e^{-\mathrm{i}E_k t}\psi_k(\mathbf{r}), \tag{2.14}$$

where $\Psi(\mathbf{r},t)$ is the wavefunction of the atomic system. According to perturbation theory, we can obtain the time-dependent expansion coefficients $c_f(t)$ by inserting Eq. 2.14 into Eq. 2.12:

$$\mathrm{i}\frac{\partial c_f(t)}{\partial t} = \sum_k \lambda c_k(t)\left\langle\psi_f\left|\hat{H}_{\mathrm{int}}(t)\right|\psi_k\right\rangle e^{\mathrm{i}(E_f-E_k)t}. \tag{2.15}$$

In the above equation, the matrix element $\left\langle\psi_f\left|\hat{H}_{\mathrm{int}}(t)\right|\psi_k\right\rangle$ denotes the transition amplitude from state ψ_k to state ψ_f.

The expansion of the coefficient $c_k(t)$ in terms of power series in λ yields:

$$c_k(t) = \lambda^0 c_k^{(0)}(t) + \lambda^1 c_k^{(1)}(t) + \lambda^2 c_k^{(2)}(t) + \ldots \tag{2.16}$$

This equation enables us to estimate the n-th perturbation from the external field with the atomic system. The zeroth order term is the un-perturbed coefficient which is used to describe the free-interaction case. And, we interpret $c_k^{(n)}(t)$ as the interaction of the atomic system with n-photon. Here, let us consider the first and second coefficients which are used to describe the atomic system from initial state ψ_i to final state ψ_f after the absorption single- and two-photon:

$$c_f^{(1)}(t) = \frac{1}{\mathrm{i}}\int_0^t \mathrm{d}t'\left\langle\psi_f\left|\hat{H}_{\mathrm{int}}(t')\right|\psi_i\right\rangle e^{\mathrm{i}(E_f-E_i)t'}, \tag{2.17}$$

[4]For simplicity, in the following description, we use $\mathbf{kr}$ to represent $\vec{k}\cdot\vec{r}$.

$$c_f^{(2)}(t) = \left(\frac{1}{\mathrm{i}}\right)^2 \sum_k \int_0^t \mathrm{d}t' \int_0^{t'} \mathrm{d}t'' \left\langle \psi_f \left| \hat{H}_{\mathrm{int}}(t') \right| \psi_k \right\rangle \left\langle \psi_k \left| \hat{H}_{\mathrm{int}}(t'') \right| \psi_i \right\rangle \times e^{\mathrm{i}(E_f - E_k)t'} e^{\mathrm{i}(E_k - E_i)t''}. \tag{2.18}$$

In the Eq. 2.18, we have to take all the possible ways of transition into account. Taking a two-level system, for example, the resonant frequency of the initial state and final state is ω, that's $E_i + \hbar\omega = E_f$. If we consider this transition to take place in an external field, then we can obtain the time-dependent first- and second-order coefficient as follows:

$$1\mathrm{st.\,order}: c_f^{(1)}(t) = \frac{A_0}{\mathrm{i}} \left\langle \psi_f \left| \mathbf{p} \cdot \varepsilon \, e^{\mathrm{i}\mathbf{kr}} \right| \psi_i \right\rangle \int_0^t \mathrm{d}t' e^{\mathrm{i}(E_f - E_i - \omega)t'}, \tag{2.19}$$

$$2\mathrm{nd.\,order}: c_f^{(2)}(t) = \left(\frac{A_0}{\mathrm{i}}\right)^2 \sum_k \left\langle \psi_f \left| \mathbf{p} \cdot \varepsilon \, e^{\mathrm{i}\mathbf{kr}} \right| \psi_k \right\rangle \left\langle \psi_k \left| \mathbf{p} \cdot \varepsilon \, e^{\mathrm{i}\mathbf{kr}} \right| \psi_i \right\rangle \times \int_0^t \mathrm{d}t' \int_0^{t'} \mathrm{d}t'' e^{\mathrm{i}(E_f - E_k - \omega)t'} e^{\mathrm{i}(E_k - E_i - \omega)t''}. \tag{2.20}$$

In quantum mechanics, the transition probability equals to the absolute square of the coefficient $c_f(t)$. The transition probability at a time t after the system interacts with the external field is

$$P_{if}^{(n)}(t) = \left| c_f^{(n)}(t) \right|^2. \tag{2.21}$$

Meanwhile, after a time T, the transition rate from initial state ψ_i to final state ψ_f can be expressed as

$$R_{if}^{(n)} = \frac{P_{if}^{(n)}(T)}{T}. \tag{2.22}$$

Using Eq. 2.19 and 2.20 inserting in Eq. 2.22, we can obtain the following equations:

$$R_{if}^{(1)} \propto I \left| \left\langle \psi_f \left| \mathbf{p} \cdot \varepsilon \, e^{\mathrm{i}\mathbf{kr}} \right| \psi_i \right\rangle \right|^2 \delta(E_f - E_i - \omega), \tag{2.23}$$

$$R_{if}^{(2)} \propto I^2 \left| \sum_k \frac{\left\langle \psi_f \left| \mathbf{p} \cdot \varepsilon \, e^{\mathrm{i}\mathbf{kr}} \right| \psi_k \right\rangle \left\langle \psi_k \left| \mathbf{p} \cdot \varepsilon \, e^{\mathrm{i}\mathbf{kr}} \right| \psi_i \right\rangle}{E_k - E_i - \omega} \right|^2 \delta(E_f - E_i - 2\omega). \tag{2.24}$$

Here, I is the light intensity. The above two equations describe the transition probabilities of an atomic system that absorbing single or two photons in a perturbing field.

Now, let us extend to the n-photon absorption process. Fabre *et al.* pointed out that the experimental ionization rates can be well-described with the lowest order perturbation theory with the absorption of n-photons [72]

$$w_{i\to f}^{(n)} = \left| \lim_{t\to\infty} c_f^{(n)}(t) \right|^2 \cdot \frac{1}{t}. \tag{2.25}$$

And, the ionization rate $w^{(n)}$ follows the power-law according to:

$$w_{i\to f}^{(n)} = \sigma^{(n)} (I/\hbar\omega)^n , \tag{2.26}$$

where σ^n is the generalized n-photon ionization cross-section. This law has been reviewed and approved for low intensities [45].

2.3.1 Dipole Approximation and Electron Angular Distribution

The dipole matrix element $d_{if} = \langle \psi_f | \mathbf{p} \cdot \varepsilon \, e^{i\mathbf{kr}} | \psi_i \rangle$ determines the coupling strength of the transition between initial state ψ_i and final state ψ_f. If the wavelength of the emitted photon is much larger than atomic dimension[5], namely, $e^{i\mathbf{kr}} \approx 1$, then we obtain the dipole approximation $d_{if} = \langle \psi_f | \mathbf{p} \cdot \varepsilon | \psi_i \rangle$. With this approximation, the angular distribution of emitted photoelectron in a single photon ionization process is given by [73]

$$\frac{d\sigma}{d\Omega}(\hbar\omega, \theta) = \frac{\sigma}{4\pi} [1 + \beta_2 P_2(cos\theta)] . \tag{2.27}$$

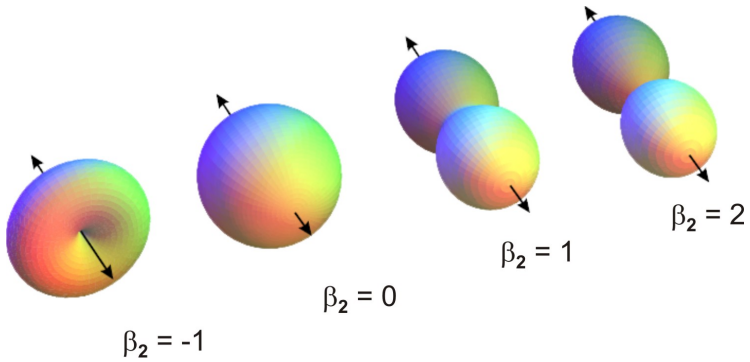

Figure 2.3: Angular distribution of emitted electrons in single-photon single-ionization for different values of the anisotropy parameter β_2. The arrow indicates the polarization axis of the radiation. Figure taken from Ref. [17].

In Eq. 2.27, Ω is the solid angle, σ is the integrated cross section, β_2 is the angular distribution anisotropy parameter, P_2 is the second-order Legendre polynomial, and θ is the angle between the polarization of the laser field and the emission direction of the emitted photoelectron. As shown in Fig. 2.3, β_2 is limited to values between -1 and +2. Thus, we can use the angular distribution of the reaction fragments to find the polarization direction of the laser pulses [74]. Furthermore, the transition pathways for various fragmentation channels are also traced by the angular distribution of fragments after absorption of several photons. For the detail can be found in Sec. 2.7.

[5] http://web.ift.uib.no/AMOS/nazila/LaserAndLight/node7.html

2.4 Many-Electron Atomic Systems

The time-dependent perturbation theory discussed above can be extended to treat the many electrons atomic systems[6]. Similar to single electron atomic system, the unperturbed Hamiltonian of N-electrons atomic system and its nucleus charge Z is given by

$$\hat{H}_0 = \sum_{i=1}^{N}\left(-\frac{1}{2}\nabla_{r_i}^2 - \frac{Z}{r_i}\right) + \sum_{i\neq j}^{N}\frac{1}{r_{ij}}, \tag{2.28}$$

where ∇_{r_i} is the single-electron nabla operator, r_i is the distance between electron i and the nucleus and $r_{ij} = \left|\mathbf{r}_i - \mathbf{r}_j\right|$ is the distance between electron i and electron j. The first term is the sum over the electron-nucleus interactions and the second term is the electron-electron interaction. Then one can obtain the Schrödinger equation for the many-electron system:

$$\hat{H}_0\Psi(\mathbf{r}_1,\mathbf{r}_2...\mathbf{r}_N) = E\Psi(\mathbf{r}_1,\mathbf{r}_2,...\mathbf{r}_N), \tag{2.29}$$

where $\Psi(\mathbf{r}_1,\mathbf{r}_2...\mathbf{r}_N)$ is the wave function of the many-electron atomic system.

According to the central field approximation, the potential experienced by i-th electrons is given by

$$V_i(r_i) = -\frac{Z}{r_i} + \left\langle \sum_{i\neq j}^{N}\frac{1}{r_{ij}} \right\rangle. \tag{2.30}$$

In this circumstance, one can use the following wave function $\phi_i(\mathbf{r}_i)$ to describe the N-electron atomic system:

$$\Psi(\mathbf{r}_1,\mathbf{r}_2...\mathbf{r}_N) = \phi_1(\mathbf{r}_1)\phi_2(\mathbf{r}_2)...\phi_N(\mathbf{r}_N) \tag{2.31}$$

and obtain the total energy of this system:

$$E = \left\langle \phi_1(\mathbf{r}_1)\phi_2(\mathbf{r}_2)...\phi_N(\mathbf{r}_N)\left|\hat{H}\right|\phi_1(\mathbf{r}_1)\phi_2(\mathbf{r}_2)...\phi_N(\mathbf{r}_N)\right\rangle. \tag{2.32}$$

2.5 Photoionization of Molecular Systems

The molecular system is more complicated than the atomic system since it has more degrees of freedom. The molecular system can be regarded as a many atoms system with N-electron. For simplicity, let us consider a diatomic molecule with N electrons and two nuclei (A and B), the wavefunction of the system depends on the motion of electrons and nuclei. The Hamiltonian of the molecular system is expressed as[7]

$$\hat{H} = \hat{T}_{\mathrm{n}} + \hat{T}_e + V(\mathbf{r},\mathbf{R}), \tag{2.33}$$

with $\hat{T}_{\mathrm{n}} = -\frac{1}{2\mu}\nabla_R^2$ the kinetic energy of the nuclei and $\hat{T}_e = \sum_{i=1}^{N}\left(-\frac{1}{2}\nabla_{r_i}^2\right)$ the kinetic energy of the N electrons. The corresponding Coulomb potential for all particles is given by

$$V(\mathbf{r},\mathbf{R}) = -\sum_{i=1}^{N}\frac{Z_A}{|\mathbf{r}_i - \mathbf{R}_A|} - \sum_{i=1}^{N}\frac{Z_B}{|\mathbf{r}_i - \mathbf{R}_B|} + \sum_{i<k}^{N}\frac{1}{|\mathbf{r}_i - \mathbf{r}_k|} + \frac{Z_A Z_B}{R}. \tag{2.34}$$

[6]The content is compiled from Refs. [55, 75].

[7]Here, $\mathbf{r}$ represents the entirety of the coordinates of all electrons.

In Eq. 2.34, $\mathbf{r}_i$ represents the spatial coordinates of the i-th electron, $\mathbf{R} = \mathbf{R}_B - \mathbf{R}_A$ is internuclear separation. The reduced mass of the nuclei is

$$\mu = (M_A M_B)/(M_A + M_B), \tag{2.35}$$

where M_A and M_B are the mass of nuclear A and B, respectively. Thus, we obtain the corresponding stationary Schrödinger equation

$$\hat{H}\Psi(\mathbf{R},\mathbf{r}) = E\Psi(\mathbf{R},\mathbf{r}). \tag{2.36}$$

In the first order approximation, energy levels of a diatomic molecule may be expressed as a sum of electronic, vibrational and rotational energies. In order to calculate the total energy E of the molecular system, we have to solve the Schrödinger equation. However, theoretically, the analytic solution of the time-dependent Schrödinger equation cannot be obtained even for the single electron H_2^+ molecule [76]. Hence, the numerical solutions of molecular systems are needed by considering reasonable approximations. In few-body quantum physics, the Born-Oppenheimer approximation is the assumption that the motion of nuclei and electrons in a molecular system can be separated, and the coupling between the electrons and the nuclei can be simplified [19]. To this end, with Born-Oppenheimer approximation, the wavefunction of a molecule can be described as a combination of the electronic wavefunction $\phi(\mathbf{r})$ and the nuclear wavefunction $\psi(\mathbf{R})$:

$$\Psi(\mathbf{R},\mathbf{r}) = \phi(\mathbf{r})\psi(\mathbf{R}), \tag{2.37}$$

where $\mathbf{r}$ are the electron spatial coordinates and $\mathbf{R}$ are the nuclear spatial coordinates.

The electronic Hamiltonian at a fixed value of $\mathbf{R}$ is given by

$$\hat{H}_e = \hat{H} - \hat{T}_{\mathrm{n}}(\mathbf{R}) = \hat{T}_e + V(\mathbf{r},\mathbf{R}). \tag{2.38}$$

with the corresponding electronic Schrödinger equation being

$$\hat{H}_e\phi_\gamma(\mathbf{r},\mathbf{R}) = \left(\hat{T}_e + V(\mathbf{r},\mathbf{R})\right)\phi_\gamma(\mathbf{r},\mathbf{R}) = V_\gamma(R)\phi_\gamma(\mathbf{r},\mathbf{R}). \tag{2.39}$$

In Born-Oppenheimer approximation for a diatomic case, the electronic energy $V(\mathbf{R})$ is called by molecular potential at each set of γ is a continuous function of $\mathbf{R}$ [77]. Thus, Eq. 2.39 can be expressed as

$$\left(\hat{T}_e + V(\mathbf{r})\right)\phi_\gamma(\mathbf{r}) = V_\gamma(R)\phi_\gamma(\mathbf{r}). \tag{2.40}$$

2.5.1 Molecular Term Symbols

The following nomenclature can note the states of diatomic molecules:

$$X^{2S+1}\Lambda_{g/u}^{+/-}. \tag{2.41}$$

Here, X denotes the ground state. Sometimes, A, B, C ... stands for the first, second, third ... excited state. Λ is the angular momentum and S is the total spin which gives the multiplicity $2S+1$.

- Λ characterizes the electron orbital angular momentum along the molecular axis. Analogous to the nomenclature in atoms ($l = 0, 1, 2, 3 \ldots \rightarrow s, p, d, f \ldots$), the Λ is designated by Σ, Π, Δ, Φ for $\Lambda = 0$, 1, 2, 3.
- The subscripts g/u and $+/-$ reflect symmetry properties of the total wavefunction Ψ. If the wavefunction has even parity this will be denoted by a g (gerade). Similarly, u (ungerade) indicates odd parity [55].
- $+/-$ are the eigenvalues of the reflection operator, which used to characterize the inversion symmetry of the wavefunction at a plane perpendicular to the internuclear axis [78].

For dipole transition, transitions between states of opposite parity are allowed [79]. The transition angular momentum Λ could be changed, depending on the direction of the transition dipole with respect to the molecular axis. Direct inspection of the integrand for dipole moments parallel and perpendicular to the molecular axis leads to permitted transitions for $\Delta\Lambda = 0, \pm 1$ [79]. These selection rules are applied to describe one-photon processes.

2.5.2 Nuclear Wave Function

Since the electronic motion was discussed above, here, we discuss the nuclear part of the molecular Schrödinger equation. According to the Born-Oppenheimer approximation, the nuclear Schrödinger equation is expressed as

$$\left(-\frac{1}{2\mu}\nabla_R^2 + V_\gamma(R)\right)\psi(R) = E_{\gamma\nu}\psi(R), \tag{2.42}$$

where $E_{\gamma\nu}$ is the total energy of the nuclei, $\psi(R)$ is the wavefunction of the nuclear motion, γ is the quantum number of the electronic state and ν is the quantum number of the nuclear state. In Eq. 2.42, the $\mathbf{R}$-dependent eigenvalues $V_\gamma(R)$ compose the potential of Schrödinger equation for nuclear motion [77]. In order to disentangle different types of motions, the electronic potential can be expanded in a Taylor series:

$$V_\gamma(R) = V_\gamma(R_{\mathrm{eq}}) + (R - R_{\mathrm{eq}})\frac{\mathrm{d}V_\gamma}{\mathrm{d}R}\bigg|_{R=R_{\mathrm{eq}}} + \frac{1}{2}(R - R_{\mathrm{eq}})^2\frac{\mathrm{d}^2V_\gamma}{\mathrm{d}R^2}\bigg|_{R=R_{\mathrm{eq}}} + \cdots, \tag{2.43}$$

where R_{eq} is the equilibrium distance, and thus we obtain the harmonic potential in the lowest non-vanishing order $\frac{\mathrm{d}V_\gamma}{\mathrm{d}R}\big|_{R=R_{\mathrm{eq}}} = 0$:

$$V_\gamma(R) \approx V_\gamma(R_{\mathrm{eq}}) + \frac{1}{2}k(R - R_{\mathrm{eq}})^2. \tag{2.44}$$

$k = \frac{\mathrm{d}^2V_\gamma}{\mathrm{d}R^2}\big|_{R=R_{\mathrm{eq}}}$ is the force constant. Thus, $\omega = \sqrt{k/\mu}$ is the angular frequency of the harmonic oscillations. In quantum mechanics, the basic treatment of harmonic oscillations can be easily found, and the energy eigenvalues can be obtained from the HERMITE functions for vibrational states [77].

2.5.3 Franck-Condon Principle

The Franck-Condon principle is an application of the Born-Oppenheimer approximation for photoexcited or photoionization [3,19]. Since the nuclear masses are much larger than the electronic mass, one can regard the nuclear coordinates is frozen during the transition from one electronic state to another. If these transitions happen on a time scale where the positions and the velocities of the nuclei do not change, then this is called a vertical or Franck-Condon transition [20]. It means their transitions take place at fixed internuclear distances (Franck-Condon region, or FC region). An electronic transition is more likely to take place if the two vibrational wavefunctions overlap more significantly.

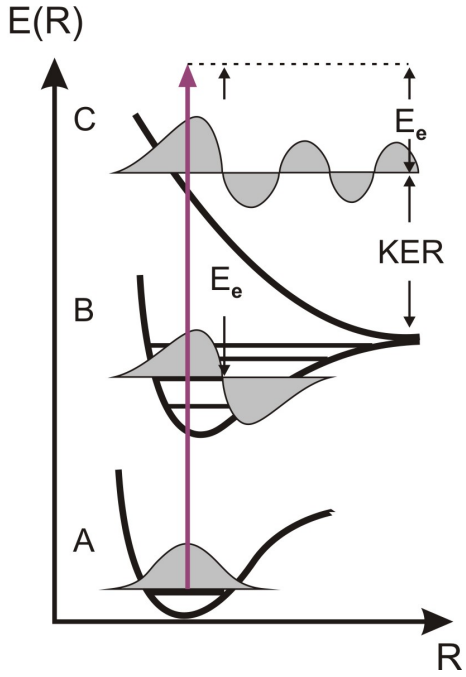

Figure 2.4: Schematic of single photon ionization of a molecule. The Franck-Condon transitions between two bound states (A $\rightarrow$ B) and from a bound to a dissociative state (A $\rightarrow$ C) are shown. Gray curves represent the nuclear wavefunction for certain vibrational levels which are indicated by the horizontal lines [45]. The figure is taken from [80].

In Fig. 2.4, the photoionization of a molecular system by the absorption of a single photon is shown to illustrate the prototypical molecular transition. A vertical transition happens if the motion of nuclei has not changed so much over the time scale of the electronic transition. In the FC region, the molecule is populated from a bound state A to another bound state B or a dissociative state C. Immediately, the nuclear wavepacket motion of state B is triggered. The excitation of the molecule into the final dissociative state C leads to a dissociation process. By applying energy conservation, one can find the following relationship between different energies:

$$E_{\hbar\omega} = E_e + KER + E_{limit}, \tag{2.45}$$

where KER is the total kinetic energy of the ionic fragments, E_e is the kinetic energy of emitted photoelectron, and E_{limit} is the energy of the fragments at infinity nuclear distance. The final state can be identified by performing KER spectroscopy. By tracing the

KER distribution for various dissociation channels, the transition pathways can be determined. If the nuclei motion is on the same timescale as the electronic motion, then the Frank-Condon principle is not true. Therefore, the Born-Oppenheimer approximation is not valid anymore [19]. In particular, some of the ultrafast relaxation processes in multielectron systems cannot be well described by Born-Oppenheimer approximation [28]. Inspite of this, the approximation still gives a good picture of the molecular dynamics after photoionization.

2.6 Relaxation Process in Atomic and Molecular Systems

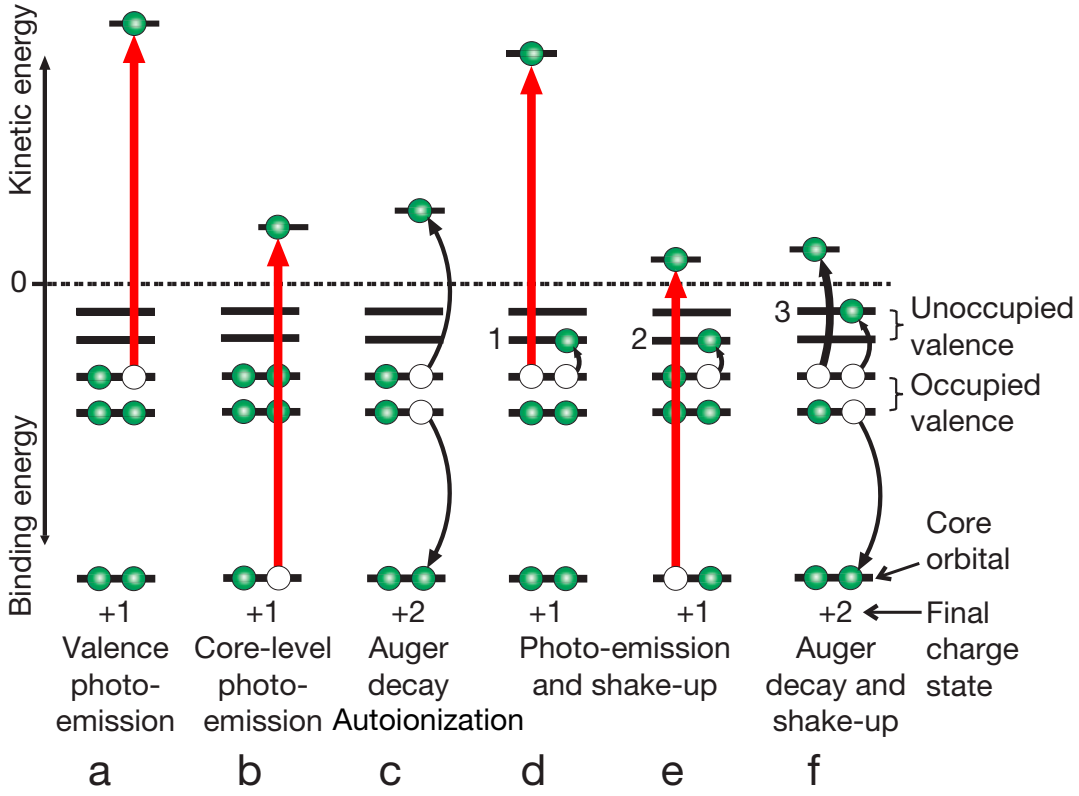

Figure 2.5: Schematics of electronic excitation and relaxation processes in atoms, molecules, and solids after XUV photoionization. Figure adapted from Ref. [10].

The XUV photons can not only ionize the valence electron but also liberate electrons from inner shells of atoms and molecules. Photoionization can be accompanied by excitation or emission of additional electrons when energetically allowed. These electrons are either excited to a un-occupied orbital ("shake-up") or excited into the continuum ("shake-off") [10, 21]. The created inner-shell vacancy decays rapidly through a variety of processes. The relaxation processes, such as Auger Decay and Autoionization after X-ray radiation, as shown in Fig. 2.5, have been intensely investigated experimentally in the past [12, 28, 81–83]. These highly excited states undergo an ultrafast relaxation process which evolves within a few to hundreds of femtoseconds [10].

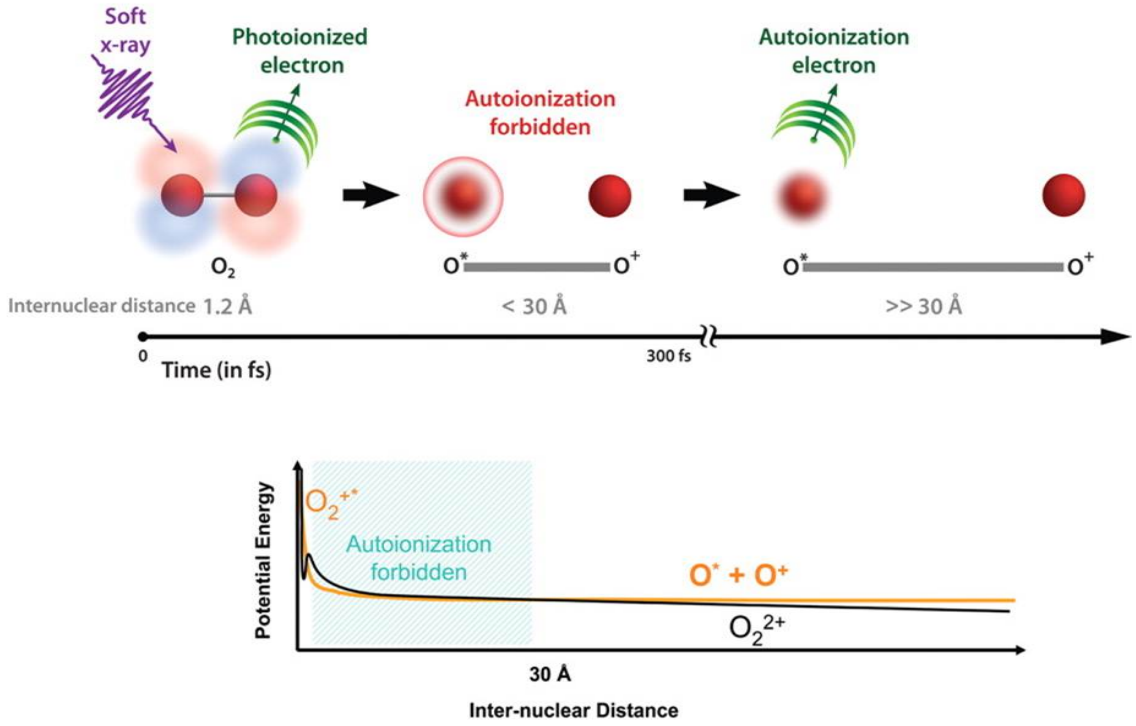

Figure 2.6: A schematic depiction of the multiple-step processes of photoionization, dissociation, and autoionization of O_2. Autoionization is allowed for the internuclear separations of 30 Å or greater [12].

Now, let us focus on the typical dynamics taking place in molecular systems. For molecules, autoionization is an essential electronic many-body problem [84]. In Fig. 2.6, the process of atomic-like autoionization in molecular oxygen is shown. The highly excited O_2^{+*} ions created by XUV radiation can further decay by emitting a secondary electron after some time delay. The secondary electron has fixed energy because the transition energy from an excited state to the other state is known. According to high-resolution electron spectroscopy of photoionization of molecular oxygen, the kinetic energy is more likely to be 0.5 eV [48]. Because autoionization is forbidden at short nuclear separation, this indirect double ionization can only be found at larger nuclear distances. A.S. Sandhu *et al.* presented the potential energy curves to illustrate this relaxation process and found that the autoionization takes place only at large internuclear distance up to 30 Å. With a pump-probe experiment, the lifetime of this process has been measured as being within 300 fs [12]. Such atomic-like autoionization processes also exist in many molecular systems, e.g. CO [13].

2.7 Fragment Ion Angular Distribution

Fragment ion angular distribution (FIAD) analysis is helpful to understand multiphoton absorption steps and the pattern of electron emission. In this section, the analysis of the

ionic fragment angular distribution for various photon absorption steps is discussed[8].

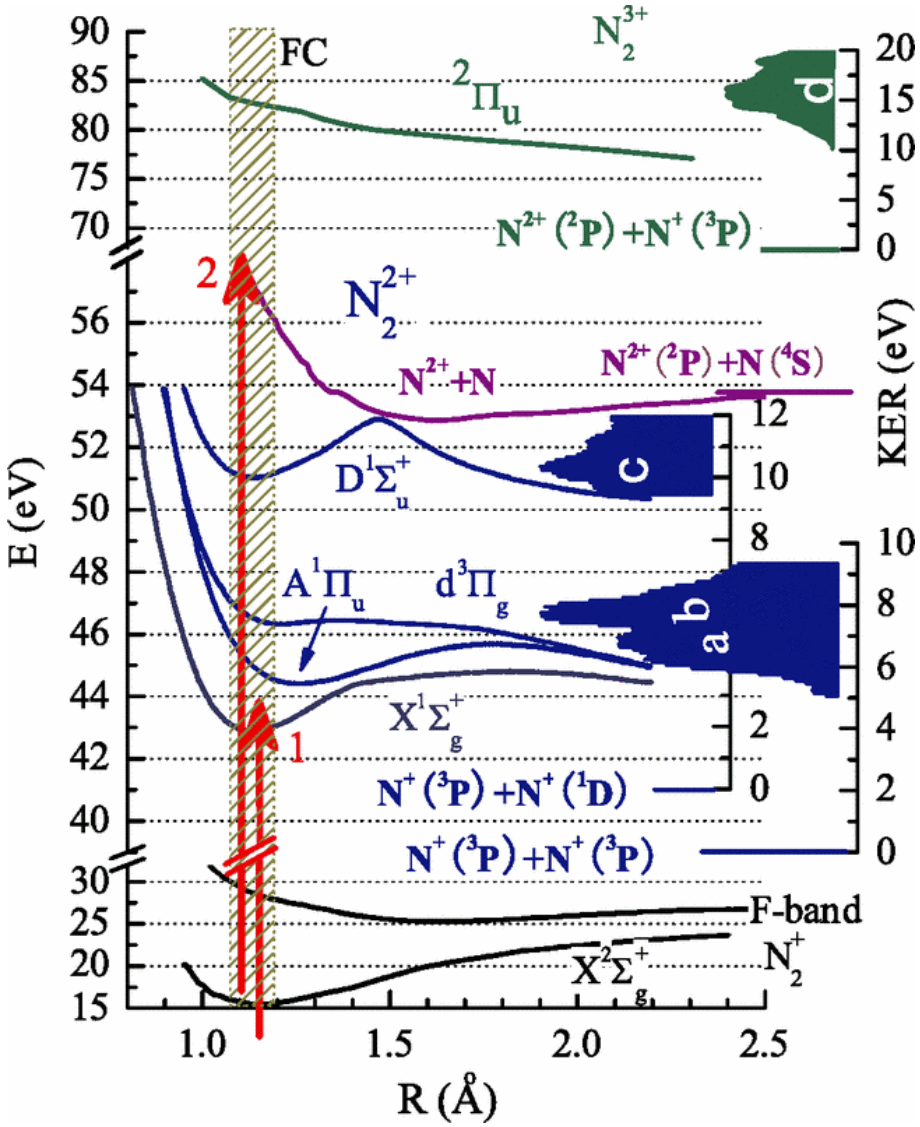

Figure 2.7: Illustration of the dominant dissociative multiple ionization pathways of N_2 and the KER spectra of coincident $N^+ + N^+$ and $N^{2+} + N^+$ for double and triple ionization, respectively. The photon energy is 44 eV and the light intensity I$\sim 10^{13}$ W/cm^2. The Frank-Condon regime (FC, vertical shaded band) and two-photon transitions (red arrows) are depicted [86].

In the experiments on N_2, the discussion is based on a previous experiment performed by Jiang *et al.* at FLASH [86]. They used 44 eV XUV photons to ionize the molecule, however, we used 28.3 eV XUV photons in combination with NIR laser to perform pump-probe experiments. In Fig. 2.7, the multiple dissociation channels of N_2 have been identified after irradiation with 44 eV XUV photons. In this case, the double ionization of this molecule is a two-photon process. Moreover, for triple ionization, five-photon absorption

[8]Most of the contents is compiled from Refs. [85, 86].

is the dominant process. By tracing the KER distributions for various dissociation channels, the final states can be determined. In the following, the FIAD of N_2 is shown in Fig. 2.8. For the single ionization process, the dissociating ionic fragments from F-band (∼28.8 eV) and H-band (∼35 eV) prefer to dissociate parallel to the FEL polarization direction. The double ionization of dissociative states $A^1\Pi_u$ and $d^3\Pi_g$ of N_2^{2+} ions prefer to dissociate perpendicular to the polarization of the XUV laser field [9]. The triple ionization fragments after Coulomb explosion also preferred to dissociate perpendicular to the FEL polarization direction. However, the state $D^1\Sigma_u^+$ of N_2^{2+} and the low-energetic N_2^{2+*} ions dissociate parallel to the polarization direction. The different ionic fragments angular distributions depend on the symmetry properties of the initial and final states during the multiphoton absorption steps.

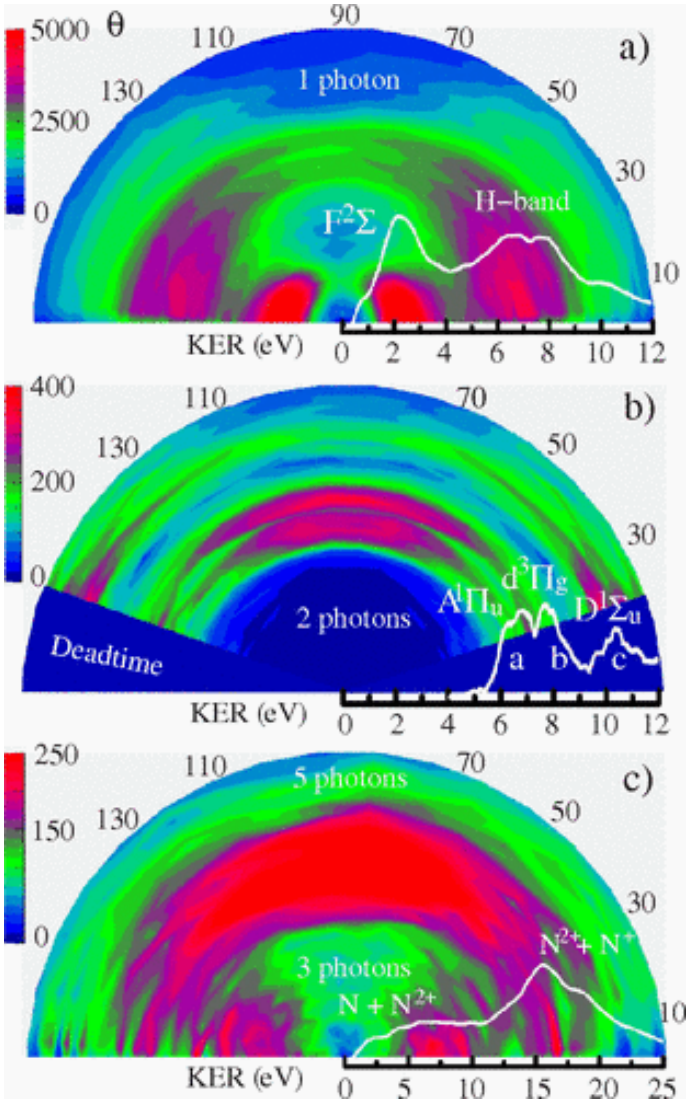

Figure 2.8: FIAD polar density plot for various dissociative channels of N_2 [86].

The Eq. 2.27 can be extended to analyze the angular distribution of the ionic fragments

[9]The dissociative state $d^3\Pi_g$ of N_2^{2+} corresponds to $D^3\Pi_g$ discussed in Chapter 6.

induced by XUV radiation. The anisotropy of the angular distribution can be used to explain the transition pathways and analyze of the ionization mechanisms. For few-XUV-photon absorption, the FIADs can be characterized by a multiple expansion regarding Legendre polynomial

$$\frac{d\sigma}{d\Omega}(\hbar\omega,\theta) = \frac{\sigma}{4\pi}\left[1+\sum_{i\cdots n}^{n}\beta_{2i}P_{2i}(cos\theta)\right], \tag{2.46}$$

where n is the number of absorbed photons, and β_i is anisotropy parameters [86,87]. From the angular distribution of the ionic fragments induced by XUV radiation, we can identify the photoionization steps and characterize the dissociation symmetry of the initial state and final state [88].

In practice, we use FIADs to identify the parallel ($\parallel$) and perpendicular ($\perp$) transitions during the photon absorption process. In a parallel transition, the fragment emission is parallel to the polarization axis. In the case of a perpendicular transition, the emission is perpendicular to the polarization axis. The symmetry of the initial state and the final state determines whether it is a parallel transition or a perpendicular transition. The anisotropy of FIAD is determined by the transition pathway, the polarization of the laser pulse, and the electric dipole moment of the molecule [85]. Here, the parallel transition such as $\Sigma \to \Sigma$ or $\Pi \to \Pi$ ($\Delta\Lambda = 0$), and the perpendicular transition such as $\Sigma \to \Pi$ or $\Pi \to \Delta$ ($\Delta\Lambda = \pm 1$) can be identified from the symmetry of the molecular states [85], respectively.

In the experiments of N_2, the angular dependence for various dissociation channels will help us to explain the alignment influence on the enhanced ionization in the two-color laser fields. The ionization rate is related to the alignment dependence induced by XUV radiation. The symmetry properties of the initial and final states determine the emission pattern of the induced ionic fragments by the XUV radiation. For the measured ionic fragments, one can obtain a rough idea of the transition pathways for various dissociation channels. The most straightforward cases are those of the single ionization and double ionization, where there are a single-XUV-photon and two-XUV-photon process, respectively.

Chapter 3

Light Sources and Experimental Setups

This chapter describes the experimental setups that have been built within the framework of this thesis. There are two main parts: the light sources and the Reaction Microscope. First, in Sec. 3.1, the Free Electron Laser's working principle is presented. In the following, the Free-Electron Laser in Hamburg, the NIR optical laser, and the THz radiation at FLASH are briefly introduced. Second, the reaction microscope which has become a multi-purpose experimental tool for kinematically complete studies of atomic and molecular dynamics is introduced in Sec. 3.2. Finally, the split-and-delay setup for pump-probe experiments, which enables us to obtain time-resolved spectroscopy of the fragments induced by the radiation, is given.

3.1 Free-Electron Lasers

Free **E**lectron **L**asers (FELs) are accelerator-based short-pulse radiation sources. The FEL facilities deliver a wavelength in the soft X-ray regime, such as the Free-Electron Laser in Hamburg (FLASH) in Germany and the FEL radiation for multidisciplinary investigations (FERMI) seeded FEL in Trieste, Italy. Examples of hard X-ray regime include the Linac Coherent Light Source (LCLS) at the SLAC National Accelerator Laboratory in California, USA, and the SPring-8 Angstrom Compact free electron LAser (SACLA) in Japan, as well as SwissFEL in Switzerland and SXFEL in China [1, 22, 89]. The European X-ray Free-Electron Laser Facility (European XFEL) is a pretty new advanced X-ray laser facility that delivers hard X-ray pulses far shorter than those from any other X-ray sources, and its peak brilliance is many orders of magnitude higher [22].

In contrast, 3rd generation synchrotron radiation produces a high photon flux but delivers a long pulse duration on the order of picoseconds [16]. However, the brilliant and temporal coherence of 4th generation light sources FELs with sub-100 fs pulses are capable of meeting the increasing demand in the field of research. FELs constitute the ultimate microscope to investigate matter at the fundamental limits of electron motion with atomic precision [89]. FELs enable scientists to explore non-linear and ultrafast dynamical processes in physics, chemistry, and biological sciences [1, 42, 90]. Furthermore, the coherence of the FEL radiation opens up the possibility for single shot holography

imaging of nanosystems and probing quantum dynamics of these systems with the sub-fs resolution [42, 91]. In this work, we used the XUV radiation to ionize and trigger a fragmentation and decay process in molecular systems, then the subsequent dissociation and relaxation processes were probed by a second probe pulse.

In this section, the basics of the working principle of FEL and the production of coherent XUV radiation are introduced[1]. Sec. 3.1.1 gives a brief introduction of the undulator radiation operation principle. In the following, in Sec. 3.1.2, a short introduction of Self-Amplified-Spontaneous-Emission (SASE) and Microbunching mechanism are presented. In the end, an overview of the facilities and the available experimental parameters at FLASH are given.

3.1.1 Undulator Radiation

In 1971, John Madey proposed the idea of the free-electron lasers [94]. However, only in recent years, with the advances in accelerator physics and laser technology, it became clear that FEL facilities have the potential to generate brilliant light sources in the X-ray regime [22].

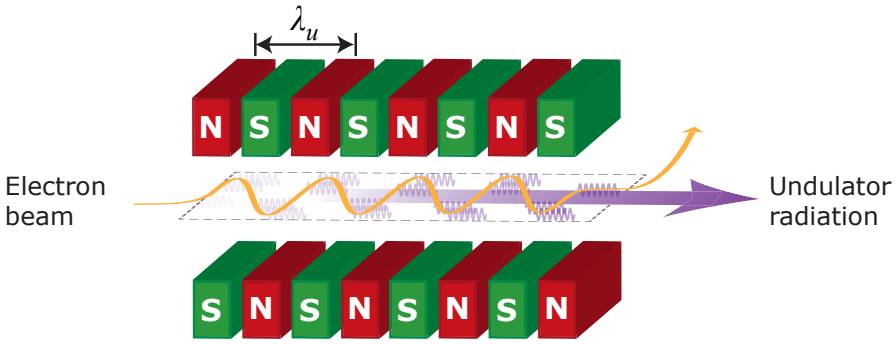

Figure 3.1: The principle of undulator radiation. FEL is operating in the Self-Amplified-Spontaneous-Emission (SASE) mode. Figure adapted from Ref. [95].

The pulsed electron gun, accelerator, and undulator are the three main components of the FEL facility. At FLASH, the electrons bunches are generated in a superconducting radio-frequency (RF) gun with a Cesium Telluride (Cs_2Te) photocathode and are accelerated by seven superconducting 1.3 GHz TESLA (Teraelectronvolt Energy Superconducting Linear Accelerator Test Facility) type accelerating modules [22]. The electrons leaving the cathode have an energy of about 5 MeV and are accelerated to about 164 MeV in the first superconducting module [92, 93]. The generated electron can be accelerated to relativistic speed by using an electric field strength of 40 MV/m in a superconducting RF-cavity. The accelerated electrons pass through the undulators generate flashes of X-ray light. As shown in Fig. 3.1, an undulator is a long periodical assembly of short dipole magnets of alternating polarity [56]. This assembly leads to a transversal oscillation of moving electrons with a frequency depending on the undulator period λ_u (the distance between two identical poles).

[1] Most of its concepts and contents are compiled from Refs. [16, 22, 32, 45, 56, 92, 93].

In Fig. 3.1, a schematic diagram of a single-pass FEL, operating in the SASE mode, is shown. The accelerated electrons have a relativistic speed v, and the corresponding Lorentz factor $\gamma = 1/\sqrt{1-v^2/c^2}$. Due to the Lorentz force produced by the alternating magnetic fields, the electrons are forced to propagate on an oscillatory path and emit synchrotron radiation. We define the initial light wave with wavelength λ_l by the spontaneously emitted undulator radiation. The radiation emitted with ultra-high speed towards an observer in the laboratory frame is blue-shifted by the relativistic Doppler-effect [22]. Therefore, the wavelength of undulator radiation in the forward direction is given by [92]

$$\lambda_l = \frac{\lambda_u}{2\gamma^2}\left(1+\frac{K^2}{2}\right). \tag{3.1}$$

The parameter K$=\frac{eB_0\lambda_u}{2\pi m_e c}$ is the so-called undulator parameter[2], which is dependent on the peak magnetic field and the undulator period. Six fixed gap planar hybrid undulators are mounted at FLASH. Each undulator has a length of 4.5 m, a period length of $\lambda_u =$ 27.3 mm with a fixed gap of 12 mm and a peak magnetic field $B_0 = 0.47$ T [3] corresponding to a K-value of 1.23 [22]. Since the undulator period is fixed, the FEL wavelength can be tuned by changing the magnetic field and the electron energy [16].

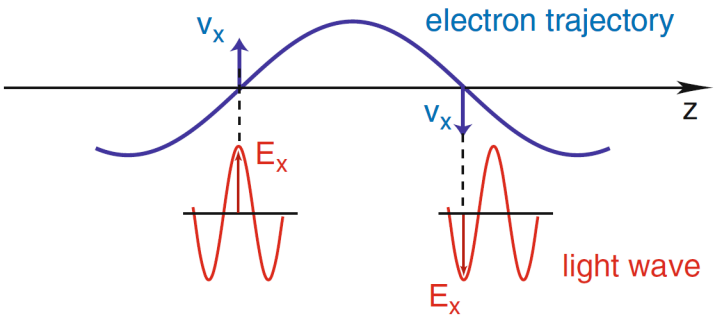

Figure 3.2: Illustration of the condition for sustained energy transfer from the electron to the light wave in an undulator. The condition is that the light wave has to advance by $\lambda_l/2$ by per half-period of the electron trajectory [92].

Now, we use the one-dimensional FEL theory to describe the production of coherent undulator radiation. First of all, let us discuss the energy exchange between the electron and the light wave. We treat the case of the undulator plane with the linear polarization as used at FLASH [93]. The direction of the electron beam is called the longitudinal direction (z-direction, see Fig. 3.2). We use a plane electromagnetic wave to depict the light-wave which is co-propagating with the relativistic electron:

$$E_x(z,t) = E_0\cos(k_l z - \omega_l t + \psi_0) \quad \text{with} \quad k_l = \omega_l/c = 2\pi/\lambda_l, \tag{3.2}$$

where E_0 is the amplitude of the plane electromagnetic wave, ω_l is the frequency, z is the longitudinal position along the macroscopic undulator beamline, and ψ_0 is the ponderomotive phase. The electric field of the light wave exerts a force $\mathbf{F} = -e\mathbf{E}$ on the electron

[2] $K = 0.934 \cdot B_0\,[\mathrm{T}] \cdot \lambda_u\,[\mathrm{cm}]$ [92]
[3] 1 tesla = 10^4 gauss

and modifies its energy. Thus, the time derivative of the electron energy can be expressed as

$$\frac{dW_e}{dt} = -e\mathbf{v}\cdot\mathbf{E} = -ev_x(t)E_x(t). \tag{3.3}$$

The light wave gains energy when the electron loses energy, so the term $\frac{dW_e}{dt}$ must be negative for the energy to be transferred from the electron to the light wave. To achieve a sustained energy transfer from the electron to the light field, the electron transverse velocity and the electric vector of the light wave must be in the same direction. As shown in Fig. 3.2, namely, v_x and E_x must be oriented in the same direction. From Eq. 3.2, we obtain the "average" electron speed in z-direction:

$$\bar{v}_z = c\cdot\left(1-\frac{1}{2\gamma^2}\left(1+\frac{K^2}{2}\right)\right). \tag{3.4}$$

The electron speed $\bar{v}_z$ is less than the speed of light as the electron propagates in a sinusoidal fashion in the undulators. Then, we calculate the electron and the light wave travel times for half period of undulator:

$$t_e = \lambda_u/(2\bar{v}_z) \quad \text{with} \quad t_l = \lambda_u/2c. \tag{3.5}$$

Thus, the difference in travel times between the electron (t_e) and light (t_l) for a half period of the undulator is expressed as

$$\Delta t = t_e - t_l = \left[\frac{1}{\bar{v}_z}-\frac{1}{c}\right]\frac{\lambda_u}{2}. \tag{3.6}$$

Because the FEL obtains its special radiation properties from the energy exchange between the radiation light field and relativistic electron bunches, the energy transfer has to be maximized between the light field and the electron [92]. Only if $\omega_l(t_e-t_l)=\pi$, the continuous energy transfer takes place. In this case, Fig. 3.2 demonstrates that the transverse velocity $\bar{v}_x$ and the field $\bar{E}_x$ stay parallel if the light wave advances by half an optical wavelength $\lambda_l/2$ in a half period of the electron trajectory. Therefore, we can obtain the condition for sustained energy transfer and amplified light with wavelength λ_l as follows:

$$c\,\Delta t = \lambda_l/2 \quad \Leftrightarrow \quad \lambda_l = \frac{\lambda_u}{2\gamma^2}\left(1+K^2/2\right). \tag{3.7}$$

In the forward direction, the produced wavelength of the light wave is identical with the undulator radiation wavelength. If $\omega_l(t_e-t_l) = 3\pi, 5\pi, 7\pi, \cdots$, the odd higher harmonics $\lambda_l/3, \lambda_l/5, \lambda_l/7, \cdots$ can be produced. In contrast, the even order harmonics are not amplified due to there is zero energy transfer from the electron to the light wave.

3.1.2 Microbunching and SASE

As discussed in Sec. 3.1.1, the light field obtains the energy from the electrons in the undulators, which results in the spontaneous undulator radiation can "seed" a Self-Amplified

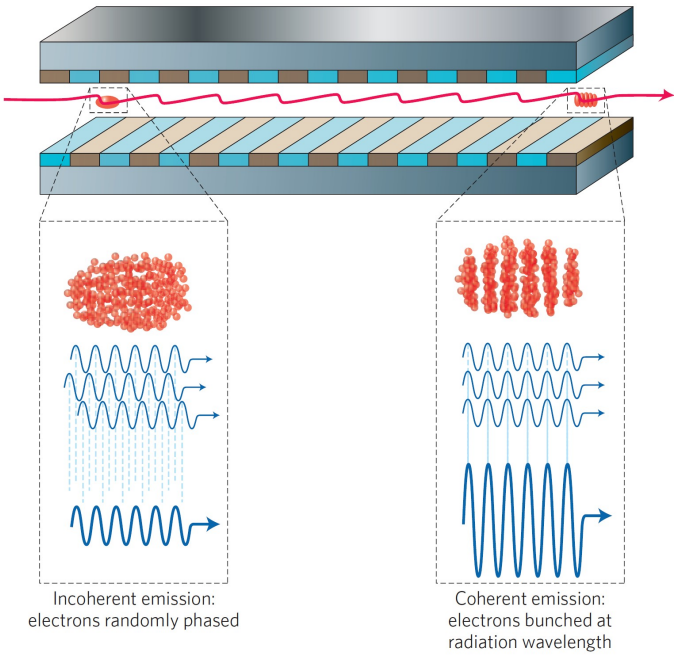

Figure 3.3: Operation principle of FEL. Electrons entering the undulator are randomly distributed and emit almost incoherent radiation at the wavelength λ_l. The electrons after microbunching caused strongly enhanced coherence and intensity. Figure is taken from Ref. [96].

Spontaneous Emission (SASE) FEL. The drawback is that only the wave with specific wavelengths fulfills the continues energy transfer condition.

The energy transfer per unit time from the electron to the light wave can be found in Ref. [92]

$$\frac{dW_e}{dt} = -\frac{ecKE_0}{2\gamma}[cos\psi + cos\chi], \tag{3.8}$$

where $\psi = (k_l + k_u)z - \omega_l t + \psi_0$ is the ponderomotive phase, and $\chi = (k_l - k_u)z - \omega_l t + \psi_0$ is the rapidly oscillating phase. As already discussed above, the condition of continuous energy transfer from electron to light wave happens when ψ is constant. The bunch is far longer than the light wavelength λ_l, this results in a phase shift ψ_0 between the light wave and the sinusoidal trajectory of the electron. In order to ensure a continuous energy transfer from the electron to the light field, $\cos\psi$ must be positive and remain constant along the entire undulators. The optimum phase was found to be $\psi = 0$. However, the condition $\psi = const$ can only be fulfilled for certain wavelengths.

The ponderomotive phase ψ can be transformed into a longitudinal coordinate insider the bunch [92]. For ponderomotive phase $\psi_0 = -\pi/2$, the electron transfers the energy to the light field, while for $\psi_0 = -\pi$ the energy transfers from the light field to the electron. In this case, the electrons are concentrated in the vicinity of the positions for which the energy transfer is maximum. The microbunches are formed near the positions where maximum energy transfer from electron to the light wave. Because electron energy repeated loss and gain throughout the electron beam over many radiation wavelengths, the beam becomes bunched on the same scale of the radiation wavelength [97]. In this case, the

electrons can be concentrated in slices by the modulation of the longitudinal velocity. As shown in Fig. 3.3, the initially unbunched electron beam produces incoherent radiation. The concentrated electrons radiate just like a single highly charged macro-particle. The coherently enhanced radiation from the microbunching beam increases the interaction between the electric field and the electrons, and thus a lasing gain process is expected [97]. Eventually, the microbunching can be further enhanced by the increasing radiation. The radiation intensity is an exponential growth of energy of radiation pulses as a function of the length of the undulator [22]. This leads to the production of high-gain FEL radiation.

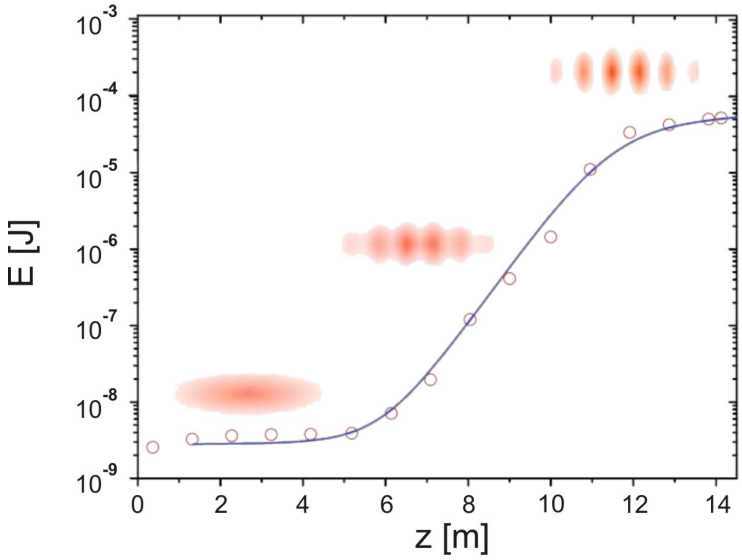

Figure 3.4: The FEL pulse energy and the electron beam microbunching versus undulator length z showing exponential growth and saturation [22].

The basic principle for SASE mechanism is that the intrinsic wavelength of the undulator radiation and the wavelength of the optimum energy transfer are equal. Over the length of the undulator, the produced light field interacts back with the electron bunch, thus producing particularly intense radiation. The prime advantage of high-gain FEL radiation in comparison with undulator radiation is the much higher light intensity as a large number of electrons radiate coherently. The radiation grows quadratically with the number of electrons: $P_N = N^2 P_1$, where P_N is the radiation power, N is the number of electrons and P_1 is the input power gain in the first gain length. The power gain length L_g of the undulator, which depends on the peak current I_{peak}, the electron beam emittance ε and the beta function β, is given by Ref. [22]:

$$L_g = C(\frac{\gamma\varepsilon\beta}{I_{peak}}) \quad \text{with} \quad C = \frac{1}{\sqrt{3}}(\frac{2m_e c\lambda_u}{\mu_0 eK^2})^{\frac{1}{3}}. \tag{3.9}$$

Thus, the FEL power grows as:

$$P(z) = \frac{P_0}{9} exp(z/L_g) \quad \text{for} \quad z \geq 2L_g, \tag{3.10}$$

where P_0 is the power of the incident light wave. In Fig. 3.4, the exponential growth of the FEL pulse energy versus the length z traveled in the undulators is shown. The

laser becomes saturated if $z \geq 12$. At FLASH, 27 m undulator magnets are long enough to bring the FEL into saturation. In this section, only a brief introduction of the FEL operation principle was given. More information can be found in Refs. [22, 32, 92, 96].

3.1.3 Free-Electron-Laser in Hamburg (FLASH)

The Free-electron LASer in Hamburg (FLASH) is a high-gain, single pass FEL that operates in a SASE mode and produces coherent XUV photon pulses in the XUV regime [93]. It is the first soft X-ray light source is open to the user community since the summer of 2005, thereby initiating a new chapter of exploring various topics in the fundamental sciences with unprecedented light intensity and shortness of the X-ray pulses, as well as their coherence. When compared with the High Harmonics Generation (HHG) based XUV radiation, the down to 10 fs ultra-short FEL laser pulses delivered at FLASH have a brilliant light intensity. Since 2016, FLASH has operated two parallel SASE beamlines-FLASH1 and FLASH2- that share the same electron bunch [98]. In comparison with FLASH1, FLASH2 has several variable-gap undulators, which ensures maximum flexibility in some parameters such as photon pulse length and wavelength. An overview of the FLASH facility and the operation principle is provided. A schematic view of the FLASH facility can be found in Fig. 3.5.

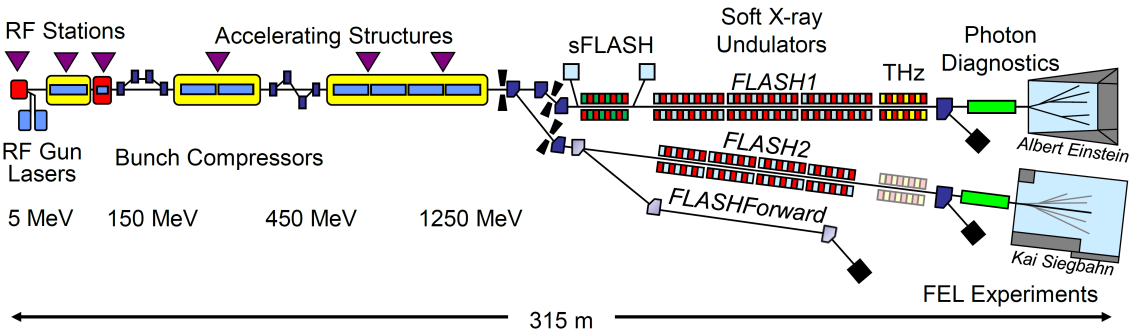

Figure 3.5: Schematic view of the FLASH facility. There are two parallel beamlines, FLASH 1 and FLASH 2. The THz undulator is installed behind the XUV undulator which is designed to XUV-THz pump-probe experiments. The total length is about 315 m. Figure taken from Ref. [22].

In Fig. 3.5, the electron pulses of FLASH come in bursts of several hundred pulses. The accelerated electrons are shared between the two beamlines delivering FEL radiation for two experimental halls at the same time with a repetition rate of 10 Hz providing each beamline with different bunch trains of varying pulse duration and spacing. The accelerator provides a range of electron energies between 350 MeV and 1.25 GeV covering a wavelength range between 52 and 4 nm [22]. The wavelength of the XUV radiation is tuned by selecting the right electron energy.

Both experiments performed at FLASH 1 use the soft X-ray radiation to ionize molecular systems and trigger the processes of fragmentation and relaxation and which is probed by the second pulse from either a near-infrared optical laser (NIR) or a Terahertz (THz) pulse.

In Tab. 3.1, the FLASH XUV photon beam parameters are summarized.

Table 3.1: FLASH parameters [22, 96]

Parameters	Typical values
Wavelength range (fund.)	4.2 - 51 nm
Average pulse energy	1 - 500 μJ
Pulse duration (FWHM)	< 10 - 200 fs
Pulse repetition rates	200 kHz
Spectral width (FWHM)	0.7 - 2 %
Electron bunches per second (typ./max)	10 - 5000
Peak power	1 - 5 GW
Photons per pulse	$10^{11} - 10^{14}$
Peak brilliance	$10^{28} - 10^{31}$

3.1.3.1 FLASH Optical Laser System

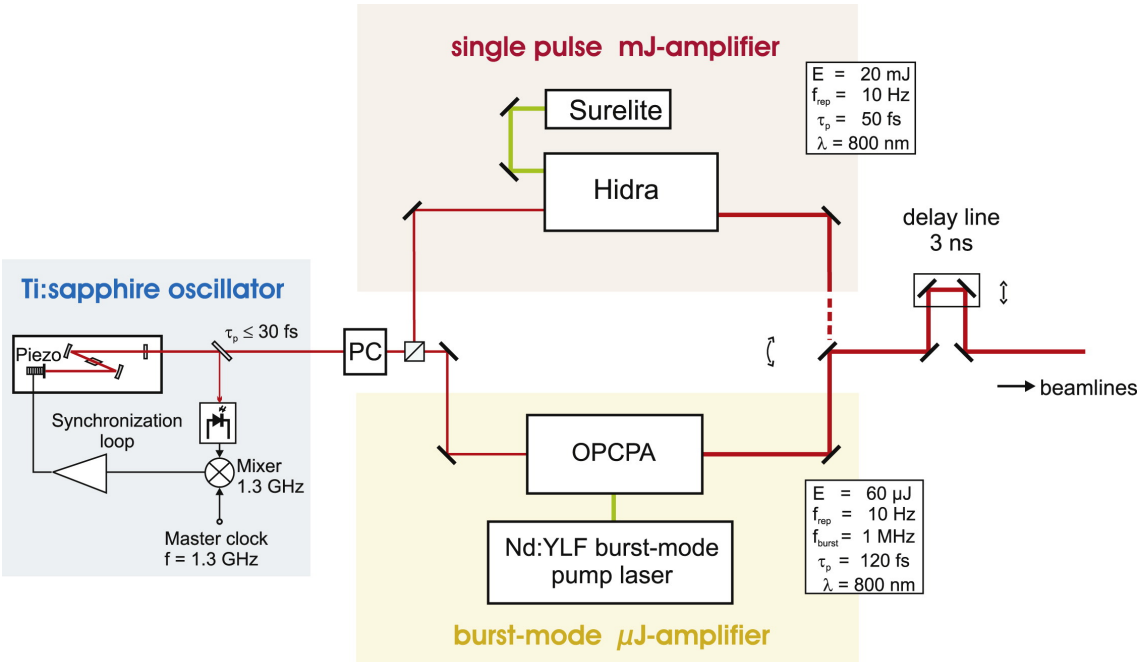

Figure 3.6: Schematic setup of the optical pump-probe lasers at FLASH1 [99].

In recent years, the time-resolved experiments in atomic and molecular physics have become an interesting topic for scientists, especially the use of synchronized XUV laser pulses and optical laser pulses [99–101]. The FEL laser pulses operate within the range of a few femtoseconds to hundreds of femtoseconds, making it possible to explore ultrafast AMO dynamics on the femtosecond timescale, or in the near future, even in the attosecond time regime at the European XFEL [32]. In order to perform XUV-IR pump-probe experiments, a NIR optical laser with femtoseconds pulse length and synchronized

XUV radiation is needed. In this section, a short introduction of the optical pump-probe laser system at FLASH is given.

In Fig. 3.6, the laser system consists of an ultrashort pulse oscillator which is synchronized to the FEL facility. Two different amplifiers are seeded by this oscillator. The signals from the rf-master oscillator at frequencies of 1.3 GHz are utilized to synchronize the optical laser pulses to the FEL pulses [99]. In this circumstance, a Ti:sapphire oscillator produces ultrashort pulses that are synchronized to the master clock of the FEL pulses. Since tens or hundreds of minibunches FEL laser pulses delivered by FLASH facility, a high repetition rate NIR laser is needed. The second amplifier, which is a Burst-mode optical parametric amplifier (OPCPA) has been designed to meet the demand for pump-probe experiments. This amplifier can produce the sub- hundreds of femtosecond laser pulses with a high light intensity to excite and ionize the atomic, molecular systems, or even big-sized clusters.

In order to perform the XUV-pump/IR-probe experiments, better synchronization and consistent temporal overlap of the pump-probe pulses are required. Because of the NIR and XUV laser pulses are generated by different facilities, they are not intrinsically synchronized each other. Therefore, it is difficult to obtain the exact overlap of the two laser pulses in the temporal region. In the experiments, a streak camera was utilized to monitor the arrival time of the NIR laser pulse with respect to the XUV laser pulse [101]. As for the temporal resolution of the pump-probe experiment of N_2 can be found in Sec. 6.4.2.

3.1.3.2 Terahertz at FLASH

In this section, the Terahertz (THz) radiation delivered at FLASH is introduced. Similar to the working principle of the production of the FELs by FLASH facility, THz superradiation is an accelerator-based light source. The relativistic electron bunches are passed through the THz undulators and generate coherent radiation in the far infrared regime.

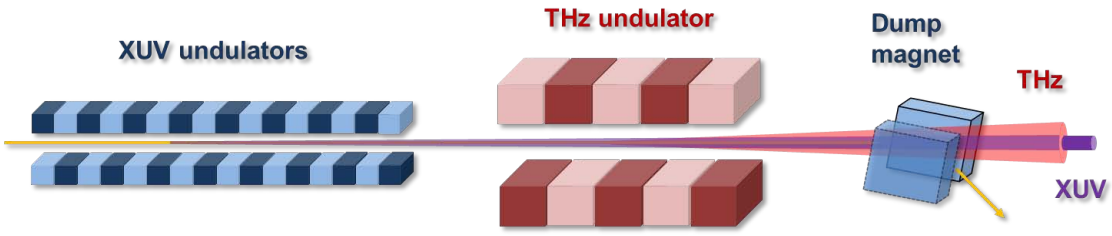

Figure 3.7: The arrangement of the XUV and THz undulators at FLASH. A dump-magnet dumps the electrons. Figure adapted from [102].

The wavelength of the THz radiation is given by

$$\lambda_{\mathrm{THz}} = \frac{\lambda_u}{2\gamma^2}\left(1+\frac{K^2}{2}\right), \tag{3.11}$$

where λ_{THz} is the wavelength of the THz radiation and λ_u is the undulator period. As shown in Fig. 3.7, the THz undulators are arranged behind the XUV undulators. A specially designed planar electromagnetic undulator produces THz radiation with nine full

periods and a period length of 40 cm [103]. The gap of the upper and down plane of the magnets of the undulator is 40 mm. The undulator parameter K = 44 corresponds to the magnetic strength of the coils is 1.18 T [104]. In Eq. 3.11, the undulator period λ_u is fixed, the wavelengths for experiments can be tuned by changing the magnetic field strength and the electron energy. THz undulators deliver radiation tunable in a broad spectral range from the mid-infrared (MIR) to the far infrared (FIR) spectral regions [103]. The wavelength of the THz undulator can be tuned between 10 μm to 230 μm (30 THz to 1.3 THz). The pulse energies which are delivered reach up to 100 μJ and peak electric fields up to 1 MV/cm. The delivered THz pulse comprises the central wavelength and the other odd harmonics wavelengths. During the experiment, the high harmonics was suppressed by one or two filters [105]. The experimental parameters of THz radiation at FLASH are shown in Table 3.2.

Table 3.2: Parameters of the THz radiation at FLASH [22].

Parameters	Typical values
Wavelength	10 - 230 μm
Period	33.3 - 767 fs
Photon energy	5 - 125 meV
Photon frequency	< 1.3 - 30 THz
Photon pulse energy (average)	10 - 100 μJ
Synchronized and phase stable to XUV	$\leqslant$ 5 fs

Since the XUV laser pulse and THz pulse are generated from the same electron bunch, the two pulses should be naturally synchronized. The THz undulator beamline has been designed to provide coherent femtoseconds to picoseconds THz pulses for pump-probe experiments using the femtoseconds XUV pulses from FLASH [22].

The source producing THz light possesses a very strong electromagnetic field, which enables us to measure and map the photoemission time delays and relaxation dynamics of the target after XUV radiation. Moreover, the XUV-pump/THz-probe experiments on the atoms, molecules, clusters, and even solid materials dynamics have attracted considerable attention in recent decades [106]. Combined with a synchronized sub-100 fs XUV laser pulse, the THz pulses are a powerful experimental tool for streaking the ultrafast dynamic response of matter to an intense laser field. The relaxation process usually takes place in molecular systems on the timescale from a few tens to hundreds of femtoseconds which can be probed by a THz pulse with pulse duration few hundreds of femtoseconds. The THz pulses are also used to control and monitor the fundamental properties of matter such as magnetization, ferroelectricity, and optical properties [106, 107]. Using the XUV radiation to trigger the fragmentation and relaxation process of matter, the structural and electronic dynamics of the matter can be mapped by the THz pulses. Nowadays, THz streaking is a powerful tool to map and image the electronic dynamics of atomic and molecular systems after photoionization [42, 105].

In the second experiment, the THz streaking of the autoionization process in O_2, the THz pulses were used to detect the charged particles ionized by XUV radiation. Utilizing a REMI, the ions can be detected in coincidence with the emerging electrons. By mapping

the streaking photoelectrons in the THz electric field, we can characterize the THz vector potential and measure the release times of different types of photoelectrons from different states.

3.2 Reaction Microscope

Recoil-ion momentum spectroscopy (REMI)[4] is a rapidly developing technique that allows one to measure the momentum of several ions and electrons resulting from photon-matter interaction [8]. In the field of recoil-ion spectroscopy, the supersonic jet has established as one standard technique for providing a target with a low thermal spread of a few Kelvin. In a unique combination, 4π solid angle and superior momentum resolutions around a few percents of an atomic unit (a.u.) are typically reached in a REMI [23].

A vital element of the two experiments performed at FLASH is the setup REMI, which allows the coincident detection of the ions and electrons after photoionization. The coincidence measurement is used to track and identify the ions and electrons from the same photoionization and/or dissociation process. By measuring the time-of-flight (TOF) and impact position of the charged particle on the detector, we can reconstruct the initial momenta of each charged particle [23]. The XUV laser beam is divided into the pump- and probe-laser by a multilayer split-and-delay (SD) unit. By adjusting the relative time delays of the two pulses, we can perform time-resolved experiments. In this case, the fully kinematically complete measurements are performed to explore the fragmentation reaction after XUV radiation.

In this section, an introduction to the REMI and its operation principle are given[5]. The supersonic gas jet, spectrometer, and multi-hit detector working principle are introduced in Sec. 3.2.2 and 3.2.3. After that, in Sec. 3.2.4, the momentum reconstruction process is presented.

3.2.1 Vacuum Requirement

Ultra high vacuum (UHV) is required for a successful FLASH experiment. First, some of the devices require a good vacuum, e.g. the Micro-Channel Plates (MCPs) need a high vacuum to avoid sparking. Furthermore, we have to minimize the influence of photon absorption and scattering on the performance of the REMI [109]. The XUV photons that interact with atoms and molecules usually leading to the ejection of valence and inner-shell electrons. The delivered intense XUV laser pulses not only ionize the target but also ionize the residual background gas in the main interaction chamber. In this case, it will produce lots of charged particles which are projected on the detectors.

The pump system of FLASH-REMI is divided into two parts: one for the supersonic gas jet with differential pumping stages, and the other for the main chamber and the beam dump of the gas jet beam. A variety of pumping techniques can reach an UHV. In practice,

[4] or, Cold Target Recoil Ion Momentum Spectroscopy (COLTRIMS)

[5] Most of the content and concepts are compiled from Refs. [8, 16, 23, 55, 56, 108].

the Turbo molecular pumps connected to many pre-pumps are used to ensure the UHV in the main chamber is down to $10^{-9} - 10^{-10}$ mbar. In this case, the vacuum is good for AMO experiments. However, due to the brilliant XUV radiation delivered by FLASH, it is far from enough to carry out the time-resolved XUV spectroscopy. In order to perform the coincidence measurement, high efforts are needed to reach such low pressures down to 10^{-11} mbar or even better. For this, all the coated materials have to be UHV compatible ensuring low outgassing rates and clean surfaces of the inner chamber. To maintain UHV conditions of the reaction chamber, the materials of the inner surface of the chamber are coated with a non-evaporable getter (NEG) material [110]. Before the beamtime, we heated the main beamline and chamber for several days, the NEG material is heated above 180° for at least 24h and cooled down again. The NEG is then activated [16]. Afterwards, the vacuum of the main chamber reaches down to 10^{-11} mbar.

3.2.2 Supersonic Gas Jet

In order to perform a high-resolution momentum spectroscopy measurement, there are some requirements for target preparation. First, a cold target is required due to a fundamental limitation of the momentum resolution of the gas thermal momentum distribution. The second technical requirement is that the target beam is well-localized and collimated to suppress molecules with large transversal kinetic energy. In order to perform the coincidence measurement with a high momentum resolution, the well-designed supersonic jet with differential stages and skimmers is introduced.

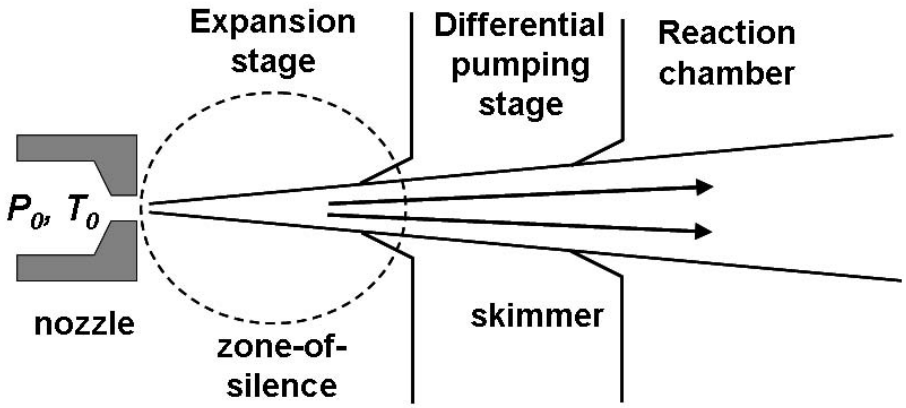

Figure 3.8: Schematic representation of a supersonic gas jet. Figure taken from [56].

Gas at high pressure (1-20 atm.) is forced through a small nozzle (10-100 μm) into a reservoir at low pressure and is thereby accelerated to supersonic speed ($\geq$ 1 Mach) [23]. Thus, the gas is effective cooled. A supersonic gas jet starts from the reservoir with backing pressure P_0 and then expands into the expansion chamber with pressure P_{exp}. If the ratio of P_0/P_{exp} is larger than two, the gas will expand adiabatically behind the nozzle to form a supersonic jet [111]. The speed ratio of the expanding gas is given by

$$S = \frac{v_{\text{jet}}}{v_{\text{therm}}} = \sqrt{\frac{5T}{2T_0}}, \tag{3.12}$$

where v_{jet} is the velocity of the gas-jet, v_{therm} is the thermal velocity, T_0 is the gas temperature before expansion, and T is the internal temperature after expansion. The corresponding limit on momentum resolution of the target along the jet-axis is

$$\Delta P = \sqrt{mk_BT} = \sqrt{5 \cdot m k_B \frac{T_0}{S^2}}, \tag{3.13}$$

where k_B is the Boltzmann constant and m is the mass of the target.

As shown in Fig. 3.8, two-stage with differential pumping are utilized to deal with the enormous gas-load and to maintain an excellent vacuum in the reaction chamber [112]. Two skimmers are placed behind the nozzle to extract a geometrically well-defined supersonic beam. A cold and well-localized gas-jet can be clipped out if the sharp edge of the skimmer immerses into the "zone-of-silence". By using two skimmers and many slits to suppress the transversal momentum of the particles, the temperature of the jet is significantly reduced. The initial momentum distribution of the target is determined by its geometry and the final velocity of the gas jet. In Eq. 3.12, the speed ratio S depends on the target species and the initial temperature before the expansion. For example, if the gas helium with a speed ratio of 50 has an initial temperature of T_0 = 300 K before the expansion, then the achievable temperature is equivalent to T = 0.83 K, and the momentum resolution is corresponding to $\Delta P \approx 0.24$ a.u. [112]. Moreover, to access ever lower temperatures, the target is pre-cooled in the reservoir before the expansion [56].

3.2.3 Spectrometer and Detectors

In this section, the spectrometer and detectors shown in Fig. 3.9 are described in detail. Accurate arrange and assembly of the electrodes and coils are implemented to create a homogeneous field along the axis of the spectrometer. Then, the TOF and impact position of the charged particles on the ion and electron detector can be recorded.

Spectrometer

The function of a spectrometer is to guide the ions and electrons from the photon-interaction onto the detectors by a homogeneous electromagnetic field along the spectrometer. This is achieved by utilizing 22 ring-like plates with isometric spacing. At the center of the REMI, there is a double-steel gap for providing a space to let the unfocused FEL beam go through the spectrometer without hitting the electronics. A constant voltage gradient along the spectrometer is formed by adding a voltage to the uppermost and lowest spectrometer rings via an array of 100 kΩ resistors [16]. The typical strength of the electric field applied to the spectrometer is 5 - 50 V/cm. The produced electromagnetic field accelerates the ions and electrons onto ion- and electron-detector according to their charge. In order to ensure the homogeneous electric field to the very end of the spectrometer, we use high transmission gratings on the top and the bottom to close the spectrometer. At the same time, the gratings prevent field distortion originating from the high voltages ($\sim$ 2700 V) applied to the detectors [16].

As shown in Fig. 3.9, the total length of the spectrometer installed at FLASH is 275 mm. The accelerating length for ions is 94.5 mm and for electrons is 180.5 mm [55]. The focused FEL beam and the supersonic gas jet are oriented perpendicular to the spectrometer

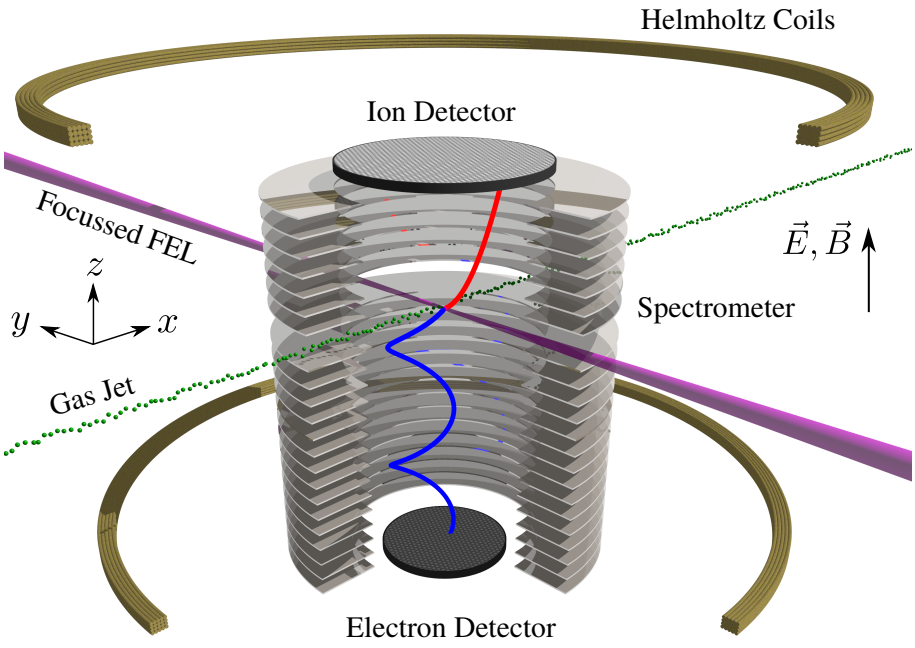

Figure 3.9: REMI setup used for the FLASH experiments. Figure taken from [55].

axis. The propagation direction of the gas jet defines as the x-axis and the FEL beam along the y-axis with its polarization along the x-axis. Meanwhile, a pair of Helmholtz coils is mounted to generate a homogeneous magnetic field which used to collect all the electrons effectively.

Micro-Channel Plate

For REMI, it is essential to install large-area position-sensitive detectors with excellent position resolution and fast timing signals (typically below 1 ns) [112]. The purpose of the detector system is to extract the TOF and position information of the charged particles produced during the photon-matter interaction. To this end, MCPs and delay-line anodes are adopted. MCPs are widely used to detect ions, electrons, and photons and to carry out spectroscopy of their impact position and TOF [113].

In Fig. 3.10, the MCPs are lead-glass plates with a metallic coating which are few millimeters thick. Capillaries perforate the glass panel with a typical diameter of 10 to 100 μm. Both sides of the panel are coated with a well-conducting material so that two equipotential surfaces are formed. A high voltage (HV, typically 1200 V) is applied to both the front and back side of the plate so that each channel acts as an electron multiplier. The primary particle impacting on the MCP releases secondary electrons that are subsequently accelerated by the field and starts an avalanche amplification process. To enhance the number of collisions by secondary electrons with the walls of a microchannel, the angle of the micro-channels with respect to the surface is titled by $\sim 8^{\circ}$. These secondary electrons become amplified by a factor of roughly 10^4 due to many further collisions with the walls inside the channel [108]. Thus, at the back side of the MCP, an electron cloud is produced. By means of two- or three layers of MCPs, the signal-to-noise ratio and detection efficiency improve considerably [55]. Moreover, the electron cloud leaving the capillary

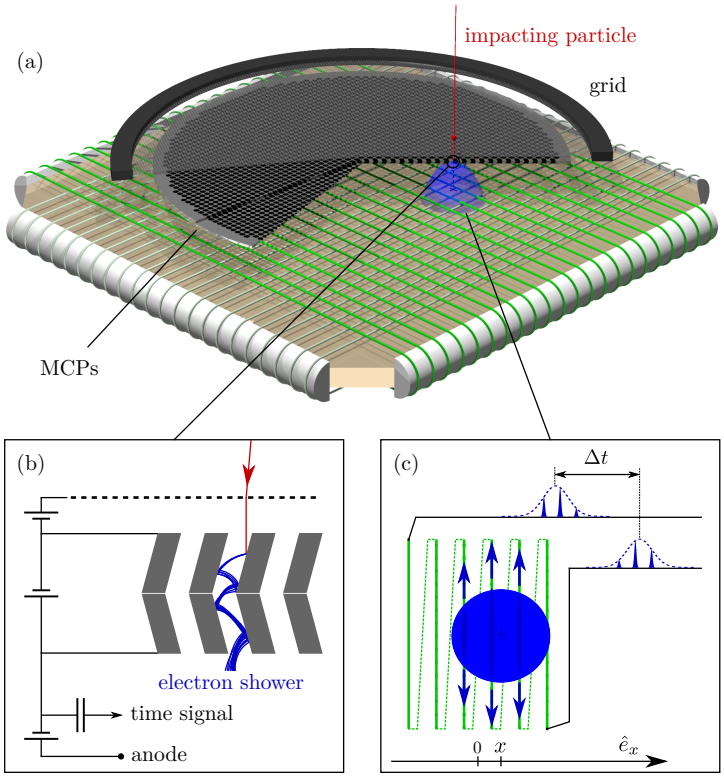

Figure 3.10: The working principle of MCPs and delay-line anode. (a) An electron cloud is created after a particle hits the inner wall of the MCP. The electron cloud is projected onto the delay line anode and produced a timing signal. (b) The impacting particle creates secondary electrons and starts an avalanche amplification process. (c) The principle of impacting position determination with the delay-line anode. Signals propagate along the wire in both directions and are detected at its ends. The time offset Δt carries the spatial information of the particle. Figure taken from Ref. [8].

is still spatially and temporarily confined, which gives rise to an excellent temporal and spatial resolution [56]. As already mentioned above, the homogeneous electric and magnetic fields produced by the spectrometer and Helmholtz coils makes sure that the charged particles can be projected on the MCP. The impact time of a particle that hits on the MCP is used to calculate the TOF. By combining the timing signal of MCP (t_{MCP}) and the FEL trigger time $t_{trigger}$[6], one can calculate the TOF:

$$t_{TOF} = t_{MCP} - t_{trigger}. \tag{3.14}$$

In FLASH-REMI, the ion detector is combined with a Chevron stack of two MCPs (diameter 120 mm), while the electron detector is equipped with a Z-stack of three MCPs (diameter 80 mm) [55]. Integrating two (Chevron stack) or three (Z-stack) MCPs allows for an increase in the amplification factor of up to 10^7 [108].

Delay-line Anode

To obtain position information of the charged particle impinging on the MCP, we utilize a delay-line anode equipped with both high count rate capabilities and excellent position

[6]Provided by FLASH, indicating the arrival time of the FEL pulses.

resolution [112]. As shown in Fig. 3.10, for this, we use a quad-anode with a quadratic shape featuring two sets of parallel wires to extract the position information. The wires are biased with a positive voltage (typically 200 V) with respect to the exit side of the MCP. t_1 and t_2 are the propagation times of the electron cloud to each end of the wire. The time-difference between the two signals is proportional to the position coordinate where the electron cloud has been recorded. In practice, a pair of wires forming a Lecher-cable is exploited for each direction. The reference and signal wires are applied. Typically, the voltage applied on the reference wire is about 50 V lower than that of the signal wire. The subtraction of the two-wire signals can suppress noise and reduce the charge dispersion [114]. Further signal processing and readout are done by fast discriminators and time-to-digital converters (TDC) [112].

If the timing information along the x- and y-direction are obtained, then two-dimensional information on the impact position can be calculated by

$$\begin{aligned} X &\propto (t_{x1} - t_{\mathrm{MCP}}) - (t_{x2} - t_{\mathrm{MCP}}) \\ Y &\propto (t_{y1} - t_{\mathrm{MCP}}) - (t_{y2} - t_{\mathrm{MCP}}) \end{aligned} \tag{3.15}$$

Here, $t_{x1} - t_{x2}$ is the time difference between the signals arriving at both ends of the wire in the x-direction, vice versa, $t_{y1} - t_{y2}$ for y-direction. For each of the ion and electron detectors, the sum of timing signals (MCP and position) which reach the end of the wires is a constant and equals to the transition time from the end of the wire to the other [112].

$$\begin{aligned} t_{\mathrm{SumX}} &= (t_{x1} - t_{\mathrm{MCP}}) + (t_{x2} - t_{\mathrm{MCP}}) = \mathrm{const} \\ t_{\mathrm{SumY}} &= (t_{y1} - t_{\mathrm{MCP}}) + (t_{y2} - t_{\mathrm{MCP}}) = \mathrm{const} \end{aligned} \tag{3.16}$$

The above time-sum condition is applied to identify the timing signals from the same event. With an advanced signal assignment and data recovery procedure, the detector dead-time is significantly reduced. In this case, we can determine all these signals from the same hit on the detector. Therefore, out of the five signals for the ions and seven signals for the electrons, each signal is only used once to prevent the false assignment. The detailed momentum reconstruction will be discussed in the next section after the timing information of TOF and impact position of the charged particles on the detector are measured.

3.2.4 Momentum Reconstruction

As described above in Sec. 3.2.3, in the experiment, we obtain the timing signals of TOF and impact position of the charged particles. In the following, we use a so-called GENERiC (General Analysis Code for Reaction Microscopes) program to process the measured timing signals and to obtain the momentum of the ions and electrons [115]. In the first step, we measured all voltage traces and translated into timing signals by a peak finding program. In the second step, the timing signals are assigned to TOF and positions information. In the last step, the momenta of each particle are calculated and calibrated [16]. Once the momentum reconstruction is complete, the spatial distribution of the reaction fragments can be obtained.

3.2.4.1 Data Acquisition

The signal decoupling, amplification, and discrimination of the decoupled signals together comprise the necessary steps to obtain the digital signals finally [108]. Each particle impact produces several current pulses which are used to retrieve the TOF and impact position of the charged particle. However, before these signals are used for further analysis, they must be decoupled from the channel plates and delay-line anodes to which high voltages are applied. In the case of the MCP, this is achieved by a high-pass filter consisting of a capacitor and a resistor. The signal can be retrieved from the front and back side of the MCP. Both sides are connected to a decoupling circuit. If we pick the signal from the front side, the decoupling circuit from the back is connected to the ground (and vice versa) [108]. As a result, the timing signal is free of external noise. Then, all signals must be amplified for further processing. The next step is the conversion of these signals into standardized NIM logic-signals. In order to obtain a high precision for the time peaking information, the constant fraction discrimination (CFD) is adopted, which produces an output that always triggers at a specified relative height of the signal pulse [16].

The repetition rate of the FEL pulses is 10 Hz with tens of minibunches. Due to the large volume of the timing traces, we used four so-called digitizer (DC282) cards to store the raw timing signals before the peak finding step. The sampling rate is 2 GHz with a maximum voltage range of $\pm$ 5 V [16]. For the distance of one minibunch of typically less than 5 μs, this was found to be far faster than the read-out time for a classical TDC. Thus, the memory of the digitizer card should have the ability to store the total amount of raw data of each FEL laser pulse.

3.2.4.2 Reconstruction of Ion Momentum

In the experiment, we measured the TOF and the corresponding position (x_i , y_i) on the detector of each charged particle. Thus, we can begin to reconstruct the initial momenta of each particle. The basic procedures to reconstruct the ions and electrons momentum in the longitudinal (along with the spectrometer axis) and transversal (perpendicular to the spectrometer axis) direction are presented. The mathematical formulae needed for a spectrometer without a drift zone are shown in this section[7].

Ions Longitudinal

The voltage is applied to the spectrometer and produces an electric field along the spectrometer. Due to the accelerating electric field, the charged particles can gain a longitudinal momentum $p_\parallel$, and the corresponding kinetic energy is $E_\parallel = p_\parallel^2/2m$. The acceleration is given by

$$\ddot{z} = \frac{qU_a}{ml_a}, \tag{3.17}$$

where q is the charge and m is the mass of the ion, U_a is the accelerating voltage, and l_a is the acceleration length over which the voltage is applied. In this case, it allows us to

[7] Most of the content is compiled from Refs. [8, 16, 55, 56, 112].

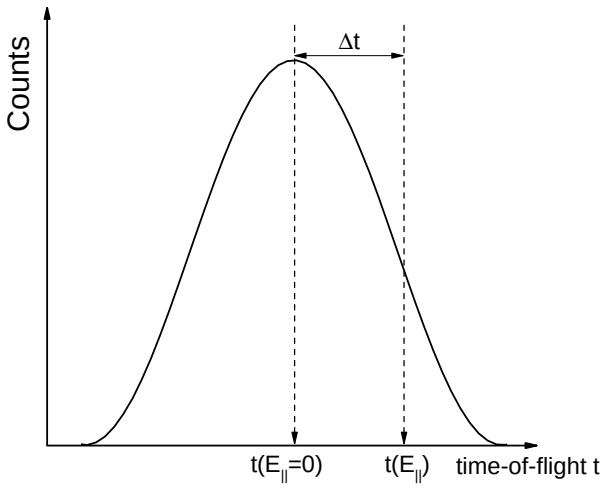

Figure 3.11: Schematic illustration of a recoil-ion time-of-flight distribution [112].

calculate the TOF of ions from the interaction point to the detector:

$$t_{\pm}(E_{\parallel}) = f \cdot \sqrt{m} \cdot \frac{2l_a}{\sqrt{E_{\parallel} + qU_a} \pm \sqrt{E_{\parallel}}} \quad \text{with} \quad f = 719.9 \, \frac{ns}{cm} \sqrt{\frac{eV}{a.u.}}. \tag{3.18}$$

Here, the "+" denotes the ions that are flying towards the ions detector after photoionization, and the "-" represents the ions that are flying away. The constant f originates from the transformation of the units [56]. Because the extraction potential qU_a is much larger than the kinetic energy $E_{\parallel}$, one can distinguish the ion species and/or charge states of the different peaks in the TOF spectrum [112]. Therefore, the position of the peak is given by

$$t_0 = t(E_{\parallel} = 0) = f \sqrt{m/qU_a} \cdot 2l_a. \tag{3.19}$$

As shown in Fig. 3.11, there is an equal probability of the ion to distribute in the forward and backward direction. Thus, one can obtain the initial kinetic energy of the ion

$$E_{\parallel} = \frac{1}{4m} \cdot (\frac{q \cdot U_a \cdot \Delta t}{l_a \cdot f})^2. \tag{3.20}$$

Here $\Delta t = t(E_{\parallel}) - t(E_{\parallel} = 0)$ is the time difference (see Fig. 3.11). According to the Eq. 3.18 and Eq. 3.20, we can obtain the longitudinal momentum $p_{\parallel}$ [8]:

$$p_{\parallel} = 8.04 \cdot 10^{-3} \times \frac{q \cdot U_a}{l_a} \cdot \Delta t. \tag{3.21}$$

The longitudinal momentum resolution is limited by inhomogeneities of the electric field and the response of the electronic modules. Besides, considering the thermal motion

[8] p in a.u., qU$_a$ in eV, l_a in cm and Δt in ns

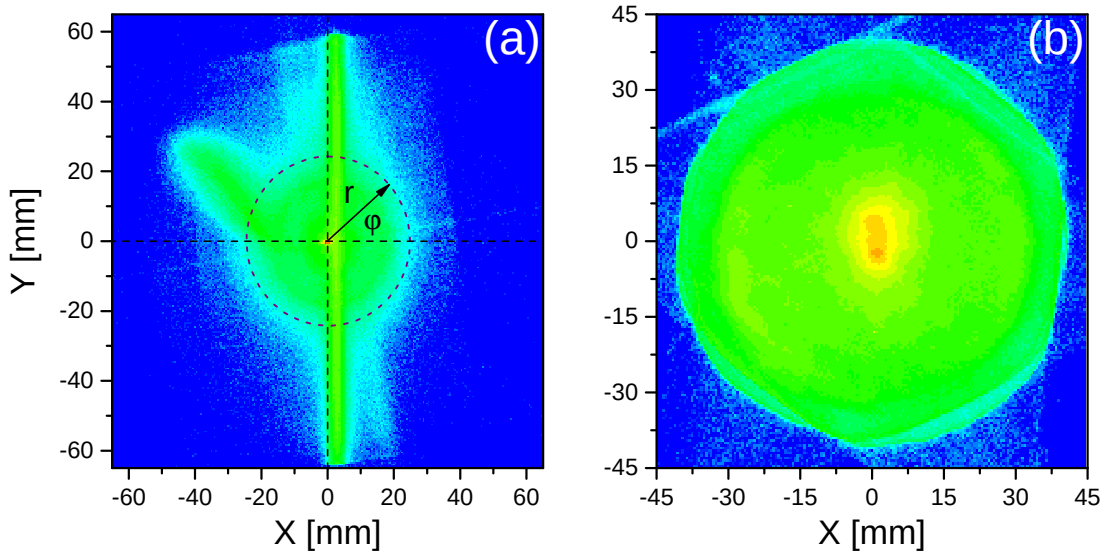

Figure 3.12: Detector image of ions and electrons recorded during the experiments. (a) The FEL beam is parallel to the y-direction and ionized the residual gas of the chamber. A purple ring-like ions distribution is shown due to the Coulomb explosion of the repulsive charged fragments of N_2. (b) Spatial spectrum of electrons ionized from O_2 at a photon energy of 60 eV.

of the gas-jet, one can obtain the quadratic-error in the longitudinal directions using the following equation:

$$\Delta p_{\parallel}^2 = (8.04 \cdot 10^{-3} \cdot \frac{q \cdot U_a}{l_a})^2 \, \Delta t'^2 + \Delta p_{therm}^2, \tag{3.22}$$

where $\Delta t'$ denotes the uncertainty of TOF measurement, and Δp_{therm} is the thermal momentum spread which is related to the temperature of the target.

Ions Transversal

Since there is no acceleration of the ion in the transversal direction, the transversal distance only depends on the initial transversal kinetic energy $E_\perp$ and the TOF. Due to the spatial symmetry distribution of the ions after the photon interaction. In this case, we can calculate the displacement r (see Fig. 3.12 (a)) with respect to the reaction area, using the given formula:

$$r = \frac{1}{f} \cdot \frac{\sqrt{E_\perp}}{\sqrt{m}} \cdot t_{E_\parallel}, \tag{3.23}$$

where m is given in amu, $E_\perp$ and $E_\parallel$ in eV, and t in ns, r in cm. The ion gains significant energy from the extraction compared to its initial recoil-ion kinetic energy:

$$r = 2 \cdot l_a \cdot \sqrt{\frac{E_\perp}{q \cdot U_a}}. \tag{3.24}$$

Therefore, the momentum in the transversal direction[9] is

$$p_\perp = 11.6 \cdot \frac{r}{2 l_a} \cdot \sqrt{q \cdot U_a \cdot m}. \tag{3.25}$$

[9] p being in a.u., qU_a in eV, r in cm and m in amu

In Fig. 3.12, the ions and electrons spectra are shown. A stray line along the center of the ion detector is evident due to the unfocused FEL beam ionizing the residual gas of the interaction chamber. Once the target N_2 is ionized by the FEL beam, the ionization rate increases around the center of the detector. Due to the repulsion of the charged fragments from Coulomb explosion and afterwards, the ring-like spatial distribution of the ions can be observed (see the purple-ring in Fig. 3.12 (a)). In Fig. 3.12 (b), the spatial spectrum of electrons from photoionization of O_2 by a 60 eV XUV radiation is given.

The momentum resolution is determined by the initial target temperature and the uncertainty of the spatial measurement. These uncertainties originate from the data acquisition and the processing of the timing signals. The other factor is also related to the design and arrangement of the experiment, e.g., the electromagnetic field applied and installation of detectors. We can obtain the quadratic-error in the transversal direction by the following equation:

$$\Delta p_{\perp}^2 = (11.6 \cdot \frac{\sqrt{q \cdot U_a \cdot m}}{2 l_a} \Delta r)^2 + \Delta p_{therm}^2, \tag{3.26}$$

where Δr presents the uncertainty of the position measurement.

Hence, the recoil-ion momentum components in the plane of the ion detector are obtained. The azimuthal angle φ in the detector plane can be determined using the two independent x and y coordinates on the detector (see Fig. 3.15). With this angle and transversal momentum $p_{\perp}$, the momentum in the detector XY-plane can be displayed in polar coordinates [56].

3.2.4.3 Coincidences

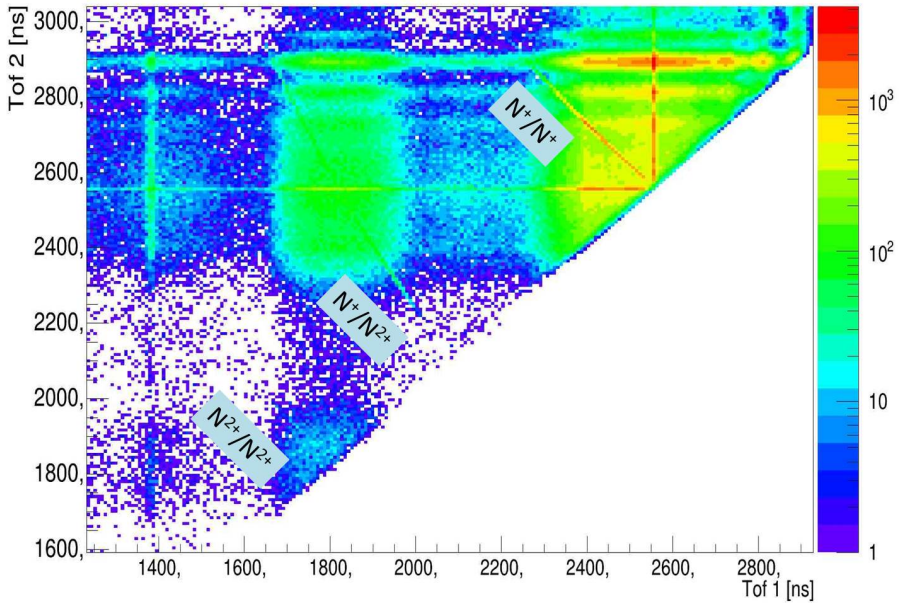

Figure 3.13: Photo-Ion-Photo-Ion Coincidence (PIPICO) spectrum for photoionization of N_2 by 28.3 eV XUV photons. Three coincident channels can be observed from the spectrum.

A principal advantage of a REMI is the ability to perform coincidence measurements and multi-hit detection, by applying the momentum conservation. In the experiment, a PIPICO spectrum was used to generate the coincidences which originated from the same photoionization event. Since the first ion and the second ion come from the same photoionization process, the sum of the TOFs is constant. Therefore, a diagonal line in the spectrum is visible. Even without the calculation of vectors momenta, as shown in Fig. 3.13, coincident channels are identified by plotting the TOF of the first ion (TOF1) against that of the second ion (TOF2) [16]. Three coincidence channels are observed in the figure, namely, the coincidence channel $N^+ + N^+$, $N^+ + N^{2+}$, and $N^{2+} + N^{2+}$. Moreover, with the condition of TOFs sum, most of the random false coincidences are reduced.

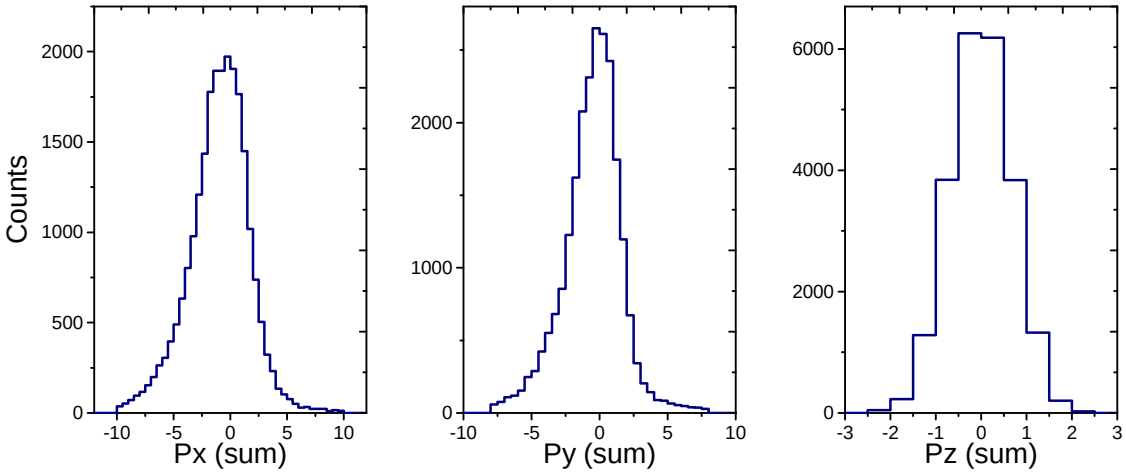

Figure 3.14: Momentum sum conditions for all three spatial directions for coincidence $N^+ + N^+$. The unit of momentum is in a.u.

In Fig. 3.14, the momentum sum of coincidence $N^+ + N^+$ in three spatial coordinates are shown. As already discussed above, the momentum resolution in the longitudinal direction only related to the uncertainty of time measurement and the thermal motion of the target, thus Pz sum is the smallest one compared to the other two directions. In contrast, Px sum is the largest one because of the intrinsic jet-temperature dictates the momentum spread.

3.2.4.4 Reconstruction of Electron Momentum

Electron Transversal

The mass of an electron is 1836 times smaller than the mass of a proton, so the electrons are much easier deflected by the electromagnetic field compare to the ions. In order to reconstruct the transverse momentum components from the TOF and impact position of the electron, the influence of the magnetic field has to be considered. As shown in Fig.3.9, the magnetic field is parallel to the spectrometer axis. An electron has a velocity component which is perpendicular to the magnetic field and travels along a circle with the radius $R = P_\perp/qB$ and the cyclotron frequency $\omega = qB/m_e = 2\pi/T_C$. T_C is the cyclotron

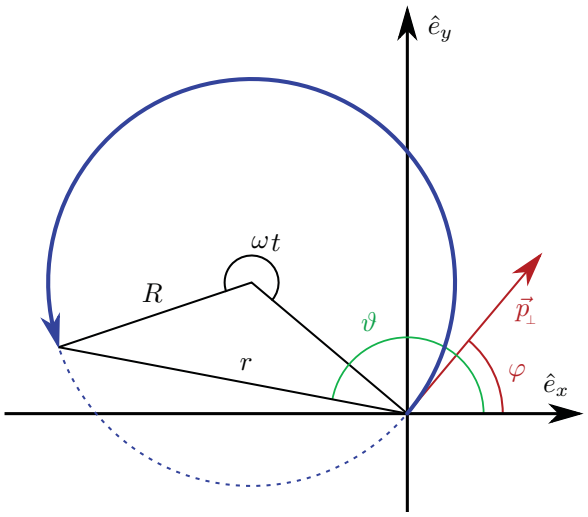

Figure 3.15: Projection of electron trajectory on the detector plane. Figure adapted from [8].

period. m_e and q denote the mass and charge of the electron. In Fig. 3.15, the chord geometry and the projection of electron trajectory on the detector plane are shown. The cyclotron frequency ω and radius R is given by [112]

$$\omega = 9.65 \times 10^{-6} \times qB/m_e \quad \text{and} \quad R = 12.39 \times P_\perp/(qB), \tag{3.27}$$

where ω in ns^{-1}, q and P in atomic units, B in Gauss, and m_e in amu.

The magnetic field does not influence the absolute value of the particle momentum but continuously changes its direction. This leads to a cyclotron motion of the particle while it is accelerated in the electric field along the spectrometer to the detector. In the experiment, we cannot directly observe the cyclotron radius from the spatial spectrum of electrons.

In Fig. 3.15, the electron is emitted with a transverse momentum $p_\perp$ under a certain angle φ with respect to the $\vec{e}_x$ axis. The electrons start to undergo a cyclotron motion from the interaction point with the transversal momentum $p_\perp$. From the geometrical considerations in Fig. 3.15, one can obtain $R = \frac{r}{2|sin(\frac{\omega t_e}{2})|}$. Thus, the transverse momentum $p_\perp$ can be calculated:

$$p_\perp = \frac{m_e \omega}{2|sin(\frac{\omega t_e}{2})|} r, \tag{3.28}$$

where t_e stands for the time-of-flight of the electron.

By measuring the angle ϑ, one can obtain the emission angle φ by the following equation:

$$\varphi = \vartheta - \frac{\omega t_e - 2\pi N}{2}, \tag{3.29}$$

where N = $\frac{t_e}{T_C}$ denotes the number of complete turns moved by the electron [8]. As shown in Fig. 3.16, independent of the initial momentum, the electrons with TOF corresponding to N·T_C are mapped on the same point on the detector. If we plot the spectrum of displacement r versus TOF, as shown in Fig. 3.16, the "wiggles" structure can be observed.

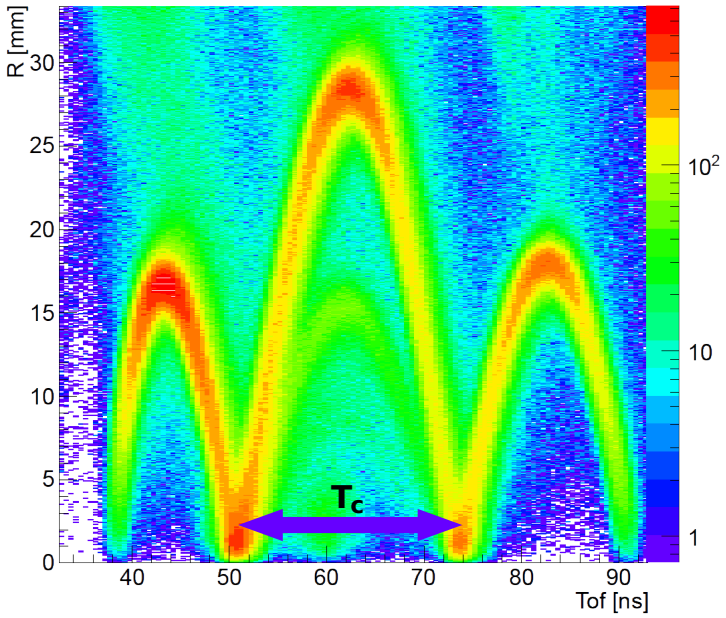

Figure 3.16: Cyclotron motion of the electrons. T_C is the cyclotron period.

If we know the magnitude of magnetic field B and the frequency ω, we can calculate the initial transversal momentum $p_\perp$:

$$p_\perp = 8.04 \cdot 10^{-3} \cdot \frac{rB}{2|sin(\frac{\omega t_e}{2})|}. \tag{3.30}$$

The uncertainty in the position and time measurement are the two factors which determine the resolution of the electron spectrometer. The influence of the target temperature is almost negligible for the energy transferred during the reaction since it is significantly greater than the thermal energy of the target. In contrast to ions, it is tough to show the resolution for all three directions. As visible in the above expressions, the momentum resolution depends on the initial momentum and the measurement of TOF [56].

Electron Longitudinal

As described in the calculation of longitudinal momentum of the ions, the longitudinal momentum of the electrons is only related to the TOF. Similar to the Eq. 3.18, we can calculate the electron momentum in the longitudinal direction:

$$p_\parallel = 0.457 \cdot \frac{L_a}{t_e} - 80.4 \cdot 10^{-3} \frac{q \cdot U_e}{L_a} t_e, \tag{3.31}$$

where L_a is the acceleration length, and U_e is the acceleration voltage.

The longitudinal electron momentum resolution increases with larger TOF. In this case, the momentum resolution in transversal and longitudinal direction can be obtained.

$$\Delta p_\parallel = (0.457 \cdot \frac{L_a}{t_e^2} - 80.4 \cdot 10^{-3} \frac{q \cdot U_e}{L_a}) \cdot \Delta t_e, \tag{3.32}$$

where Δt_e denotes the uncertainty of the time measurement.

To summarize, from the above discussion, we can obtain the full three-dimensional momentum vector of the ion and electron. Therefore, the kinematically complete measurement allows us to map and track the fragmentation after XUV radiation.

3.3 Split and Delay Setup

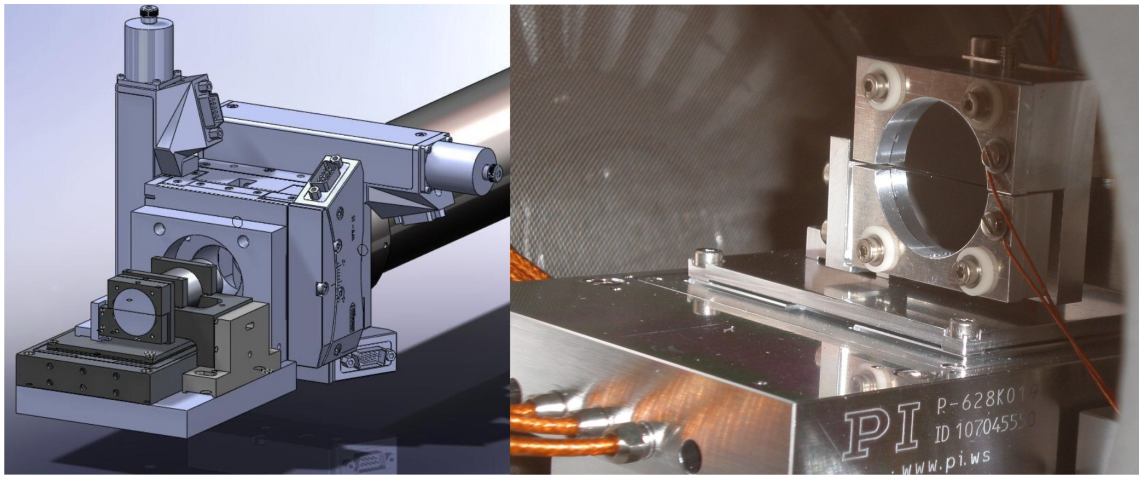

Figure 3.17: Left: the CAD technical drawing of the split-mirror. Right: the SD combined with REMI at FLASH. Figure taken from [45].

In this section, the split and delay (SD) setup installed at FLASH-REMI is introduced. With a pump-probe experimental scheme, we used a REMI in combination with the SD unit to detect the ions in coincidence with the electrons to map the spatial and temporal distribution of fragments after the XUV radiation. In Fig. 3.17, the CAD drawing of SD and a real picture of the mirror chamber is shown [45]. The main function of this set-up is to produce the XUV pulse pairs and adjust the time delay of the pump- and probe-pulse. The back-reflection of this mirror is designed in such a way that the unfocussed FEL light beam passing through the main interaction chamber hits the two split-mirrors, and both of the divided XUV beams can be focused to cross the molecular jet at the center of REMI [56]. In Fig. 3.17 (a), the upper mirror can be easily tipped and tilted with a precision of 0.5 μm to ensure the separated FEL beams overlap in the spatial regime. Within a small distance, we can ensure that two XUV beams spatially and temporally overlap. Meanwhile, the lower mirror is fixed on a delay stage to achieve the time delays scanning up to $\pm$ 2.6 ps with an accuracy of 4 as [56]. In both of two experiments performed at FLASH, this SD unit was used to achieve the scanning of the fragmentation and the relaxation processes that took place in molecular systems.

Chapter 4

The Principle of Streaking

The prime advantage of the streaking technique is the ability to transform the temporal information of a light pulse into spatial information. In recent decades, Attosecond metrology has become a well-established technique to measure the attosecond timescale atomic photoemission and sub-fs decay dynamics [116–121]. In the present THz streaking experiment, we extended this technique by using a long wavelength Terahertz radiation delivered at FLASH combined with a synchronized XUV radiation to perform XUV-pump/THz-probe experiments. Such experiments enable us to investigate photon-matter dynamics with the timescale of up to a few hundreds of femtoseconds.

In this chapter, the principle of streaking and experimental results are presented. The background of streaking photoelectrons with a Terahertz field is introduced in Sec. 4.1. This section will provide a basis for the understanding of the streaking spectroscopy. In Sec. 4.2, the characterization of the THz pulses delivered by the FLASH facility is introduced. Sec. 4.3 gives a short theoretical description of photoemission time delays. In Sec. 4.3.2, the Coulomb-laser-coupling time shifts of the low-energetic photoelectrons from the O_2 photoionization process by 60 eV XUV radiation are given. Finally, the chapter ends with a conclusion in Sec. 4.4.

4.1 Streaking Photoelectrons with a Terahertz Field

The basic principle of THz streaking of photoelectron will be discussed[1]. In a classical picture, the electron ejected via photoionization by XUV radiation, is treated as a charged particle instead of a wave-packet.

The photoelectron jumps into a THz electric field with the initial momentum p_i:

$$p_i = \sqrt{2m_e E_{kin,i}} = \sqrt{2m_e(\hbar\omega_{XUV} - E_{bind})}\,, \tag{4.1}$$

where $E_{kin,i}$ is the initial kinetic energy, $\hbar\omega_{XUV}$ is the XUV photon energy, and E_{bind} is the binding energy of the electron.

[1] Most of the content is compiled from [122, 123].

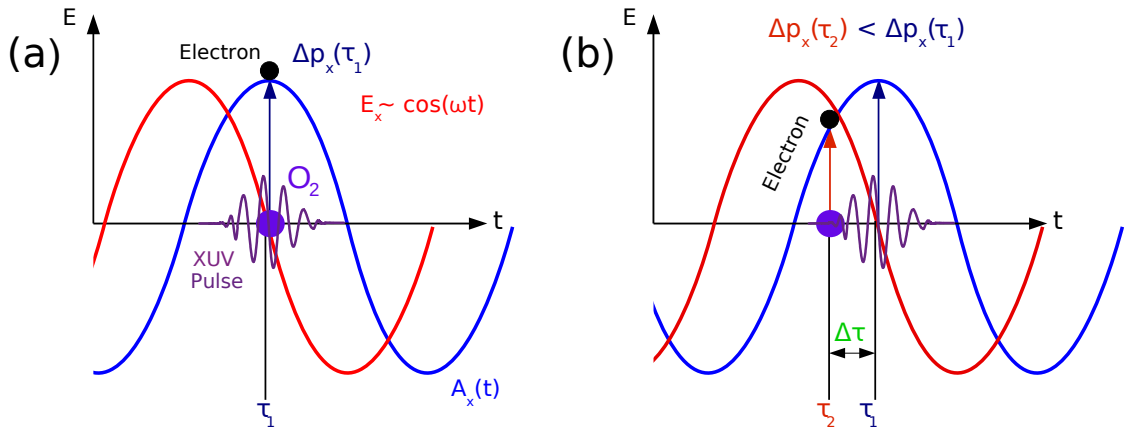

Figure 4.1: Principle of the THz streaking with a linearly polarized pulse. The solid red and blue lines represent the electric field and vector potential of the streaking field, respectively. The photoelectrons are emitted via ionization by XUV photon. Photoelectrons obtain a momentum shift, depending on the vector potential of the streaking field at the moment of ionization. (a) An electron is released at the time τ_1 and gains the momentum shift $\Delta p_x(\tau_1)$. (b) The secondary electron is released at time τ_2 with the momentum shift $\Delta p_x(\tau_2)$. Since the momentum shift is proportional to the magnitude of the vector potential, thus $\Delta p_x(\tau_2) < \Delta p_x(\tau_1)$. The time delay $\Delta\tau$ between the first emitted photoelectron and the secondary photoelectron carries the information on photoemission time delays of the two photoelectrons and the relaxation of the system after XUV radiation. Figure adapted from [124].

For simplicity, we use the following equation to describe the THz electric field:

$$E_{THz}(t) = E_0(t)\, cos(\omega_{THz} t + \varphi), \tag{4.2}$$

where E_0 is the amplitude, ω_{THz} is the frequency, and φ is the initial phase of the electric field. In the presence of the THz electric field, the freed electron can be streaked by gaining or losing energy in the electric field. THz streaking field is linearly polarized along the x-axis at FLASH. Therefore, the momentum shift of an electron is given by

$$\Delta p_x(\tau) = -e \int_{\tau}^{\infty} E_0(t)\, cos(\omega_{THz} t + \varphi) dt = -eA_{THz}(\tau), \tag{4.3}$$

where τ is the initial release time of the electron into the electric field. $A_{THz}(t) = \int_t^{\infty} E_{THz}(t')dt'$ is the corresponding vector potential. In Fig. 4.1, the THz streaking principle is presented. The momentum shift experienced by the secondary electron $\Delta p_x(\tau_2)$ is smaller than the first released electron momentum shift $\Delta p_x(\tau_1)$. The time delay $\Delta\tau$ between the first released electron and secondary electron can be used to interpret time delays in photoemission steps and lifetimes of relaxation.

According to the adiabatic approximation which is $dE_0(t)/dt \ll E_0\omega_{THz}$, this means that the temporal deviation of the envelope of the THz pulse is far less than the frequency of its carrier wave [122]. The analytical expression of the time-dependent streaked photo-

electron can be expressed as

$$\Delta p_x(\tau) \approx \frac{eE_0(\tau)}{\omega_{THz}} sin(\omega_{THz}\tau + \varphi) = \sqrt{4U_p(\tau)m_e} sin(\omega_{THz}\tau + \varphi). \tag{4.4}$$

In this case, the final momentum of the electron is given by

$$p_f^2 = p_i^2 + 2p_i p_x cos(\theta) + \Delta p_x^2, \tag{4.5}$$

where detection angle θ is the angle between the polarization axis and the final momentum emission direction (see Fig. 4.2).

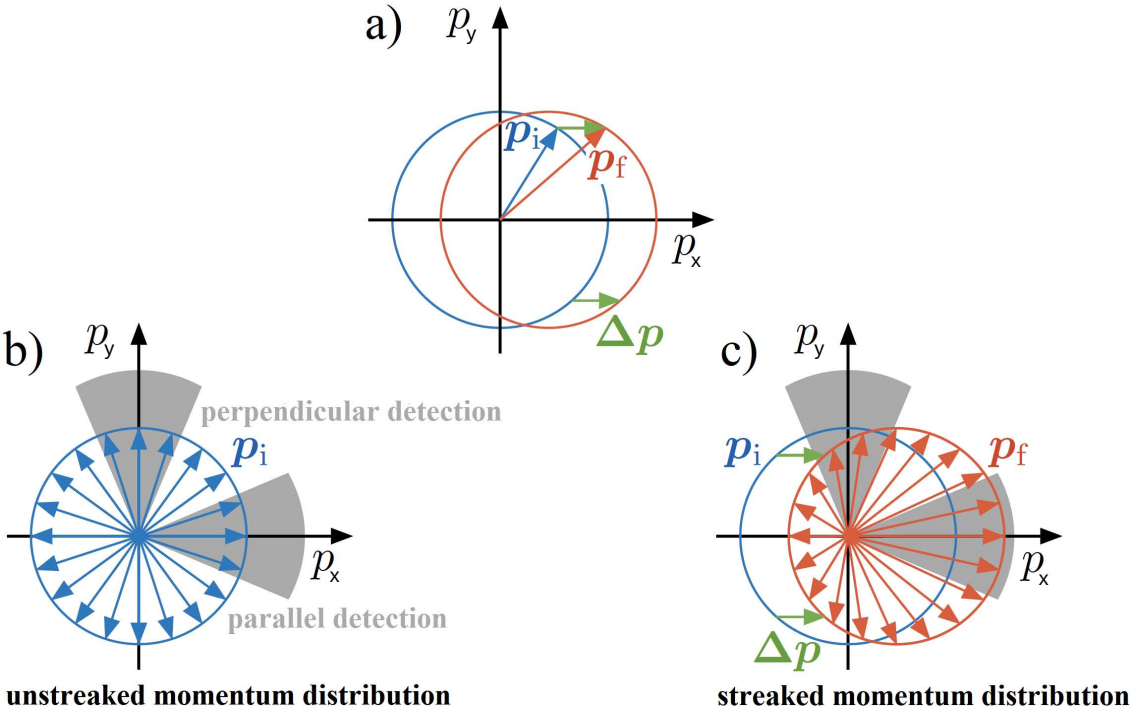

Figure 4.2: Illustration of the angle-dependent effect of a THz electric field on the photoelectrons ionized by XUV radiation. The polarization of the THz pulse is along the p_x direction. (a) Due to the streaking field, the initial momentum p_i is shifted to p_f along the THz polarization direction. (b) The un-streaked momentum is an isotropic distribution in either parallel detection or perpendicular detection. (c) Schematic of the streaked momentum distribution in perpendicular and parallel direction. Adapted from [122].

In our case, after the oxygen molecule was ionized by XUV radiation, the photoelectrons have altered their momentum component in the direction of the THz electric field. Thus, the final kinetic energy of the freed electron with a final drift velocity parallel to the electric field can be described as

$$\begin{aligned} E_{kin,f}(\tau) = \frac{p_f^2}{2m_e} &= E_{kin,i} + 2U_p(\tau)cos(2\theta)sin^2(\omega_{THz}\tau + \varphi) \\ &+ \sqrt{8E_{kin,i}U_p(\tau)}cos(\theta)\,sin(\omega_{THz}\tau + \varphi) \end{aligned} \tag{4.6}$$

with $U_p = \frac{e^2 E_0^2(t)}{4 m_e \omega_{THz}^2}$ being the ponderomotive potential of the THz electric field. For a wavelength of the THz pulse at 150 μm, the corresponding ponderomotive potential U_p is on the order of a few tens meV which is far less than the initial kinetic energy of the photoelectron[2]. Hereby, the second term in the Eq. 4.6 can be ignored. Thus, the final kinetic energy is obtained which depends on the moment τ of the freed electron released into the THz electric field. Moreover, the final kinetic energy is also related to the detection angle θ. The influence of the instant ionization on the electron momentum is expected to be isotropic (un-streaked momentum distribution, see Fig. 4.2). In a parallel orientation which means the detection angle $\theta = 0$ between detector axis and the polarization axis of the THz electric field, the time-dependent kinetic energy shift of the streaked photoelectron can be expressed as

$$\Delta E_{kin}(\tau) = E_{kin,f} - E_{kin,i} \approx \sqrt{8 E_{kin,i} U_p(\tau)} sin(\omega_{THz}\tau + \varphi). \tag{4.7}$$

Hence, by adjusting the time delay of the XUV laser pulse and THz pulse, the vector potential $A_{THz}(t)$ is mapped to the momentum or energy shifts of the photoelectron.

In recent decades, with the development of light sources and techniques, the THz streaking technique has become a powerful experimental tool in experiments on the diagnostics of the X-ray pulses, AMO dynamics, and solid material properties [22,101,103,105,106]. Ulrike Frühling *et al.* has examined the single-shot characterization of soft X-ray pulses from FLASH [105]. By monitoring the fluctuation of the streaking kinetic energy of photoelectrons of Krypton, the arrival time jitter of two FEL pulses was measured. The second vital application of the THz streaking technique relates to the use of the external optical laser-driving THz light source that allows characterizing the temporal profile of individual FEL pulses with sub-10 fs accuracy [125].

Using the XUV radiation and super-radiation THz light source at FLASH, allows us to extend the attosecond streaking technique to explore the relaxation dynamics of AMO systems with up to a few 100 femtoseconds of time resolution in experiments [106, 126]. If the time scale of the relaxation processes is shorter than half of the optical cycle of the THz field, the temporal evolution process can be streaked by the THz field. A wavelength of 154.2 μm THz radiation has a period of 514 fs. It can be used to trace relaxation processes in atomic and molecular systems which taking place within a 257 fs. Utilizing the THz-streaking technique, we can trace the ICD process in Neon dimer, Auger decay in the Xenon atom, and the autoionization process of O_2.

4.2 Characterization of THz Vector Potential

As discussed in Sec. 3.1.3.2, the FEL pulse and the THz pulse are generated by the same electron bunch at FLASH [103], therefore, the jitter and long-term drift of the two pulses are small, and a good synchronization is expected [22, 127]. In the THz streaking experiment, the FEL beam and THz beam was overlapped in the spatial and temporal regime, making it possible to perform XUV-pump/THz-probe experiment.

[2] In the present experiment, the estimated ponderomotive energy U_p is 1.3 meV.

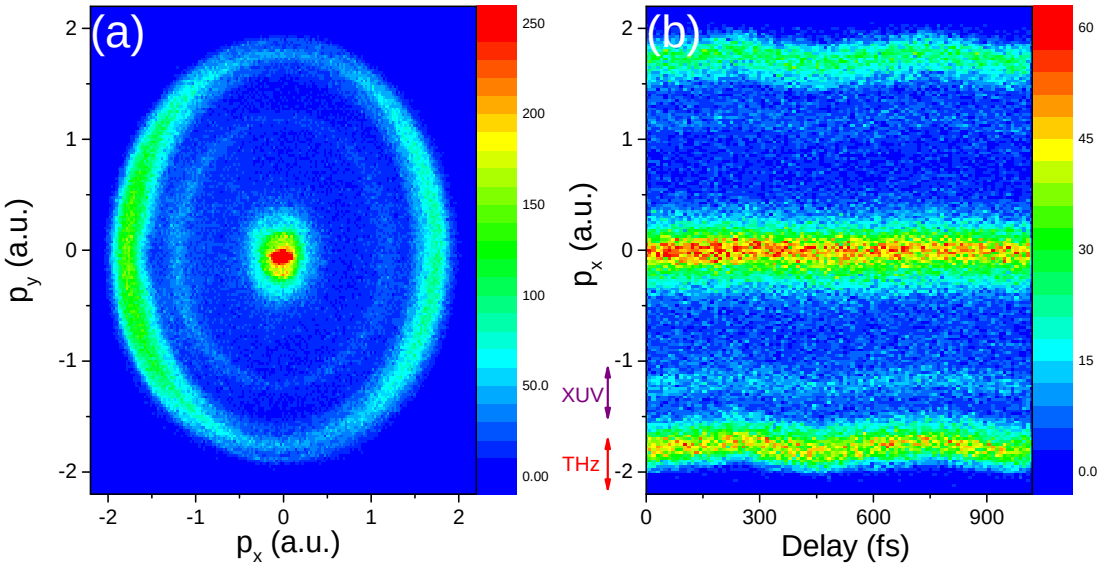

Figure 4.3: (a) The electron momentum distribution (momentum condition $-0.35 < p_z < +0.35\,a.u.$). (b) Time-dependent photoelectrons momentum trace (momentum slice conditions: $-0.35 < p_{y/z} < +0.35\,a.u.$). The selected photoelectrons along the polarization of the THz electric field. The polarization of the XUV laser pulse and the THz electric field are both parallel to the p_x axis. The red and the purple arrows mark the THz and XUV polarization, respectively.

In order to resolve the timing information on photoemission or relaxation processes, in the first place, we have to characterize the THz pulse. As already described in Sec. 4.1, the momentum shift $\Delta p(\tau) = -eA(\tau)$ transferred to the photoelectrons in the THz vector potential $A(t)$ is mapped on the photoelectron momentum in addition to its initial momentum p_i [124]. As already introduced in Sec. 3.2, the kinematically complete experiments ensure a solid angle acceptance of 4π for ions and electrons by using the REMI [23]. By measuring the time-dependent momentum traces of photoelectrons along the polarization of the THz vector potential, we can characterize the basic parameters of the THz vector potential, e.g., the wavelength, the oscillation period and the initial phase.

As shown in Fig. 4.2 and described in Eq. 4.6, there are two detection methods, a perpendicular orientation with a detection angle of $\theta = 90°$ between the detector axis and the polarization axis of the THz pulse. In this circumstance, we can observe only an asymmetrical broadening in energy and a periodic shift by two THz frequencies to lower energies in the photoelectron spectra [122, 128, 129]. However, in the case of parallel detection where $\theta = 0°$, one can observe a periodic up- and down-shift in the energy of the photoelectron traces is detected in the spectra [130]. The photoelectrons obtain the maximum momentum shift along the polarization of the THz electric field.

Thus, we select the photoelectrons emitted along the polarization within a small emission angle for the photoelectrons gain more in momentum shift along the polarization of the THz pulse. In Fig. 4.3 (a), the electron momentum distribution in polarization plane is shown with the condition on p_z from -0.35 a.u. to +0.35 a.u. In order to subtract the "background", we select the photoelectrons with a further condition on p_y from -0.35 a.u. to +0.35 a.u., then we get the electron momentum traces as a function of the

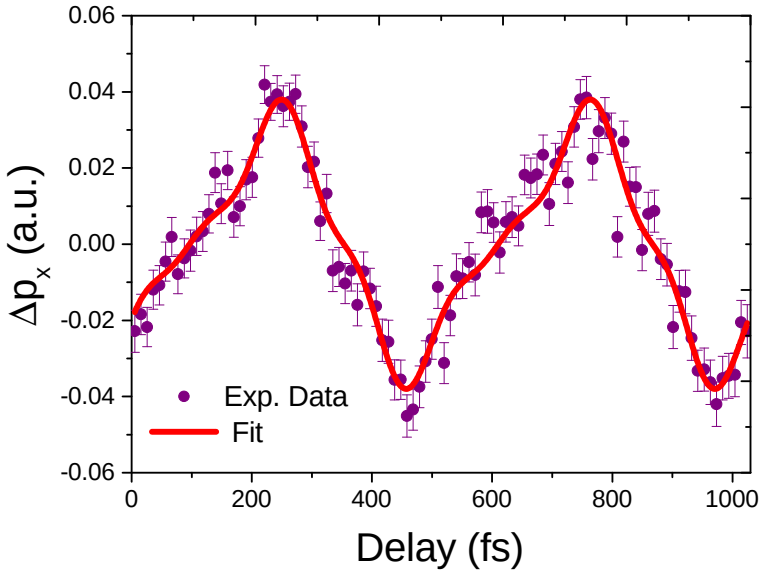

Figure 4.4: The momenta shift Δp_x as a function of the time delay between the XUV laser pulse and the THz pulse. Only the electrons emitted along the THz polarization are selected. The purple dots from experimental data are fitting by a Fourier series of triangle functions. The red line is the fit.

time delay between the XUV laser pulse and the THz pulse. In Fig. 4.3 (b), the plot of the time-dependent momentum of all the photoelectrons is shown. From the photoelectron momentum traces, we can directly map the THz vector potential.

In the time-resolved experiments on autoionization process of molecular oxygen, we merely focus on the time delays or phase shifts information. Thus, in the course of data analysis, we adopted an "Averaging Method" to get the momentum center of the photoelectrons trace by calculating the average of the momenta for each delay range:

$$\overline{p_x} = \frac{\Sigma_{i=1}^{n} p_{x_i}(t) \cdot N_i}{N}, \tag{4.8}$$

where $\overline{p_x}$ is the average momenta of the selected photoelectron, N_i is the statistical number of the electron at each $p_{x_i}(t)$, and N is the total number of each delay t. In the following, we intend to obtain detailed THz pulse parameters. As shown in Fig. 4.4, using the temporal profile of photoelectrons (momenta peaked at -1.73 a.u. in Fig. 4.3 (b)) to obtain the time-dependent average momenta trace. The THz vector potential can be well-described by the Fourier series of triangle functions with up to fourth order of harmonics:

$$A_{THz}(t) = A_0 \Sigma_{i=1}^{n} \frac{(-1)^{(n-1)/2}}{n^2} sin(n\pi \cdot \omega_{THz} t + \varphi), \tag{4.9}$$

where A_0 is the amplitude, ω_{THz} is the frequency and φ is the initial phase of the THz vector potential. From the fit results, we find that the maximum momentum shift A_0 is 0.044 $\pm$ 0.002 a.u., the oscillation period T_0 is 514 $\pm$ 3.6 fs (the corresponding wavelength is 154.2 $\pm$ 1.1 μm), and the initial phase of the vector potential is -96.4 $\pm$ 3.9 fs. In Eq. 4.4,

the induced momentum shift by the streaking field is proportional to the amplitude of the vector potential $A_{THz}(t)$ of which the maximum electric field strength $E_{max} = \frac{2\pi\Delta p_{max}}{eT_0}$ reaches up to 6.7 MV/m.

As mentioned above, the momentum shift Δp_i of emitted electrons (and ions) depends on the release time τ into the THz field. A relative phase shift between the momentum traces of two different photoelectron species indicates a temporal time delay existing in their photoemission steps or the lifetimes of the relaxation processes [124]. The typical pulse length of the XUV laser pulse τ_{XUV} is roughly 100 fs and the present period of the THz pulse is near 514 fs which fulfill the streaking condition: $\tau_{XUV} \leq T_{THz}/2$, where T_{THz} is the period of one cycle of the THz electric field [131]. In the case, we can use this technique to resolve the relaxation processes of the molecular systems that take place within 257 fs time scales. As mentioned by Ref. [12], the lifetime order of magnitude of autoionization in molecular oxygen is within 300 fs, in this case, the autoionization and its electronic relaxation process in molecular oxygen can be properly traced in the XUV-pump/THz-probe experiment.

From the above discussion, the experimental parameters of the THz pulse are listed in Table. 4.1.

Characterization of THz Pulse	
Frequency ω_{THz}	1.946 ± 0.014 THz
Wavelength λ	154.2 ± 1.1 μm
Period T_0	514 ± 3.6 fs
Max. amplitude $p_{\max}$	0.044 ± 0.002 a.u.
Max. field strength	6.7 MV/m
Intensity I_{pulse}	$\approx 10^7 W/cm^2$

Table 4.1: Experimental parameters of THz pulse.

4.3 Photoionization Time Delays

How long does the photoionization process take [132]? What is the precise physics behind the time delays measured in our experiments? These questions touch upon fundamental issues of quantum mechanics and have been a subject of long-standing controversy [133, 134]. In the following, the photoemission time delay principle and Coulomb laser coupling induced time delays in atomic and molecular systems are discussed[3].

The characterization of the dynamics of a photoelectron wavepacket commonly refers to the notion of "Scattering time delay" developed in the context of quantum collision theory [138, 139]. A scattered wave packet experiences a phase shift when compared with free motion. In the 1950s, Eisenbud, Wigner, and Smith [138–140] pointed out that the delay can be characterized through the spectral derivative of the phase shift δ. The time delay is called Eisenbud-Wigner-Smith (EWS) time delay.

[3]The content is compiled from Refs. [124, 132, 135–137]

We treat an incident electron wave packet $\Psi_{\text{in}}(x,t)$ which is expressed as a superposition of plane waves $\psi_k(x,t)$ with amplitudes A_k, momenta k, and energies E_k [141]:

$$\Psi_{\text{in}}(x,t) = \int \mathrm{d}k\,\psi_k(x,t) = \int \mathrm{d}k A_k\, e^{\mathrm{i}(kx - E_k t)}. \tag{4.10}$$

The wavefunction propagates an attractive short-range potential $V_0(x)$ in one spatial dimension. By passing the attractive potential, the individual traveling plane waves $\psi_k(x,t)$ will accumulate scattering phases δ_k. Depending on the values of the phase δ_k, wavefronts of the scattering wave are shifted relative to the incident wave. In Fig. 4.5, the outgoing electron wavefunction acquires a phase δ compared to the free case during it propagates through a short-range potential [137].

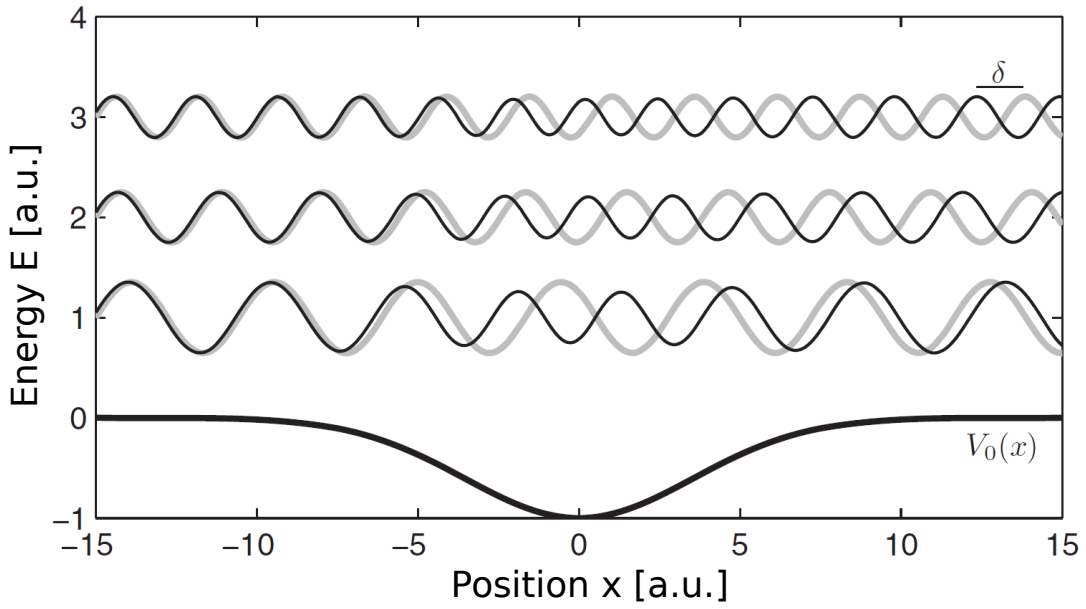

Figure 4.5: The photoelectrons at three different energies E = 1, 2, 3 a.u. passing through an attractive potential $\mathrm{V}_0(x)$ accumulate a phase shift δ compared to a free case (thick grey curve). Figure is taken from [137].

Thus, the outgoing electron wave packet is given by the equation provided in Ref. [141]:

$$\Psi_{\text{out}}(x,t) = \int \mathrm{d}k A_k\, e^{\mathrm{i}\delta_k}\, e^{\mathrm{i}(kx - E_k t)}. \tag{4.11}$$

δ_k is the phase shift of each spectral component relative to the initial phase of the incident wave. Therefore, the phase shifts of the outgoing electron wavepacket of a partial wave with angular momentum quantum number l with respect to a free partial wave is defined as

$$t_{\text{EWS}}(E,l) = \frac{\mathrm{d}\delta_l(E)}{\mathrm{d}E}. \tag{4.12}$$

In the above equation, t_{EWS} can be interpreted as the ejected electron "situated" in the quasi-bound state [142]. Moreover, the equation indicates that photoionization is a half-scattering process [143].

An electron ejected via photoionization by XUV radiation. Thus, t_{EWS} has to be constructed regarding the transition matrix element of the dipole operator $\mathbf{d} = \langle \psi_f | \mathbf{r} | \psi_i \rangle$ between the bound initial state ψ_i and the continuum final state ψ_f for emission in every solid angle [142]:

$$t_{\mathrm{EWS}} = \frac{\mathrm{d}}{\mathrm{d}E} \arg \left[\langle \psi_f | \mathbf{d} | \psi_i \rangle \right]. \tag{4.13}$$

$\mathrm{t_{EWS}}$ is typically on the order of tens or hundreds of attoseconds and the absolute time delay in photoemission is not available in the experiment. Most of the experiments performed to measure photoemission time delays so far has only measured relative time delays. For atomic ionization, we can often use two partial-wave channels to describe the scattering potential results. However, for molecular ionization, the anisotropic character of the potential means that more partial waves are required to depict the photoelectron wavepacket due to the nature of the complexity of the molecules [136]. The phase shift is also related to the spatial properties and energy-based geometry of the molecular system.

4.3.1 The Coulombic Time Delays

The detailed introduction of the Coulomb time delays can be found in Refs. [142,143]. As discussed above, the EWS time delay is the energy variation of the partial-wave scattering phase shift at short-range potential. However, during the photoemission, the outgoing electron is exposed to the long-range Coulomb interaction[4]. Now, let us consider the long-range Coulomb interaction on the phase distortion. As shown in Refs. [142–144], the energy and position dependent phase of the whole Coulomb wave is given by

$$\phi(E,l,r) = \sigma_l(E) + \frac{Z_{eff}}{p} \ln[2pr], \tag{4.14}$$

where l is the partial wave, Z_{eff} is the effective core charge, $p = \sqrt{2E}$ is the asymptotic momentum and $\sigma_l(E) = \arg\Gamma[1 + l - \mathrm{i}Z_{eff}/p]$ is the r-independent term which is the Coulomb analogue to the phase shift in scattering theory. Then, the time delay to the Coulomb-phase by the energy derivative:

$$t_{\mathrm{c}}(E,l,r) = \frac{\partial}{\partial E}\phi(E,l,r) = t_{\mathrm{EWS}}(E,l) + \Delta t_{\mathrm{c}}(E,r). \tag{4.15}$$

The r-independent term $t_{\mathrm{EWS}}(E,l) = \frac{\partial}{\partial E}\sigma_l(E)$ is the Coulomb time shift analogue of the EWS time delay which depends on the initial state [132]. While the r-dependent term is expressed as

$$\Delta t_{\mathrm{c}}(E,r) = \frac{Z_{eff}}{(2E)^{\frac{3}{2}}} \left(1 - \ln\left[2\sqrt{2E}r\right]\right). \tag{4.16}$$

The term $\Delta t_{\mathrm{c}}(E,r)$ is a Coulomb distortion which depends only on the energy E of the electron and the strength of the Coulomb field. However, it is independent of the partial wave l or the initial state. The Coulomb-induced time shift Δt_c is a crucial parameter in atomic photoemission. And the lucky thing is that we can use the analytical expressions to describe this time shift.

[4]Most of the following content from Ref. [132] supplemental material.

4.3.2 Measurement-Induced Time Shift

The EWS time delay is not directly accessible in streaking measurements. At some point, the influence of the probe electric field should be taken into consideration of the time shifts we measure. In the present section, the measurement induced time-shift is discussed[5].

The final momentum $p_f(\tau)$ of an electron with the initial momentum $p_i(\tau)$ in the vicinity of the core and which reaches the continuum at position $r(\tau) \approx 0$, is given by

$$p_f(\tau) = p_i(\tau) + \int_{\tau}^{\infty} F\left[E_c(r(t)), E_p(t)\right] dt. \tag{4.17}$$

$F\left[E_c(r(t)), E_p(t)\right]$ is the force that results from the interaction between Coulomb field $E_c(r(t))$ and probe field $E_p(t)$. If the momentum of the electron is only perturbed by the probe field, namely, the term $E_c(r(t)) = 0$, then the Eq. 4.17 reduces to the Eq. 4.3. Now, let us consider the final momentum at the time τ including the influence the probe electric field $E_p(t)$:

$$p_f(\tau) = p_0 - eA(\tau) + \int_{\tau}^{\infty} \left\{F\left[E_c(r(t)), E_p(t)\right] - F_c\left[E_c(r(t)), 0\right] - F_p\left[0, E_p(t)\right]\right\} dt, \tag{4.18}$$

where p_0 is the asymptotic momentum of the photoelectron.

From the above discussion, we get the final measurement time shift which includes the Coulomb-laser coupling (CLC). If we Taylor expand the integral term in Eq. 4.18:

$$\int_{\tau}^{\infty} \left\{F\left[E_c(r(t)), E_p(t)\right] - F_c\left[E_c(r(t)), 0\right] - F_p\left[0, E_p(t)\right]\right\} dt \approx \xi(E, Z, \omega_p) E_p(\tau), \tag{4.19}$$

where $\xi(E, Z, \omega_p)$ is constant that depends on the kinetic energy E of the emitted electron, the ionic charge Z, the frequency ω_p of the probe field. However, $\xi(E, Z, \omega_p)$ is independent of the field strength of the probe field. Consequently, in the absence of any intrinsic delay, we obtain the final momentum of the emitted electron by including the Coulomb-laser coupling:

$$p_f(\tau) = p_0 - \alpha A(\tau + t_{\text{clc}}) \tag{4.20}$$

with a field strength independent time shift t_{clc}

$$t_{\text{clc}} = \frac{1}{\omega_p} \tan^{-1} \xi(E, Z, \omega_p) \tag{4.21}$$

and a field strength parameter α

$$\alpha = \frac{eE_p}{\omega_p} \sqrt{1 + \xi(E, Z, \omega_p)^2}. \tag{4.22}$$

Up to now, the total time delays of the photoemission include two parts: one is the intrinsic EWS time delay, and the other is the CLC time delay:

$$t_{\text{tot}} = t_{\text{EWS}} + t_{\text{clc}}. \tag{4.23}$$

[5] Most of the content is compiled from [124, 131, 142]

According to the analytical expressions given by [142] and Eq. 4.16, the measurement-induced time shifts that arise from Coulomb-laser coupling is

$$t_{\rm clc}(E,\omega_{\rm p}) = \frac{Z}{(2E)^{3/2}}\left(1-\ln[2k^2 t_0]\right) \approx \frac{Z}{(2E)^{3/2}}\left(1-\ln\left[\frac{0.37E}{2\pi\omega_{\rm p}}\right]\right), \tag{4.24}$$

where ω_p is the frequency of the probe laser field, t_0 is a fit parameter which is related to the numerical simulation of classical trajectory [145].

If the effective core charge Z = 1 and the probe laser is the THz pulse, then we obtain

$$t_{\rm clc}(E) \approx -\frac{1}{E^{3/2}}\left(\ln\left[0.37\frac{2\pi E}{\omega_{\rm THz}}\right]-1\right). \tag{4.25}$$

In order to understand the measurement induced time shift, many analytical formulas are proposed. For instance, the analytical expression proposed in Ref. [146]:

$$t_{\rm clc}(E) = -\frac{1}{E^{3/2}}\left(\ln\left[\frac{4E}{\omega_{\rm THz}}\right]-\gamma_{\rm E}+\frac{\pi\omega_{\rm THz}}{6E}\right), \tag{4.26}$$

where $\gamma_{\rm E}$ is the Euler parameter[6]. Or, the other analytical expression given by Ref. [147]

$$t_{\rm clc}(E) = -\frac{1}{E^{3/2}}\left(\ln\left[\frac{4E}{\omega_{\rm THz}}\right]-\gamma_{\rm E}-1+\frac{3\pi\omega_{\rm THz}}{4(2E)^{3/2}}\right). \tag{4.27}$$

From the above discussion, the formulas of Eq. 4.25, 4.26 and 4.27 have all similar expression like:

$$t_{\rm clc}(E,\omega_{THz}) \propto -\frac{1}{E^{3/2}}\left(\ln\frac{E}{\omega_{THz}}+const.\right). \tag{4.28}$$

The only difference in the above three formulas is that the factors are different. The Coulomb-laser coupling time shift $t_{\rm clc}$ depends on the energy of the ejected electron and the wavelength of the probe field λ.

In the past, the Attosecond metrology is used to measure time delays in atomic photoemission. The difference of the present experiment compared with the past experiments is that we used a long wavelength probe field instead of a NIR laser field. In the following, the measurement induced time delay is studied in the present THz electric field. The discussion below will focus on the analytic formulas proposed in Ref. [131] for the measurement induced time shift. Within the temporal resolution of the present experiment ($\sim$1 fs), in the presence of time shift t_{clc}, the streaked momentum is given by

$$p_f(t+t_{clc}(E)) = p_i - eA(t+t_{clc}(E)), \tag{4.29}$$

where $t_{clc}(E)$ is the measurement induced time shift.

In the Fig. 4.6 (a), the time-dependent low-energetic electron momentum is shown. Fig. 4.6 (b) shows the time-dependent momenta shifts of the high kinetic energy photoelectrons (fast photoelectrons) and low kinetic energy photoelectrons (slow photoelectrons). The purple dots and violet triangles are from the experimental measurement.

[6]Euler constant $\gamma_{\rm E} = 0.57721$

Since we adopted an average momenta method to calculate the center position of each traces, thus the amplitude of the temporal profile of the low energetic photoelectrons momenta is smaller than the high kinetic energy photoelectrons. If we zoom in the delay of Fig. 4.6 (b), a time shift between the purple-arrow and violet-arrow can be observed. By tracing all the low-energetic electrons ($p_x \leq \pm$ 0.4 a.u. and $-0.35 < p_{y/z} < +0.35\,a.u$ momentum slice) after the XUV radiation, the relative time shift is 23.9 ± 6.4 fs, it means the collective release times of the low-energetic electrons are late with respect to the first emitted photoelectrons. The low-energetic electrons with the maximum kinetic energy of 4 eV. The time shift can be best described as coming from the THz probing field induced time delay as for the EWS time delay is far less than the temporal resolution of the experiment ($\sim$ 1 fs).

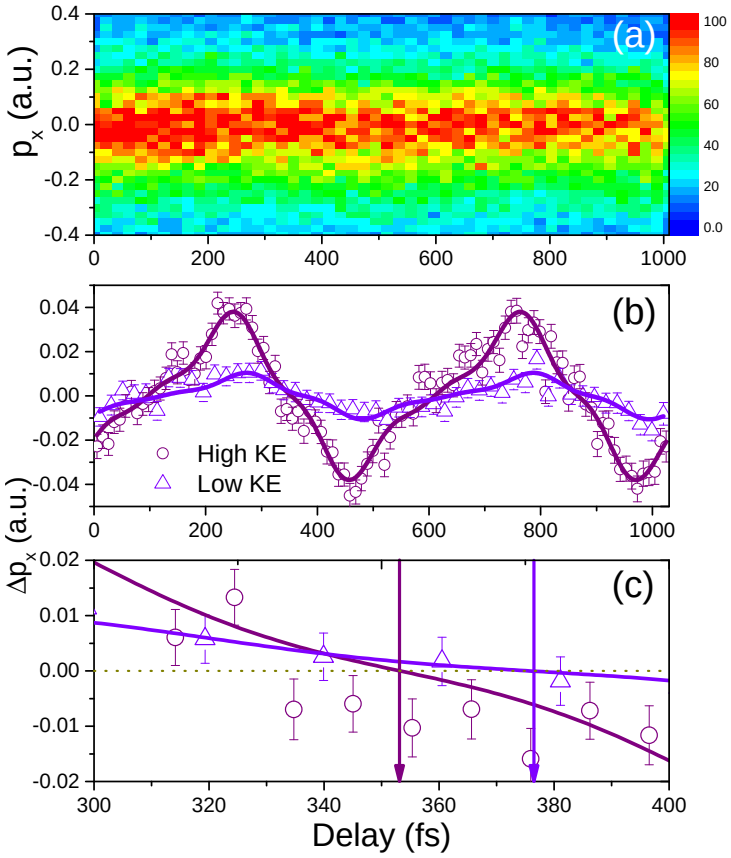

Figure 4.6: (a) Time-dependent momentum distribution of the low-energetic photoelectrons. We only selected the photoelectrons under the condition $-0.35 < p_{y/z} < +0.35\,a.u.$ (b) The momentum shift Δp_x as a function of time delay for the high kinetic energy (High KE) photoelectrons (purple dots) and low kinetic energy (Low KE) photoelectrons (violet triangles). For the fitting, the frequency of the THz pulse is fixed. (c) Zoom in the delay of (b) ranging from 300 fs to 400 fs. The time shift between the low-energetic photoelectrons and fast photoelectrons is $\tau = 23.9 \pm 6.4$ fs.

In Eq. 4.28, the probe field induced time shift is related to its energy of the electron and the frequency of the electric field. As reported in Ref. [143], the photoionization time delay induced by an NIR laser field ($\lambda_{IR} = 800$ nm, $\omega_{IR} = 0.057$ a.u.) $t_{clc} = 30$ as at the

energy of 30 eV. In our experiment, the wavelength of the THz pulse is 154 μm, and the frequency is $\omega_{THz} = 2.96 \times 10^{-4}$ a.u. In this case, with the scale rule described in the above equations (Eq. 4.28), we obtain the time shift of low-energetic photoelectrons at the energy of 0.4 eV of 26 fs, which is in good agreement with the present experiment.

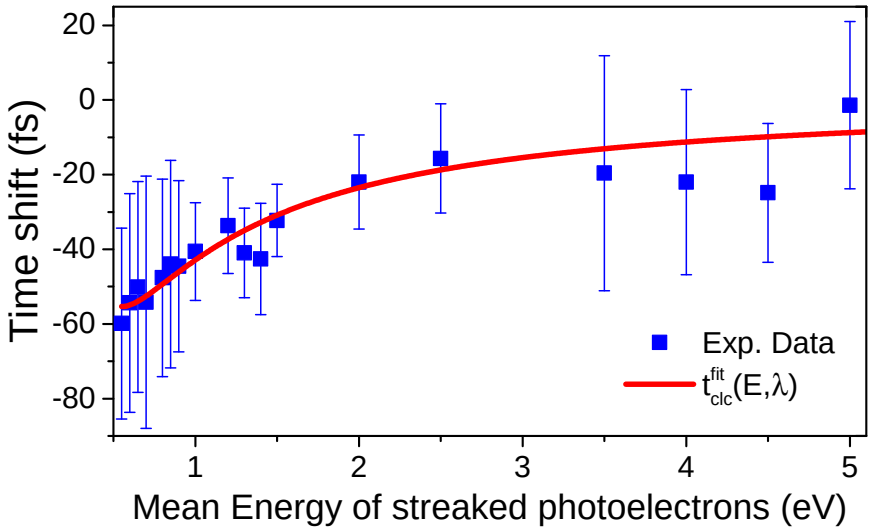

Figure 4.7: Time shift of the low energetic electrons with respect to the first emitted photoelectrons as a function of the mean energy of streaked photoelectrons. The time shifts are fitted by Eq. 4.30.

Moreover, as mentioned above, the time shift t_{clc} is pronounced for low-energetic photoelectrons. In the present experiment, due to the limitation of our spectrometer, it is tough to resolve the low-energetic photoelectrons. However, we can use the kinetic energy of the photoelectrons to select the photoelectrons with specific kinetic energy by adding a condition on its momentum selection. In this way, we can "tune" the mean energy of the streaked photoelectrons by selecting electrons that are less or more energetic [131]. In Fig. 4.7, the energy-dependent time shifts are shown. The lower energetic electrons gained more time shifts compared with the first emitted photoelectron.

As mentioned above, this time shift can be described by using the Eq. 4.28. Thus, we use the following equation to fit the measured energy-dependent time shifts of the low-energetic photoelectrons:

$$t_{clc}^{fit}(E,\lambda) = -\frac{a}{2E^{3/2}}[\ln(b \cdot E) + c], \tag{4.30}$$

where a, b, and c are the fit parameters. The additional Coulomb laser coupling time delays Δt_{clc} is an essential parameter in atomic and molecular photoemission. The absolute CLC time shift depends on the energy of the ejected electron and frequency of the probe field, therefore, the smaller the energy of the electron, the more significant the time shift. We measured this energy-dependent time shift up to 60 fs in the photoemission of the low-energetic photoelectrons and the first emitted photoelectrons.

For the more complex molecular O_2 compared to Neon [124], the production of the low-energetic electrons may come from shake-up and autoionization processes [12]. Since a

single 60 eV XUV photon is sufficient to populate O_2 to highly excited states and at the same time excited the other electron to an excited state. Besides, the autoionization processes in this molecular system resulted in the production of the low-energetic electrons (typically less than 3 eV) [48]. Therefore, it is a challenge to separate all those electrons by kinetic energies. In this section, we only focus on the energy-dependent time shifts without further discussion. For more details, please read the discussion in Chapter 5.

4.4 Conclusion

In summary, in the first place, we introduced the THz streaking working principle. In the experiment, employing the REMI and SD setup, the momentum distribution of the photoelectrons as a function of the time delay of the XUV laser pulse and the THz pulse was obtained. From the selected momentum traces of the "fast" photoelectrons emitted along the polarization of the THz pulse, we characterized the basic experimental parameters of the THz pulse. The essential aspect of THz streaking is that from the time shift of temporal profiles of momenta traces of two different photoelectrons, the information can be interpreted regarding photoemission steps or the lifetimes of autoionization processes in O_2. Second, the theoretical descriptions of photoemission and Coulomb-laser coupling time delays are given. Considering the long wavelength of the THz radiation delivered at FLASH, the Coulomb-laser-coupling time shift $\tau = 23.9 \pm 6.4$ fs is an essential parameter for us to treat and analyze the phase shifts between the low-energetic photoelectrons and the first emitted photoelectrons. In the end, from the energy-dependent time shifts of the low-energetic photoelectrons, we can extend the present THz streaking technique to explore the field-induced time shifts up to 60 fs. In the future, the present experimental results can be used to disentangle the EWS and CLC time shift in Attosecond streaking experiments.

Chapter 5

XUV-Pump/THz-Probe Experiments on Oxygen

The interaction of XUV radiation with small molecules leading to the population of highly excited states that evolves on femtosecond time scales has attracted considerable theoretical and experimental interest in the past [12, 126, 148]. For molecules, autoionization of the highly excited states is an important electronic many-body problem. The understanding of the formation and relaxation of inner-valence excited states is essential for the theory of the ultrafast correlated electronic dynamics with X-rays.

With an XUV-pump/THz-probe experimental scheme, the dissociation and relaxation dynamics of highly excited states in O_2 created by exposure to 60 eV XUV photons has been investigated using a REMI at FLASH. The subsequent autoionization process of a highly excited cation state has been traced and mapped using the so-called THz streaking technique [106]. The THz streaking principle has been introduced in Sec. 4.1. By tracing the emission of different types of photoelectrons, the ultrafast relaxation dynamics is directly recorded by the coherent intense THz electric field. The relative time shift between different types of photoelectrons was analyzed with respect to photoemission time delays or lifetimes of autoionization. The photoemission time delays can be found in Sec. 4.3.

In this chapter, the photoionization and autoionization processes in O_2 are discussed. First, the experimental setup of the XUV-pump/THz-probe experiment is introduced in Sec. 5.1. With a kinematically complete measurement, the emitted photoelectrons are streaked by the simultaneously acting THz electric field and they are detected in coincidence with the emerging ion(s). The detailed characterization of the THz pulse delivered by the FLASH facility can be found in Sec. 4.2. The long-wavelength THz pulse is properly adopted to trace the release times of the first emitted photoelectron and the secondary autoionization photoelectron. Second, in Sec. 5.2, the single XUV-photon ionization of O_2 is presented. Several dissociation channels are traced which is helpful to disentangle the direct ionization process and autoionization process. In Sec. 5.3, the atomic autoionization in molecular oxygen is discussed. Atomic autoionization is the dominant process in dissociative ionization of O_2. As already mentioned before, the autoionization process in the molecular system can be found in Sec. 2.6. In the end, in Sec. 5.4, the experimental result of THz streaking of the autoionizing excited cation state $^4\Sigma_g^-$ is given.

5.1 XUV-Pump/THz-Probe Setup

The THz streaking experiment was performed at FLASH using the FEL beamline BL3 in combination with synchronized Terahertz (THz) radiation [103]. Since the XUV and THz pulses are produced by the same electron bunch, they are intrinsically synchronized. FEL pulses with 60 $\pm$ 0.5 eV photons were delivered at a pulse repetition rate of 10 Hz with 80 minibuches and the intensity was 10^{10} W/cm^2. As shown in Fig. 5.1, the FEL beam utilized a back-reflection split-mirror focused onto the supersonic gas jet containing O_2 molecules. Meanwhile, the THz beam from the experimental hutch was focused by multiple lenses and deflected by 90° with a perforated mirror and overlapped collinearly with the focused FEL beam at the center of the interaction chamber. The produced ions and electrons were guided by a homogenous electric and magnetic field (E = 15.8 V/cm and B = 14.8 Gauss, respectively) towards the time- and position-sensitive MCPs (diameter 120 mm for ions and 80 mm for electrons) with delay-line readout [23]. A triple coincidence condition requiring detection of two ions and one electron was used during data acquisition in order to disentangle different channels. The focused THz light beam peak intensity was estimated up to 10^7 W/cm^2. The relative arrival time of the XUV pulse to the THz pulse can be adjusted by changing the split-mirror optics position. By adjusting the time delays of the XUV and THz pulses, we can perform the XUV-pump/THz-probe experiment. In the experiment, the total time delay is about 1 ps, roughly equal to two cycles of the THz pulse.

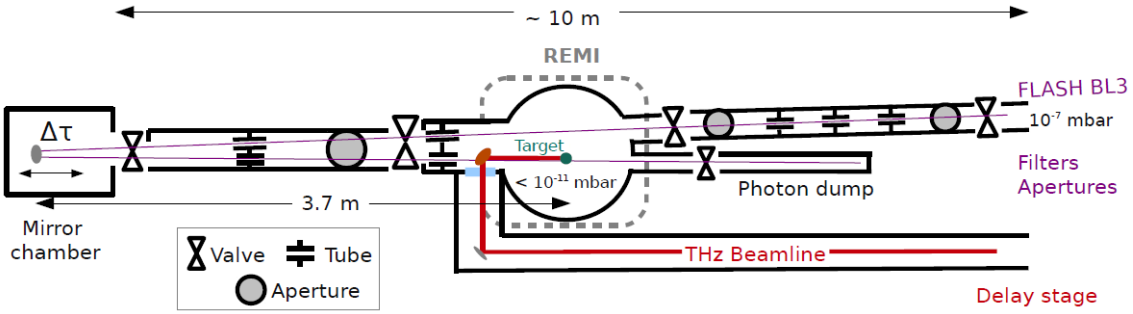

Figure 5.1: Schematic display of the experimental setup of the THz streaking experiments. The unfocused XUV beam from BL3 is guided through the interaction chamber onto a multilayer mirror of the SD optics, that focuses the beam into the O_2 target. The long focal length of the XUV beam is required to account for the additional path of ∼7 m the THz is traveling with respect to the XUV pulse [131]. The THz beam is collinearly overlapped with the XUV beam using a 3.0° polished copper mirror with a hole in the center through which the back reflection focused XUV beam can pass. Figure is taken from Ref. [124].

5.2 Single XUV Photon Ionization of O_2

The photoionization of O_2 has been explored in utmost detail in the past by using different light sources, e.g., synchrotron radiation, FELs, HHG, and NIR optical lasers [11, 48,

49, 149–151]. Dissociative photoionization of this molecule can result in the creation of fragments with various kinetic energies. By tracing the kinetic energies of the ionic fragments, the mechanisms of the dissociation processes can be understood.

The purpose of this experiment is to measure the time delays of different types of photoelectrons. We intend to measure the relative time delay between the first emitted photoelectron and the secondary autoionization electron. In this case, we attenuated the FEL light intensity to ensure the single XUV-photon absorption is the dominant process. We focus on how the molecular response after absorption of one XUV photon. In the first place, we have to distinguish the photoelectrons coming from either the direct ionization process or the autoionization process. Thus, the simultaneously acting THz-electric-field was used to monitor and disentangle the "fast" photoelectron and the "slow" autoionization photoelectron.

The photon energy is 60 eV which means that a single photon can singly or doubly ionize the molecule. Thus, first of all, we have to identify each dissociation channel. The single ionization $O_2 + \hbar\omega(XUV) \rightarrow {O_2}^+ + e^-$ and double ionization $O_2 + \hbar\omega(XUV) \rightarrow {O_2}^{2+} + 2e^-$ are style. In the following, the assignment of each dissociation process is presented.

5.2.1 Single Ionization

The ionization threshold of single ionization of O_2 is 12.07 eV [152]. Single ionization of O_2 is observed in the experiment. In the following, the single ionization process is studied by tracing kinetic energies of the ions, thus the final dissociative states can be identified.

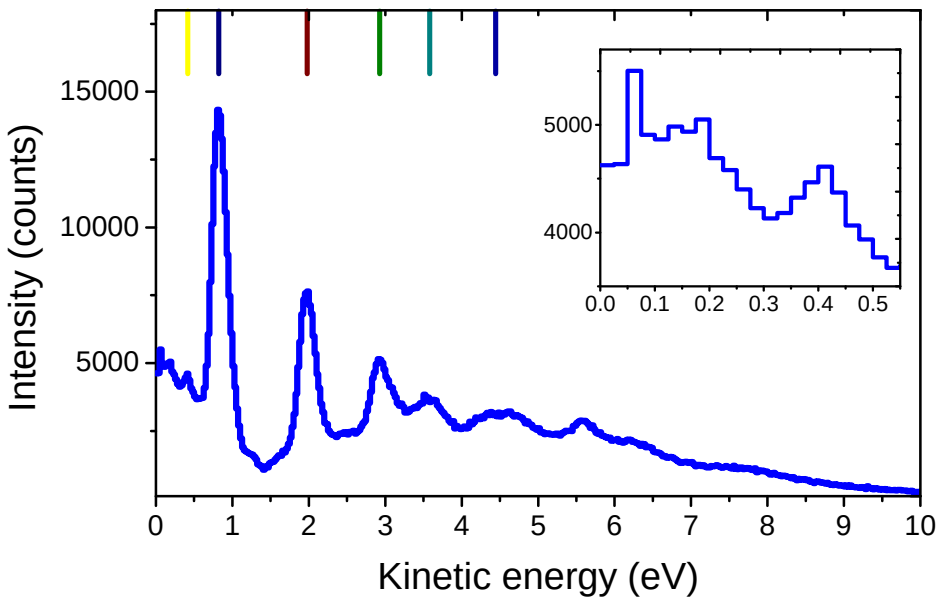

Figure 5.2: Kinetic energy distribution of non-coincident O^+ fragments observed with photon energy at 60 eV.

In Fig. 5.2, the kinetic energy spectrum for O^+ ions is shown. The zero-kinetic energy ionic fragments ($\leqslant 0.5$ eV) indicate that the dissociation takes place near the dissociation limit. Thus, the zero-kinetic energy O^+ ions could come from the predissociation of the $b^4\Sigma_g^-$ via f $^4\Pi_g$ and $d^4\Sigma_u^+$ ionic states to the first dissociation limit $O^+(^4S)$ + $O(^3P)$ at 18.73 eV. Alternatively, the zero-kinetic energy ions may come from the direct ionization of $a^4\Pi_u$ and $A^2\Pi_u$ states. According to and in excellent agreement with previous works [46], two main dissociative states $3^2\Pi_u$ and $B^2\Sigma_g^-$ can be attributed to the kinetic energy spectrum of O^+ peaked at about 0.4 eV and 0.8 eV, respectively. The related potential energy curves of O_2^+ ion are shown in Fig. 5.3 (a). The kinetic energy of O^+ ions peaked at 1.96 eV and 2.93 eV are identified from the predissociation of state $O_2^+(C^4\Sigma_u^-)$ which dissociated into the limits $O^+(^4S)$ + $O(^1D)$ (20.70 eV) and $O^+(^4S)$ + $O(^3P)$ (18.73 eV), respectively [46, 151]. Meanwhile, a single XUV photon also pumped O_2 to the highly excited states, e.g. $3^2\Sigma_g^-$ and $5^2\Sigma_g^-$ which dissociated into different dissociation limits with higher kinetic energy of about 4-6 eV [150, 153].

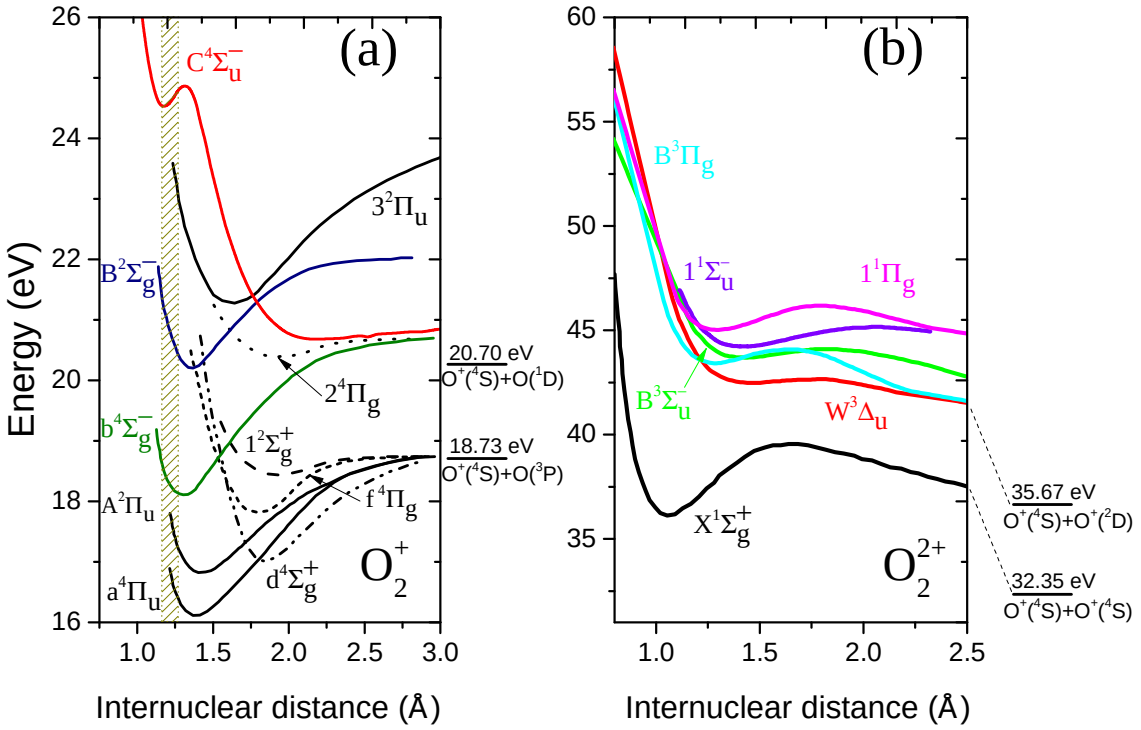

Figure 5.3: Potential energy curves of (a) O_2^+ and of (b) O_2^{2+} molecular ion. The Frank-Condon regime centered at 1.21 Å (vertical shaded band) is sketched. Potential energy curves are adapted from Refs. [46, 154].

5.2.2 Double Ionization

Since the XUV photon energy is higher than the double ionization threshold (36.13 eV) [48], so the double ionization has to be taken into account. The assignment of double ionization is discussed as follows. Here, we only focus on the final states which resulted

in the production of the singly charged ion pairs. In the Frank-Condon region, the neutral molecule is pumped to many dication states and these states underwent dissociation rapidly to different dissociation limits. KER peaks above ca. 7 eV are indicative of the direct population of O_2^{2+} states. The arrows in Fig. 5.4 labeled a-e can be assigned to the direct population of the O_2^{2+} $W^3\Delta_u$, $B^3\Sigma_u^-$, $1^1\Sigma_u^-$, $B^3\Pi_g$ and $1^1\Pi_g$ states [51, 154]. The electronic states and final states are listed in Table 5.1. The dissociative states have the feature that two outer-valence electrons are kicked out during photoionization. We assume there is no time delay between the two emitted photoelectrons from direct double ionization at least within the temporal resolution of the present experiment.

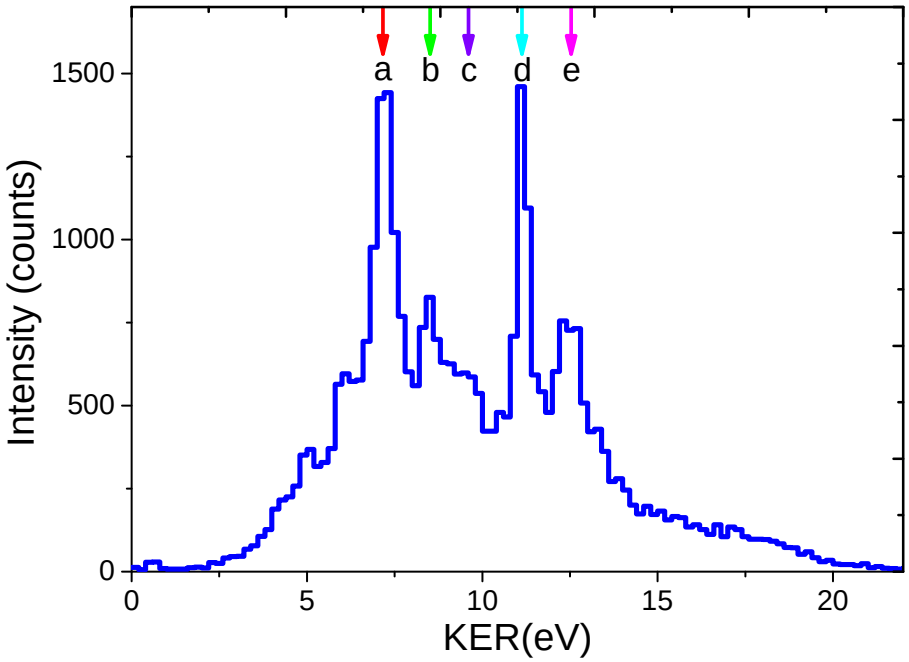

Figure 5.4: Kinetic energy release spectrum for O^+ - O^+.

Table 5.1: Electronic states and KER of the dissociative states O_2^{2+} molecular ion. The ground state configuration of the neutral O_2 is $1\sigma_g^2 1\sigma_u^2 2\sigma_g^2 2\sigma_u^2 3\sigma_g^2 1\pi_u^4 1\pi_g^2$. Adapted from [51, 154].

Figure 5.4	State	Major configuration	KER (eV)	Final state
a	$W^3\Delta_u$	$(1\pi_u)^{-1}(1\pi_g)^{-1}$	7.2	$O^+(^4S) + O^+(^2D)$
b	$B^3\Sigma_u^-$	$(1\pi_u)^{-1}(1\pi_g)^{-1}$	8.5	$O^+(^4S) + O^+(^2D)$
c	$1^1\Sigma_u^-$	$(1\pi_u)^{-1}(1\pi_g)^{-1}$	9.6	$O^+(^4S) + O^+(^2D)$
d	$B^3\Pi_g$	$(3\sigma_g)^{-1}(1\pi_g)^{-1}$	11.1	$O^+(^4S) + O^+(^4S)$
e	$1^1\Pi_g$	$(3\sigma_g)^{-1}(1\pi_g)^{-1}$	12.5	$O^+(^4S) + O^+(^4S)$

In summary, the single- and double-ionization processes of O_2 after absorption of an XUV-photon are presented. The detailed dissociation processes are not covered in this chapter. By tracing the direct single and double ionization of O_2 is helpful to identify and

disentangle the direct ionization and autoionization process. Furthermore, the molecular ions at low kinetic energy may come from the autoionization processes.

5.3 Atomic Autoionization in Molecular Oxygen

A 60 eV XUV-photon ionizes the molecule O_2 and creating an inner-valence vacancy. Autoionization of these states with an inner-valence vacancy is commonly energetically forbidden in the case of individual atoms. However, the molecular environment plays a role which enable the autoionization energetically allowed in molecules [14]. Feifel *et al.* performed a high-resolution photoelectron-photoelectron coincidence study of inner-valence ionized O_2 and pointed out that the autoionization in molecular oxygen is energetically forbidden at a short nuclear distance and only takes place at large internuclear separations [48].

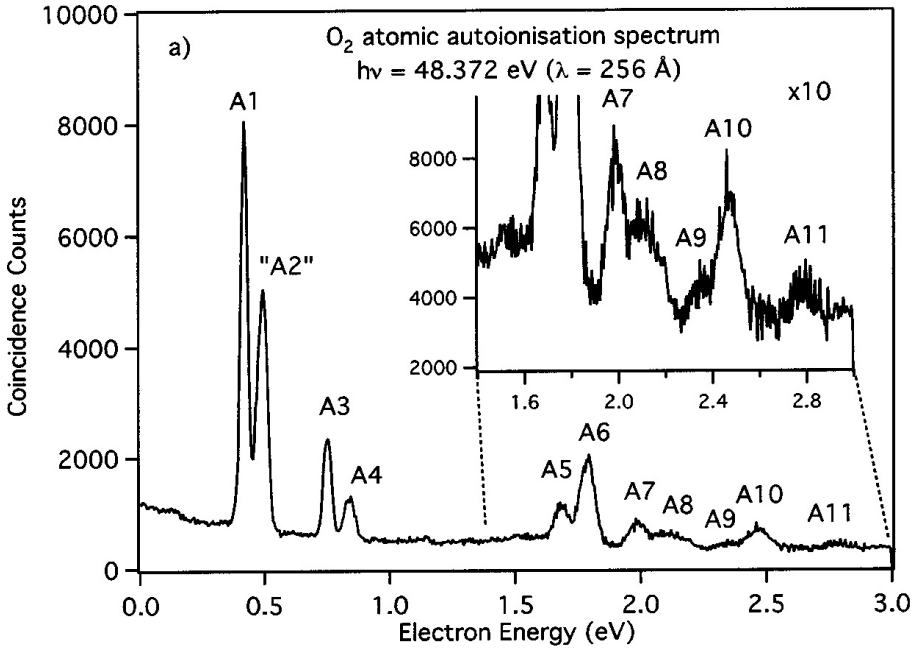

Figure 5.5: Secondary electron kinetic energy spectrum in high-resolution coincident electron studies of the O_2^{+*} autoionization mechanism. The peaks labeled "A1"-"A11" correspond to different atomic autoionization processes. Figure is taken from [48].

The basic two-step reaction pathway can be assigned to this autoionization process: $O_2 + \hbar\omega_{XUV} \rightarrow O_2^{+*} + e_1^-$, subsequently, the autoionization of excited atomic oxygen happened, namely, $O_2^{+*} \rightarrow O^+ + O^+ + e_2^-$. e_1^- and e_2^- are the first emitted photoelectron and secondary autoionization electron, respectively. It is an indirect double ionization process in molecular oxygen. The main feature of this decay is that the atomic-like autoionization exists in the autoionizing process of the molecular ions. During the nuclear motion, the excited molecular ion O_2^{+*} would decay to O_2^{2+} dissociation limits. Because it takes some time for the excited molecular ion to reach the stable state, thus, in temporal properties of the two photoelectrons were recorded by THz streaking technique. From the release

times of the first emitted photoelectron and the secondary photoelectron, the lifetimes of the autoionization can be extracted by mapping the temporal profiles of momentum or energies of the photoelectrons in the THz electric field.

In previous studies on photoionization of O_2, the atomic autoionization process is frequently observed [11,48,155,156]. The atomic-like autoionization process can be treated as $O^* \rightarrow O^+ + e^-$. Therefore, the kinetic energy of the secondary photoelectron has a fixed value. At large internuclear distance, the coupling between the excited atomic oxygen and the atomic ion is small, at some point, we can treat the molecular ion just like an individual atom or ion. As mentioned by Feifel, the indirect-double ionization is the main relaxation process in molecular oxygen. Specifically, the producing O_2^{+*} state will undergo an autoionization some time later. The assignment of the low-energetic autoionization electrons can be found in Fig. 5.5, and the final dissociation states are listed in Table. 5.2.

Table 5.2: Energies and assignments of the atomic autoionization lines shown in Fig. 5.5. Table adapted from [48].

Label	Electron energy (eV)	Excited states $\rightarrow O^+(^4S)$	Excited states $\rightarrow O^+(^2D)$
A1	0.425	$3p'(^3D)$	
A2	0.495	$3p'(^3F)$, $3s''(^3P)$	
A3	0.754	$3s''(^1P)$	$5s''(^{3,1}P)$
A4	0.840	$3p'(^1D)$	$4d''(^{3,1}P, ^{3,1}D)$
A5	1.685	$3d'(^3P)$	
A6	1.785	$3d'(^{3,1}G, ^{3,1}F, ^3S)$	
A7	1.977	$4p'(^3D)$	
A8	2.13	$3p''(^3P)$	
A9	2.33	$3p''(^1D)$	
A10	2.48	$4d'(^{3,1}G, ^{3,1}F, ^3D, ^3P)$	
A11	2.78	$5d'(^{3,1}G, ^{3,1}F, ^3D, ^3P)$	

Due to the limited resolution of our spectrometer, it is difficult to resolve the subtle excited states from our kinetic energy spectrum of the photoelectron. However, the atomic-like electron spectra provided by Feifel are helpful for us to trace the autoionizing states and final dissociation states.

5.4 THz Streaking the Dynamics of Autoionizing State of O_2^{+*}

With a kinematically complete measurement, the emitted photoelectrons are streaked by the simultaneously acting THz-electric-field and they are detected in coincidence with the emerging ion(s) [126]. Both, the photoelectron as well as the secondary electron from the autoionization process, are exposed to the streaking field [105]. This leads to a momentum or energy shift that allows determining the moment of autoionization. Thus, the time

shift between the streaking traces of the photoelectron and the secondary electron carries information about the autoionization lifetime [126]. In this section, we experimentally investigated an autoionization process of the highly excited cation state $^4\Sigma_g^-(2s\sigma_g^{-1})$ which is populated after the absorption of one XUV-photon. By tracing the kinetic energy of ions and photoelectrons, we identified the formation of the excited cation state $^4\Sigma_g^-$ and its relaxation pathway. Besides, we have measured the lifetime of this autoionizing cation state.

5.4.1 Assignment of Cation States

As discussed above, the single XUV-photon ionization is the dominant process in this experiment. The ionic fragments with higher KERs have already been summarized in Sec. 5.2. However, the low-energetic ionic fragments and photoelectrons have not been discussed. As discussed above, atomic autoionization is the primary relaxation process for molecular oxygen. It means that the autoionization can be found by tracing the kinetic energy of the ions or photoelectrons. In the present section, we focus on the autoionization process associated with the production of 2 eV O^+ ions as depicted in Fig. 5.2 [1].

First of all, we have to identify and disentangle which channel can produce the 2 eV O^+ ions. There are two approaches to identify detailed channels. One is to trace the kinetic energy of the ions, and the other is to trace the kinetic energy of photoelectrons. Now, let us talk about the first approach. By tracing the kinetic energy of the ions, according to previous works [151, 155], there are two cation states fragmentation processes can result in the production of the 2 eV kinetic energy ions. In Fig. 5.6 (a), the relative intensities of cation states $C^4\Sigma_u^-$ and $^4\Sigma_g^-$ are shown. The ions mainly come from the excited state $^4\Sigma_g^-$.

As the second approach, in Fig. 5.6 (c), the double coincidence correlation plot is shown. The ions kinetic energy versus the electrons kinetic energy correlation is presented. Both the single ionization and indirect double ionization are included. If we project the kinetic energy of photoelectron on the y-axis, then we obtain the photoelectron kinetic energy spectrum in Fig. 5.6 (b). Both cation states are labeled. The binding energy of $C^4\Sigma_u^-$ state is 24.6 eV [150], so the first emitted photoelectron kinetic energy is 35.4 eV. The kinetic energy of electrons below 27.65 eV come from the double ionization process. As reported in Refs. [48, 49], the binding energy of state $^4\Sigma_g^-$ is 38.7 eV and corresponding the first emitted photoelectron kinetic energy is 21.3 eV. In Fig. 5.6 (b), the second peak is centered at 21.3 $\pm$ 0.2 eV. Therefore, we confirmed the second peak photoelectron mainly comes from the state $^4\Sigma_g^-$. After the removal of an inner-valence $2\sigma_g$ electron which producing several excited states with varying amounts of valence character [49]. For instance, according to Ref. [153], the highly excited state $5^4\Sigma_g^-$ binding energy in the range 36.25 - 42 eV corresponds to the kinetic energy of the first photoelectron is 18 - 23.75 eV. For simplicity, in the chapter, we still use $^4\Sigma_g^-$ to represent the highly excited states which were measured in our experiment.

After the assignment of the cation states, we intend to find the creation of the excited cation states and its relaxation pathways. In Fig. 5.7, the potential energy curves of O_2^+

[1] We have already checked there is no time shift of the photoelectrons from the rest dissociative channels, at least within the error bar.

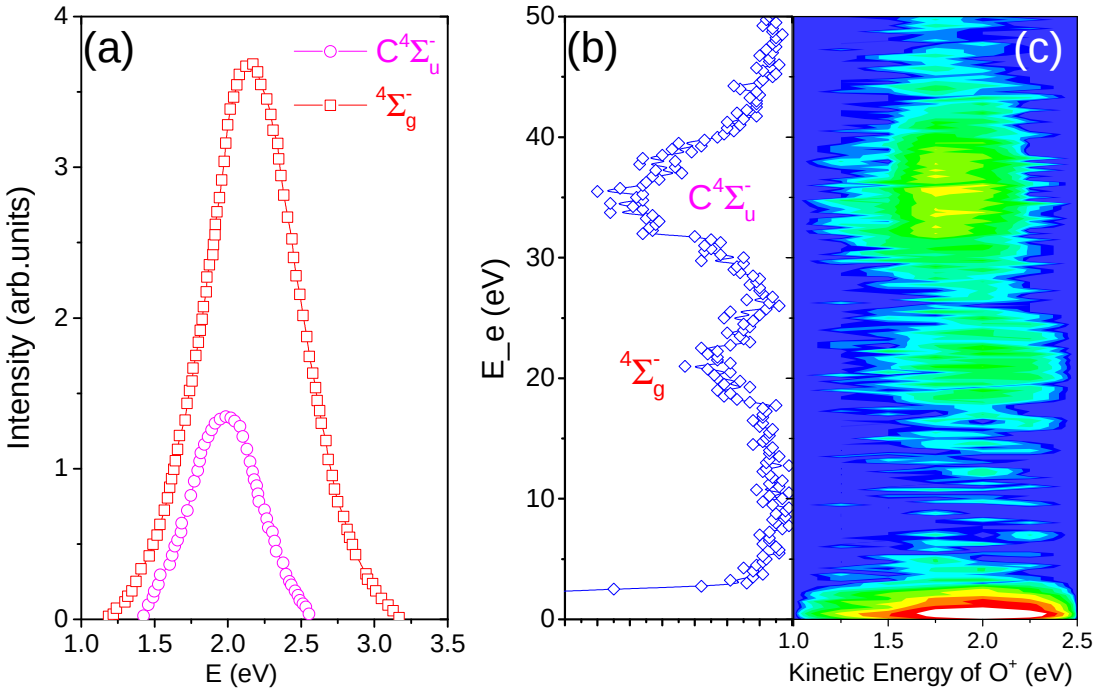

Figure 5.6: (a) The ion spectrum for cation states $C^4\Sigma_u^-$ and $^4\Sigma_g^-$, respectively. The data was taken from [155]. (b) The photoelectron energy spectrum is associated with the production of the 2 eV ions. The electrons within 3 eV mainly come from autoionization processes [48]. (c) O^+ recoil kinetic energy vs electron kinetic energy when illuminated by XUV radiation. We only selected the photoelectrons emitted along the polarization of XUV pulse within a small angle (see Chapter 4).

and O_2^{2+} molecular ions are shown for both, short and large internuclear distances. The state $C^4\Sigma_u^-$ dissociates into $O^+(^4S)$ + $O(^1D)$ at 20.7 eV. It is a direct single ionization process and we will not go into detail in this section.

In contrast, a 60 eV XUV photon also pumps the molecule to the inner-valence excited state $O_2^{+*}(^4\Sigma_g^-)$, then the first photoelectron e_1 emitted, subsequently, this excited state undergoes an autoionization by emitting the secondary low-energetic electron e_2. Within the Franck-Condon region around 1.2 Å, the highly excited state $^4\Sigma_g^-$ is above the ground state $X^1\Sigma_g^+$ of O_2^{2+}. Around 39 eV excited states involve a $2\sigma_g$ vacancy which will further autoionize to the different dissociation limits. The highly excited states exhibit strong configuration mixing and numerous potential energy curves crossing [49]. As shown in Fig. 5.7, the excited state $^4\Sigma_g^-$ crosses the ground dication state $X^1\Sigma_g^+$ twice. One is at a short internuclear distance, and the other is at large internuclear distance. The main electronic configuration of the excited state is $O^*(\ldots 2s^2 2p^3[^2D^0]3p^1,^3D)/O^+(^4S)$. Within a short internuclear distance, autoionization is closed because of the decay from the $2s^2 2p^3[^2D^0]3p^1\ ^3D$ state of O^* to the excited state $2s^2 2p^3[^2D^0]$ of O^+ is energetically forbidden [12]. Only the autoionization will take place at large internuclear separation. Thus, the potential energy curve of $^4\Sigma_g^-$ will cross the potential energy curve of the lowest dication state at the critical distance R_c. At the crossing point, the excited state $^4\Sigma_g^-$ can autoionize into the $O^+(^4S)/O^+(^4S)$ limit by ejecting the secondary photoelectron [49].

To summarize, we have identified and disentangled the production of 2 eV ions mainly come from the autoionizing excited cation state $^4\Sigma_g^-$.

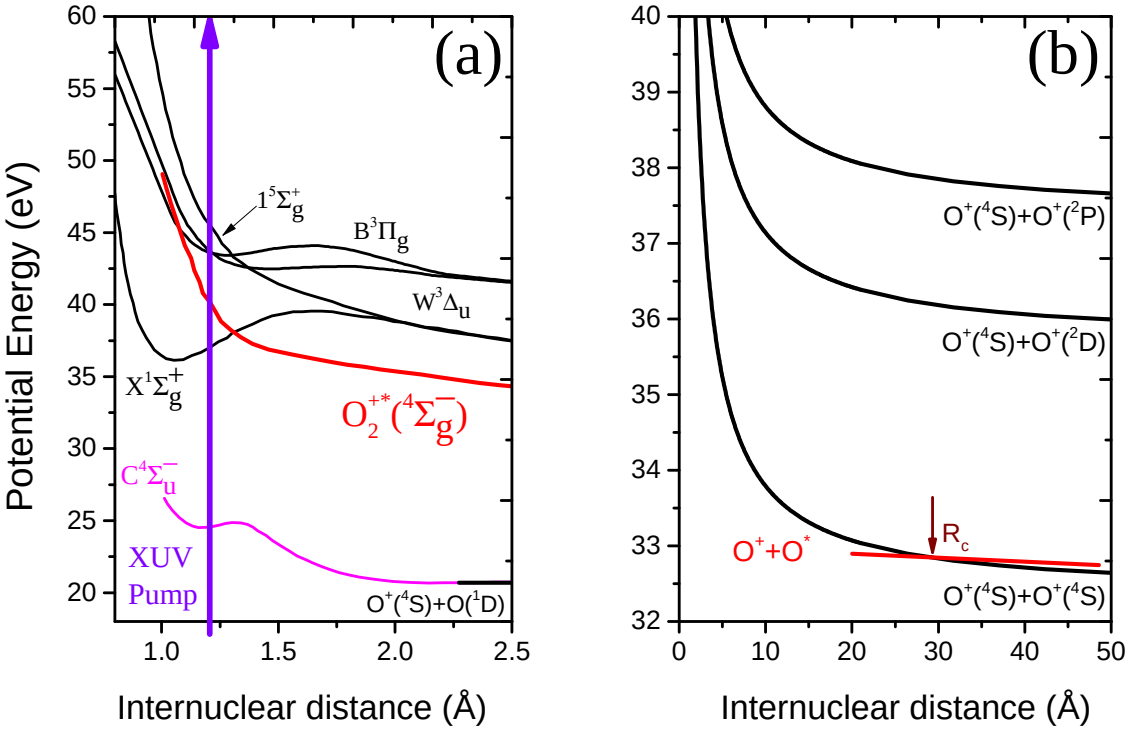

Figure 5.7: (a) The black potential energy curves of O_2^{2+} and the magenta solid line is the excited cation state $C^4\Sigma_u^-$ potential energy curve. The red-solid line is the calculated potential energy curve corresponding to the state $O_2^{+*}(^4\Sigma_g^-)$ [49]. The violet arrow stands for a 60 eV XUV photon. (b) Potential energy curves of each dissociation limits and the excited state $^4\Sigma_g^-$ are shown for large internuclear distances. The crossing point of autoionizing state $O_2^{+*}(^4\Sigma_g^-)$ with the dissociation limit $O^+(^4S) + O^+(^4S)$ is at R_c. Potential energy curves are adapted from Refs. [49, 154].

5.4.2 Lifetime of Autoionizing Cation State $^4\Sigma_g^-$

The lifetime of the autoionizing cation states is predicted to be within 300 fs [12]. Thus, THz-streaking with a temporal resolution of 1 fs can be used to measure the lifetime of autoionization. In the following, the determination of the lifetime of the excited state $^4\Sigma_g^-$ by THz streaking technique is discussed. We can directly measure the relative time shift between the streaking traces of the "fast" photoelectron and autoionization electron in the time axis. The extraction of the lifetime of the highly excited state $^4\Sigma_g^-$ is discussed as follows.

In the previous section, the assignment of cation states which resulted in the production of 2 eV ions (or KER = 4 eV) was presented, and we only discussed the high kinetic energy photoelectrons. Here, we begin to discuss the low energetic autoionization electrons from

the excited state $^4\Sigma_g^-$. At large internuclear distances, because of the coupling between the separated O^+ and O^* is small, the atomic autoionization process takes place.

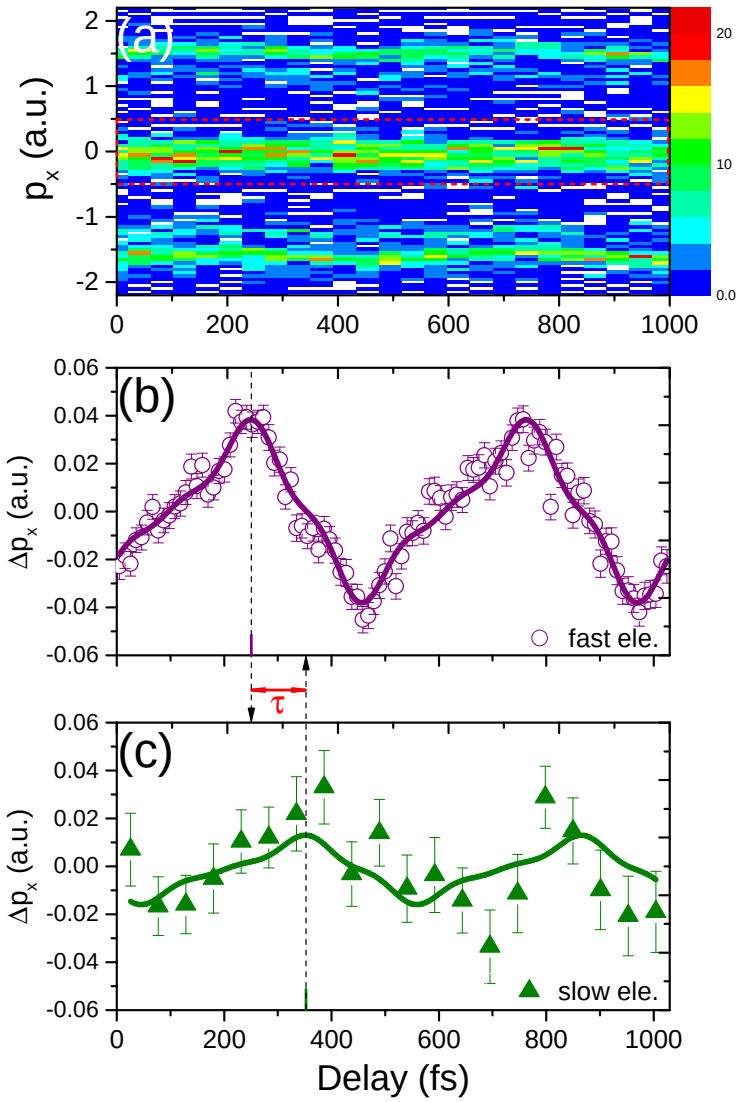

Figure 5.8: The autoionizing excited state $^4\Sigma_g^-$ relaxation process streaked by the THz electric field. (a) Time-dependent momentum distribution with the condition of ions with kinetic energy at 2 eV. (b, c) The time-dependent momentum shifts for the "fast" photoelectrons and the "slow" low-energetic autoionization electron, respectively. A Fourier series of triangle function is used to fit both streaking traces. The relative time shift between the fast photoelectrons and slow electrons is $\tau = 102 \pm 30$ fs.

In Fig. 5.6 (c), the low-energetic electrons kinetic energy is centered at 0.5 eV, thus the beginning of autoionization of the state $^4\Sigma_g^-$ is about 0.5 eV above the dissociation limit $O^+(^4S)/O^+(^4S)$ at 32.352 eV. Therefore, the crossing point R_c is at the internuclear distance where the excited state potential energy curve crosses the ground state dissociation limit at 32.852 eV. In Fig. 5.7, the critical distance R_c is around 30 Å. The value of the critical nuclear distance R_c is related to the kinetic energy of the secondary autoionization electron. A simple estimation is $R_c = 27.2112/E_{kin}(e_2)$, where $E_{kin}(e_2)$ is the kinetic en-

ergy of the electron. The secondary electron from the atomic-like autoionization kinetic energy spectrum is shown in Fig. 5.5. Since the center of low-energetic autoionization electrons in Fig. 5.6 (c) is about 0.5 eV, therefore, their autoionization electrons mainly come from the "A1" and "A2" process described in Fig. 5.5 [49, 149]. The corresponding autoionization pathways can be found in Table 5.2.

Now, let us discuss the THz streaking experimental results of the autoionizing cation state $^4\Sigma_g^-$. In Fig. 5.8 (a), the time-dependent momentum distribution of the photoelectrons with the condition of the ions at 2 eV is shown. We selected the low-energetic photoelectrons with a small emission angle with respect to the polarization of the THz pulse (momentum slice conditions: $-0.35 < p_{y/z} < +0.35\,a.u.$). The Fourier series of triangle functions were used to fit the streaking traces of the "fast" photoelectrons and the "slow" autoionization electrons with the same frequency. Fig. 5.8 (b) is the time-dependent momentum shift of the "fast" photoelectrons (correspond to the THz vector potential, see Sec.4.2). Fig. 5.8 (c) is the time-dependent momentum shift of the "slow" photoelectrons which are labeled by red-rectangle in Fig. 5.8 (a). What we measured is the relative shift of the two momentum traces of photoelectrons. Two arrows are used to show there is a time shift between the first emitted photoelectron and the secondary autoionization electron. It is experimental evidence that we identify the first emitted photoelectrons and the secondary autoionization electrons. And those autoionization electrons mainly come from the autoionizing cation state $^4\Sigma_g^-$. From the fit results, we obtain the relative time shift τ is 102 ± 30 fs. It means that the lifetime of autoionizing cation state $^4\Sigma_g^-$ is determined. In our case, with low KER of 4 eV the autoionizing cation state $^4\Sigma_g^-$ molecular ion needs about 102 fs to reach the crossing point R_c before the autoionization takes place. Since we have not considered the fragmentation of the ionic fragments, what we measured is the start point of the autoionization. From the measured kinetic energies of autoionizing electrons[2], the maximum kinetic energy is about 3 eV which corresponds to the critical nuclear distance is 4.8 Å. Thus, the measured lifetime of 102 ± 30 fs is quantitatively agreed with previous measurements by W. Cao and A.S. Sandhu [12, 49].

5.5 Conclusion

To summarize, the XUV laser pulse in combination with intrinsically synchronized THz pulse delivered at FLASH was used to perform the XUV-pump/THz-probe experiments. Employing a REMI and SD optics, we performed the time-resolved coincident ion and electron spectroscopy. In this chapter, we experimentally investigated the single XUV-photon ionization and autoionization processes of O_2.

First, according to and in good agreement with previous works, the dissociation channels were identified by tracing the kinetic energy of ionic fragments or KER distributions of the ion pairs. Second, the basis of atomic-like autoionization dynamics in molecular oxygen was introduced. The atomic autoionization only takes place in O_2 at large internuclear distances. Third, the dynamics of an autoionizing cation state $^4\Sigma_g^-$ with KER of 4 eV

[2] As reported by W. Cao [49], the secondary autoionization electron kinetic energy E = 0.4, 0.7, and 1.6 eV which correspond to the critical distance R_c = 36, 20.6, and 9 Å, respectively.

to the lowest dissociation limit $O^+(^4S)/O^+(^4S)$ was studied. This highly excited cation state was populated after an inner-vacancy was created by absorption of single 60 eV XUV-photon. The binding energy of $^4\Sigma_g^-$ is 38.7 eV, thus the first emitted photoelectron has the kinetic energy of 21.3 eV which is in excellent agreement with our experimental result. Additionally, the opening of autoionization of the state $^4\Sigma_g^-$ to the dissociation limit $O^+(^4S)/O^+(^4S)$ is at the critical point $R_c \approx 30$ Å. Furthermore, we have measured the lifetime of this autoionizing cation state to be 102 ± 30 fs by THz streaking technique. The present work is excellent in agreement with previous works [12, 49].

To fully understand the experimental results, an advanced theoretical description and refined explanation are needed due to the states mixing and coupling between electronic and nuclear during fragmentation. In the future, we will propose to use a shorter XUV laser pulse to resolve the electronic and nuclear motion at a very short internuclear distance (e.g. less than 3 Å). Moreover, we will propose to use a longer wavelength and high-intensity THz pulse to explore the complex multistep autoionization process in O_2 or the similar molecular systems to exact the detailed relaxation path. Such an experiment could be carried out at European XFEL or upgraded FLASH 2 [22, 32]. Furthermore, high-resolution electron spectroscopy is called to resolve the peaks of low-energetic electrons, which is used to determine the lifetimes of each autoionization processes.

Chapter 6

IR-assisted XUV Multiphoton Ionization of Nitrogen

Experiments on ultrafast photoionization and fragmentation of atoms and molecules which are irradiated by XUV and NIR radiation are essential to understanding ionization mechanisms and the process of dissociation [25, 83, 157, 158]. Moreover, the development of FELs and pump-probe techniques allow us to directly map the fragmentation and subsequent reaction in real time and space [53, 159]. The molecular dynamics which is induced by different light sources are essential not only for understanding the light-matter interaction but also for practical application in astrophysics and plasma physics [160,161].

A simple molecule such as N_2 is one of the most important atmospheric gas species with a diatomic structure which has been studied considerably in recent years [162–165]. Few-photon multiple ionization (MPI) of N_2 by XUV radiation (44 eV photons) at FLASH was reported [86], and the sequential ionization was pointed out as the dominant process for molecules in the XUV regime. IR-assisted XUV ionization experiments of atoms and molecules were performed and the ultrafast fragmentation and electron shake-up process were observed [28, 100, 166, 167]. The multielectron dissociation ionization of molecular systems in intense laser pulses is a fundamental subject of interest as it allows us to understand the laser-driven molecular dynamics better.

In Chapter 2, the basic theoretical description of molecular photoionization, and mechanisms of sequential-ionization and non-sequential-ionization were introduced. Additionally, the fragment ion angular distribution (FIAD) method is introduced to analyze the emission of fragments after photoionization. In this chapter, the IR-assisted XUV multiphoton ionization experiments on N_2 will be presented. In order to understand the experimental results comprehensibly, the chapter is divided into four parts. First, the XUV-IR pump-probe experimental setup is introduced in Sec. 6.1. Second, the multiple ionization and dissociation of N_2 in NIR laser field (Sec. 6.2) and XUV laser field (Sec. 6.3) are presented. After that, the XUV-IR pump-probe results are presented in Sec. 6.4. For the aligned N_2^{n+} ions created by sequential absorption of XUV photons and further excited or ionized them by a delayed NIR laser pulse. The transition pathways can be traced via the KER and angular distribution of ionic fragments. In the end, a summary is given.

6.1 XUV-IR Pump-Probe Setup

In Fig. 6.1, the experimental setup of IR-assisted XUV multiphoton ionization of N_2 at FLASH is shown. A fluorescence screen (1×1 cm^2) was used to find the spatial overlap of the FEL and NIR laser beams [55]. A CCD camera images the fluorescence induced by the XUV or the NIR light, and the shift and shape of focused beams can be observed by a Ce:YAG crystal. For the temporal overlap of the FEL pulse and NIR laser pulse, we used the ionization signal of molecular Hydrogen to find the zero point of the two pulses. In order to receive the shot-to-shot FEL pulse energy, a copper plate was installed at the dump side of the beamline to record the FEL light intensity. Differential pumping stages were installed to make sure ultrahigh vacuum conditions in the interaction chamber [16]. More information on XUV-IR pump-probe experiments at FLASH can be found in Refs. [53, 55, 99, 100].

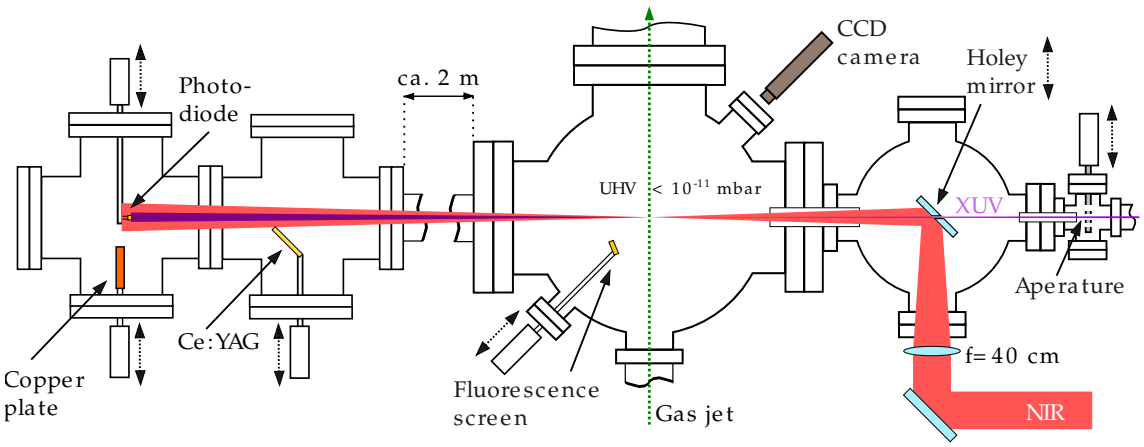

Figure 6.1: Schematic illustration of the experimental setup of the experiments on N_2. Figure is taken from [55].

The FEL pulses with 28.3 ± 0.5 eV photons were delivered at a repetition rate of 10 Hz, and a pulse length of approximately 100 fs (FWHM). The FEL beam was focused into a supersonic gas jet containing N_2 molecules. The gas was expanded through a 30 μm diameter nozzle to generate a cold supersonic jet with a density of up to 10^{10} molecules/cm^3. The NIR laser beam with a pulse length of 350 fs was focused by lens beside the main experimental chamber, being deflected by 90° with a perforated mirror and overlapping collinearly with the FEL beam [53]. In this case, both the FEL and the NIR laser beams overlapped in the spatial and temporal region. By means of a REMI, we detected in coincidence ionic fragments due to ionization by the intense FEL and NIR laser radiation. The ionic fragments were guided by a parallel uniform electric field (47 V/cm) towards a position- and time-sensitive MCP (diameter 120 mm) with delay-line readout [23]. With a pump-probe experimental scheme, the time-dependent ionic fragments spectra were obtained by adjusting the arrival time of the NIR laser pulse with respect to the XUV laser pulse. The polarization direction of the NIR laser field is parallel to the spectrometer. In contrast, the polarization direction of the XUV pulse is perpendicular to the polarization of the NIR laser pulse.

6.2 Molecular Nitrogen in NIR Laser Field

In this section, the photoionization and dissociation of the N_2 molecule in the NIR laser field are discussed. First, the NIR laser intensity is estimated by two approaches which are used to explain the formation of multiply charged molecular ions. Second, the potential energy curves (PECs) are used to depict the multielectron dissociative ionization of N_2. Finally, the angular distribution of ionic fragments is shown to illustrate the relationship between the emission of ionic fragments and the polarization of the NIR laser field.

6.2.1 Estimation of NIR Laser Intensity

Since the photoionization process strongly depends on the field strength, the estimation of the laser intensity in the experiment is critical in order to discriminate the different ionization mechanisms.

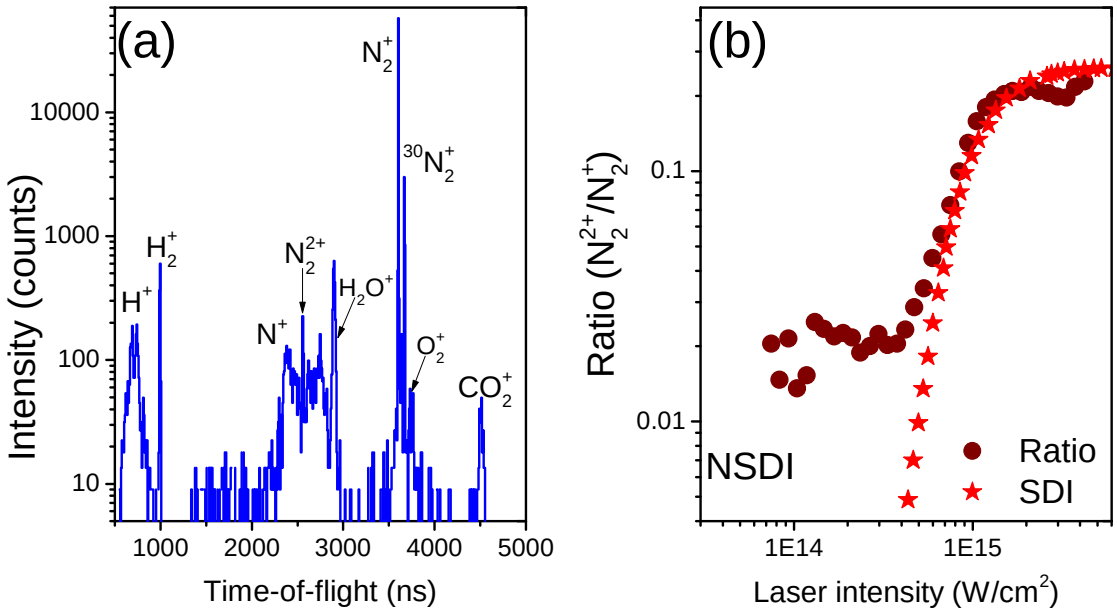

Figure 6.2: (a) Ion time-of-flight mass spectra of N_2 measured at 1.55 eV NIR radiation. The pulse duration of the NIR laser pulse is 350 fs. (b) The ratio of N_2^{2+}/N_2^+ as a function of the laser intensity. The data (wine circles and red stars) is taken from [168]. In low laser intensities, the non-sequential double ionization (NSDI) is the dominant process, while in high laser intensities, the sequential double ionization (SDI) is the dominant process.

Ratio of N_2^{2+}/N_2^+ Ions

In Fig. 6.2, (a) the ions TOF spectra in the NIR laser field and (b) the ratio of double ionization yield and single ionization yield as a function of NIR laser light intensity are shown. In the course of data processing, we observed the coincident channel $N^+ + N^+$ in PiPiCo spectrum. Therefore, the NIR laser is intense enough to doubly ionize the molecule. The counts of N_2^{2+} and N_2^+ ions can be found in Fig. 6.2 (a), the measured ratio of N_2^{2+}/N_2^+ is 0.8%. According to Ref. [168], the light intensity of the NIR laser is

estimated in the range of 5×10^{13} - 3×10^{14} W/cm^2. In Fig. 6.2 (b), for the laser intensities below 10^{14} W/cm^2, the ratio of N_2^{2+}/N_2^+ does not show a significant change with the laser intensities. Therefore, the non-sequential mechanism can be used to interpret the double ionization of N_2. For laser intensities above 7×10^{14} W/cm^2, the sequential model is commonly be used to describe the double ionization process [168].

ADK Theory

In order to precisely estimate the NIR laser intensity, the second approach is proposed. Similar to the Eq. 2.6 in Chapter 2, the following equation is used to describe the width of recoil-ion momentum parallel the polarization of the NIR laser pulse:

$$\Gamma_{\mathrm{ADK}}(p_{||}) = A \cdot \exp\left(-(p_{||}-p_0)^2 \frac{\omega^2(2I_p)^{3/2}}{3I^{3/2}}\right), \tag{6.1}$$

where A is amplitude, $p_{||}$ momentum along laser polarization, p_0 central momentum, ω laser frequency, ionization potential I_p and laser intensity I.

Considering the single ionization of the molecule N_2:

$$N_2 \xrightarrow{\mathrm{IR}} {N_2}^+ + e^-. \tag{6.2}$$

The NIR laser pulse is center wavelength at 800 nm with a pulse length of 350 fs, and the corresponding laser frequency $\omega = 0.057\,a.u.$ The ionization energy I_p of N_2 is 0.5728 a.u. Using the Eq. 6.1 to fit the momentum of N_2^+ ions along the polarization. The fit result is shown in Fig. 6.3.

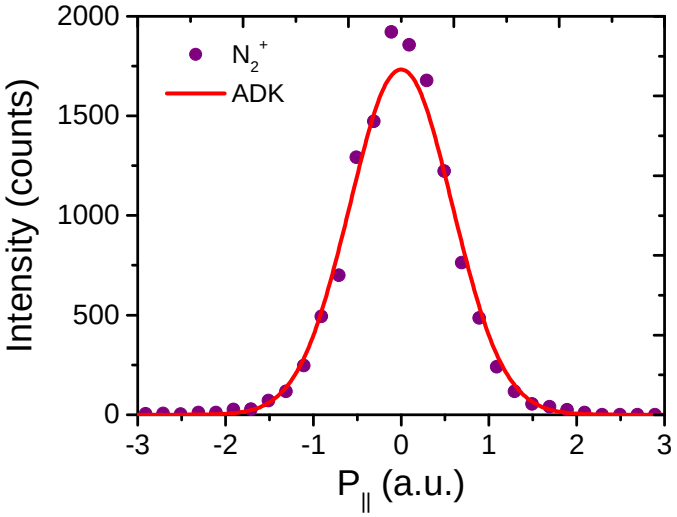

Figure 6.3: Momentum distribution $p_{||}$ of N_2^+ ions. The polarization of the NIR laser is along the horizontal axis.

From the fit results, the NIR laser intensity is estimated to be $(2.56\pm0.50)\times10^{14}$ W/cm^2. We compared our present estimation with the experimental results analyzed by Georg Schmid [55] from the same beam-time at FLASH, and he estimated the intensity of the

NIR laser was 2.5×10^{14} W/cm^2 by measuring the ratio of Ar^{2+}/Ar^{+} ions. Our estimation is in good agreement with his result. For the intensity of the NIR laser pulse ($\lambda = 800$ nm, 350 fs) is about 2.56×10^{14} W/cm^2 with an uncertainty of 0.5×10^{14} W/cm^2. Therefore, we calculate the corresponding Keldysh parameter $\gamma = 0.7$ and $U_p \cong 15.3$ eV. In this case, both multiphoton ionization and tunneling ionization contribute to the photoionization process of the molecule.

6.2.2 Ionization and Dissociation Channels

The single ionization potential of N_2 is 15.58 eV and double ionization threshold is 42.88 eV [169]. As introduced in previous Chapter 5, we can determine the final dissociative states by the tracing kinetic energy of the ions or KER of ion pairs. Throughout this chapter N(A,B) designates the dissociation channel $N_2^{(A+B)+} \rightarrow N^{A+} + N^{B+}$.

In Fig. 6.4, the single- and double ionization processes of N_2 are shown. The KER of non-coincident N^+ ions centred at 1.31 eV corresponds to the dissociative ionization pathway: $N_2^+(C^2\Sigma_u^+, D^2\Pi_g) \rightarrow N^+(^3P) + N(^4S)$(L1) [159]. The dissociative state $3^2\Sigma_g^+$ dissociated into $N^+(^3P) + N(^2D)$(L3) with a KER of 6.7 eV. The dissociation of $5^2\Sigma_g^+$ state into $N^+(^1D) + N(^2P)$(L7), $N^+(^1D) + N(^2D)$(L6), and $N^+(^3P) + N(^2D)$(L3) limits resulted in KERs of 7-12 eV [86]. For the dissociation limits of the N_2^+ molecular ions can be found in Table. 6.1.

According to previous works [86, 170, 171], five main dissociative states $A^1\Pi_u$, $D^3\Pi_g$, $c^1\Delta_g$, $d^1\Sigma_g^+$, and $D^1\Sigma_u^+$ of N_2^{2+} can be attributed to the KER spectra which peaked at 6.7, 8.0, 8.1, 8.4, and 10.4 eV for N(1,1) in Fig. 6.4.

Table 6.1: Dissociation energies for the lowest ten dissociation limits of N_2^+ ions [172].

Limit label	Configuration $N^+ + N^*$	Energy (eV)
L1	$^3P + {}^4S^0$	24.293
L2	$^1D + {}^4S^0$	26.192
L3	$^3P + {}^2D^0$	26.676
L4	$^3P + {}^2P^0$	27.869
L5	$^1S + {}^4S^0$	28.345
L6	$^1D + {}^2D^0$	28.575
L7	$^1D + {}^2P^0$	29.768
L8	$^1S + {}^2D^0$	30.728
L9	$^1S + {}^2P^0$	31.921
L10	$^3P + (3s)^4S$	34.629

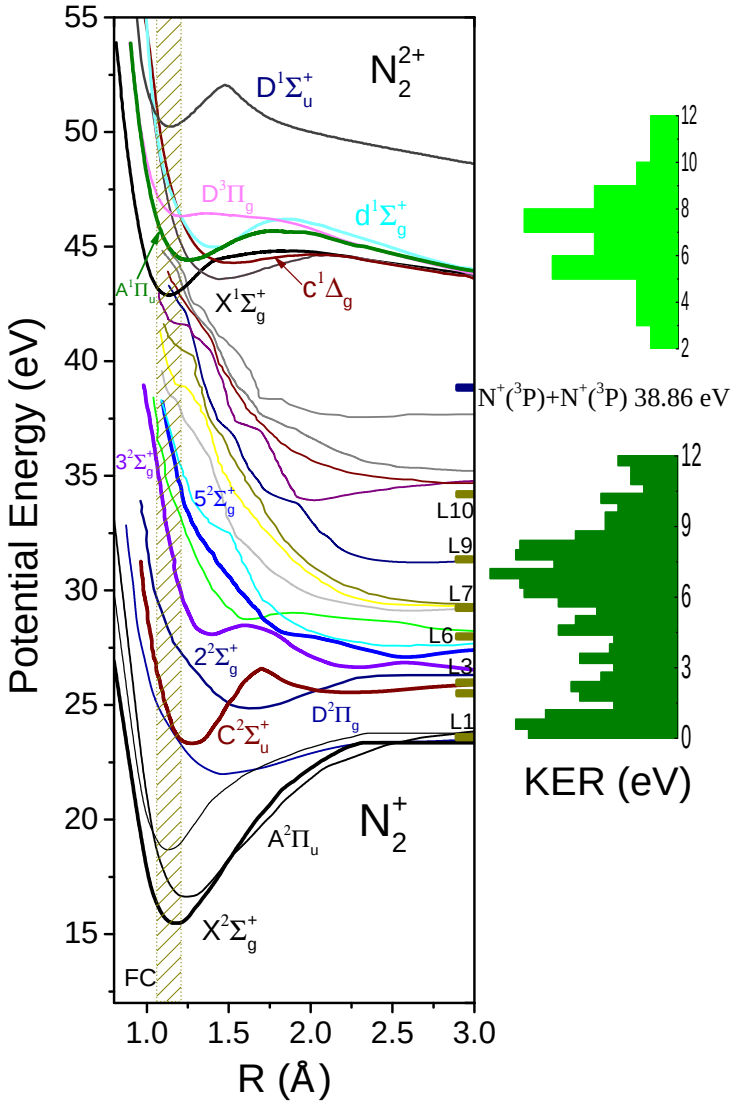

Figure 6.4: Potential energy curves (PECs) of N_2^+ and N_2^{2+} molecular ions. The KER of coincident channel N(1,0) and N(1,1) are plotted in the right of this figure. The Frank-Condon regime (FC, vertical shaded band) is sketched. PECs are adopted from Refs. [159, 170, 172].

In Fig. 6.5, two ionization pictures are used to explain the creation of N_2^+ and N_2^{2+} ions. First, as described in Ref. [173], at laser intensity approximately 2×10^{14} W/cm^2, the authors assumed to be a non-sequential regime of excitation. In this case, the tunneling ionization plays a role. As discussed in Sec. 2.1, the tunneling electron can rescatter with parent ion to high lying dissociative states. If the NIR laser intensity of the present experiment is assumed to be $I_{NIR} = 2.56 \times 10^{14}$ W/cm^2 and the corresponding ponderomotive energy U_p is about 15.3 eV. Thus, the maximum collision electron energy is $3.2\,U_p$ = 48.9 eV. Therefore, two electrons in N_2 are removed in a non-sequential way. Therefore, the rescattering process is sufficient to explain the double ionization of the molecule. In Refs. [51, 52], for double ionization, the first step is the removal of the outmost electron from the molecule through tunneling ionization. The second step is the rescattering excitation of the singly charged molecular ion. The final step is the removal of the other

outermost electron from the singly charged molecule and reaching an excited dication state.

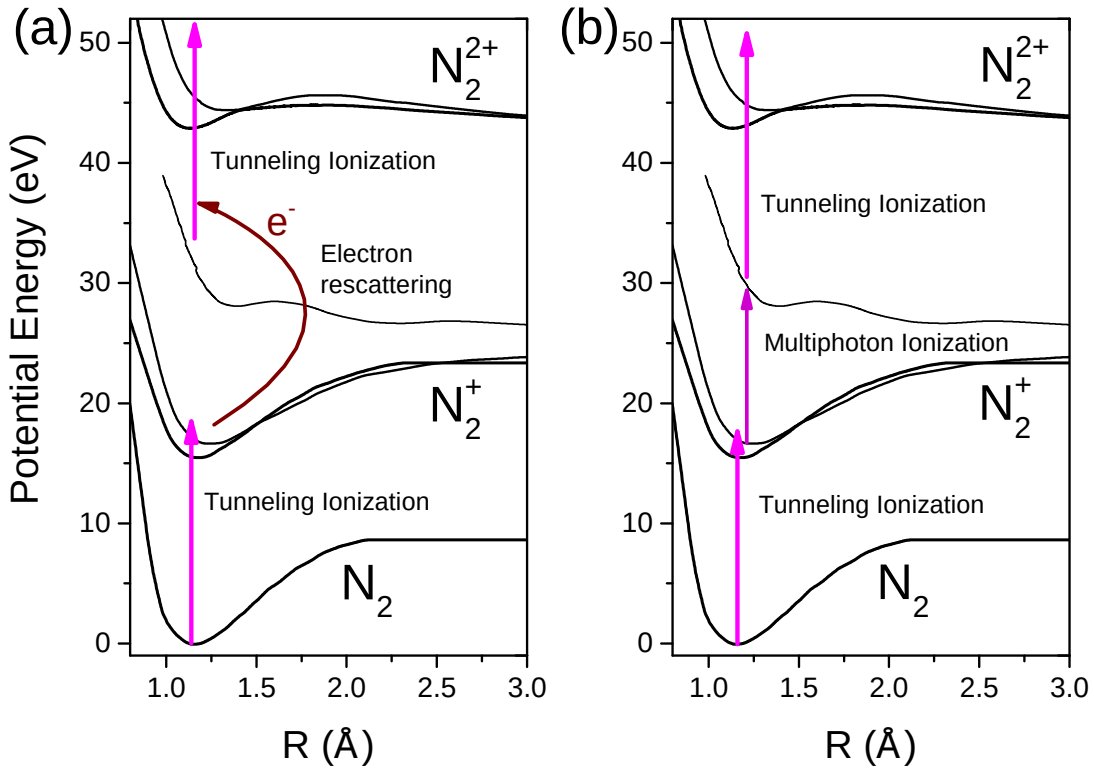

Figure 6.5: Schematic diagrams for (a) rescattering process and (b) sequential MPI process. PECs are adapted from [159, 170, 172].

Second, the sequential multiphoton picture is utilized to explain the formation of each molecular ions. In the first step, the neutral molecule is ionized by tunneling ionization. The singly charged molecular ion is further excited by absorbing more IR photons to a highly excited state. After some time, the singly charged molecular ion is populated to doubly charged molecular ion states by tunneling ionization. As reported in Ref. [51] and shown in Fig. 6.2 (b), if the NIR laser intensity is higher than 5×10^{14} W/cm^2, the sequential multiphoton ionization is the dominant process. Thus, the rescattering picture is sufficient to explain the double ionization of N_2 in the NIR laser field.

6.2.3 FIAD in NIR Laser Field

In the present experiment, the polarization of the NIR laser field is parallel to the axis of the spectrometer (TOF-direction, see Sec. 3.2). The ionic fragments due to photoionization by NIR radiation are more likely to dissociate along the polarization of the laser field.

According to the molecular ADK (Ammosov-Delone-Krainov) model [174], the angular distribution of the ionic fragments will be strongly parallel to the polarization of the NIR laser field. As can be seen from the angular distribution in Fig. 6.6, the dissociative

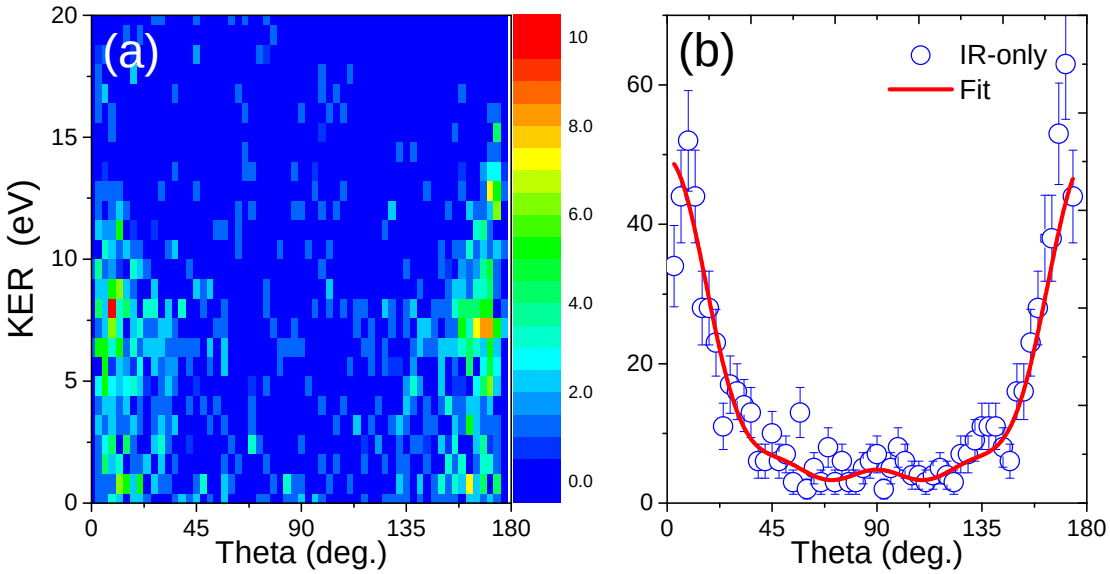

Figure 6.6: (a) KER vs Theta of non-coincident N^+ ions. Theta is the angle with respect to the polarization axis of the linearly polarized NIR laser. (b) Angular distribution of non-coincident N^+ ionic fragments with $0 < \text{KER} < 10\,\text{eV}$.

ionic fragments of non-coincident N^+ ions emitted along the polarization of the NIR laser field. It's a "back-to-back" emission pattern. As mentioned in Sec. 2.7, the dissociated fragments carry the symmetry information about the initial and final states. From the angular distribution of the ionic fragments, the "parallel transition" way is expected. For the molecular symmetry of N_2 ground state is Σ_g, thus the final dissociative states should also with Σ symmetry property which agrees well with the above assignment of each dissociative channel. On the other hand, the angular distribution shows the behavior expected from the symmetry of the $3\sigma_g$ outer orbital for N_2, which is in excellent agreement with the previous works [51, 173].

6.3 Multiple Ionization of N_2 by XUV Radiation

In the section, the multiphoton absorption steps of the formation of N_2^{n+} ions by a single XUV laser pulse are discussed. First, the calibration of the FEL light intensity is given. In the following, the few-photon multiple ionization of N_2 by XUV radiation is presented.

6.3.1 Estimation of FEL Intensity

As mentioned in Sec. 6.1, the FEL light intensity was obtained by measuring the current induced by the FEL pulse on a copper plate. Thus, we can estimate the real light intensity by measuring the pulse energy, the pulse duration and its focal spot size [55]. The FEL light intensity I_{FEL} is estimated by taking the pulse energy $E_{pulse} \approx 9.9$ µJ as measured by a Gas-Monitor Detector (GMD) [101], the focal spot size A_{focus} with diameter $d \approx 20\,\mu\text{m}$

and the pulse duration $\tau_{FEL} \approx 100$ fs:

$$I_{FEL} = \frac{E_{pulse}}{A_{focus}\,\tau_{FEL}} = 3 \times 10^{13}\,\frac{W}{cm^2}. \tag{6.3}$$

6.3.2 Calibration of FEL Light Intensity

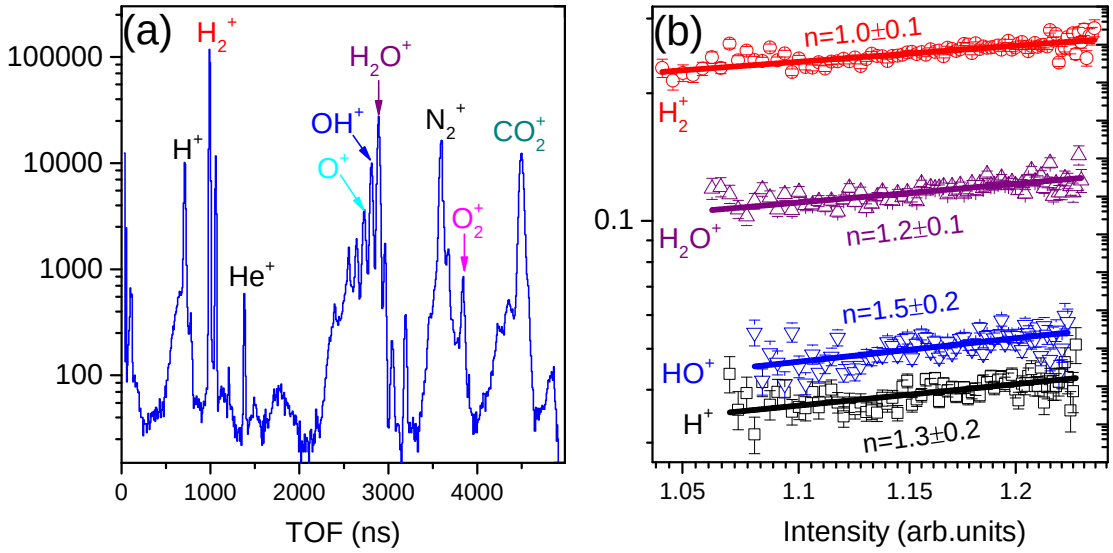

Figure 6.7: (a) Time-of-flight spectrum of ions of the residual gas induced by XUV radiation. (b) Ion yields as a function of the FEL light intensity. The units of the two figures are in arbitrary units. Solid lines are fit by $Y = \sigma_n I^n$ for the four background ions. The slops of fitting solid line denote the number of absorbed photons. Error bars are statistical.

According to perturbation theory, the ionization yields (Y) should increase with light intensity (I) as $Y = \sigma_n I^n$, where σ_n is the generalized n-photon cross section and n is the number of photons [86]. By measuring the ion yields as a function of the light intensity, the number of absorbed photons can be obtained. In Fig. 6.7 (a), the time-of-flight spectrum of the ions of the residual gas induced by XUV radiation is shown. For the ion yield of H^+, the slope of the fitting line is n = 1.3 $\pm$ 0.2, for H_2O^+ is n= 1.2 $\pm$ 0.1, and for HO^+ is n = 1.5 $\pm$ 0.2, respectively. The single XUV-photon absorption is the dominant process for the residual gas in the interaction chamber. In case of XUV-only, H_2 as the residual gas of the interaction chamber was ionized by a single 28.3 eV XUV photon, for which the slope of the fitting solid line n = 1.0 $\pm$ 0.1 provides further evidence for the light intensity calibration [175]. In the following, the determination of the few-photon multiple XUV ionization of N_2 is based on the present light intensity calibration.

6.3.3 Few Photon Multiple Ionization of N_2

In Chapter 2, sequential ionization (SI) and non-sequential ionization (NSI) are two basic ionization pictures of the multiphoton ionization process for atoms and molecules. In the

past, SI and NSI of Neon and Argon atoms have already been reported in Ref. [175]. In this section, few-photon multiple ionization (MPI) of N_2 by 28.3 eV XUV radiation is discussed. We can identify the transition pathways for the formation of various molecular ions by inspecting the photon absorption steps. Here, we only focus on how many XUV photons involved in the formation of different charge molecular ions. As the detailed molecular states involving will be discussed in Sec. 6.4.

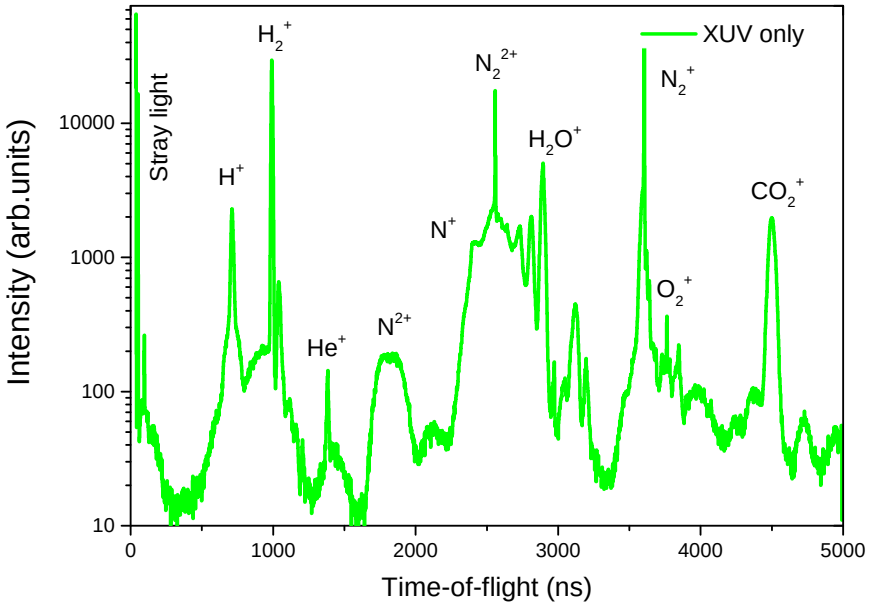

Figure 6.8: Ion time-of-flight mass spectrum of N_2 measured at photon energy 28.3 eV XUV radiation and FEL light intensity $I_{FEL} = 3\times10^{13}$ W/cm^2.

In Fig. 6.8, the TOF spectrum of the ions induced by XUV radiation is shown. As already mentioned in Sec. 3.13, three coincident channels are observed in our experiment, namely, the coincidence channel N(1,1), N(2,1), and N(2,2). Selecting the TOF of each ion, the light intensity dependence of ion yields for various molecular ions and coincident channels are obtained.

In Fig. 6.9 (a-d), the ion yields as a function of FEL light intensities are shown. The unit of the FEL light intensity is in arbitrary units. The integer number of photons n is marked for various dissociation channels. A single 28.3 eV XUV-photon is sufficient to singly ionize the molecule. At the low FEL intensity, the production of non-coincident N^+ ions is a single XUV-photon absorption process. As discussed in Sec. 6.2.2, the single ionization of N_2 with a higher KERs (KER ≥ 4 eV) main come from the highly states e.g. $3^2\Sigma_g^+$ ($E_B \sim 32$ eV) and $5^2\Sigma_g^+$ ($E_B \sim 38$ eV). Thus, a single XUV photon is insufficient to create higher kinetic energies N^+ ions. In this case, the two XUV photons absorption is needed. With the increase of light intensity, the ion yields reach the saturation region. For the low KERs of the N_2^{2+} ions, it is a two XUV-photon process except for some of higher excited states, e.g. $D^1\Sigma_u^+$ is a three XUV-photon process. A three-XUV-photon process dominates the production of non-coincident N^{2+} ions. Surprisingly, we find up to five XUV-photons absorbed for the creation of N_2^{3+} ions while already three photons would be enough via vertical transition.

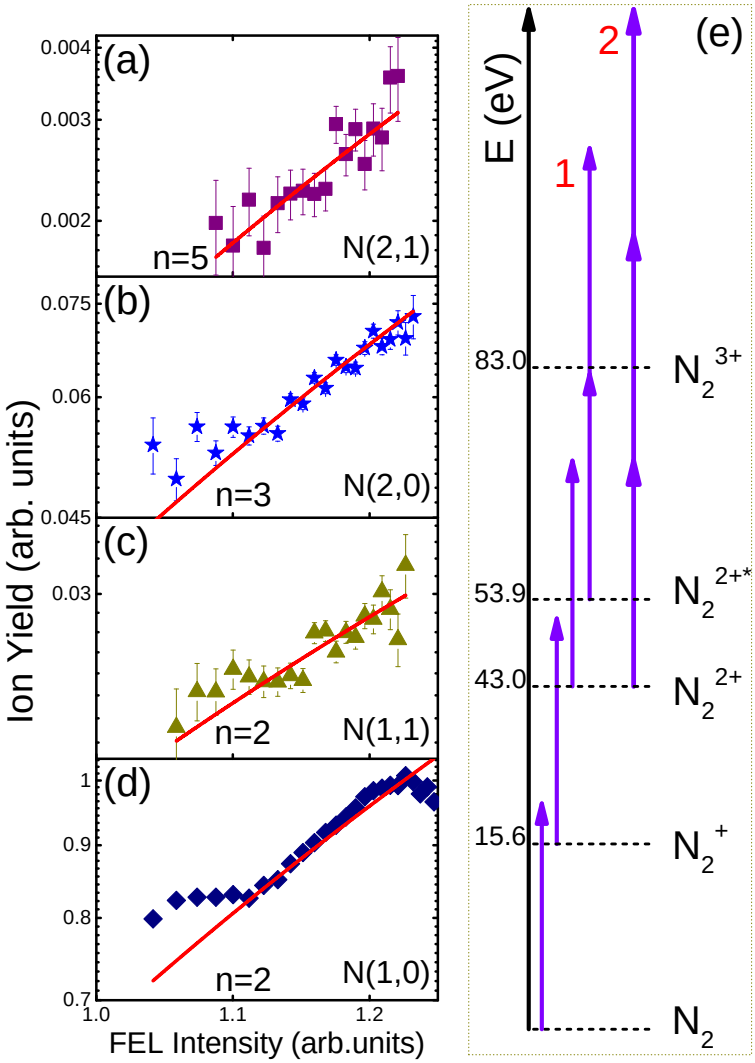

Figure 6.9: Ion yields of coincident channel (a) N(2,1), (b) N(2,0), (c) N(1,1), and (d) N(1,0) as a function of the FEL light intensity I_{FEL}. Solid lines are fit by $Y = \sigma_n I^n$ for various dissociation channels. Red-solid lines with slope n = 5, 3, 2 are shown. The uncertainty of the FEL certainty is expected to be $\pm 10\%$. (e) The transition pathways for the creation of various molecular ions. The violet arrow represents a 28.3 eV XUV photon. Two possible population ways 1 and 2 are labeled for the formation of N_2^{3+} ions.

For the atomic Nitrogen, the ionization threshold for N^+ and N^{2+} is 14.53 eV and 29.6 eV, respectively [176]. The molecule needs two-photon for double ionization. The appearance energy for the creation of N^{2+} ions is 53.9 eV, thus at least three XUV photons are required to create the dissociation channel N(2,0) [177]. The population of the N_2^{3+} may come from the further ionization of N_2^{2+} ions by another two or three XUV photons. Alternatively, it may come from the excited N_2^{2+*} ions absorption the other two XUV photons. The two population ways are shown in Fig. 6.9 (e) is based on the molecular system is still frozen at a short internuclear distance. The photon absorption ways (see Fig. 6.9 (e)) are listed as follows:

$$N_2 \xrightarrow{\text{1-XUV}} {N_2}^+ + e^- \tag{6.4}$$

$${N_2}^+ \xrightarrow{\text{1-XUV}} {N_2}^{2+} + e^- \tag{6.5}$$

$${N_2}^{2+} \xrightarrow{\text{1-XUV}} {N_2}^{2+*} \tag{6.6}$$

$${N_2}^{2+*} \xrightarrow{\text{2-XUV}} {N_2}^{3+} + e^-, \tag{6.7}$$

or, the formation of the N_2^{3+} molecular ions may by the following pathway:

$${N_2}^{2+} \xrightarrow{\text{3-XUV}} {N_2}^{3+} + e^-. \tag{6.8}$$

The absorption processes are finished within an ultrashort time ($\sim$25 fs) [178]. In our experiment, using a 100 fs FEL pulse to ionize the molecule, we found as much as five XUV photons are absorbed for the creation of channel N(2,1). In Jiang's experiment, in which they used 44 eV XUV photons, it was also observed that the molecule absorbed up to five photons to create the N_2^{3+} ions. It means there are several bound states which always play a role in the photon absorption process. We assume these bound states are deeply bounded with longer dissociation times [159]. To summarize, since the molecule prefers to absorb more photons than the minimum number needed, thus sequential ionization is determined to be the dominant and most efficient process for photoionization of molecules in the X-ray regime.

6.4 XUV-IR Pump-Probe Results

In this section, the XUV-IR pump-probe experimental results are presented. First, the time-of-flight mass spectra of the molecular ions in different laser fields are shown. The ion yields increased once the NIR laser overlapped with the XUV laser pulse in the temporal domain. In the following, the temporal resolution of the experiment is given. The time-dependent KERs spectra for N_2^{n+} ions were obtained. Finally, the detailed dissociative pathways by inspecting the KERs and angular distribution of the ionic fragments are discussed. In the end, the angular dependence of molecular ions is presented to explain the enhanced ionization of N_2 in two-color laser fields.

6.4.1 Time of Flight Spectrum with XUV and IR Laser

The FEL pulses were delivered with 28.3 ± 0.5 eV photons and the pulse length is roughly 100 fs. As discussed in Sec. 6.3.1, the light intensity of the FEL beam up to 3×10^{13} W/cm^2 was reached. Besides, the estimated maximum NIR intensity is 2.56×10^{14} W/cm^2 (see Sec. 6.2.1). With a pump-probe experimental scheme, the time-dependent ionic fragments spectra were obtained by adjusting the arrival time of the NIR laser pulse with respect to the XUV laser pulse in a range up to 10 ps. IR-early denotes the NIR laser pulse arrived on the target before the XUV laser pulse, and vice versa IR-late means that the NIR laser pulse arrived on the target late of the XUV laser pulse. XUV-only stands for the molecule was ionized by XUV radiation only. The detailed pump-probe method is explained in Sec. 6.1. Utilizing a REMI and SD optics (see Sec. 3.2), the spatial and temporal distribution of the ionic fragments were obtained.

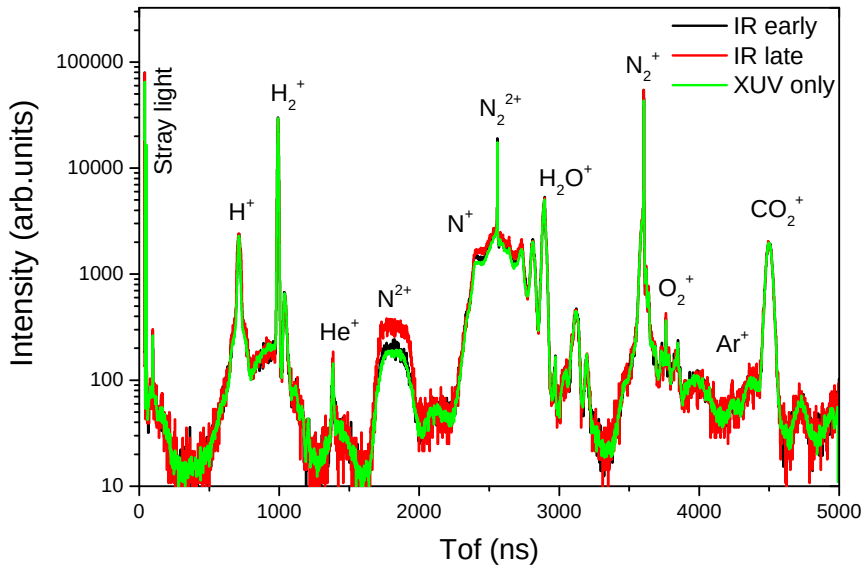

Figure 6.10: Ion time-of-flight mass spectra of N_2 measured at 28.3 eV in three different laser fields.

In Fig. 6.10, the TOF spectra show that the yields of the ions created in the case of IR-late are enhanced compared to IR-early, in particular, the N^+ and N^{2+} molecular ions. The relative enhancement of the doubly charged N^{2+} ions is higher than that of the singly charged N^+ ions. In contrast, in the case of IR-early and XUV-only, the ion yields are almost identical.

6.4.2 Temporal Resolution

Since the NIR and XUV laser pulses are generated by different facilities, they are not intrinsically synchronized. The jitter and long-term drift of the two pulses are crucial parameters for the temporal resolution. In Fig. 6.11 (a, b), the time-dependent KER spectra

for non-coincident N^+ and N^{2+} ions are shown. Negative delays denote the case that the NIR pulse arrives at the target before the XUV pulse (IR-early), positive delays present the case that the NIR pulse arrives after the XUV laser pulse (IR-late) [53]. A clear signature is that the ion yields increase once the two laser pulses overlapped in the temporal region.

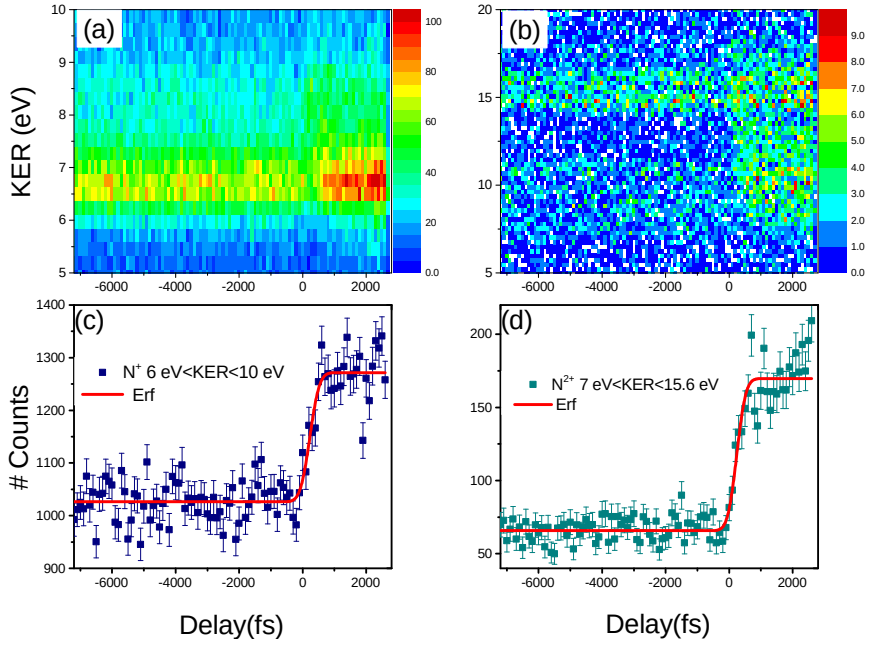

Figure 6.11: (a, b) Time-dependent KER spectra for non-coincident N^+ and N^{2+} ions, respectively. (c, d) The ion yields of N^+ (6 eV$<$ KER $<$10 eV) and N^{2+} (7 eV$<$ KER $<$15.6 eV) as a function of the time delay between the NIR and XUV laser pulse, respectively. The solid red lines are the fit with an error function (see Eq. 6.9). The energy of N^+ ions with KER at 6-10 eV does not change with pump-probe delay. However, the N^{2+} ions with KER at 15 eV around time-zero is converging for a long time delays to a different final KER with 10 eV.

By using the following error function (Erf)

$$f(t) = A \cdot \mathrm{erf}[(t - T_0)/\sqrt{2}\sigma] + C, \tag{6.9}$$

with A being the amplitude, T_0 delay offset, σ standard deviation, and C offset [55], to estimate the temporal resolution of the pump-probe experiments. In Fig. 6.11 (c, d), we use the above error function to fit the enhanced parts of the non-coincident ions. From the fit results, the temporal resolution is determined to be 545 $\pm$ 133 fs. The pulse-to-pulse intrinsic timing jitter, as well as long-time drift between the XUV and NIR laser pulses, are the limiting factors for this large temporal resolution [53]. Most of the lifetimes of the highly excited states of the N_2^{n+} ions are typically below 100 fs, except for some intermediate states [86]. Since the temporal resolution is roughly on the order of half picosecond, it is impossible to resolve the sub-100 fs ultrafast fragmentation process of molecular ions N_2^{n+}.

6.4.3 Channel N(1,0)

In this section, the single-ionization process N(1,0) is discussed.

$$N_2 \xrightarrow{XUV} {N_2}^+ + e^- \xrightarrow{diss.} N^+ + N + e^-, \tag{6.10}$$

where *diss.* stands for dissociation. In order to easily understand the measured experimental results, we interpret the following results are based on multiphoton ionization picture.

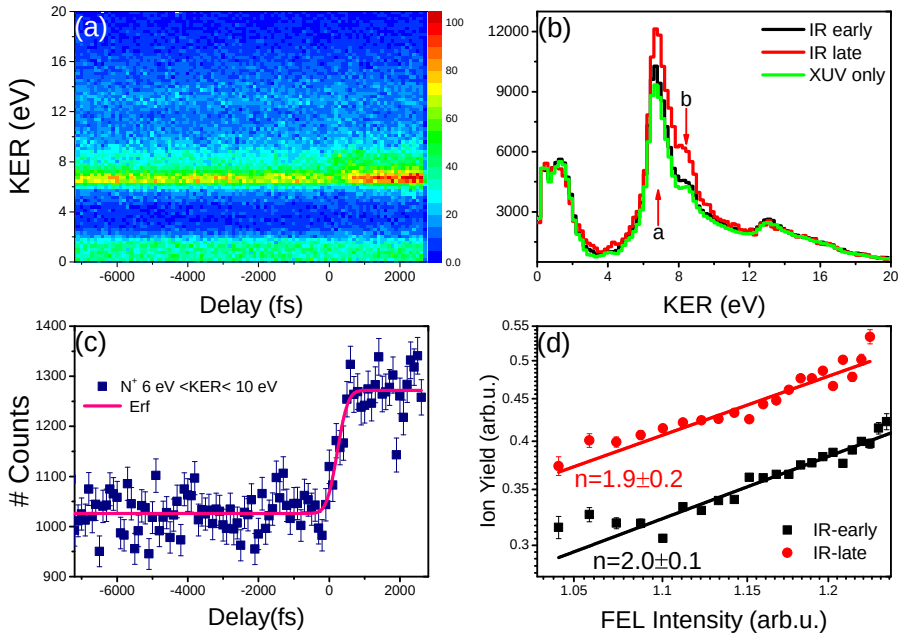

Figure 6.12: (a) Time-dependent KER spectrum for non-coincident N^+ ions. (b) KERs distribution of N(1,0) ions in different laser fields. All the coincident ion pairs statistics is normalized to the counts in a 10 ps delay range. (c) Time-dependent ion yield of N^+ (6 eV$<$ KER $<$10 eV) fit with error function. The solid pink line is the fit with error function (see Eq. 6.9). (d) The light intensity dependence of N^+ ions with KER at 6-10 eV in IR-early (black-solid line) and IR-late (red-solid line) are shown. The numbers of photons absorbed are shown. Error bars are statistical.

In Fig. 6.12 (a), the KER of the N(1,0) ions as a function of time delay between the XUV and NIR laser pulses is shown. We can observe the N^+ ions with 6 eV$<$ KER $<$10 eV increase. The ion yield of N^+ suddenly increases when the NIR laser pulse overlapped with the XUV laser pulse in the temporal domain. We plot the KERs of N(1,0) in different laser fields. The two red arrows (**a** and **b**) shown in Fig. 6.12 (b) denote the ion yields enhanced in case of IR-late compared with the XUV-only or IR-early case. In Fig. 6.12 (c), the projection of Fig. 6.12 (a) with the condition 6 eV$<$ KER $<$ 10 eV. The ratio of Y(IR-late)/Y(IR-early) is used to calculate the enhancement factor of the production of ions in IR-late and IR-early, where Y(IR-late) stands for the statics of ions in the presence of the NIR laser and Y(IR-late) stands for the statics of ions without the NIR laser. We find Y(IR-late)/Y(IR-early) = 1.24 for the non-coincident N^+ ions.

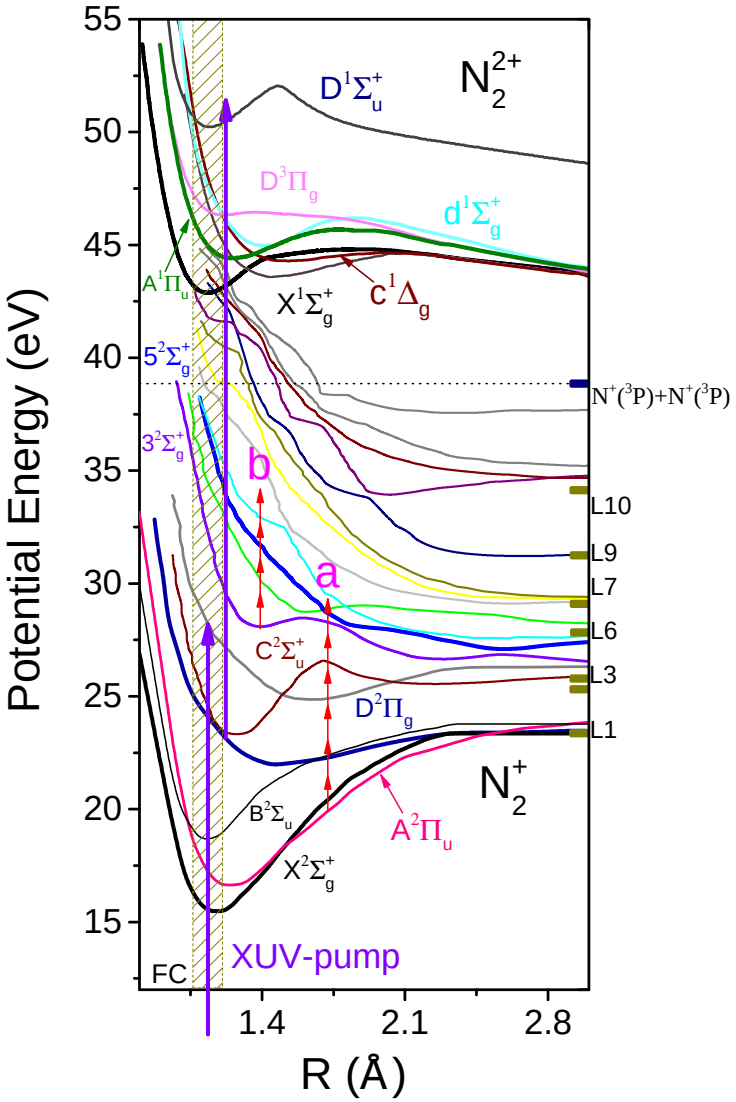

Figure 6.13: Schematic illustration of the dominant dissociative multiple ionization pathways for the formation of N_2^+ ions. Potential energy curves are adapted from Refs. [159, 170]. The violet-arrows and red-arrows stand for XUV and IR photons. Two transition pathways **a** and **b** are shown.

In the following, the discussion on the formation of the dissociative channel N(1,0) in XUV and IR laser fields is given. The photoionization can be investigated via state-resolved manner. By tracing the KER distribution and the number of XUV photons absorption, the dissociative states of each peak in Fig. 6.12 (b) can be assigned properly. As mentioned previous, we have already identified the final dissociative states for various channels (see Sec. 6.2.2). As the zero-kinetic energy N^+ ions, it may come from the first three excited states $A^2\Pi_u$, $B^2\Sigma_g^+$ and $D^2\Pi_g$ of N_2^+. Considering the angular distribution of fragments from state $3^2\Sigma_g^+$, the intermediate state could be $A^2\Pi_u$ at 16.93 eV and $D^2\Pi_g$ at around 22 eV [77]. The dissociative states $C^2\Sigma_u^+$ and $D^2\Pi_g$ are assigned to the peak centered at $\sim$ 1.3 eV. The ionic fragments originated from these states are not enhanced in the presence of the NIR laser field. Comparing the KERs distribution in different laser

fields, we find two peaks in Fig. 6.12 (b) are obtained enhancement when the NIR laser pulse arrived late of the first coming XUV laser pulse. As discussed in Sec. 6.2.2, the dissociative state $3^2\Sigma_g^+$ and $5^2\Sigma_g^+$ can be assigned to red-arrows *a* and *b* in Fig. 6.12 (b). If we look in the details of the Fig. 6.12 (a), we find there is a "hole" of the KER spectrum peaked at 6.7 eV when the XUV laser pulse and the NIR laser pulse overlapped in the temporal domain. Moreover, at the same time, the fragments with KER at 8.4 eV are enhanced. By increasing the time delays, the state $5^2\Sigma_g^+$ are converging onto $3^2\Sigma_g^+$.

In the following discussion, the excitation picture is used to explain the enhancement ionization. Since the XUV photon energy at 28.3 eV just below $2^2\Sigma_g$ (F-band, ~ 28.8 eV), thus single XUV-photon cannot reach those excited states above $2^2\Sigma_g^+$, e.g. $3^2\Sigma_g^+$, $5^2\Sigma_g^+$, $6^2\Sigma_g^+$. In this circumstance, the population to those excited states two XUV photons are required (see Fig. 6.12 (d)). Figure. 6.13 shows the transition pathways for the creation of N_2^+ ions in the XUV with NIR laser field. The sequential absorption of one or two XUV photons are shown (violet arrows).

The IR-assisted excitation pathways **a** and **b** are labeled to explain the enhancement ionization. The sequential ionization can be assigned to explain the enhancement of the peak *a* and *b* in Fig. 6.12 (b). This transition pathway corresponds to the pump-probe scheme which is labeled **a** in Figure. 6.13. Part of the enhancement ionization comes from the bound states of N_2^+ which are further excited to highly excited states in the presence of the NIR laser. In this scheme, at least 6-IR photons are required to excite the first two excited states of N_2^+ to $3^2\Sigma_g^+$ and $5^2\Sigma_g^+$.

$$\text{Pump}: \ N_2 \xrightarrow{\text{1-XUV}} {N_2}^+(A^2\Pi_u, D^2\Pi_g) + e^-, \tag{6.11}$$

$$\text{Probe}: \ {N_2}^+(A^2\Pi_u, D^2\Pi_g) \xrightarrow{\text{6-IR}} {N_2}^{+*}(3^2\Sigma_g^+, 5^2\Sigma_g^+) \xrightarrow{\text{diss.}} N^+ + N. \tag{6.12}$$

As the further excitation process **b**. The pump-probe reaction way:

$$\text{Pump}: \ N_2 \xrightarrow{\text{2-XUV}} {N_2}^{+*}(3^2\Sigma_g^+) + e^-, \tag{6.13}$$

$$\text{Probe}: \ {N_2}^{+*}(3^2\Sigma_g^+) \xrightarrow{\text{4-IR}} {N_2}^{+*}(5^2\Sigma_g^+) \xrightarrow{\text{diss.}} N^+ + N. \tag{6.14}$$

From the depletion signal of state $3^2\Sigma_g^+$ and the enhancement ionization of state $5^2\Sigma_g^+$, the further excitation happens. The enhancement of the creation of the ions from $5^2\Sigma_g^+$ main come from the further excitation of the low excited states $3^2\Sigma_g^+$. From the potential energy curve of $3^2\Sigma_g^+$, the excitation from $3^2\Sigma_g^+$ to $5^2\Sigma_g^+$ could take place at the internuclear separation reaches of 1.38 Å. At least 4-IR photons are required to populate to the excited state $5^2\Sigma_g^+$.

6.4.4 Channel N(1,1)

As shown in Fig. 6.14 (a), the coincident ions pair with the KER at 6-9 eV are enhanced in a delayed NIR laser pulse. The enhancement factor is Y(IR-late)/Y(IR-early) = 2.2 for

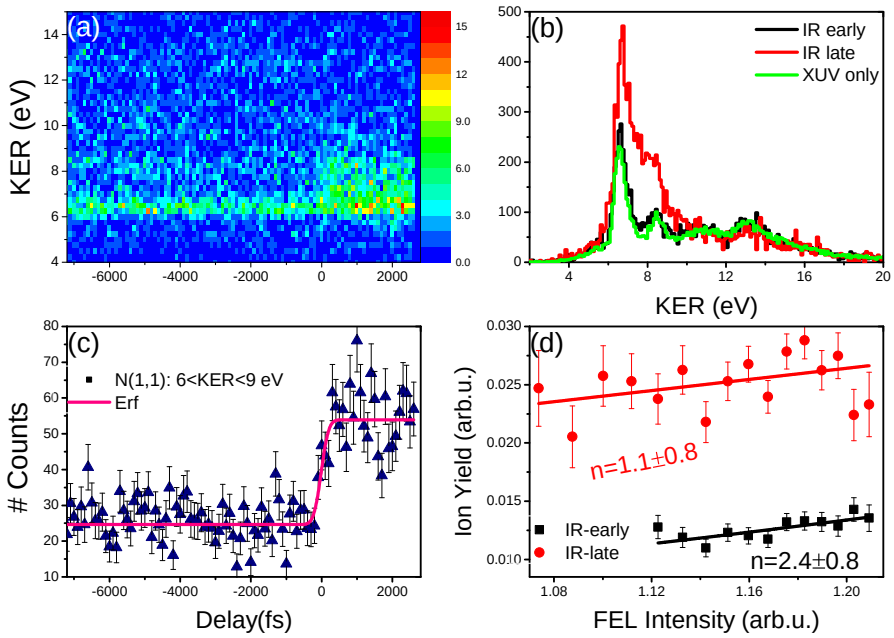

Figure 6.14: (a) Time-dependent KER spectrum for coincident N(1,1) ion pair. (b) KERs of coincident N(1,1) channel in different laser fields. (c) The time-dependent ion yields of N(1,1) coincidence (6 eV< KER < 9 eV). The solid pink line is the fit with error function. (d) The light intensity dependence of N(1,1) ions in IR-early and IR-late is shown.

N(1,1) compared to that without NIR. According to previous works [86, 170, 171], five main dissociative states $A^1\Pi_u$, $D^3\Pi_g$, $c^1\Delta_g$, $d^1\Sigma_g^+$, and $D^1\Sigma_u^+$ of N_2^{2+} can be attributed to the KER spectra which peaked at 6.7, 8.0, 8.1, 8.4, and 10.4 eV for N(1,1). The same treatment as the last channel N(1,0), the further excitation and ionization by the delayed NIR laser is employed to explain the enhancement ionization. The related excited states and PECs can be found in Figure. 6.13, the bound molecular dication states can be further excited to the final dissociative states which resulted in the enhancement ionization[1].

Excitation Picture

$$\text{Pump}: \ N_2 \xrightarrow{\text{2-XUV}} N_2{}^{2+}(X^1\Sigma_g^+, A^1\Pi_u, D^3\Pi_g, c^1\Delta_g, d^1\Sigma_g^+, D^1\Sigma_u^+) + 2e^-, \tag{6.15}$$

$$\text{Probe}: \ N_2{}^{2+}(X^1\Sigma_g^+) \xrightarrow{\text{4-IR}} N_2{}^{2+}(A^1\Pi_u, D^3\Pi_g, c^1\Delta_g) \xrightarrow{\text{diss.}} N^+ + N^+. \tag{6.16}$$

Further Ionization Picture

The ion yield of the fragments with a KER of 6-10 eV main come from the further ionization of the singly excited molecular states which are below the double ionization potential by the delayed NIR laser pulse. That's the reason why the number of XUV photons involved in the two laser fields are different. Such a process is similar to the "shake-up"

[1] As reported in Ref. [179], the low-lying quasibound states $a^3\Pi_g$ and $c^3\Sigma_u^+$ whose lifetimes lie in the 0.05-100 μs time scale. In this case, such metastable states could be treated as the intermediate states which can be further excited to the final dissociative states.

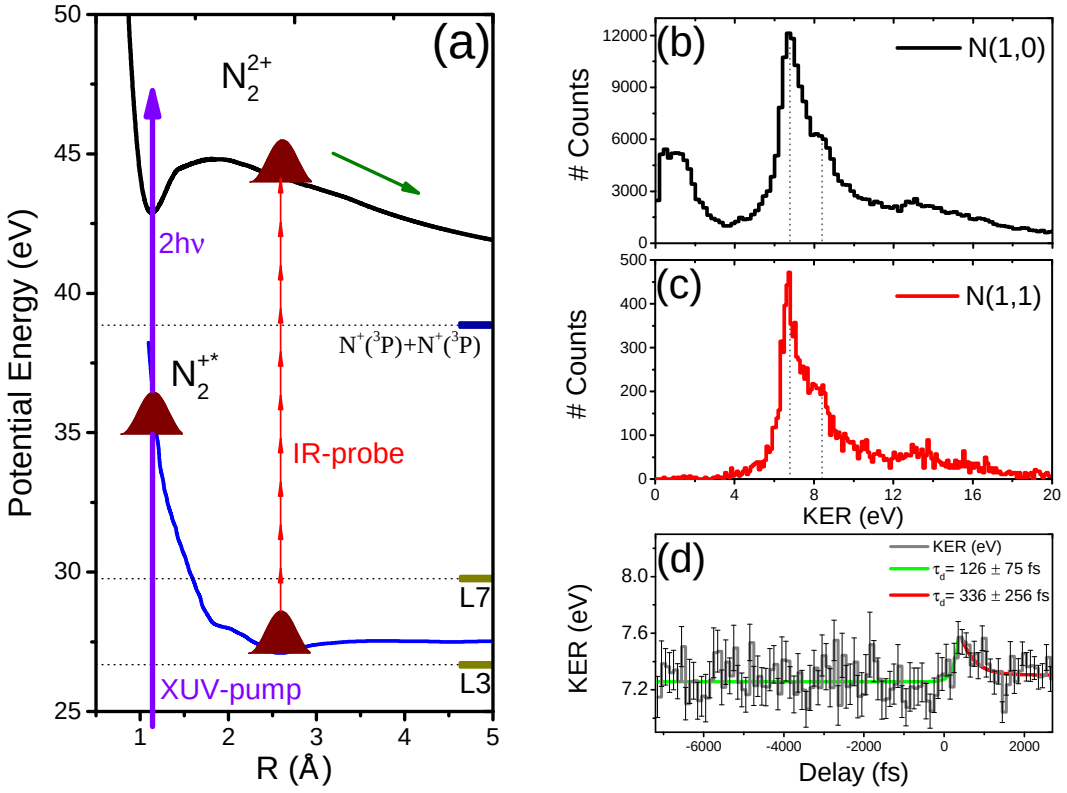

Figure 6.15: (a) Schematic diagrams for the IR-assisted excitation of the highly excited cation state to the ground dication state. The black PEC represents the excited states $A^1\Pi_u$, $D^3\Pi_g$ and $c^1\Delta_g$ of N_2^{2+}. And, the blue-line stands for excited states $3^2\Sigma_g^+$ and $5^2\Sigma_g^+$. (b, c) KERs of N(1,0) and N(1,1). The dashed lines shown in the two figures have the same KER. (d) Time-dependent mean KER spectrum of the N(1,1) ions with KER at 6-10 eV. An exponential function is used to fit the increase and decrease of the ion yield.

process which was described in Ref. [83]. The induced excited states of N_2^{+*} can be further populated to the final dissociative states $A^1\Pi_u$, $D^3\Pi_g$ and $c^1\Delta_g$ of N_2^{2+} by the delayed NIR laser field. The transition pathways are shown in Fig. 6.15. The transition pathways are described as:

$$\text{Pump}: \ N_2 \xrightarrow{\text{2-XUV}} {N_2}^{+*}(3^2\Sigma_g^+, 5^2\Sigma_g^+) + e^-, \tag{6.17}$$

$$\text{Probe}: \ {N_2}^{+*}(3^2\Sigma_g^+, 5^2\Sigma_g^+) \xrightarrow{\text{n-IR}} {N_2}^{2+}(A^1\Pi_u, D^3\Pi_g, c^1\Delta_g) + e^- \xrightarrow{\text{diss.}} N^+ + N^+ + e^-. \tag{6.18}$$

The minimum number of IR photons n can be calculated by measuring the energy difference between the dissociation limit of N_2^{2+} ions and the cation dissociation limits (L3, L7). Thus, the excited state $3^2\Sigma_g^+$ has to absorb at least 8-IR photons to reach the dissociative dication states. And, for the excited state $5^2\Sigma_g^+$ needs at least 6-IR photons. The blue potential energy curve stands for the highly excited cation states, e.g., $3^2\Sigma_g^+$, $5^2\Sigma_g^+$, or even the higher ones. In the present experiment, the excited state $3^2\Sigma_g^+$ and $5^2\Sigma_g^+$ are attributed to enhancement ionization of N(1,1) with the KERs at 6.7 eV and 8.4 eV, respectively.

For the further ionization process, the time-dependent mean-KER spectrum of N(1,1) carries the timing information on the depletion dynamics of $3^2\Sigma_g^+$ and the dissociation process of $5^2\Sigma_g^+$. In Fig. 6.14 (d), the time-dependent of the mean KER of the enhanced yields is shown. From the fit results, the depletion time of state $3^2\Sigma_g^+$ is of $\tau = 126 \pm 75$ fs and the state $5^2\Sigma_g^+$ lifetime of $\tau = 336 \pm 256$ fs. Since the temporal resolution of the present experiment is 545 fs, thus the measured lifetimes are the mean lifetimes of depletion or dissociation for each state.

6.4.5 Channel N(2,0)

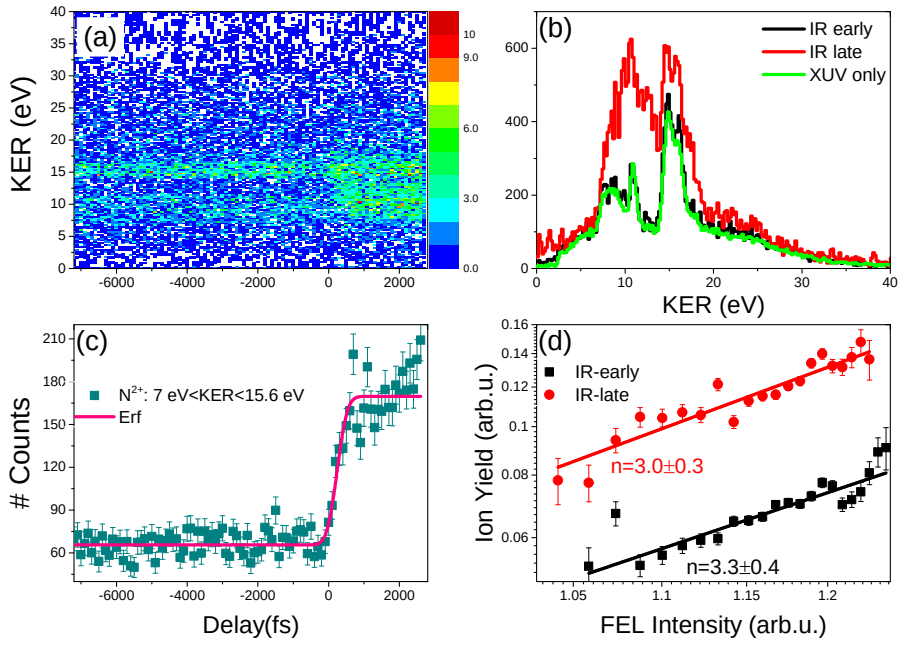

Figure 6.16: (a) Time-dependent KER spectrum for non-coincident N^{2+} ions. (b) KERs of non-coincident N^{2+} ions in different laser fields. (c) Time-dependent ion yields of N^+ (7 eV$<$ KER $<$15.6 eV). The solid pink line is the fit with error function. (d) The light intensity dependence of N^{2+} ions in IR-early and IR-late are shown.

In Fig. 6.16 (a), the total ion yield of non-coincident N^{2+} ions increases when the XUV and NIR laser pulses overlapped around the zero-time delay. A dissociative channel is observed which corresponds to an excited state created and probed by the delayed NIR laser pulse. For N^{2+} ions with KER 7-15.6 eV, the enhancement factor Y(IR-late)/Y(IR-early) is 2.58 which is higher than that of non-coincident N^+ ions.

In the first place, we have to find out from which dissociative states these molecular ions come. According to previous works, the N^{2+} ions mainly come from the dissociative ionization of highly excited molecular states $^1\Sigma_g$, $^1\Sigma_u$, and $^1\Pi_u$ of N_2^{2+*} [82] (see Fig. 6.18). The KER spectrum peak at 8.4 eV corresponds to the dissociation channel $N_2^{2+}(^1\Sigma_g) \rightarrow N^{2+}(^2P) + N(^2D)$, while the peaks at 10.6 eV and 14.6 eV can be assigned to the dissociation channel: N_2^{2+} $(^1\Sigma_u) \rightarrow N^{2+}(^2P) + N(^4S)$, and the peak at 16.2 eV can be assigned to N_2^{2+} $(^1\Pi_u)$ dissociating into $N^{2+}(^2P)$ + $N(^2P)$ limit at 57.5 eV [177] (see Table 6.2). As

demonstrated in Ref. [180], about 60% of highly excited molecular dications will dissociate into N(1,1) and the rest dissociate into N(2,0).

Table 6.2: Electronic states of the dissociative states of N_2^{2+} ions. Adapted from Refs. [82, 177].

State	Major configuration	KER (eV)	Final state	Energy (eV)
$^1\Sigma_g$	$2\sigma_g^{-1}3\sigma_g^{-1}$	8.4	D_2: $N^{2+}(^2P)$ + $N(^2D)$	56.3
$^1\Sigma_u$	$2\sigma_g^{-1}3\sigma_u^{-1}$	10.6	D_1: $N^{2+}(^2P)$ + $N(^4S)$	53.9
$^1\Sigma_u$	$2\sigma_g^{-1}3\sigma_u^{-1}$	14.6	D_1: $N^{2+}(^2P)$ + $N(^4S)$	53.9
$^1\Pi_u$	$2\sigma_g^{-1}1\pi^{-1}$	16.2	D_3: $N^{2+}(^2P)$ + $N(^2P)$	57.5

As mentioned above in Sec. 6.3.3, the molecule has to absorb three XUV photons to create the N^{2+} ions. In Fig. 6.16 (d), in the case either IR-early or IR-late, three XUV photons absorption is the dominant process. The excitation picture is attributed to explain the enhancement ionization in the delayed NIR laser field. It may come from the bound states of N_2^{2+} and further excited to dissociative states $^1\Sigma_g$, $^1\Sigma_u$, and $^1\Pi_u$ of N_2^{2+*}. The related potential energy curves of N_2^{2+*} can be found in the next section.

6.4.6 Channel N(2,1)

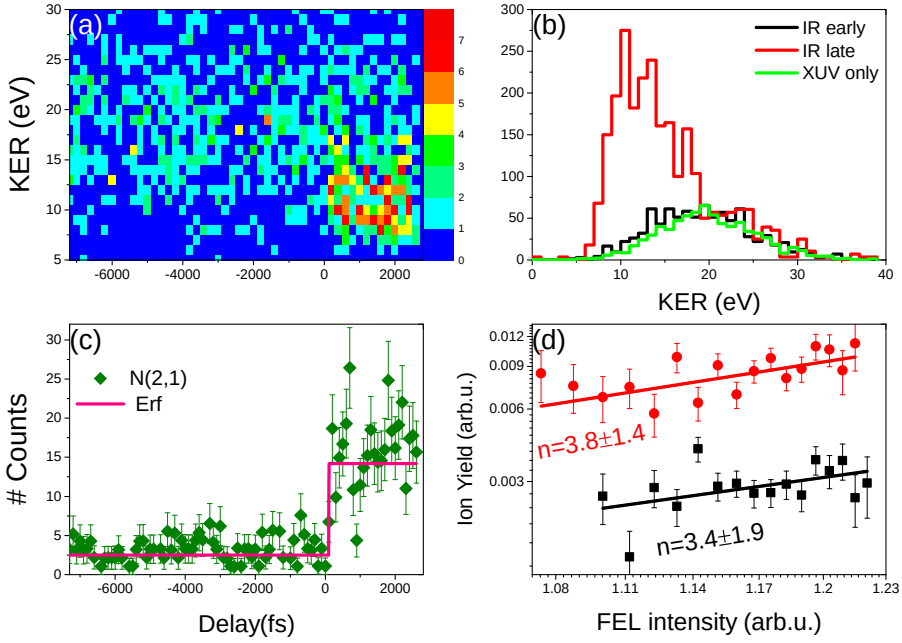

Figure 6.17: (a) Time-dependent KER spectrum for coincident N(2,1) ions. The enhancement factor Y(IR-late)/Y(IR-early) is 5.7 for N(2,1) compared to that without NIR. (b) KERs of coincident N(2,1) in different laser fields. (c) Time-dependent ion yield of N(2,1). The solid pink line is the fit with error function. (d) The light intensity dependence of coincident N(2,1) ions in IR-early and IR-late are shown.

In Sec. 6.3, the molecule absorbed five XUV photons to create the N_2^{3+} molecular ions. The sequence of absorption of XUV photons can be found in Fig. 6.9. The lowest dissociative state $^2\Pi_u$ of N_2^{3+} can be attributed to the KER spectra which peaked at 13.5 eV of N(2,1) and 20 eV can be assigned to the Coulomb repulsive potential curve 2/R or the excited state $3^2\Pi_u$ [181].

If we compare the KERs of N(2,0) and N(2,1), it is found that the KER produced in IR-late is roughly in the same energy range as N(2,1). The lower KER of N_2^{2+*} ions is assigned to contribute the enhancement ionization of N(2,1) in a delayed NIR laser field. At least three XUV photons are required to populate to those highly excited N_2^{2+*} states, and then further ionized by a delayed NIR laser pulse to the lowest excited molecular states $^2\Pi_u$. A dissociation process is observed from the time-dependent KER spectrum of N^{2+} ions which is accounted for the enhancement ionization of channel N(2,1).

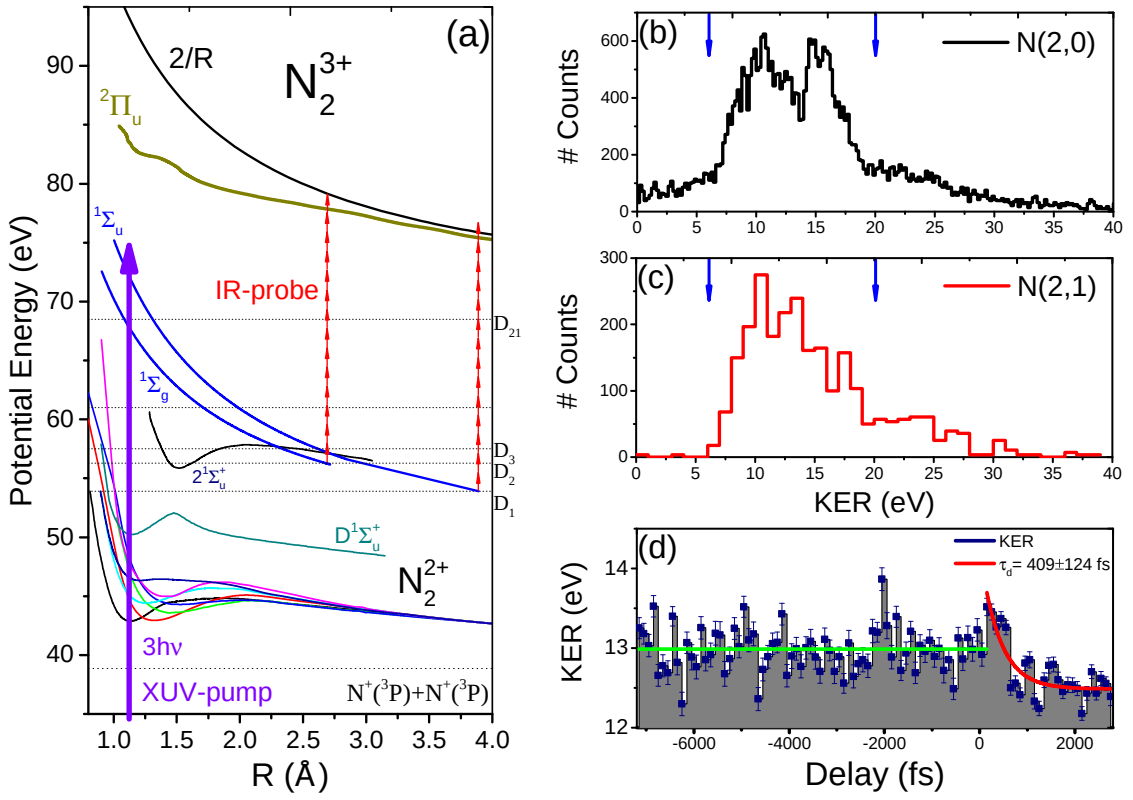

Figure 6.18: (a) Schematic diagrams for the IR-assisted ionization of the highly excited dication state to N_2^{3+} states. The dissociation limits D_1-D_3 can be found in Table 6.2. D_{21} stands for the lowest dissociation limit of N_2^{3+} ions: $N^{2+}(^2P)$ + $N^+(^3P)$. (b, c) KERs of the non-coincident N^{2+} ions and coincident N(2,1) ion pairs. The two blue arrows in Fig. (b, c) have the same KER. (d) The time-dependent KER spectrum of the N^{2+} ions with KER at 8-20 eV. An exponential function is used to fit the decrease of the ion yield.

Further Ionization Picture

$$\text{Pump}: \ N_2 \xrightarrow{\text{3-XUV}} N_2{}^{2+*}(^1\Sigma_g, ^1\Sigma_u) + 2e^-, \tag{6.19}$$

$$\text{Probe}: \ {N_2}^{2+*}({}^1\Sigma_g, {}^1\Sigma_u) \xrightarrow{\text{n-IR}} {N_2}^{3+}({}^2\Pi_u) + e^- \xrightarrow{\text{diss.}} N^{2+} + N^+ + e^-. \tag{6.20}$$

The detailed pump-probe scheme is shown in Fig. 6.18 and Eq. 6.19 and 6.20. We assume the further ionization takes place near the dissociation limits, for $N_2^{2+*}({}^1\Sigma_g) \rightarrow N_2^{3+}({}^2\Pi_u)$ and $N_2^{2+*}({}^1\Sigma_u) \rightarrow N_2^{3+}({}^2\Pi_u, 2/R)$ can be found in the figure. The dissociation lifetime of the lower KER of τ_d = 409 $\pm$ 124 fs. To our knowledge, the potential energy curves of highly excited N_2^{2+*} ions are scant. Thus, theoretical work is strongly needed.

6.4.7 Enhanced Ionization of N_2 in Two-Color Laser Fields

In this section, the enhanced ionization of N_2 in the two-color laser fields is analyzed by the angular distribution of the ionic fragments. Aligned N_2^{n+} ions are created by absorption of one or more XUV photons and can be further excited or ionized by a delayed NIR laser field. We find only the "perpendicular transition" ionic fragments in the XUV laser field which emitted along to the polarization of the NIR laser field can be enhanced in the delayed NIR laser pulse.

Aligned N_2^{n+} Ions

As discussed above, the ion yields and fragmentation for the case of IR-early are roughly the same as for the XUV-only case. Here, we only focus on the angular distribution of ionic fragments in the XUV laser field. The ionic fragments dissociated at a small angle (near 0° or 180°) along the horizontal direction are coming from a "parallel transition". Moreover, we define a "perpendicular transition" if the fragments are emitted at a large angle (e.g. near 90°). In Fig. 6.19, fragment ions angular distribution (FIAD) for three dissociation channels by the 28.3 eV XUV radiation are shown. The final dissociative states for various channels are labeled in the figure. In the present experiment, the polarization of the NIR laser pulse is perpendicular to the polarization of the XUV laser pulse.

As discussed in Sec. 2.7, the ionic fragments is a parallel explosion or perpendicular explosion depends on the symmetry of the initial state and the final state. The symmetry can also show the signatures of electronic configuration interaction [28]. By tracing the symmetry properties of each dissociation channel, the emission pattern can be identified. For the high KERs N^+ fragments with KER near 7 eV prefer to dissociate perpendicular to the polarization of the XUV laser pulse. The transition pathway could be $X^1\Sigma_g^+ \rightarrow A^2\Pi_u$ or $D^2\Pi_g \rightarrow 3^2\Sigma_g^+$. From this transition pathway, the symmetry of molecular states is $\Sigma \rightarrow \Pi \rightarrow \Sigma$, thus a perpendicular transition took place. Moreover, the N(1,1) fragments with a KER less than 10 eV also favor the perpendicular explosion instead of the parallel explosion. Taking the state $A^1\Pi_u$ of N_2^{2+} for example, the possible transition pathway is $X^1\Sigma_g^+ \rightarrow A^2\Pi_u \rightarrow A^1\Pi_u$. Considering the perpendicular transition of the Coulomb explosion fragments of N(1,1) with KERs of 6-10 eV, the dissociative states $D^3\Pi_g$ and $c^1\Delta_g$ are attributed to the KER spectra peaked at 8.0 and 8.1 eV, respectively. The non-coincident N^{2+} ionic fragments with the lower KERs (0-10 eV) dissociate in perpendicular direction while the higher KER (10-20 eV) ionic fragments dissociate parallel to the polarization direction. Depending on the symmetry property of each transition and photon absorption

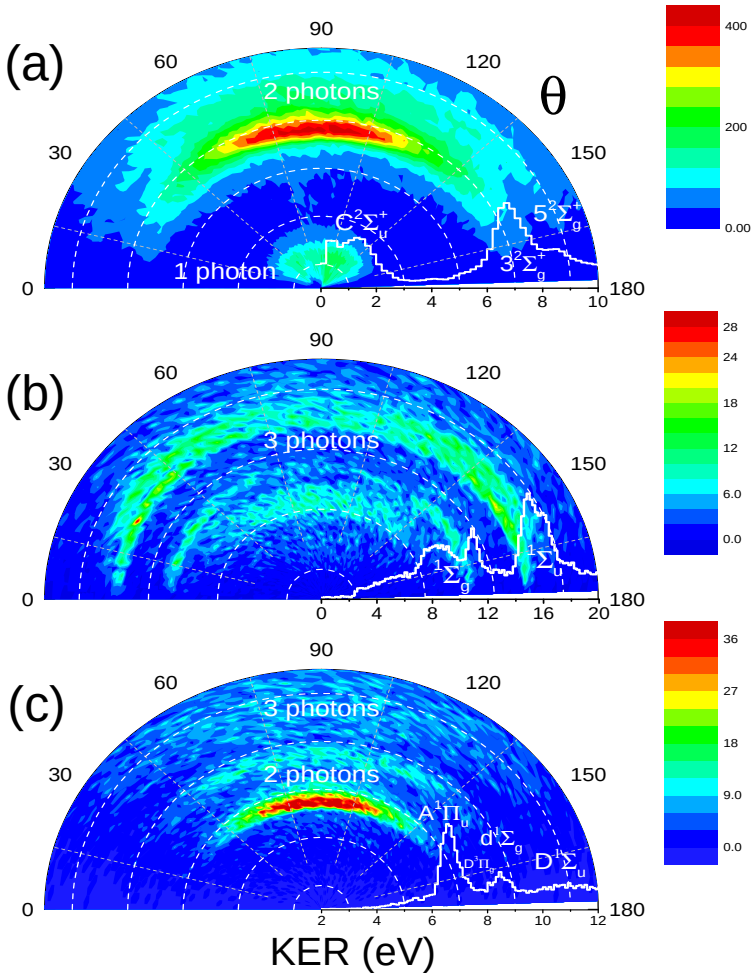

Figure 6.19: FIAD polar density plots differential in the KERs for various dissociation channels. (a-c) The angular distribution of ionic fragments of N(1,0), N(2,0) and N(1,1), respectively. θ represents the angle with respect to the polarization of the FEL laser pulse (horizontal). The radius stands for the KER of each channel. The final dissociative states with corresponding KERs of each channel are labeled.

steps, the aligned N_2^{n+} ions created and characterized by different KERs. The ionic fragments are aligned or oriented by their ionization steps. If we trace the final dissociative states in the XUV with NIR laser fields, we find that the enhanced fragments mainly come from the perpendicular explosion. It means that the final ejected ionic fragments which are emitted along the polarization of the NIR laser are more likely to be further enhanced.

Enhancement of Ionization

Litvinyuk *et al.* measured the ionization yield of N_2 for two molecular alignment distribution and found that ionization is about 4 times more likely for molecules aligned parallel to the laser field than for molecules perpendicular to it [182, 183]. In Ref. [184], the significance of alignment in molecular ionization was reported. The probability of ionization is related to the alignment of the molecular axis with respect to the polarization of the probe laser field. The polarized laser pulse influenced the following dissociation process and aligned the molecule [53, 182]. From the ionization yield spectra shown in

Fig. 6.14 and Fig. 6.17, the enhancement factor is 2.2 for N(1,1) (6 eV< KER < 10 eV), and the enhancement factor is 5.7 for N(2,1) (KER below 18 eV). The higher charge states of the molecular ions, the more enhanced they are in the delayed NIR laser field.

According to Coulomb's law, we estimate the nuclear distance R_c to be 2.15 Å for N(1,1) with a KER of 6.7 eV and 2.13 Å for N(2,1) with KER of 13.5 eV, respectively. As shown in Fig. 6.20, the transition possibility of the electron in the molecular system is proportional to the charge and alignment between the molecular axis and the polarization of the laser field [185]. At a short nuclear distance (R $\leqslant$ 4.5 Å), the A_2^{3+} and A_2^{7+} ions show strongly enhanced ionization in the same regime of internuclear distances. For higher charge molecular states the enhancement is more significant.

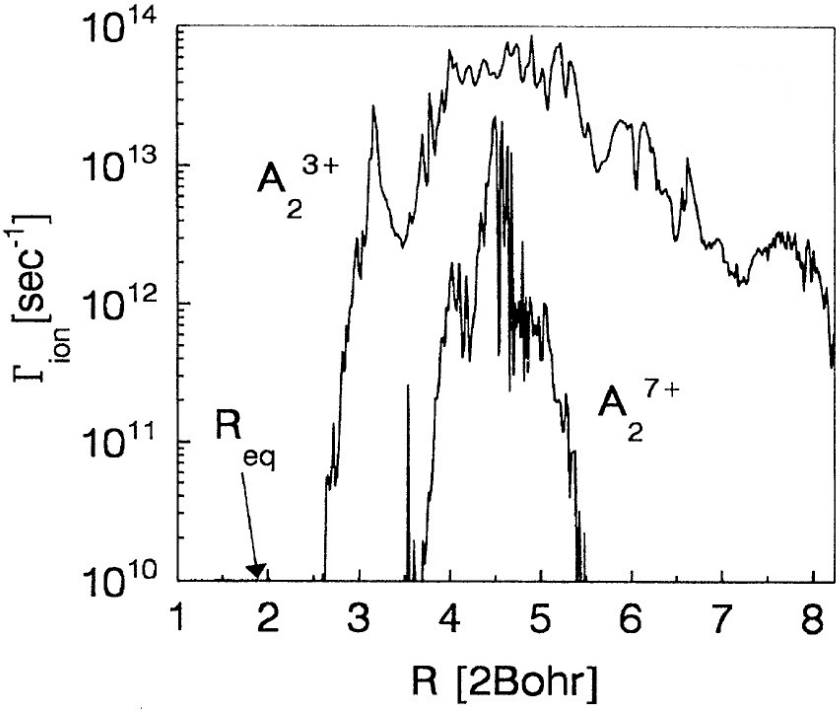

Figure 6.20: Ionization rate Γ_{ion} as a function of the internuclear distance R for A_2^{3+} and A_2^{7+} ions. Figure is taken from Ref. [185].

As mentioned in Sec. 2.7, for few-XUV-photon absorption, the FIADs can be characterized by a multiple expansion regarding Legendre polynomial:

$$\frac{d\sigma}{d\Omega}(\hbar\omega,\theta) = \frac{\sigma}{4\pi}\left[1+\sum_{i\cdots n}^{n}\beta_{2i}P_{2i}(cos\theta)\right], \tag{6.21}$$

where n is the number of absorbed photons, θ is the angle between the polarization axis of the laser field and the molecular axis, and β_i are anisotropy parameters [86]. Since we identified that two XUV photons are required to create the higher KER N^+ ions, and three XUV photons are needed to produce the higher KER N^{2+} ions. Therefore, we use Eq. 6.21 to fit the angular distribution of the ionic fragments from different dissociation processes by considering the photon absorption steps.

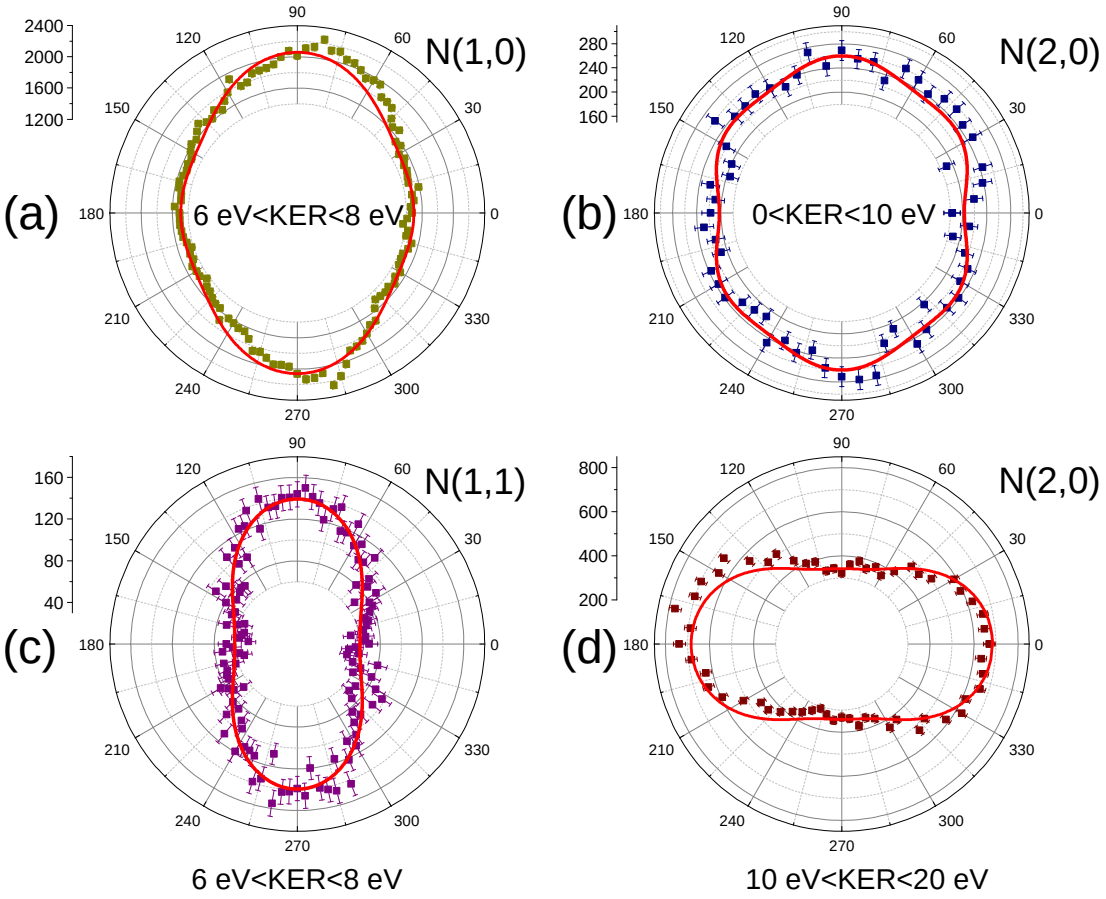

Figure 6.21: Angular distribution of (a) non-coincident N^+ with a KER of 6-8 eV, (b) the lower KERs non-coincident N^{2+} ions, (c) the coincident N(1,1) with a KER of 6.7 eV, and (d) the large KERs non-coincident N^{2+} ions. The polarization of the XUV laser pulse is along the horizontal direction. The angular distributions of ionic fragments are fitted by Eq. 6.21. The red lines are the fit results.

The corresponding fit results are shown in Fig. 6.21. We identified that only the perpendicular explosion fragments instead of the parallel explosion fragments are enhanced in the delayed NIR laser field. Moreover, we find that the enhancement factor can be characterized by the relative distribution of the perpendicular direction over parallel direction. Here, we define the enhancement factor: $A = Y(\perp)/Y(\parallel)$ to find the perpendicular alignment to parallel alignment ratio, where $Y(\perp)$ stands for the statistics of the emitted ionic fragments perpendicular to the polarization of the XUV laser pulse and $Y(\parallel)$ stands for the statistics of the emitted ionic fragments parallel to the polarization of the XUV laser pulse. For the non-coincident N^+ ions (KER 6-10 eV), at the FEL light intensities $I \approx 10^{13}$ W/cm^2, the measured factor A is 1.38 $\pm$ 0.01. For the non-coincident N^{2+} ions, A is 1.28 $\pm$ 0.01, this factor is little smaller than the total enhancement for N^{2+} of 1.7[2]. We interpret that other channels also have a contribution to the perpendicular alignment. For the coincident channel N(1,1), the ionization ratio A is 2.3 $\pm$ 0.1 in the XUV laser field.

[2]This comes from the calculation of Y(IR-late)/Y(IR-early) of the total ion yield of N^{2+}.

However, we find the high KER (10-20 eV) N^{2+} ions belong to a parallel alignment which cannot be further ionized by a delayed NIR laser pulse. Therefore, the alignment ratio can be used to characterize how much the dissociated fragments enhanced in the presence of the NIR laser field. In summary, in this section, we have identified that the molecule aligned parallel to the polarization of the NIR laser field are more likely to ionized than those aligned perpendicularly. As the detailed theoretical explanation, we assume that the molecular ADK theory may be applied to calculate the enhancement of ionization in N_2 [174].

6.5 Conclusion

In this chapter, the detailed dissociative channels in N_2 after the absorption one or several XUV photons were studied by employing the time-, energy-, and angular-resolved ion spectroscopy. With an XUV-pump/IR-probe experimental scheme, the time-dependent ions spectroscopy were obtained. By tracing the KERs of double ionization and triple ionization as a function of the time delay, we found the enhancement factor for the double ionization to be 2.2 and for triple ionization N(2,1) to be 5.7. Moreover, the higher charge molecular ions, the more enhanced ionization in the two-color laser fields. Within a short nuclear separation ($R \leqslant 4.5$ Å), the aligned higher charge ions have gained more enhancement compared to the lower charge ions which can be used to explain the different enhancement factors for N(1,1) and N(2,1) [182, 185]. The aligned N_2^{n+} ions created by sequential absorption of XUV photons and further excited or ionized them by a delayed NIR laser pulse. The transition pathways can be traced via the KERs and angular distribution of ionic fragments. In addition, the parallel and perpendicular transition for the formation of various charge molecular ions can be identified and traced. Because the polarization of the XUV laser pulse was perpendicular to that of the NIR laser pulse, only the perpendicularly aligned dissociating fragments prepared by the first incoming XUV laser pulse were ionized with an enhanced ionization yield in the delayed NIR laser field.

The research on multielectron dissociative ionization of diatomic molecules is of importance to shed more light into the correlated electron dynamics and highly excited states during the multiphoton ionization process [28]. In order to thoroughly understand the complex molecular dynamics in two-color laser fields, more advanced theory is required. In the future, ion-electron coincidence measurement with shorter laser pulses will be able to provide more information on the intermediate states involved. The electron emission pattern and the evolution of the electronic configuration interaction after X-ray radiation can be traced and controlled by adjusting the relative polarization degree of the two laser pulses [186]. The experiment is proposed to be performed at the updated FLASH2 [22] to find the detailed steps of sequential photon absorption and the influence of angular alignment on the ionization of molecular systems.

Chapter 7

Summary and Outlook

The understanding of how high-intensity FEL radiation interacts with matter is a subject of fundamental interest which has attracted considerable experimental and theoretical research in the past. In this dissertation, two-color pump-probe experiments on small diatomic molecules have been carried out at Free-Electron Laser FLASH to explore the processes of photoionization, fragmentation, and relaxation in molecular systems. The delivered sub-100 fs XUV laser pulses with high intensities are used to initiate ultrafast molecular dynamics. The probe-laser pulse can probe and map the following fragmentation and relaxation processes.

In order to properly describe and understand the molecular dynamics induced by XUV radiation, the underlying theoretical description of photon-matter interaction, photoionization mechanisms, and the relaxation dynamics was summarized in Chapter 2. A brief description of the light sources and the experimental set-ups were given in Chapter 3. In order to perform the two-color pump-probe experiments, the split-and-delay unit was installed to adjust the time delay between the pump- and probe-pulse. This setup was combined with a reaction microscope that allowed us to reconstruct the three-dimensional momentum of ions and electrons from the photon interaction between small molecular systems and the XUV radiation. Thus, the time-resolved imaging of XUV-induced fragmentation and relaxation dynamics in small molecular systems can be obtained. In the following, the conclusions of the time-resolved experiments are summarized.

7.1 Summary of Oxygen Experiments

Using the synchronized THz light source provided by the FLASH facility in combination with the XUV radiation, the XUV-pump/THz-probe experiments on O_2 were performed. We have extended the well-established Attosecond metrology to an XUV-pump/THz-probe approach [126]. The basic idea of the streaking experiment is to monitor the momentum or energy of photoelectrons as a function of the time delay between the XUV laser pulse and THz pulse. The phase difference in streaking traces of photoelectrons carried the information about photoemission time delays and lifetimes of autoionization. In this experiment, the photoionization and relaxation of O_2 after the absorption of a single

XUV photon was investigated.

First, in Chapter 4, the principle of THz streaking and photoionization time delays were introduced. The Fourier series of triangle functions were used to fit the temporal profile of the momenta trace of the first emitted photoelectrons. Therefore, the basic experimental parameters of the THz pulse were characterized. The wavelength of the THz pulse is 154.2 $\pm$1.1 μm, and the period of one cycle of the THz pulse is 514 ± 3.6 fs. The maximum momentum shift of a photoelectron is 0.044 ± 0.002 a.u. We used the THz streaking technique to trace the photoemission time delays and found all the low-energetic photoelectrons (kinetic energies less than 4 eV) have a time shift of 23.9 ± 6.4 fs compared with the fast photoelectrons. The reason for this shift comes from the THz probing field induced time shift. Furthermore, we obtained the energy-dependent time shifts up to 60 fs in the emission of photoelectrons from autoionization and direct ionization.

Second, in Chapter 5, the photoionization and autoionization processes of O_2 were investigated. In the first place, by tracing kinetic energies of the ions and KER distribution of the ion pairs, the direct single and double ionization were determined. In the following, an autoionizing excited cationic state has been identified and traced. The fundamental two-step reaction pathway can be assigned to the autoionization process: $O_2 + \hbar\omega(XUV) \rightarrow O_2^{+*} + e_1^-$, subsequently, the autoionization of excited cation state took place: $O_2^{+*} \rightarrow O^+ + O^+ + e_2^-$. e_1^- and e_2^- are the first emitted photoelectron and secondary autoionization electron, respectively. By comparing the relative time shift between the "fast" photoelectron e_1^- and "slow" secondary autoionization electron e_2^- from their momentum traces, we can obtain the lifetime of autoionization process. Two dissociative states $C^4\Sigma_u^-$ and $^4\Sigma_g^-$ can be assigned to explain the production of the ions with KER of 4 eV. The formation of state $C^4\Sigma_u^-$ is a single ionization process and thereby the first emitted photoelectron has no time shift. However, we observed a time shift of 102 ± 30 fs between the low-energetic electrons and the first emitted photoelectrons. Therefore, those electrons must be from an autoionization process, namely, from the autoionizing molecular cation state $O_2^{+*}(^4\Sigma_g^-)$. The binding energy of $^4\Sigma_g^-$ is 38.7 eV, thus the corresponding the kinetic energy of the first emitted photoelectron is 21.3 eV which is in good agreement with the measured kinetic energy of the first emitted photoelectron at 21.3 ± 0.2 eV. In the end, the relaxation pathways were presented to illustrate the formation and autoionization processes of the state $^4\Sigma_g^-$. This excited state autoionized to the dissociation limit $O^+(^4S)/O^+(^4S)$ at large internuclear distance around 30 Å. The measured experimental results are in excellent agreement with previous works [12, 49].

7.2 Summary of Nitrogen Experiments

We used 28.3 $\pm$ 0.5 eV XUV laser pulses with the pulse length of approximately 100 fs to ionize N_2 and the subsequent molecular dynamics was probed by a delayed NIR laser ($\lambda = 800$ nm, pulse length 350 fs). The FEL intensity was estimated to be up to 3×10^{13} W/cm^2 and the NIR laser intensity was reached about $5 \times 10^{13} - 3 \times 10^{14}$ W/cm^2. In the experiment, the various dissociative channels in N_2 after absorption one or several XUV photons were studied by employing time-, energy-, and angular-resolved ion spectroscopy.

First, the photoionization and dissociation of N_2 in the NIR laser field were discussed. The corresponding Keldysh parameter is 0.7 ($I_{NIR} \sim 2.56 \times 10^{14}$ W/cm^2). Thus, the rescattering process was used to explain the double ionization of the molecule in the NIR laser field. The molecule was ionized from the neutral ground state to an excited state and then the outgoing electron re-scattered with the parent ion, which resulted in the double ionization of the molecule. From the angular dependence of non-coincident N^+ ions, it is straightforward to expect that ionic fragments dissociated along the polarization of the NIR laser field.

Second, the FEL light intensity dependence for various dissociation channels of N_2 was investigated. Two XUV photons absorption is the dominant process for the double ionization. Besides, three XUV photons are required to create the N^{2+} ions. Surprisingly, five XUV photons were absorbed to triply ionize the molecule rather than three XUV photons via a vertical transition. Thus, the sequential ionization was identified to be the dominant and effective multiphoton absorption pathway for molecules in the XUV regime.

Third, the experimental results of the XUV-pump/IR-probe experiment were shown. The yields of multiply charged N_2^{n+} ions were measured as a function of the time delays and the light intensities. The temporal resolution of the present experiment was determined to be 545 ± 133 fs by using an error function to fit the time-dependent yields of non-coincident N^+ ions and N^{2+} ions. By tracing the time-dependent ions spectroscopy, with the delayed NIR laser pulse, the double ionization was enhanced by a factor of 2.2. For triple ionization, the enhancement factor was 5.7. Few-photon absorption pathways were traced by inspecting KERs and ionic fragment angular distributions. By tracing the formation of the various molecular ions, we found the excited states prepared by the first incoming XUV laser pulse can be further excited or ionized by a delayed NIR laser pulse. Moreover, only the perpendicular Coulomb explosion fragments induced by the first XUV laser pulse were more likely to be further enhanced in the delayed NIR laser field. Finally, we found the enhancement ionization is related to the alignment of the molecule with respect to the polarization of the NIR laser pulse.

7.3 Outlook

In order to fully understand the observed dynamic evolution of highly excited molecular states, more advanced theory will be required. A reliable quantum chemistry calculation by taking the strong electron-electron and electron-nuclear couplings into account is needed. For instance, the calculation of potential energy curves and the simulation of the subsequent fragmentation of the highly excited states after the molecule absorption of one or more photons, are welcomed.

A REMI was installed as a permanent endstation at FLASH2. In the future, we will use a newly updated split-and-delay optics in combination with the REMI to perform the time-resolved experiments on more complex molecular systems. First, the wavelength provided by FLASH2 is easily and quickly tuned by the flexible undulator gap [22]. By changing the wavelengths of the XUV radiation, we can perform resonant excitation experiments to trace the autoionization of Rydberg states in molecular or dimer sys-

tems [151]. Furthermore, the multidimensional transient spectroscopy of molecular systems can be obtained. Second, a new high repetition (up to 50 kHz) sub-20 femtoseconds optical laser in combination with XUV radiation which enables us to perform XUV/IR pump-probe experiments or XUV/UV pump-probe experiments [22]. For instance, the proposed ion-electron coincidence measurement of N_2 is planned to extract the valuable information about photoelectron emission patterns after the molecule absorbs one or more photons. Then we can enhance the understanding of the laser-induced electronic rearrangement from the angular distribution of electrons. From the angular dependence of ionization, we can monitor the accurate transition by varying the laser intensity and rotating the NIR polarization by from 0° to 90° with respect to the XUV laser pulse which will shed light into control the few-body quantum dynamics in the near future. Third, in cooperation with a group at Hanover University, an HHG source will be integrated into the REMI beamline FL26 [55, 187]. A combination of HHG- and FEL-based light sources exploiting the specific advantages of each will open up additional possibilities to address the most fundamental dynamics of matter [42]. In this case, we are able to extend femtosecond spectroscopy to attosecond spectroscopy on electronic dynamics. To this end, we can understand the attosecond dynamics of electrons in atomic and molecular systems. Over the coming years, with the development of FELs, an increased repetition rate, reduced pulse duration, and spectral stability XUV radiation light sources would improve most existing ultrafast X-ray pump-probe schemes [1,42]. The molecular breathing dynamics [188], hydrogen migration in the ethanol cation and dication [189], the ring formation in hydrocarbonic cations [190], and ICD process in biological molecules [191] and so on, may be possible carried out at FLASH2.

Appendix A

Appendix

A.1 Atomic Units

In the course of experiments and data analysis, the units conversion is frequently used. The conversion factors are listed as follows. Taken from Ref. [7].

Base units and natural constants

$\hbar = m_e v_e r_e = 1\,a.u.$	Reduced Planck constant
$c = e^2/(\hbar\alpha) = 137\,a.u.$	Speed of light
$r_e = 1 a.u. = 5.2918 \cdot 10^{-11}\,m$	Bohr radius
$m_e = 1 a.u. = 9.1095 \cdot 10^{-31}\,kg$	Rest mass of the electron
$q_e = e = 1\,a.u. = 1.6022 \cdot 10^{-19}\,As$	Charge of the electron
$e/{r_e}^2 = 1\,a.u. = 5.14 \cdot 10^{9}\,V/cm$	Electric field

The conversion factors to other common units are:

Time	$t[s] = 4.134 \cdot 10^{16} \cdot t[a.u.]$
Momentum	$p[Ns] = 1.995 \cdot 10^{-24} \cdot p[a.u.]$
Energy	$E[eV] = 27.21 \cdot E[a.u.]$
Velocity	$v_e = 1\,a.u. = 2.1877 \cdot 10^{6}\,m/s$
Magnetic field	$1\,a.u. = 2.35 \cdot 10^{5}\,Tesla$
Max. ele. field strength in a laser pulse	$1\,a.u. \hat{=} 3.51 \cdot 10^{16}\,W/cm^2$

A.2 Momentum Shift of Photoelectrons

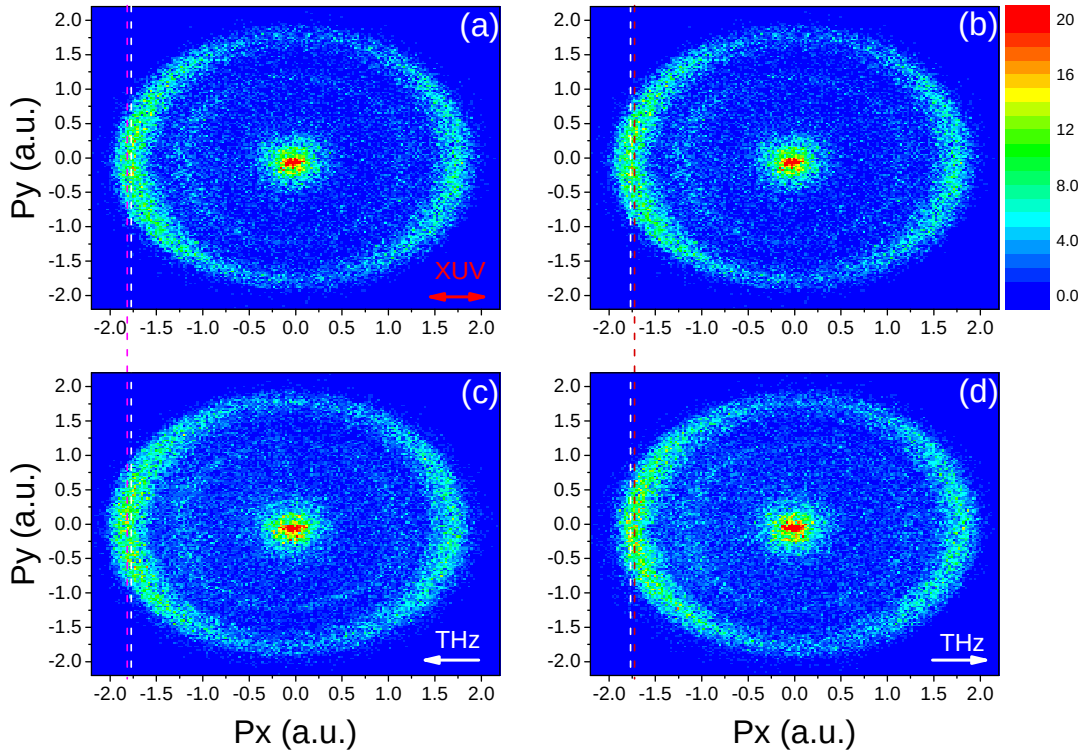

Figure A.1: Momentum distribution for (a,b) the un-streaked shift, (c) the maximum negative shift, and (d) the maximum positive shift, respectively. The white dashed lines note the unstreaked momentum peaked at -1.771 a.u., and the red dash lines note the negative peaked at -1.814 a.u. and positive shift peaked at -1.725 a.u. along the polarization of the THz electric field (polarized along Px).

A negative momentum shift (428.4 fs $\leq$ delay $\leq$ 488.4 fs) and a positive momentum shift (218.5 fs $\leq$ delay $\leq$ 278.5 fs) are displayed. For the negative momentum shift, we can observe a shift towards more negative Px for all the photoelectrons. For the positive momentum shift, accordingly, we observe a shift towards more positive values. The maximum momentum shifts are marked by using red-dashed lines. The maximum momentum shift is about 0.04 a.u. The maximum momentum shift is only observed for electrons emitted at the crest and trough of the THz vector potential.

A.3 Characterize the THz Pulse by Ions Momentum Trace

Considering the single XUV-photon ionization of O_2:

$$O_2 + \hbar\omega_{XUV} \rightarrow O_2^+ + e, \tag{A.1}$$

With momentum conservation, thus $\vec{P_{O_2^+}} + \vec{P_e} = 0$. As already discussed in Chapter 4, the THz vector potential has been characterized. It is straightforward that the vector potential can be mapped from the ions momentum trace. We can use the asymmetry distribution of the ionic fragments along the polarization of the THz pulse to map the vector potential. Namely, using the asymmetry parameter which is defined as below:

$$A = \frac{N_{\text{Down}} - N_{\text{Up}}}{N_{\text{Down}} + N_{\text{Up}}}, \tag{A.2}$$

where N_{Down} is the number of counted ions with the momenta less than zero, and N_{Up} is the number of counted ions with the momenta larger than zero. The fit results are shown in Fig. A.2.

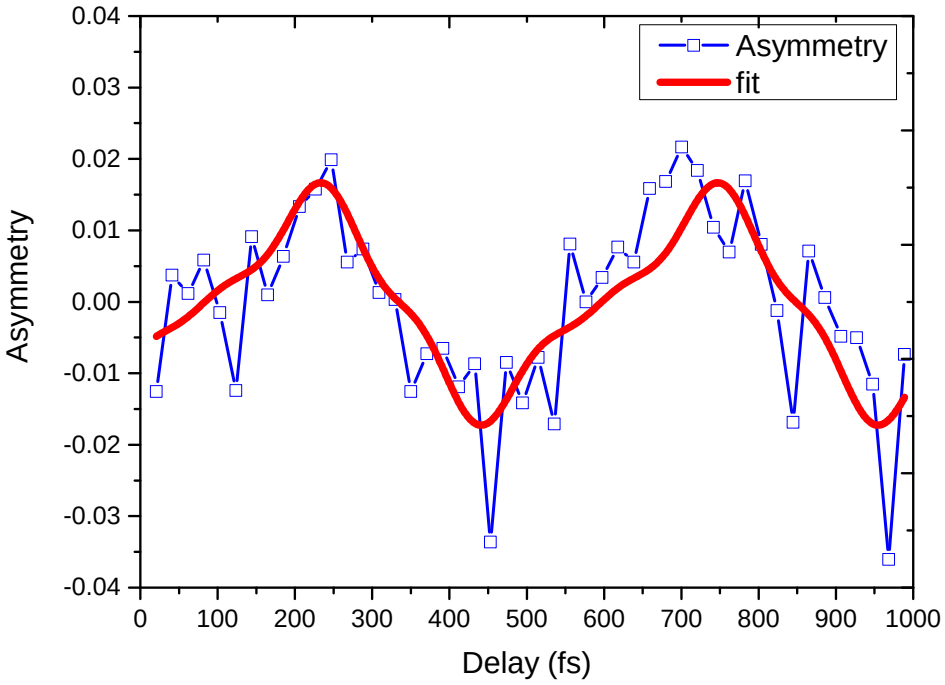

Figure A.2: Using Fourier series of triangle functions to fit the asymmetry parameter of O_2^+ molecular ion.

Here the maximum asymmetry is 0.01314, and the initial phase with respect to the results of electron momenta fitting is $\Delta\tau = 16.0 \pm 8.7$ fs. We interpret it that the momentum resolution of the ions is worse than the electrons'.

A.4 N_2 Molecular Orbital

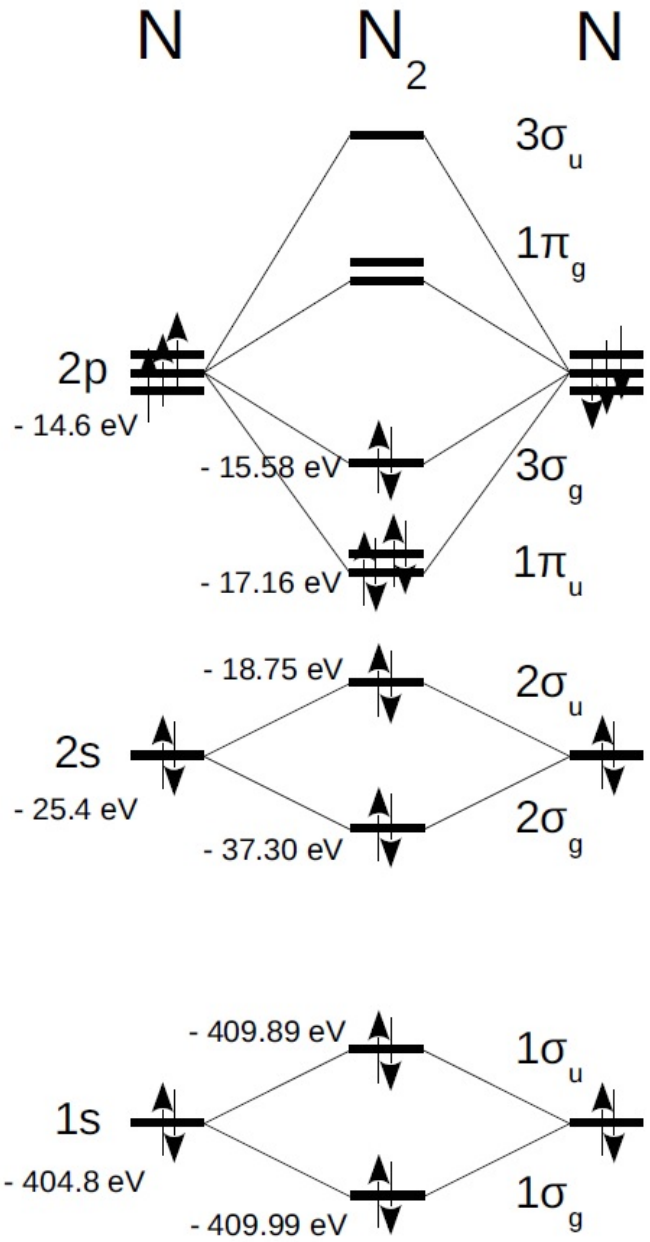

Figure A.3: Molecular orbital diagram for the $^1\Sigma_g$ ground state of N_2 [176].

A.5 Dissociative States of N_2^{n+} Ions

Table A.1: Electronic states of the dissociative states of N_2^{n+} ions. Adapted from Refs. [82, 170, 172, 177, 181]. The ground state electronic configuration of N_2 is known to be $(1\sigma_g)^2(1\sigma_u)^2(2\sigma_g)^2(2\sigma_u)^2(1\pi_u)^4(3\sigma_g)^2$ [176].

Molecular ion	State	Major configuration	KER (eV)	Final state
N_2^+	$C^2\Sigma_u^+$	$(3\sigma_g)^{-1}(1\pi_u)^{-1}(1\pi_g)^1$	0.6-1.3	$N^+(^3P) + N(^4S)$
	$D^2\Pi_g$	$(2\sigma_u)^{-1}(1\pi_u)^{-1}(1\pi_g)^1$	1.7	$N^+(^3P) + N(^4S)$
	$3^2\Sigma_u^+$	$(2\sigma_g)^{-1}$	5.3	$N^+(^3P) + N(^2D)$
	$3^2\Sigma_g^+$	$(2\sigma_g)^{-1}$	6.7	$N^+(^3P) + N(^2D)$
	$5^2\Sigma_g^+$	$(2\sigma_g)^{-1}$	11.4	$N^+(^3P) + N(^2D)$
	$5^2\Sigma_g^+$	$(2\sigma_g)^{-1}$	9.4	$N^+(^1D) + N(^2D)$
	$5^2\Sigma_g^+$	$(2\sigma_g)^{-1}$	8.2	$N^+(^1D) + N(^2P)$
N_2^{2+}	$A^1\Pi_u$	$\pi_u^{-1}3\sigma_g^{-1}$	6.7	$N^+(^3P) + N^+(^3P)$
	$D^3\Pi_g$	$\pi_u^{-2}3\sigma_g^0\pi_g^1$	8.0	$N^+(^3P) + N^+(^3P)$
	$c^1\Delta_g$	π_u^{-2}	8.1	$N^+(^3P) + N^+(^3P)$
	$d^1\Sigma_g^+$	$\pi_u^{-2}3\sigma_g^0$	8.4	$N^+(^3P) + N^+(^3P)$
	$D^1\Sigma_u^+$	$\pi_u^{-2}3\sigma_g^0\pi_g^1$	10.4	$N^+(^3P) + N^+(^1D)$
	$D^1\Sigma_u^+$	$\pi_u^{-2}3\sigma_g^0\pi_g^1$	12.2	$N^+(^3P) + N^+(^3P)$
N_2^{2+*}	$^1\Sigma_g$	$2\sigma_g^{-1}3\sigma_g^{-1}$	8.4	$N^{2+}(^2P) + N(^2D)$
	$^1\Sigma_u$	$2\sigma_g^{-1}3\sigma_u^{-1}$	10.6	$N^{2+}(^2P) + N(^4S)$
	$^1\Sigma_u$	$2\sigma_g^{-1}3\sigma_u^{-1}$	14.6	$N^{2+}(^2P) + N(^4S)$
	$^1\Pi_u$	$2\sigma_g^{-1}1\pi^{-1}$	16.2	$N^{2+}(^2P) + N(^2P)$
N_2^{3+}	$^2\Pi_u$	$2\sigma_u^{-1}1\pi_u^{-1}3\sigma_g^{-1}$	13.5	$N^{2+}(^2P) + N^+(^3P)$
	$^4\Sigma$	$2\sigma_u^{-1}1\pi_g^{-3}1\pi_u^1$	19.77	$N^{2+}(^2P) + N^+(^3P)$

A.6 Momentum Distribution of the Coulomb Explosion Fragments

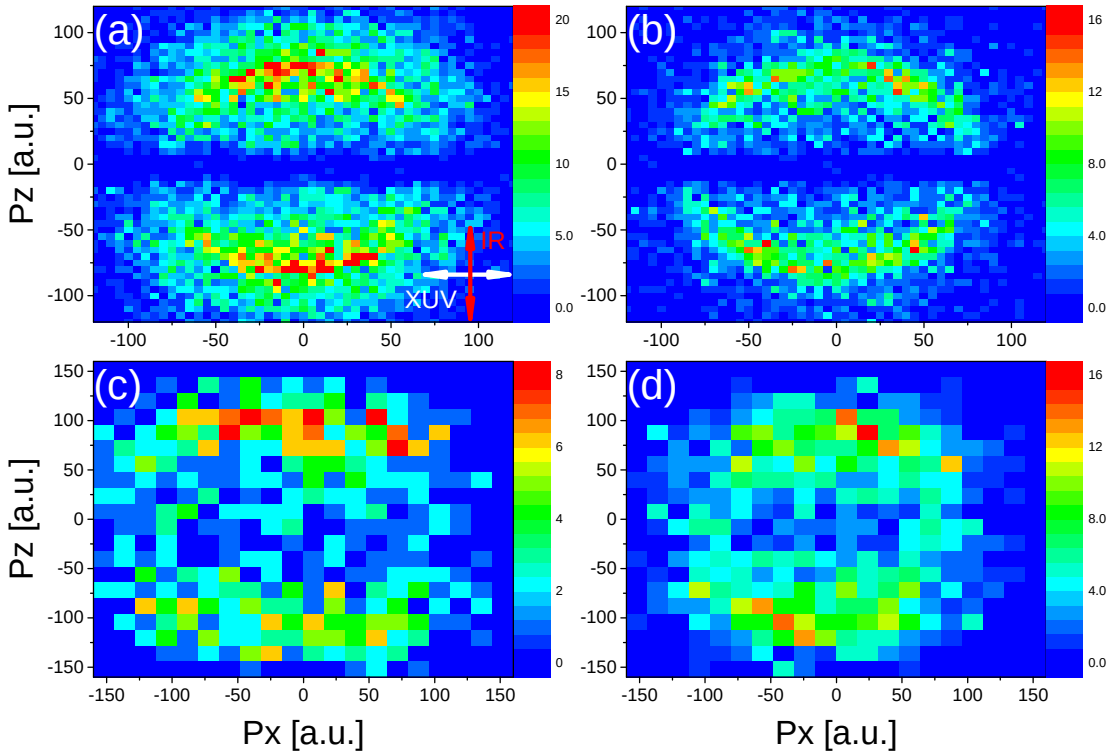

Figure A.4: For the N^+ ion in N(1,1) from Coulomb explosion with the infrared pulse well before the XUV pulse (a), and with the two pulses temporally overlapped (b). (c,d) Similar to a and b, but for the N^+ ion in N(2,1). The white and the red arrows mark the XUV and NIR polarization, respectively.

List of Publications

Parts of this work have been published or prepared in the following references:
Y.F. Liu, K. Schnorr, G. Schmid, S. Augustin, S. Meister, H. Lindenblatt, A. Rudenko, M. Kübel, C. Burger, N. Stojanovic, R. Treusch, S. Düsterer, T. Jahnke, M.F. Kling, C.D. Schröter, T. Pfeifer and R. Moshammer. *THz Streaking of the Autoionization Dynamics of O_2 at the Free-Electron-Laser FLASH*. Journal of Physics: Conf. Series **875** (2017) 032031.

Articles in preparation:
Y.F. Liu, K. Schnorr, G. Schmid, S. Augustin, T. Ding, S. Meister, H. Lindenblatt, Y.H. Jiang, R. Treusch, S. Düsterer, M. Gisselbrecht, C.D. Schröter, T. Pfeifer and R. Moshammer. *IR-assisted XUV multiphoton ionization of N_2 at FLASH*.

Y.F. Liu, K. Schnorr, G. Schmid, S. Augustin, S. Meister, H. Lindenblatt, A. Rudenko, M. Kübel, C. Burger, N. Stojanovic, R. Treusch, S. Düsterer, T. Jahnke, M.F. Kling, C.D. Schröter, T. Pfeifer and R. Moshammer. *THz streaking the Photoemission and Autoionization dynamics of O_2*.

Further publications with own contributions:

S. Augustin, M. Schulz, G. Schmid, K. Schnorr, E.V. Gryzlova, H. Lindenblatt, S. Meister, Y.F. Liu, F. Trost, L. Fechner, A.N. Grum-Grzhimailo, S.M. Burkov, M. Braune, R. Treusch, M. Gisselbrecht, C.D. Schröter, T. Pfeifer, R. Moshammer. *Signatures of autoionization in the angular electron distribution in two-photon double ionization of Ar*.
Phys. Rev. A. 98, 033408 (2018).

Georg Schmid, Kirsten Schnorr, Sven Augustin, Severin Meister, Hannes Lindenblatt, Florian Trost, YiFan Liu, Nikola Stojanovic, Alaa Al-Shemmary, Torsten Golz, Rolf Treusch, Michael Gensch, Matthias Kübel, Lutz Foucar, Artem Rudenko, Joachim Ullrich, C.D. Schröter, T. Pfeifer, R. Moshammer. *Terahertz field induced time shifts in atomic photoemission*.
Phys. Rev. Lett. 122, 073001(2019).

Georg Schmid, Kirsten Schnorr, Sven Augustin, Severin Meister, Hannes Lindenblatt, Florian Trost, YiFan Liu, Markus Braune, Rolf Treusch, C.D. Schröter, T. Pfeifer, R. Moshammer. *Reaction Microscope Endstation at FLASH2*.
J. Synchrotron Rad. (2019). 26, 854âĂŞ867

Georg Schmid, Kirsten Schnorr, Sven Augustin, Severin Meister, Hannes Lindenblatt, Florian Trost, YiFan Liu, Mathieu Gisselbrecht, Stefan Düsterer, Harald Redlin, Rolf Treusch, Tsveta Miteva, Kirill Gokhberg, Alexander I. Kuleff, Lorenz S. Cederbaum, Claus Dieter Schröter, Thomas Pfeifer, and Robert Moshammer. *Tracing Charge Transfer in Argon Dimers by XUV-Pump IR-Probe Experiments at FLASH*.
Journal of Chemical Physics (submitted).

Acknowledgements

In the end, I would like to express my sincere gratitude to the people who helped me to achieve this dissertation.

First of all, I am deeply grateful to my supervisor **Dr. Robert Moshammer** for accepting the risk of taking me as his Ph.D. student. His scientific insights and his powerful way of doing sciences have impressed me. I have learned so much from not only his scientific skills but also his noble personalities.

I want to express my deepest gratitude to **Prof. Dr. Thomas Pfeifer** not only for giving me the excellent opportunity to work in his group but also for the financial support in my Ph.D. study. Thanks a lot for many times discussions and suggestion.

A special thanks goes to **Prof. Dr. Andreas Wolf**, **Prof. Dr. Thomas Leisner**, and **Prof. Dr. Jörg Jäckel** to be my examiners.

Many thanks to **Prof. Dr. Yuhai Jiang** for providing me a chance to study at MPIK after two-years at the Shanghai Advanced Research Institute.

I want to show my gratitude to **Dr. Claus Dieter Schröter** for teaching me a lot of experimental techniques and the uncounted fruitful discussions.

I am very grateful to Dr. Georg Schmid, Dr. Kirsten Schnorr, and Dr. XueGuang Ren, for teaching me many skills to prepare the beamtime at FLASH and data analysis.

I should thank my family for supporting me to finish my Ph.D. work in Germany. Also, forgive me so many times I have no time to stay with them to celebrate family time.

I also want to thank many colleagues at MPIK, Niels Kurz, Dr. Nicolas Camus, Patrick Fross, Dr. Anne Harth, Hemkumar Srinivas, Florian Tross, Dr. Chunhai lvy, Dr. Shikha Bhadoria, Frans Schotsch, and Farshad Shobeiry, for helping me to review the thesis. Thanks a lot to FLASH-REMI colleagues who have never hesitated to offer me warm-hearted help at all time. Finally, I want to thank all members and colleagues of the group of Prof. Dr. Thomas Pfeifer for the friendly discussions as well as the help they gave me in many ways.

Bibliography

[1] J. Ullrich, A. Rudenko, and R. Moshammer.
Free-Electron Lasers: New Avenues in Molecular Physics and Photochemistry.
Annual Review of Physical Chemistry **63**, 635–660 (2012).

[2] A. Einstein.
Über einen die Erzeugung und Verwandlung des Lichtes betreffenden heuristischen Gesichtspunkt.
Annalen der Physik **322**, 132–148 (1905).

[3] C. Neidel.
Attosecond time-resolved experiments - towards biomolecules.
PhD Thesis, Humboldt Universität, Berlin (2017).

[4] A. Einstein.
Zur Quantentheorie der Strahlung.
Phys. Z. **18**, 121–128 (1917).

[5] T. H. Maiman.
Stimulated Optical Radiation in Ruby.
Nature **187**, 493–494 (1960).

[6] L. V. Keldysh.
Ionization in the field of a strong electromagnetic wave.
Soviet Physics JETP **20**, 1307 (1965).

[7] N. Camus.
Non-sequential double ionization of atoms with phase-controlled ultra-short laser pulses.
PhD Thesis, Ruprecht-Karls-Universität, Heidelberg (2013).

[8] L. Fechner.
High resolution experiments on strong-field ionization of atoms and molecules:test of tunneling theory, the role of doubly excited states, and channel-selective electron spectra.
PhD Thesis, Ruprecht-Karls-Universität, Heidelberg (2014).

[9] R. Dörner, T. Weber, M. Weckenbrock, A. Staudte, M. Hattass, R. Moshammer, J. Ullrich, and H. Schmidt-B"ocking.
Multiple Ionization in Strong Laser Fields.
Advances in Atomic and Molecular Physics (2002).

[10] M. Uiberacker, T. Uphues, M. Schultze, A. J. Verhoef, V. Yakovlev, M. F. Kling, J. Rauschenberger, N. M. Kabachnik, H. Schroder, M. Lezius, K. L. Kompa, H. G. Muller, M. J. J. Vrakking, S. Hendel, U. Kleineberg, U. Heinzmann, M. Drescher, and F. Krausz.
Attosecond real-time observation of electron tunnelling in atoms.
Nature **446**, 627–632 (2007).

[11] A. A. Wills, A. A. Cafolla, and J. Comer.
The production of autoionizing states of atomic oxygen by the photodissociation of O_2.
Journal of Physics B: Atomic, Molecular and Optical Physics **24**, 3989 (1991).

[12] A. S. Sandhu, E. Gagnon, R. Santra, V. Sharma, W. Li, P. Ho, P. Ranitovic, C. L. Cocke, M. M. Murnane, and H. C. Kapteyn.

Observing the Creation of Electronic Feshbach Resonances in Soft X-ray–Induced O_2 Dissociation.
Science **322**, 1081–1085 (2008).

[13] W. Cao, S. De, K. P. Singh, S. Chen, M. S. Schöffler, A. S. Alnaser, I. A. Bocharova, G. Laurent, D. Ray, S. Zherebtsov, M. F. Kling, I. Ben-Itzhak, I. V. Litvinyuk, A. Belkacem, T. Osipov, T. Rescigno, and C. L. Cocke.
Dynamic modification of the fragmentation of CO^{q+} excited states generated with high-order harmonics.
Phys. Rev. A **82**, 043410 (2010).

[14] E. Gagnon, V. Sharma, W. Li, R. Santra, P. Ho, P. Ranitovic, C. Cocke, M. Murnane, H. Kapteyn, and A. Sandhu.
Autoionization dynamics and Feshbach resonances: Femtosecond EUV study of O_2 excitation and dissociation.
Journal of Physics: Conference Series **194** (2009).

[15] R. Santra, J. Zobeley, L. S. Cederbaum, and N. Moiseyev.
Interatomic Coulombic decay in van der Waals clusters and impact of nuclear motion.
Phys. Rev. Lett. **85**, 4490–4493 (2000).

[16] K. Schnorr.
XUV Pump-Probe Experiments on Electron Rearrangement and Interatomic Coulombic Decay in Diatomic Molecules.
PhD Thesis, Ruprecht-Karls-Universität, Heidelberg (2014).

[17] T. Jahnke.
Interatomic Coulombic Decay: Experimentelle Untersuchung eines neuartigen, interatomaren Abregungsmechanismus.
PhD Thesis, Johann-Wolfgang-Goethe-Universität Frankfurt am Main (2005).

[18] S. Chelkowski, P. B. Corkum, and A. D. Bandrauk.
Femtosecond Coulomb Explosion Imaging of Vibrational Wave Functions.
Phys. Rev. Lett. **82**, 3416–3419 (1999).

[19] M. Born and R. Oppenheimer.
Zur Quantentheorie der Molekeln.
Annalen der Physik **389**, 457–484 (1927).

[20] E. U. Condon.
Nuclear Motions Associated with Electron Transitions in Diatomic Molecules.
Phys. Rev. **32**, 858–872 (Dec 1928).

[21] B. M. D. Erk.
Fragmentation Dynamics of Small Molecules upon Multiple Ionization by X-Ray Free-Electron Laser Pulses.
PhD Thesis, Ruprecht-Karls-Universität, Heidelberg (2013).

[22] Deutsches-Elektronen-Synchrotron.
Free-electron laser FLASH.
`https://flash.desy.de/`.

[23] J. Ullrich, R. Moshammer, A. Dorn, R. Dörner, L. P. H. Schmidt, and H. Schmidt-Böcking.
Recoil-ion and electron momentum spectroscopy: reaction-microscopes.
Reports on Progress in Physics **66**, 1463 (2003).

[24] Y. H. Jiang, A. Rudenko, M. Kurka, K. U. Kühnel, L. Foucar, T. Ergler, S. Lüdemann, K. Zrost, T. Ferger, D. Fischer, A. Dorn, J. Titze, T. Jahnke, M. Schöffler, S. Schössler, T. Havermeier, M. Smolarski, K. Cole, R. Dörner, T. J. M. Zouros, S. Düsterer, R. Treusch, M. Gensch, C. D. Schröter, R. Moshammer, and J. Ullrich.
EUV-photon-induced multiple ionization and fragmentation dynamics: from atoms to molecules.
Journal of Physics B: Atomic, Molecular and Optical Physics **42**, 134012 (2009).

[25] T. Ergler, B. Feuerstein, A. Rudenko, K. Zrost, C. D. Schröter, R. Moshammer, and J. Ullrich.
Quantum-Phase Resolved Mapping of Ground-State Vibrational D_2 Wave Packets via Selective Depletion in Intense Laser Pulses.
Phys. Rev. Lett. **97**, 103004 (Sep 2006).

[26] I. A. Bocharova, H. Mashiko, M. Magrakvelidze, D. Ray, P. Ranitovic, C. L. Cocke, and I. V. Litvinyuk.
Direct Coulomb-explosion imaging of coherent nuclear dynamics induced by few-cycle laser pulses in light and heavy hydrogen.
Phys. Rev. A **77**, 053407 (2008).

[27] M. Magrakvelidze, O. Herrwerth, Y. H. Jiang, A. Rudenko, M. Kurka, L. Foucar, K. U. Kühnel, M. Kübel, N. G. Johnson, C. D. Schröter, S. Düsterer, R. Treusch, M. Lezius, I. Ben-Itzhak, R. Moshammer, J. Ullrich, M. F. Kling, and U. Thumm.
Tracing nuclear-wave-packet dynamics in singly and doubly charged states of N_2 and O_2 with XUV-pump–XUV-probe experiments.
Phys. Rev. A **86**, 013415 (Jul 2012).

[28] X. Zhou, P. Ranitovic, C. W. Hogle, J. H. D. Eland, H. C. Kapteyn, and M. M. Murnane.
Probing and controlling non-Born-Oppenheimer dynamics in highly excited molecular ions.
Nat. Phys. **8**, 232 (2012).

[29] N. Berrah, L. Fang, B. F. Murphy, E. Kukk, T. Y. Osipov, R. Coffee, K. R. Ferguson, H. Xiong, J.-C. Castagna, V. S. Petrovic, S. C. Montero, and J. D. Bozek.
Two mirror X-ray pulse split and delay instrument for femtosecond time resolved investigations at the LCLS free electron laser facility.
Opt. Express **24**, 11768–11781 (May 2016).

[30] K. Nagaya, K. Motomura, E. Kukk, H. Fukuzawa, S. Wada, T. Tachibana, Y. Ito, S. Mondal, T. Sakai, K. Matsunami, R. Koga, S. Ohmura, Y. Takahashi, M. Kanno, A. Rudenko, C. Nicolas, X.-J. Liu, Y. Zhang, J. Chen, M. Anand, Y. H. Jiang, D.-E. Kim, K. Tono, M. Yabashi, H. Kono, C. Miron, M. Yao, and K. Ueda.
Ultrafast Dynamics of a Nucleobase Analogue Illuminated by a Short Intense X-ray Free Electron Laser Pulse.
Phys. Rev. X **6**, 021035 (Jun 2016).

[31] A. H. Zewail.
Femtochemistry: Atomic-Scale Dynamics of the Chemical Bond.
J. Phys. Chem. A **104**, 5660–5694 (2000).

[32] Deutsches-Elektronen-Synchrotron.
European X-ray free-electron laser.
`https://www.xfel.eu/facility/overview/index_eng.html`.

[33] P. Emma.
First lasing and operation of an angstrom-wavelength free-electron laser.
Nature Photonics **4**, 641–647 (2010).

[34] T. Ishikawa et al.
A compact X-ray free-electron laser emitting in the sub-angstrom region.
Nature Photonics **6**, 540–544 (2012).

[35] P. J. Ho, C. Bostedt, S. Schorb, and L. Young.
Theoretical Tracking of Resonance-Enhanced Multiple Ionization Pathways in X-ray Free-Electron Laser Pulses.
Phys. Rev. Lett. **113**, 253001 (Dec 2014).

[36] B. Erk, D. Rolles, L. Foucar, B. Rudek, S. W. Epp, M. Cryle, C. Bostedt, S. Schorb, J. Bozek, A. Rouzee, A. Hundertmark, T. Marchenko, M. Simon, F. Filsinger, L. Christensen, S. De, S. Trippel, J. Küpper, H. Stapelfeldt, S. Wada, K. Ueda, M. Swiggers, M. Messerschmidt, C. D. Schröter, R. Moshammer, I. Schlichting, J. Ullrich, and A. Rudenko.

Ultrafast Charge Rearrangement and Nuclear Dynamics upon Inner-Shell Multiple Ionization of Small Polyatomic Molecules.
Phys. Rev. Lett. **110**, 053003 (2013).

[37] F. Bencivenga, R. Cucini, F. Capotondi, A. Battistoni, R. Mincigrucci, E. Giangrisostomi, A. Gessini, M. Manfredda, I. P. Nikolov, E. Pedersoli, E. Principi, C. Svetina, P. Parisse, F. Casolari, M. B. Danailov, M. Kiskinova, and C. Masciovecchio.
Four-wave mixing experiments with extreme ultraviolet transient gratings.
Nature **520**, 205–208 (April 2015).

[38] S. Tanaka and S. Mukamel.
Coherent X-Ray Raman Spectroscopy: A Nonlinear Local Probe for Electronic Excitations.
Phys. Rev. Lett. **89**, 043001 (2002).

[39] L. Young, E. P. Kanter, B. Krassig, Y. Li, A. M. March, S. T. Pratt, R. Santra, S. H. Southworth, N. Rohringer, L. F. DiMauro, G. Doumy, C. A. Roedig, N. Berrah, L. Fang, M. Hoener, P. H. Bucksbaum, J. P. Cryan, S. Ghimire, J. M. Glownia, D. A. Reis, J. D. Bozek, C. Bostedt, and M. Messerschmidt.
Femtosecond electronic response of atoms to ultra-intense X-rays.
Nature **466**, 56–U66 (2010).

[40] T. Mazza, A. Karamatskou, M. Ilchen, S. Bakhtiarzadeh, A. J. Rafipoor, P. O'Keeffe, T. J. Kelly, N. Walsh, J. T. Costello, M. Meyer, and R. Santra.
Sensitivity of nonlinear photoionization to resonance substructure in collective excitation.
Nature Communications **6**, 6799 (April 2015).

[41] C. Bostedt, M. Adolph, E. Eremina, M. Hoener, D. Rupp, S. Schorb, H. Thomas, A. R. B. de Castro, and T. Möller.
Clusters in intense FLASH pulses: ultrafast ionization dynamics and electron emission studied with spectroscopic and scattering techniques.
Journal of Physics B: Atomic, Molecular and Optical Physics **43**, 194011 (2010).

[42] L. Young, K. Ueda, M. Gühr, P. H. Bucksbaum, M. Simon, S. Mukamel, N. Rohringer, K. C. Prince, C. Masciovecchio, M. Meyer, A. Rudenko, D. Rolles, C. Bostedt, M. Fuchs, D. A. Reis, R. Santra, H. Kapteyn, M. Murnane, H. Ibrahim, F. Légaré, M. Vrakking, M. Isinger, D. Kroon, M. Gisselbrecht, A. L. Huillier, H. J. Wörner, and S. R. Leone.
Roadmap of ultrafast x-ray atomic and molecular physics.
Journal of Physics B: Atomic, Molecular and Optical Physics **51**, 032003 (2018).

[43] A. Arthur, M. Gérad, and S. Donna.
The Nobel Prize in Physics 2018 (2018).
URL `https://www.nobelprize.org/prizes/physics/2018/summary/`.

[44] H. Mashiko, A. Suda, and K. Midorikawa.
Focusing multiple high-order harmonics in the extreme-ultraviolet and soft-x-ray regions by a platinum-coated ellipsoidal mirror.
Appl. Opt. **45**, 573–577 (Jan 2006).

[45] M. Kurka.
Zwei-Photonen-Doppelionisation von Helium und D2 -Molekülen am Freie-Elektronen-Laser in Hamburg.
PhD Thesis, Ruprecht-Karls-Universität, Heidelberg (2011).

[46] Y. Lu, Z. He, J. Cutler, S. Southworth, W. Stolte, and J. Samson.
Dissociative photoionization study of O_2.
Journal of Electron Spectroscopy and Related Phenomena **94**, 135 – 147 (1998).

[47] S. D. Price and J. H. D. Eland.
Single photon double ionization of the oxygen molecule.
Journal of Physics B: Atomic, Molecular and Optical Physics **24**, 4379 (1991).

[48] R. Feifel, J. H. D. Eland, and D. Edvardsson.

Valence double ionization of O_2 at photon energies below and above the molecular double ionization threshold.
The Journal of Chemical Physics **122**, 144308 (2005).

[49] W. Cao, G. Laurent, S. De, M. Schöffler, T. Jahnke, A. S. Alnaser, I. A. Bocharova, C. Stuck, D. Ray, M. F. Kling, I. Ben-Itzhak, T. Weber, A. L. Landers, A. Belkacem, R. Dörner, A. E. Orel, T. N. Rescigno, and C. L. Cocke.
Dynamic modification of the fragmentation of autoionizing states of O_2^+.
Phys. Rev. A **84**, 053406 (2011).

[50] W. Becker and H. Rottke.
Many-electron strong-field physics.
Contemporary Physics **49**, 199–223 (2008).

[51] A. S. Alnaser, S. Voss, X. M. Tong, C. M. Maharjan, P. Ranitovic, B. Ulrich, T. Osipov, B. Shan, Z. Chang, and C. L. Cocke.
Effects Of Molecular Structure on Ion Disintegration Patterns In Ionization of O_2 *and* N_2 *by Short Laser Pulses*.
Phys. Rev. Lett. **93**, 113003 (Sep 2004).

[52] E. Eremina, X. Liu, H. Rottke, W. Sandner, M. G. Schätzel, A. Dreischuh, G. G. Paulus, H. Walther, R. Moshammer, and J. Ullrich.
Influence of Molecular Structure on Double Ionization of N_2 *and* O_2 *by High Intensity Ultrashort Laser Pulses*.
Phys. Rev. Lett. **92**, 173001 (2004).

[53] K. Schnorr, A. Senftleben, G. Schmid, A. Rudenko, M. Kurka, K. Meyer, L. Foucar, M. Kubel, M. F. Kling, Y. H. Jiang, S. Dusterer, R. Treusch, C. D. Schroter, J. Ullrich, T. Pfeifer, and R. Moshammer.
Multiple ionization and fragmentation dynamics of molecular iodine studied in IR-XUV pump-probe experiments.
Faraday Discuss. **171**, 41–56 (2014).

[54] K. Schnorr, A. Senftleben, M. Kurka, A. Rudenko, L. Foucar, G. Schmid, A. Broska, T. Pfeifer, K. Meyer, D. Anielski, R. Boll, D. Rolles, M. Kübel, M. F. Kling, Y. H. Jiang, S. Mondal, T. Tachibana, K. Ueda, T. Marchenko, M. Simon, G. Brenner, R. Treusch, S. Scheit, V. Averbukh, J. Ullrich, C. D. Schröter, and R. Moshammer.
Time-Resolved Measurement of Interatomic Coulombic Decay in Ne_2.
Phys. Rev. Lett. **111**, 093402 (2013).

[55] G. Schmid.
Two-Color Pump-Probe Experiments on Small Quantum Systems at the Free-Electron Laser in Hamburg.
PhD Thesis, Ruprecht-Karls-Universität, Heidelberg (2018).

[56] O. Herrwerth.
Atomic and molecular ionization dynamics in strong IR and XUV fields probed by time-resolved coincidence spectroscopy.
PhD Thesis, Ludwig-Maximilians-Uniersität München (2011).

[57] M. Protopapas, C. H. Keitel, and P. L. Knight.
Atomic physics with super-high intensity lasers.
Reports on Progress in Physics **60**, 389 (1997).

[58] P. Agostini, F. Fabre, G. Mainfray, G. Petite, and N. K. Rahman.
Free-Free Transitions Following Six-Photon Ionization of Xenon Atoms.
Phys. Rev. Lett. **42**, 1127–1130 (Apr 1979).

[59] E. Cormier and P. Lambropoulos.
Above-threshold ionization spectrum of hydrogen using B-spline functions.
Journal of Physics B: Atomic, Molecular and Optical Physics **30**, 77 (1997).

[60] Wikipedia contributors.
Tunnel ionization — Wikipedia, The Free Encyclopedia.
https://en.wikipedia.org/w/index.php?title=Tunnel_ionization&oldid=856176722 (2018).
[Online; accessed 18-November-2018].

[61] M. V. Ammosov, N. B. Delone, and V. P. Krainov.
Tunnel ionization of complex atoms and of atomic ions in an alternating electromagnetic field.
Soviet Physics JETP **64**, 1191–1194 (1986).

[62] V. S. Popov.
Tunnel and multiphoton ionization of atoms and ions in a strong laser field (Keldysh theory).
Physics-Uspekhi **47**, 855 (2004).

[63] A. Wirth.
Attosecond Transient Absorption Spectroscopy.
PhD Thesis, Ludwig-Maximilians-Uniersität München (2011).

[64] A. l'Huillier, L. A. Lompre, G. Mainfray, and C. Manus.
Multiply charged ions induced by multiphoton absorption in rare gases at 0.53 μm.
Phys. Rev. A **27**, 2503–2512 (May 1983).

[65] B. Walker, B. Sheehy, L. F. DiMauro, P. Agostini, K. J. Schafer, and K. C. Kulander.
Precision-Measurement of Strong-Field Double-Ionization of Helium.
Phys. Rev. Lett. **73**, 1227–1230 (1994).

[66] M. Ferray, A. Lhuillier, X. F. Li, L. A. Lompre, G. Mainfray, and C. Manus.
Multiple-Harmonic Conversion of 1064-Nm Radiation in Rare-Gases.
J. Phys. B **21**, L31–L35 (1988).

[67] L. A. A. Nikolopoulos and P. Lambropoulos.
Helium double ionization signals under soft-x-ray coherent radiation.
Journal of Physics B: Atomic, Molecular and Optical Physics **39**, 883–893 (2006).

[68] R. W. Boyd.
Chapter 1 - The Nonlinear Optical Susceptibility.
In R. W. Boyd (Ed.), *Nonlinear Optics (Third Edition)*, third edition edition, pp. 1 – 67. Academic Press, Burlington (2008).
URL http://www.sciencedirect.com/science/article/pii/B9780123694706000010.

[69] A. Rudenko, V. L. B. de Jesus, T. Ergler, K. Zrost, B. Feuerstein, C. D. Schröter, R. Moshammer, and J. Ullrich.
Correlated Two-Electron Momentum Spectra for Strong-Field Nonsequential Double Ionization of He at 800 nm.
Phys. Rev. Lett. **99**, 263003 (Dec 2007).

[70] I. Grant.
Relativistic Quantum Theory of Atoms and Molecules: Theory and Computation.
Springer Series on Atomic, Optical, and Plasma Physics. Springer New York (2007).

[71] B. Bransden and C. Joachain.
Physics of Atoms and Molecules.
Longman Group (1983).

[72] F. Fabre, G. Petite, P. Agostini, and M. Clement.
Multiphoton above-threshold ionisation of xenon at 0.53 and 1.06 μm.
Journal of Physics B: Atomic and Molecular Physics **15**, 1353 (1982).

[73] U. Becker and D. A. Shirley.
VUV Photoionization and Soft X-Ray Photoionization.
Plenum Press (1996).

[74] G. V. Marr, J. M. Morton, R. M. Holmes, and D. G. McCoy.
Angular distribution of photoelectrons from free molecules of N_2 and CO as a function of photon energy.
Journal of Physics B: Atomic and Molecular Physics **12**, 43 (1979).

[75] I. V. Hertel and C.-P. Schulz.
Helium and Other Two Electron Systems, pp. 341–375.
Springer Berlin Heidelberg, Berlin, Heidelberg (2015).
URL `https://doi.org/10.1007/978-3-642-54322-7_7`.

[76] G. Lagmago Kamta and A. D. Bandrauk.
Imaging electron molecular orbitals via ionization by intense femtosecond pulses.
Phys. Rev. A **74**, 033415 (Sep 2006).

[77] I. Hertel and C. Schulz.
Atoms, Molecules and Optical Physics 2: Molecules and Photons - Spectroscopy and Collisions.
Springer-Lehrbuch. Springer-Verlag GmbH (2015).

[78] M. Meckel.
Strong-Field Ionization of Aligned Oxygen.
PhD Thesis, Johann Wolfgang Goethe Universität, Frankfurt am Main (2006).

[79] H. Lefebvre-Brion and R. W. Field.
The Spectra and Dynamics of Diatomic Molecules: Revised and Enlarged Edition.
Academic Press, New York (2004).

[80] R. Schinke.
Photodissociation Dynamics.
Cambridge University Press (1993).

[81] W. Eberhardt, G. Kalkoffen, and C. Kunz.
Measurement of the Auger Decay after Resonance Excitation of Xe 4*d and Kr* 3*d Resonance Lines*.
Phys. Rev. Lett. **41**, 156–159 (Jul 1978).

[82] W. Eberhardt, E. W. Plummer, I. W. Lyo, R. Carr, and W. K. Ford.
Auger-electron ion coincidence studies of soft-x-ray–induced fragmentation of N_2.
Phys. Rev. Lett. **58**, 207–210 (Jan 1987).

[83] E. Gagnon, P. Ranitovic, X.-M. Tong, C. L. Cocke, M. M. Murnane, H. C. Kapteyn, and A. S. Sandhu.
Soft X-ray-Driven Femtosecond Molecular Dynamics.
Science **317**, 1374–1378 (2007).

[84] S. Hsieh and J. H. D. Eland.
Direct and indirect dissociative double photoionization of diatomic molecules.
Journal of Physics B: Atomic, Molecular and Optical Physics **29**, 5795 (1996).

[85] R. Zare.
Photoejection Dynamics.
Mol. Photochem. **4**, 1–37 (Nov. 1972).

[86] Y. H. Jiang, A. Rudenko, M. Kurka, K. U. Kühnel, T. Ergler, L. Foucar, M. Schöffler, S. Schössler, T. Havermeier, M. Smolarski, K. Cole, R. Dörner, S. Düsterer, R. Treusch, M. Gensch, C. D. Schröter, R. Moshammer, and J. Ullrich.
Few-Photon Multiple Ionization of $\mathbf{N}_2$ *by Extreme Ultraviolet Free-Electron Laser Radiation*.
Phys. Rev. Lett. **102**, 123002 (2009).

[87] Y. H. Jiang, A. Rudenko, J. F. Pérez-Torres, O. Herrwerth, L. Foucar, M. Kurka, K. U. Kühnel, M. Toppin, E. Plésiat, F. Morales, F. Martín, M. Lezius, M. F. Kling, T. Jahnke, R. Dörner, J. L. Sanz-Vicario, J. van Tilborg, A. Belkacem, M. Schulz, K. Ueda, T. J. M. Zouros, S. Düsterer, R. Treusch, C. D. Schröter, R. Moshammer, and J. Ullrich.
Investigating two-photon double ionization of D_2 *by XUV-pump–XUV-probe experiments*.
Phys. Rev. A **81**, 051402 (May 2010).

[88] B. Paulus, J. F. Pérez-Torres, and C. Stemmle.
Time-dependent description of the predissociation of $N_2{}^+$ *in the* $C^2\Sigma_u{}^+$ *state*.
Phys. Rev. A **94**, 053423 (Nov 2016).

[89] W. Helml, I. Grgura, P. N. Jurani, S. Düsterer, T. Mazza, A. R. Maier, N. Hartmann, M. Ilchen, G. Hartmann, L. Patthey, C. Callegari, J. T. Costello, M. Meyer, R. N. Coffee, A. L. Cavalieri, and R. Kienberger.
Ultrashort Free-Electron Laser X-ray Pulses.
Applied Sciences **7** (2017).

[90] R. Moshammer, Y. H. Jiang, L. Foucar, A. Rudenko, T. Ergler, C. D. Schroter, S. Ludemann, K. Zrost, D. Fischer, J. Titze, T. Jahnke, M. Schoffler, T. Weber, R. Dorner, T. J. M. Zouros, A. Dorn, T. Ferger, K. U. Kuhnel, S. Dusterer, R. Treusch, P. Radcliffe, E. Ploenjes, and J. Ullrich.
Few-photon multiple ionization of Ne and Ar by strong free-electron-laser pulses.
Phys. Rev. Lett. **98**, 203001 (2007).

[91] K. Meyer, C. Ott, P. Raith, A. Kaldun, Y. Jiang, A. Senftleben, M. Kurka, R. Moshammer, J. Ullrich, and T. Pfeifer.
Noisy Optical Pulses Enhance the Temporal Resolution of Pump-Probe Spectroscopy.
Phys. Rev. Lett. **108**, 098302 (2012).

[92] P. Schmüser, M. Dohlus, J. Rossbach, and C. Behrens.
Low-Gain FEL Theory, pp. 25–38.
Springer International Publishing, Cham (2014).
URL `https://doi.org/10.1007/978-3-319-04081-3_3`.

[93] S. Ackermann.
Experimental and numerical investigations on seeding options for the multi-beam line Free-Electron Laser facility FLASH.
PhD Thesis, Universität Hamburg (2016).

[94] J. M. J. Madey.
Stimulated Emission of Bremsstrahlung in a Periodic Magnetic Field.
J. Appl. Phys. **42**, 1906 –1913 (1971).

[95] T. Ding.
Quantum dynamics in weak and strong fields measured by XUV nonlinear spectroscopy.
PhD Thesis, Ruprecht-Karls-Universität, Heidelberg (2018).

[96] B. W. J. McNeil and N. R. Thompson.
X-ray free-electron lasers.
Nat Photon **4**, 814–821 (December 2010).

[97] S. Jamison.
X-ray FEL shines brightly.
Nature Photonics **4**, 589 (2010).

[98] B. Faatz et al.
Simultaneous operation of two soft x-ray free-electron lasers driven by one linear accelerator.
New Journal of Physics **18**, 062002 (2016).

[99] H. Redlin, A. Al-Shemmary, A. Azima, N. Stojanovic, F. Tavella, I. Will, and S. Düsterer.
The FLASH pump-probe laser system: Setup, characterization and optical beamlines.
Nuclear Instruments and Methods in Physics Research Section A: Accelerators, Spectrometers, Detectors and Associated Equipment **635**, S88 – S93 (2011).

[100] M. Meyer, D. Cubaynes, J. Dardis, P. Hayden, P. Hough, V. Richardson, E. Kennedy, J. Costello, S. Düsterer, W. Li, P. Radcliffe, H. Redlin, J. Feldhaus, S. Strakhova, E. Gryzlova, A. Grum-Grzhimailo, R. Taïeb, and A. Maquet.
Two-color experiments in the gas phase at FLASH.
Journal of Electron Spectroscopy and Related Phenomena **181**, 111 – 115 (2010).

[101] K. Tiedtke, A. Azima, N. von Bargen, L. Bittner, S. Bonfigt, S. DÃijsterer, B. Faatz, U. Fruehling, M. Gensch, C. Gerth, N. Guerassimova, U. Hahn, T. Hans, M. Hesse, K. Honkavaar, U. Jastrow, P. Juranic, S. Kapitzki, B. Keitel, T. Kracht, M. Kuhlmann, W. B. Li, M. Martins, T. Nunez, E. PlÃűnjes, H. Redlin, E. L. Saldin, E. A. Schneidmiller, J. R. Schneider, S. Schreiber, N. Stojanovic, F. Tavella, S. Toleikis, R. Treusch, H. Weigelt, M. Wellhoefer, H. Wabnitz, M. V. Yurkov, and J. Feldhaus.
The soft x-ray free-electron laser FLASH at DESY: beamlines, diagnostics and end-stations.
New Journal of Physics **11**, 023029 (2009).

[102] R. Pan, E. Zapolnova, T. Golz, A. J. Krmpot, M. D. Rabasovic, J. Petrovic, V. Asgekar, B. Faatz, F. Tavella, A. Perucchi, S. Kovalev, B. Green, G. Geloni, T. Tanikawa, M. Yurkov, E. Schneidmiller, M. Gensch, and N. Stojanovic.
Photon diagnostics at the FLASH THz beamline.
Journal of Synchrotron Radiation **26**, 700–707 (2019).

[103] M. Gensch, L. Bittner, A. Chesnov, H. Delsim-Hashemi, M. Drescher, B. Faatz, J. Feldhaus, U. Fruehling, G. Geloni, C. Gerth, O. Grimm, U. Hahn, M. Hesse, S. Kapitzki, V. Kocharyan, O. Kozlov, E. Matyushevsky, N. Morozov, D. Petrov, E. Ploenjes, M. Roehling, J. Rossbach, E. Saldin, B. Schmidt, P. Schmueser, E. Schneidmiller, E. Syresin, A. Willner, and M. Yurkov.
New infrared undulator beamline at FLASH.
Infrared Physics and Technology **51**, 423 – 425 (2008).

[104] J. Feldhaus, O. Grimm, O. Kozlov, E. Plönjes, J. Rossbach, E. Saldin, E. Schneidmiller, and M. Yurkov.
The Infrared Undulator Project at the VUV-FEL.
In *Proceedings of FEL 2005, Stanford, California, USA* (2005).

[105] U. Fruhling, M. Wieland, M. Gensch, T. Gebert, B. Schutte, M. Krikunova, R. Kalms, F. Budzyn, O. Grimm, J. Rossbach, E. Plonjes, and M. Drescher.
Single-shot terahertz-field-driven X-ray streak camera.
Nat Photonics **3**, 523–528 (Sept 2009).

[106] N. Stojanovic and M. Drescher.
Accelerator- and laser-based sources of high-field terahertz pulses.
Journal of Physics B: Atomic, Molecular and Optical Physics **46**, 192001 (2013).

[107] T. Kampfrath, K. Tanaka, and K. A. Nelson.
Resonant and nonresonant control over matter and light by intense terahertz transients.
Nat Photonics **7**, 680–690 (Sept 2013).

[108] S. Birkner.
Strong Field Ionization of Atoms and Molecules: Electron-Ion Coincidence Measurements at High Repetition Rate.
PhD Thesis, Freien Uniersität Berlin (2015).

[109] B. Rudek.
Multiple Ionization of Heavy Atoms by Intense X-Ray Free-Electron Laser Pulses.
PhD Thesis, Ruprecht-Karls-Universität, Heidelberg (2012).

[110] C. Benvenuti, J. Cazeneuve, P. Chiggiato, F. Cicoira, A. E. Santana, V. Johanek, V. Ruzinov, and J. Fraxedas.
A novel route to extreme vacua: the non-evaporable getter thin film coatings.
Vacuum **53**, 219 – 225 (1999).

[111] D. R. Miller.
Free jet sources, volume 1, pp. 14–53.
Oxford University Press (1988).

[112] R. Moshammer, D. Fischer, and H. Kollmus.
Recoil-Ion Momentum Spectroscopy and "Reaction Microscopes", volume 35 of *Springer Series on Atomic, Optical, and Plasma Physics*, chapter 2, pp. 33–58.
Springer Berlin Heidelberg (2003).

[113] O. Jagutzki, V. Mergel, K. Ullmann-Pfleger, L. Spielberger, U. Spillmann, R. Dörner, and H. Schmidt-Böcking.
A broad-application microchannel-plate detector system for advanced particle or photon detection tasks: large area imaging, precise multi-hit timing information and high detection rate.
Nuclear Instruments and Methods in Physics Research Section A: Accelerators, Spectrometers, Detectors and Associated Equipment **477**, 244 – 249 (2002).
5th Int. Conf. on Position-Sensitive Detectors.

[114] W. Demtröder.
Der elektrische Strom, pp. 43–82.
Springer Berlin Heidelberg, Berlin, Heidelberg (2013).

[115] A. Senftleben.
Kinematically complete study on electron impact ionisation of aligned hydrogen molecules.
PhD Thesis, Ruprecht-Karls-Universität, Heidelberg (2009).

[116] L. R. Moore, M. A. Lysaght, J. S. Parker, H. W. van der Hart, and K. T. Taylor.
Time delay between photoemission from the $2p$ *and* $2s$ *subshells of neon*.
Phys. Rev. A **84**, 061404 (Dec 2011).

[117] R. Kienberger, E. Goulielmakis, M. Uiberacker, A. Baltuska, V. Yakovlev, F. Bammer, A. Scrinzi, T. Westerwalbesloh, U. Kleineberg, U. Heinzmann, M. Drescher, and F. Krausz.
Atomic transient recorder.
Nature Phys. **427**, 123002 (2004).

[118] A. L. Cavalieri, N. Müller, T. Uphues, V. S. Yakovlev, A. Baltuška, B. Horvath, B. Schmidt, L. Blümel, R. Holzwarth, S. Hendel, M. Drescher, U. Kleineberg, P. M. Echenique, R. Kienberger, F. Krausz, and U. Heinzmann.
Attosecond spectroscopy in condensed matter.
Nature **449**, 1029–1032 (2007).

[119] P. B. Corkum and F. Krausz.
Attosecond science.
Nat. Physics **3**, 381–387 (2007).

[120] M. Drescher, M. Hentschel, R. Kienberger, M. Uiberacker, V. Yakovlev, A. Scrinzi, T. Westerwalbesloh, U. Kleineberg, U. Heinzmann, and F. Krausz.
Time-resolved atomic inner-shell spectroscopy.
Nature **419**, 803–807 (2002).

[121] D. M. Villeneuve.
Attosecond science.
Contemporary Physics **59**, 47–61 (2018).

[122] R. P. Heider.
Attosecond Metrology ? Characterization of X-ray Free-electron Laser Pulses via Angular Streaking and Application of Attosecond Spectroscopy on Liquid H_2O.
PhD Thesis, Technischen Uniersität München (2018).

[123] J. Itatani, F. Quéré, G. L. Yudin, M. Y. Ivanov, F. Krausz, and P. B. Corkum.
Attosecond Streak Camera.
Phys. Rev. Lett. **88**, 173903 (2002).

[124] G. Schmid.
XUV-pump THz-probe experiments on Neon at the Free-Electron Laser in Hamburg.
Master's thesis, Ruprecht-Karls-Universität, Heidelberg (2013).

[125] I. Grguras, A. R. Maier, C. Behrens, T. Mazza, T. J. Kelly, P. Radcliffe, S. Dusterer, A. K. Kazansky, N. M. Kabachnik, T. Tschentscher, J. T. Costello, M. Meyer, M. C. Hoffmann, H. Schlarb, and A. L. Cavalieri.
Ultrafast X-ray pulse characterization at free-electron lasers.
Nat Photonics **6**, 852–857 (Dec 2012).

[126] Y. Liu, K. Schnorr, G. Schmid, S. Augustin, S. Meister, H. Lindenblatt, A. Rudenko, M. Kübel, C. Burger, N. Stojanovic, R. Treusch, S. Düsterer, T. Jahnke, M. Kling, C. Schröter, T. Pfeifer, and R. Moshammer.
THz Streaking of the Autoionization Dynamics of O_2 at the Free-Electron-Laser FLASH.
Journal of Physics: Conference Series **875**, 032031 (2017).

[127] F. Tavella, N. Stojanovic, G. Geloni, and M. Gensch.
Few-femtosecond timing at fourth-generation X-ray light sources.
Nat Photonics **5**, 162–165 (Nov 2011).

[128] M. Hentschel, R. Kienberger, C. Spielmann, G. A. Reider, N. Milosevic, T. Brabec, P. Corkum, U. Heinzmann, M. Drescher, and F. Krausz.
Attosecond metrology.
Nature **414**, 509–513 (2001).

[129] M. Drescher, M. Hentschel, R. Kienberger, G. Tempea, C. Spielmann, G. A. Reider, P. B. Corkum, and F. Krausz.
X-ray Pulses Approaching the Attosecond Frontier.
Science **291**, 1923–1927 (2001).

[130] E. Goulielmakis, M. Uiberacker, R. Kienberger, A. Baltuška, V. Yakovlev, A. Scrinzi, T. Westerwalbesloh, U. Kleineberg, U. Heinzmann, M. Drescher, and F. Krausz.
Direct measurement of light waves.
Science **305**, 1267–1269 (2004).

[131] G. Schmid, K. Schnorr, S. Augustin, S. Meister, H. Lindenblatt, F. Trost, Y. Liu, N. Stojanovic, A. Al-Shemmary, T. Golz, R. Treusch, M. Gensch, M. Kübel, L. Foucar, A. Rudenko, J. Ullrich, C. D. Schröter, T. Pfeifer, and R. Moshammer.
Terahertz-Field-Induced Time Shifts in Atomic Photoemission.
Phys. Rev. Lett. **122**, 073001 (2019).

[132] X. Song, G. Shi, G. Zhang, J. Xu, C. Lin, J. Chen, and W. Yang.
Attosecond Time Delay of Retrapped Resonant Ionization.
Phys. Rev. Lett. **121**, 103201 (Sep 2018).

[133] M. Schultze, M. Fiess, N. Karpowicz, J. Gagnon, M. Korbman, M. Hofstetter, S. Neppl, A. L. Cavalieri, Y. Komninos, T. Mercouris, C. A. Nicolaides, R. Pazourek, S. Nagele, J. Feist, J. Burgdorfer, A. M. Azzeer, R. Ernstorfer, R. Kienberger, U. Kleineberg, E. Goulielmakis, F. Krausz, and V. S. Yakovlev.
Delay in Photoemission.
Science **328**, 1658–1662 (2010).

[134] P. Eckle, A. N. Pfeiffer, C. Cirelli, A. Staudte, R. Dörner, H. G. Muller, M. Büttiker, and U. Keller.
Attosecond Ionization and Tunneling Delay Time Measurements in Helium.
Science **322**, 1525–1529 (2008).

[135] J. M. Dahlström, M. Vacher, A. Maquet, J. Caillat, and S. Haessler.
Photoionization Time Delays, pp. 177–202.
Springer International Publishing, Cham (2016).

[136] P. Hockett, E. Frumker, D. M. Villeneuve, and P. B. Corkum.
Time delay in molecular photoionization.
Journal of Physics B: Atomic, Molecular and Optical Physics **49**, 095602 (2016).

[137] J. M. Dahlström, A. L.Huillier, and A. Maquet.
Introduction to attosecond delays in photoionization.
Journal of Physics B: Atomic, Molecular and Optical Physics **45**, 183001 (2012).

[138] E. P. Wigner.
Lower Limit for the Energy Derivative of the Scattering Phase Shift.
Phys. Rev. **98**, 145–147 (Apr 1955).

[139] F. T. Smith.
Lifetime Matrix in Collision Theory.
Phys. Rev. **118**, 349–356 (Apr 1960).

[140] L. Eisenbud.
The formal properties of nuclear collisions.
Dissertation, Princeton University (1948).

[141] C.-H. Zhang and U. Thumm.
Streaking and Wigner time delays in photoemission from atoms and surfaces.
Physical Review A **84**, 033401 (2011).

[142] R. Pazourek, S. Nagele, and J. Burgdorfer.
Time-resolved photoemission on the attosecond scale: opportunities and challenges.
Faraday Discuss. **163**, 353–376 (2013).

[143] R. Pazourek, S. Nagele, and J. Burgdörfer.
Attosecond chronoscopy of photoemission.
Rev. Mod. Phys. **87**, 765–802 (Aug 2015).

[144] J. Dahlström, A. LHuillier, and A. Maquet.
Introduction to attosecond delays in photoionization.
Journal of Physics B: Atomic, Molecular and Optical Physics **45**, 183001 (2012).

[145] R. Pazourek, S. Nagele, K. Doblhoff-Dier, J. Feist, C. Lemell, K. Tökési, and J. Burgdörfer.
Probing scattering phase shifts by attosecond streaking.
Journal of Physics: Conference Series **388**, 012029 (nov 2012).

[146] M. Ivanov and O. Smirnova.
How accurate is the attosecond streak camera?
Phys. Rev. Lett. **107**, 213605 (2011).

[147] V. V. Serov, V. L. Derbov, and T. A. Sergeeva.
Interpretation of the time delay in the ionization of Coulomb and two-center systems.
arXiv preprint arXiv:1304.2686 (2013).

[148] E. Gagnon, P. Ranitovic, X. M. Tong, C. L. Cocke, M. M. Murnane, H. C. Kapteyn, and A. S. Sandhu.
Soft X-ray-driven femtosecond molecular dynamics.
Science **317**, 1374–1378 (2007).

[149] E. Gagnon.
Femtosecond molecular dynamics driven by extreme ultra violet radiation.
PhD Thesis, University of Colorado (2008).

[150] P. Johnsson, W. Siu, A. Gijsbertsen, J. Verhoeven, A. Meijer, W. Van Der Zande, and M. Vrakking.
Velocity map imaging of atomic and molecular processes at the free electron laser in Hamburg (FLASH).
Journal of Modern Optics **55**, 2693–2709 (2008).

[151] H. Timmers, N. Shivaram, and A. Sandhu.
Ultrafast Dynamics of Neutral Superexcited Oxygen: A Direct Measurement of the Competition between Autoionization and Predissociation.
Phys. Rev. Lett. **109**, 173001 (Oct 2012).

[152] L.-E. Berg, P. Erman, E. Källne, S. Sorensen, and G. Sundström.
Synchrotron radiation study of photoionization and photodissociation processes of O_2 in the 12-26 eV region.
Physica Scripta **44**, 328–335 (oct 1991).

[153] Y. Hikosaka, T. Aoto, R. I. Hall, K. Ito, R. Hirayama, N. Yamamoto, and E. Miyoshi.
Inner-valence states of O_2^+ and dissociation dynamics studied by threshold photoelectron spectroscopy and a configuration interaction calculation.
The Journal of Chemical Physics **119**, 7693–7700 (2003).

[154] M. Lundqvist, D. Edvardsson, P. Baltzer, M. Larsson, and B. Wannberg.
Observation of predissociation and tunnelling processes in O_2^{2+}: a study using Doppler free kinetic energy release spectroscopy and ab initio CI calculations.
Journal of Physics B: Atomic, Molecular and Optical Physics **29**, 499 (1996).

[155] J. L. Gardner and J. A. R. Samson.
Photoion and photoelectron spectroscopy of oxygen.
The Journal of Chemical Physics **62**, 4460–4463 (1975).

[156] J. A. Samson, J. Gardner, and G. Haddad.
Total and partial photoionization cross-sections of O_2 from 100 to 800 Å.
Journal of Electron Spectroscopy and Related Phenomena **12**, 281 – 292 (1977).

[157] A. S. Alnaser, B. Ulrich, X. M. Tong, I. V. Litvinyuk, C. M. Maharjan, P. Ranitovic, T. Osipov, R. Ali, S. Ghimire, Z. Chang, C. D. Lin, and C. L. Cocke.
Simultaneous real-time tracking of wave packets evolving on two different potential curves in $H_2{}^+$ and $D_2{}^+$.
Phys. Rev. A **72**, 030702 (Sep 2005).

[158] F. Légaré, K. F. Lee, I. V. Litvinyuk, P. W. Dooley, A. D. Bandrauk, D. M. Villeneuve, and P. B. Corkum.
Imaging the time-dependent structure of a molecule as it undergoes dynamics.
Phys. Rev. A **72**, 052717 (Nov 2005).

[159] M. Magrakvelidze, O. Herrwerth, Y. H. Jiang, A. Rudenko, M. Kurka, L. Foucar, K. U. Kühnel, M. Kübel, N. G. Johnson, C. D. Schröter, S. Düsterer, R. Treusch, M. Lezius, I. Ben-Itzhak, R. Moshammer, J. Ullrich, M. F. Kling, and U. Thumm.
Tracing nuclear-wave-packet dynamics in singly and doubly charged states of N_2 and O_2 with XUV-pump–XUV-probe experiments.
Phys. Rev. A **86**, 013415 (Jul 2012).

[160] M. Eckstein, C.-H. Yang, M. Kubin, F. Frassetto, L. Poletto, H.-H. Ritze, M. J. J. Vrakking, and O. Kornilov.
Dynamics of N_2 Dissociation upon Inner-Valence Ionization by Wavelength-Selected XUV Pulses.
The Journal of Physical Chemistry Letters **6**, 419–425 (2015).

[161] D. J. Hollenbach and A. G. G. M. Tielens.
Photodissociation regions in the interstellar medium of galaxies.
Rev. Mod. Phys. **71**, 173–230 (Jan 1999).

[162] T. Weber, O. Jagutzki, M. Hattass, A. Staudte, A. Nauert, L. Schmidt, M. H. Prior, A. L. Landers, A. Bräuning-Demian, H. Bräuning, C. L. Cocke, T. Osipov, I. Ali, R. D. Muiño, D. Rolles, F. J. G. de Abajo, C. S. Fadley, M. A. V. Hove, A. Cassimi, H. Schmidt-Böcking, and R. Dörner.
K-shell photoionization of CO and N_2: is there a link between the photoelectron angular distribution and the molecular decay dynamics?
Journal of Physics B: Atomic, Molecular and Optical Physics **34**, 3669 (2001).

[163] M. Ahmad, P. Lablanquie, F. Penent, J. G. Lambourne, R. I. Hall, and J. H. D. Eland.
Structure and fragmentation dynamics of N_2^{2+} ions in double photoionization experiments.
Journal of Physics B: Atomic, Molecular and Optical Physics **39**, 3599 (2006).

[164] M. S. Schöffler, J. Titze, N. Petridis, T. Jahnke, K. Cole, L. P. H. Schmidt, A. Czasch, D. Akoury, O. Jagutzki, J. B. Williams, N. A. Cherepkov, S. K. Semenov, C. W. McCurdy, T. N. Rescigno, C. L. Cocke, T. Osipov, S. Lee, M. H. Prior, A. Belkacem, A. L. Landers, H. Schmidt-Böcking, T. Weber, and R. Dörner.
Ultrafast Probing of Core Hole Localization in N_2.
Science **320**, 920–923 (2008).

[165] J. Viefhaus, R. Dörner, V. McKoy, and U. a. Becker.
Localization and loss of coherence in molecular double-slit experiments.
Nat. Physics **4**, 649 (2008).

[166] B. Schütte, F. Campi, M. Arbeiter, T. Fennel, M. J. J. Vrakking, and A. Rouzée.
Tracing Electron-Ion Recombination in Nanoplasmas Produced by Extreme-Ultraviolet Irradiation of Rare-Gas Clusters.
Phys. Rev. Lett. **112**, 253401 (2014).

[167] X. M. Tong, P. Ranitovic, C. W. Hogle, M. M. Murnane, H. C. Kapteyn, and N. Toshima.
Theory and experiment on laser-enabled inner-valence Auger decay of rare-gas atoms.
Phys. Rev. A **84**, 013405 (Jul 2011).

[168] C. Cornaggia and P. Hering.
Nonsequential double ionization of small molecules induced by a femtosecond laser field.
Phys. Rev. A **62**, 023403 (2000).

[169] Lucchini, Matteo, Seung Kim, Kyung, Calegari, Francesca, Kelkensberg, Freek, Siu, Wing Kiu, Sansone, Giuseppe, Vrakking, Marc J.J., Hochlaf, Majdi, and Nisoli, Mauro.
Ultrafast Relaxation Dynamics of Highly-excited States in N2 Molecules Excited by Femtosecond XUV Pulses.
EPJ Web of Conferences **41**, 02004 (2013).

[170] M. Lundqvist, D. Edvardsson, P. Baltzer, and B. Wannberg.
Doppler-free kinetic energy release spectrum of N_2^{2+}.
Journal of Physics B: Atomic, Molecular and Optical Physics **29**, 1489 (1996).

[171] A. Pandey, B. Bapat, and K. R. Shamasundar.
Charge symmetric dissociation of doubly ionized N2 and CO molecules.
The Journal of Chemical Physics **140**, 034319 (2014).

[172] T. Aoto, K. Ito, Y. Hikosaka, A. Shibasaki, R. Hirayama, N. Yamamono, and E. Miyoshi.
Inner-valence states of N_2^+ and the dissociation dynamics studied by threshold photoelectron spectroscopy and configuration interaction calculation.
The Journal of Chemical Physics **124**, 234306 (2006).

[173] S. Voss, A. S. Alnaser, X.-M. Tong, C. Maharjan, P. Ranitovic, B. Ulrich, B. Shan, Z. Chang, C. D. Lin, and C. L. Cocke.
High resolution kinetic energy release spectra and angular distributions from double ionization of nitrogen and oxygen by short laser pulses.
Journal of Physics B: Atomic, Molecular and Optical Physics **37**, 4239 (2004).

[174] X. M. Tong, Z. X. Zhao, and C. D. Lin.
Theory of molecular tunneling ionization.
Phys. Rev. A **66**, 033402 (Sep 2002).

[175] R. Moshammer, Y. H. Jiang, L. Foucar, A. Rudenko, T. Ergler, C. D. Schröter, S. Lüdemann, K. Zrost, D. Fischer, J. Titze, T. Jahnke, M. Schöffler, T. Weber, R. Dörner, T. J. M. Zouros, A. Dorn, T. Ferger, K. U. Kühnel, S. Düsterer, R. Treusch, P. Radcliffe, E. Plönjes, and J. Ullrich.
Few-Photon Multiple Ionization of Ne and Ar by Strong Free-Electron-Laser Pulses.
Phys. Rev. Lett. **98**, 203001 (May 2007).

[176] M. Eckstein.
Investigation of Ultrafast Electronic and Nuclear Dynamics in Molecular Nitrogen using an XUV Time Delay Compensating Monochromator.
PhD Thesis, Freien Universität Berlin (2015).

[177] P. Franceschi, D. Ascenzi, P. Tosi, R. Thissen, J. abka, J. Roithová, C. L. Ricketts, M. De Simone, and M. Coreno.
Dissociative double photoionization of N_2 using synchrotron radiation: Appearance energy of the N_2^+ dication.
The Journal of Chemical Physics **126** (2007).

[178] K. Boyer, T. S. Luk, J. C. Solem, and C. K. Rhodes.
Kinetic energy distributions of ionic fragments produced by subpicosecond multiphoton ionization of N_2.
Phys. Rev. A **39**, 1186–1192 (Feb 1989).

[179] C. Cornaggia, J. Lavancier, D. Normand, J. Morellec, and H. X. Liu.
Intensity dependence of the multielectron dissociative ionization of N_2 *at 305 and 610 nm*.
Phys. Rev. A **42**, 5464–5472 (1990).

[180] H. Iwayama, T. Kaneyasu, Y. Hikosaka, and E. Shigemasa.
Stability and dissociation dynamics of N_2^{++} *ions following core ionization studied by an Auger-electron photoion coincidence method*.
The Journal of Chemical Physics **145**, 034305 (2016).

[181] A. D. Bandrauk, D. G. Musaev, and K. Morokuma.
Electronic states of the triply charged molecular ion N_2^{3+} *and laser-induced Coulomb explosion*.
Phys. Rev. A **59**, 4309–4315 (Jun 1999).

[182] I. V. Litvinyuk, K. F. Lee, P. W. Dooley, D. M. Rayner, D. M. Villeneuve, and P. B. Corkum.
Alignment-Dependent Strong Field Ionization of Molecules.
Phys. Rev. Lett. **90**, 233003 (Jun 2003).

[183] D. Pavičić, K. F. Lee, D. M. Rayner, P. B. Corkum, and D. M. Villeneuve.
Direct Measurement of the Angular Dependence of Ionization for N_2*,* O_2*, and* CO_2 *in Intense Laser Fields*.
Phys. Rev. Lett. **98**, 243001 (Jun 2007).

[184] H. Niikura, F. Legare, R. Hasbani, A. D. Bandrauk, M. Y. Ivanov, D. M. Villeneuve, and P. B. Corkum.
Sub-laser-cycle electron pulses for probing molecular dynamics.
Nature **417**, 917–922 (2002).

[185] T. Seideman, M. Y. Ivanov, and P. B. Corkum.
Role of Electron Localization in Intense-Field Molecular Ionization.
Phys. Rev. Lett. **75**, 2819–2822 (Oct 1995).

[186] D. Ray, F. He, S. De, W. Cao, H. Mashiko, P. Ranitovic, K. P. Singh, I. Znakovskaya, U. Thumm, G. G. Paulus, M. F. Kling, I. V. Litvinyuk, and C. L. Cocke.
Ion-Energy Dependence of Asymmetric Dissociation of $\mathbf{D}_2$ *by a Two-Color Laser Field*.
Phys. Rev. Lett. **103**, 223201 (2009).

[187] G. Schmid, K. Schnorr, S. Augustin, S. Meister, H. Lindenblatt, F. Trost, Y. Liu, M. Braune, R. Treusch, C. D. Schröter, T. Pfeifer, and R. Moshammer.
Reaction microscope endstation at FLASH2.
Journal of Synchrotron Radiation **26**, 854–867 (2019).

[188] H. T. Lemke, K. S. Kjær, R. Hartsock, T. B. van Driel, M. Chollet, J. M. Glownia, S. Song, D. Zhu, E. Pace, S. F. Matar, M. M. Nielsen, M. Benfatto, K. J. Gaffney, E. Collet, and M. Cammarata.
Coherent structural trapping through wave packet dispersion during photoinduced spin state switching.
Nat Communications **8**, 15342 (May 2017).

[189] N. Ekanayake, T. Severt, M. Nairat, N. P. Weingartz, B. M. Farris, B. Kaderiya, P. Feizollah, B. Jochim, F. Ziaee, K. Borne, K. Raju P., K. D. Carnes, D. Rolles, A. Rudenko, B. G. Levine, J. E. Jackson, I. Ben-Itzhak, and M. Dantus.
H_2 roaming chemistry and the formation of H_3^+ from organic molecules in strong laser fields.
Nature Communications **9**, 5186 (December 2018).

[190] A. R. Attar, A. Bhattacherjee, C. D. Pemmaraju, K. Schnorr, K. D. Closser, D. Prendergast, and S. R. Leone.
Femtosecond x-ray spectroscopy of an electrocyclic ring-opening reaction.
Science **356**, 54–59 (2017).

[191] X. Ren, E. Wang, A. D. Skitnevskaya, A. B. Trofimov, K. Gokhberg, and A. Dorn.
Experimental evidence for ultrafast intermolecular relaxation processes in hydrated biomolecules.
Nat. Physics **14**, 1062–1066 (2018).